Understanding the Effects of Mineralogy, Ore Texture and Microwave Power Delivery on Microwave Treatment of Ores

by

Abubeker Yimam Ali

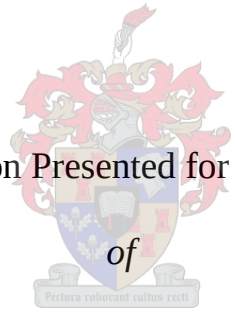

Dissertation Presented for the Degree

of

DOCTOR OF PHILOSOPHY (CHEMICAL ENGINEERING)

In the Department of Process Engineering
At the University of Stellenbosch

Promoter

Prof S. M. Bradshaw

STELLENBOSCH

March 2010

Declaration

I, the undersigned, hereby declare that the work contained in this thesis is my own original work and that I have not previously in its entirety or in part, submitted it at any university for a degree.

Signature

Abubeker Yimam Ali

Name in full

05 / 02 / 2010

Date

Synopsis

Previous work has shown that microwave heating of mineral ores induces fractures around grain boundaries due to the differences in absorption of microwaves and the resulting differential thermal expansion among the various mineral phases in the ore particles. As a consequence, this reduces the energy required in subsequent grinding and enhances liberation of valuable minerals. In this study, first, the influences of different variables on bulk strength reduction of microwave treated ores have been investigated. Nine different binary ore models were constructed by randomly disseminating 10 vol.% microwave absorbing minerals in transparent matrices. Computational simulations of heating, thermal damage and unconfined compressive strength (UCS) tests on the conceptual binary ores have been undertaken by using finite-difference modelling techniques. The influence of thermo-mechanical properties of minerals on strength reduction of microwave treated ores was examined. It was shown that in general the thermal properties of the microwave absorbing mineral and the mechanical properties of the transparent matrix have the most significant effect on the strength reduction. Binary ores containing a microwave absorbing mineral that has a high thermal expansion coefficient in a strong transparent matrix achieved higher reductions in strength. The influence of absorbent phase grain size on strength reduction of ores was also quantified. It was shown that for the same energy inputs and mineral types, the reductions in strength were much higher in coarse-grained ores. It has also been shown that for the same mineralogy and treatment condition, ores with poorly disseminated heated phase achieved much higher strength reduction. The effect of microwave treatment on the mechanical state of an ore sample was also examined. It was demonstrated that unconfined compressive strength is less sensitive to microwave-induced micro-fractures and found to be a poor descriptor of liberation behaviour.

A new method of characterizing damage in microwave treated ore using a continuum approach was developed. The method measures the damage around the grain boundary regions during the heating process. Using the method, it was possible to elucidate in detail the influences of power density, mineralogy, ore texture on microwave treatment of ore. It was shown that the amount of grain boundary damage incurred at a specific power density and energy input is dependent both on the ore

mineralogy and its texture. The energy inputs that were required for significant (> 10%) grain boundary damage in the ores range from 0.09 to 7.06 kWh/t depending on the power density applied, the ore mineralogy and its texture. It was also shown that for a given mineralogy and ore texture there is a power density level below which no further increase in grain boundary damage is possible by increasing exposure time. The effect of pulse repetition frequency on grain boundary damage was also elucidated using the method. It was found that high pulse repetition frequencies (≥ 50 Hz) resulted in an amount of grain boundary damage that was indistinguishable from that caused by continuous wave operation for a fixed energy input. It has also been shown that for a fixed microwave energy input the best result would be obtained by using the lowest possible pulse repetition frequency and highest peak pulse power.

The effect of microwave treatment of ores at different treatment conditions on the extent of damage and crack pattern was also investigated in detail using bonded-particle model (BPM). It has been shown that the amount of micro-cracks and also the cracks pattern in an ore sample after microwave treatment significantly depend on its mineralogy, microwave treatment condition (power density) and absorbent phase grain size. It has also been shown that a minimum power density is required to localize damage around the grain boundary in an ore sample. This minimum power density was found to strongly depend on the ore mineralogy and its texture.

Initial simulation test work concerning the effect of microwave treatment on liberation of minerals is also presented. It has been shown that microwave irradiation considerably changed the fracture pattern of an ore in simulated single particle crushing. The fracture pattern of the ore treated at high power density (P_d *= 0.1 kW /mm*^{3}*abs for 1 ms*) *was along the grain boundary and the absorbent mineral was intact. In the ore treated at lower power density for the same energy input* (P_d *= 1 W/mm*^{3}*abs for 0.1 s) both intergranular and transgranular fractures were observed. However, in all cases the fracture patterns were preferentially localized around the grain boundary compared to that of the untreated ore.*

Opsomming

Vorige studies het getoon dat mikrogolfverhitting van mineraalertse tot breuke om die ertskorrelgrense aanleiding gee, omdat die verskillende mineraalfases in die ertsdeeltjies die mikrogolwe verskillend absorbeer, en dus ook verskillend uitsit. Korrelgrensbreuke verminder die vereiste energie vir latere slypwerk, en verhoog die vrystelling van waardevolle minerale. Hierdie studie het eerstens die uitwerking van verskillende veranderlikes op die algehele sterktevermindering van mikrogolfbehandelde ertse ondersoek. Hiervoor is nege verskillende binêre ertsmodelle vervaardig deur mikrogolfabsorberende minerale met ŉ volumepersentasie van 10% lukraak in deursigtige matrikse te versprei. Met behulp van eindigeverskilmodelleringstegnieke is berekeningsimulasies van verhitting, warmteskade en onbegrensde druksterkte ("unconfined compressive strength") op die konseptuele binêre ertse uitgevoer. Die invloed van termomeganiese mineraaleienskappe op die sterktevermindering van mikrogolfbehandelde ertse is eerste onder die loep geneem. Daar is bevind dat die warmte-eienskappe van die mikrogolfabsorberende mineraal, en die meganiese eienskappe van die deursigtige matriks, die beduidendste uitwerking op sterktevermindering het. Binêre ertse wat ŉ mikrogolfabsorberende mineraal bevat met ŉ hoë warmte-uitsettingskoëffisiënt in ŉ sterk deursigtige matriks, het groter sterktevermindering getoon. Die invloed van korrelgrootte in die absorbeerfase op die sterktevermindering van ertse is volgende versyfer. Die studie het getoon dat, op grond van dieselfde energie-insette en mineraalsoorte, grofkorrelrige ertse groter sterktevermindering ondergaan het. Eweneens is bewys dat, met dieselfde mineralogie en behandelingsomstandighede, ertse met ŉ swak verspreide verhittingsfase ook groter sterktevermindering ervaar. Die uitwerking van mikrogolfbehandeling op die meganiese toestand van ŉ ertsmonster is boonop ondersoek. Die studie het getoon dat onbegrensde druksterkte minder gevoelig vir mikrogolfgeïnduseerde mikrobreuke is, en as ŉ swak aanwyser van vrystellingsgedrag beskou word.

ŉ Nuwe metode om skade by mikrogolfbehandelde ertse te tipeer is gevolglik met behulp van ŉ kontinuumbenadering ontwikkel. Dié metode meet die skade rondom die korrelgrens gedurende die verhittingsproses. Deur middel van voormelde metode was dit dus moontlik om die invloed van kragdigtheid, mineralogie en ertstekstuur op die mikrogolfbehandeling van erts deeglik te ondersoek. Daar is bevind dat die mate van

korrelgrensskade by 'n bepaalde kragdigtheid en energie-inset, van sowel die ertsmineralogie as ertstekstuur afhang. Na gelang van die toegepaste kragdigtheid, die ertsmineralogie en ertstekstuur, het die vereiste energie-insette vir beduidende (>10%) korrelgrensskade van 0,09 tot 7,06 kWh/t gewissel. Dit het voorts geblyk dat enige bepaalde mineralogie en ertstekstuur oor 'n minimum kragdigtheidsvlak beskik, onder welke vlak geen verlenging in blootstellingstyd enige verdere korrelgrensskade kan veroorsaak nie. Die uitwerking van pulsherhaalfrekwensie op korrelgrensskade is ook met behulp van bogenoemde metode verklaar. Die studie het getoon dat, op grond van 'n vaste energie-inset, hoë pulsherhaalfrekwensies (≥50 Hz) en gelykgolfwerking presies dieselfde hoeveelheid korrelgrensskade tot gevolg het.

Volgende is daar met behulp van 'n gebondedeeltjiemodel ("bonded-particle model") noukeurig ondersoek ingestel na die uitwerking van verskillende mikrogolfbehandelingsomstandighede op die hoeveelheid skade en die kraakpatroon by ertse. Die studie het getoon dat die hoeveelheid mikrokrake sowel as die kraakpatroon in 'n mikrogolfbehandelde ertsmonster in 'n groot mate van die betrokke erts se mineralogie, mikrogolfbehandelingsomstandighede (kragdigtheid) en korrelgrootte in die absorbeerfase afhang. Daar is ook bevind dat 'n minimum kragdigtheid nodig is om skade tot die gebied om die korrelgrens te beperk, welke minimum kragdigtheid oënskynlik grotendeels deur die ertsmineralogie en -tekstuur bepaal word.

Die studie bevat ook die resultate van aanvangsimulasietoetse oor die uitwerking van mikrogolfbehandeling op mineraalvrystelling. Die toetse het getoon dat mikrogolfbestraling 'n beduidende verandering tot gevolg het in die ertsbreekpatroon met gesimuleerde enkeldeeltjievergruising. Die breekpatroon van die erts wat by hoë kragdigtheid (P_d = 0,1 kW/mm^{3}abs vir 1 ms) behandel is, het ál langs die korrelgrens gestrek, terwyl die absorberende mineraal nog ongeskonde was. In die erts wat by laer kragdigtheid dog dieselfde energie-inset behandel is (P_d = 1 W/mm^{3}abs vir 0,1 s), is sowel tussenkorrel- as oorkorrelbreuke opgemerk. In teenstelling met die onbehandelde erts, was die breekpatrone by die behandelde erts egter in alle gevalle steeds merendeels rondom die korrelgrens geleë.

Acknowledgements

I would like to express my sincere thanks to Prof Steven Bradshaw of Process Engineering, Stellenbosch University for his supervision and financial support of this project.

Thanks goes to Dr Aled Jones of University of Nottingham for helping me with *FLAC* code and for his technical expertise. I would also like to thank Prof Sam Kingman of University of Nottingham for his valuable comments.

I would like to thank my wife and my family, for their patience and encouragement throughout. Finally, I would like to thank God for everything.

List of Contents

List of Figures

List of Tables

List of Symbols

P_d	power density (W/m^3)
f	frequency of the microwave radiation (Hz)
ε_o	permittivity of free space (8.854×10^{-12} F/m)
ε''	dielectric loss factor
E_o	electric field (V/m)
q_{ii}	heat flux per unit length (W/m^3)
q_v	volumetric heat intensity (W/m^3)
ρ	density of the material (kg/m^3)
C_p	specific heat capacity (J/kg K).
λ	thermal conductivity (W/m.K)
Δt	time increment
Δx	zone dimension in x direction
Δy	zone dimension in y direction
ε_{ij}	strain in zone i,j.
α_{ij}	thermal expansion coefficient of zone i,j (1/K)
ΔT_{ij}	temperature change in zone i,j (K)
$\sigma_{i,j}$	stress within the zone i,j (Pa)
$E_{i,j}$	Young's modulus of zone i,j (GPa)
$\nu_{i,j}$	Poisson's ratio of zone i,j
K	bulk modulus (GPa)

G shear modulus (GPa)

δ skin depth (m)

μ_0 $4\pi \times 10^{-7}$ (H/m)

μ_r relative permeability of the medium

μ' permeability (H/m)

μ'' magnetic loss factor

ε' dielectric constant

ρ' resistivity of the medium (Ωm)

tanδ loss tangent

D_p penetration depth (m)

H_O magnetic field (A/m)

λ_0 free space wavelength (m)

τ_s shear strength(Pa)

ϕ angle of friction

C cohesion strength (Pa)

ϕ' equivalent angle of friction for Hoek-Brown material

c' equivalent cohesion strength for Hoek-Brown material (Pa)

θ rupture angle

σ_c uniaxial compressive strength (Pa)

σ_t tensile strength (Pa)

σ_n normal stress (Pa)

σ_1	major principal stress at failure (Pa)
σ_3	minor principal stress at failure (Pa)
k	slope of the line relating σ_1 and σ_3
m	material constant in Hoek-Brown failure criterion
s	material constant in Hoek-Brown failure criterion
a	material constant in Hoek-Brown failure criterion
D	degree of disturbance (0-1)
GSI	geological survey index (0-100)
I_{s50}	point load index (pa)
UCS	unconfined compressive strength (pa)
hi	drop weight initial height (cm)
$\overline{m}$	mean mass of the drop weight (kg)
Md	mass of the drop weight (kg)
E_{is}	specific input energy (kWh/t)
A	ore impact breakage parameter
b	ore impact breakage parameter
E_{CS}	specific comminution energy (kWh/t)
t_{10}	amount passing 10% the original mean size (%)
K_{IC}	mode 1 fracture toughness
WI	Bond work index
σ_{peak}	peak strength (Pa)

σ_{res} residual strength (Pa)

t_a ore abrasion parameter

e^e elastic part of strain

e^p plastic part of strain

φ texture parameter

S^{AB} interphase length per unit area of the absorbent phase

X total particle size

g_A area fraction of the absorbent phase

P pressure (Pa)

V volume (m^3)

τ pulse duration (ms)

T period (s)

PRF pulse repetition frequency (Hz)

ρ_b ball density (kg/m^3)

n average porosity of the PFC^{2D} material

R_{min} minimum radius of the ball (mm)

R_{max} maximum radius of the ball (mm)

$\overline{\lambda}$ radius multiplier used to set the parallel-bond radii

E_C Young's modulus at each particle-particle contact (GPa)

k_n particle normal stiffness

k_s particle shear stiffness

$\bar{k}_n$ parallel-bond normal stiffness

$\bar{k}_s$ parallel-bond shear stiffness

(k_n/k_s) ratio of particle normal to shear stiffness

$\bar{E}_C$ Young's modulus of each parallel bond (GPa)

$(\bar{k}_n/\bar{k}_s)$ ratio of parallel-bond normal to shear stiffness

μ particle friction coefficient

F_n normal force (N)

F_s shear force (N)

U_n normal displacement

U_s shear displacement

$\bar{\sigma}_c$ normal (tensile) strength of the cement (MPa)

$\bar{\tau}_c$ shear strength of the cement (MPa)

w specimen width (mm)

V_p platen velocity (m/s)

F_f peak force in Brazilian tensile strength test (N)

R radius of the Brazilian disk (mm)

η thermal resistance (°C /W.m)

Q power (W)

$\bar{k}_n$ bond normal stiffness (Pa/m)

A area of the bond cross section (m^2)

$\overline{\alpha}$ expansion coefficient of the bond material (1/°C)

L bond length (m)

Chapter 1

Introduction

The mining and the mineral processing industries are major consumers of energy and contributors to environmental degradation. For instance, about 4% of the CO_2 emitted to the atmosphere comes from the worldwide extractive metallurgy industry (Forrest and Szekely, 1991). In mineral processing, the extraction of values in an ore from the waste is an energy intensive and energy inefficient process. It has been reported that about 1.14 - 1.86% of the total national energy consumption is attributable to comminution in different mining countries (Tromans, 2008). And according to Fuerstenau and Abouzeid (2002) only 0.1 - 1% of the energy input in conventional grinding is used to create new surfaces, the rest is turned into noise and heat. Microwave processing of ores provides substantial benefits in reducing energy consumption and environmental impacts of these industries.

Microwave heating of mineral ores offers a potential mechanism to induce fractures between the value in the ores and the waste material surrounding it, due to the differential in absorption of microwaves and the differences in thermal expansion among various minerals in ore particles (Walkiewicz et al., 1991; Whittles et al., 2003; Jones et al., 2005). As a consequence, this reduces the energy required in grinding to separate the value from the waste material (gangue). Further, there is evidence that the microwave-induced micro-fractures result in improved liberation and recovery due to grain boundary fracture and/or preferential breakage, depending on the ore (Sayhoun et al., 2005).

Most of the earlier research has focused on laboratory-scale, exploratory efforts (Walkiewicz et al., 1991; Kingman, 1998; Kingman et al., 2000a, b; Vorster et al., 2001; Kingman et al., 2004a, b ; Sayhoun et al., 2005). The work by Kingman et al. (2004a, b) has shown for the first time that microwave treatment of ores may be economically viable by using very high power density for short exposure times. The results from laboratory work showed a reduction in the required breakage

energy of 30% and also an increase in liberation of over 100% in the +500 μm size fraction using an energy input of less than 1 kWh/t.

However, in order to realize the potential benefits of microwave processing of ores, much work remains to be done to scale up the process and system designs. Process scaling needs model development, simulation and understanding of the effect of microwave on the process materials (Bradshaw et al., 2007).

To date, there are no good models for understanding the behaviour of microwave treated ores and there exist no predictive tools to forecast expected damage in an ore for a given microwave treatment condition. Also it is difficult to analyze the micro-fractures that are believed to occur during microwave treatment. Further, no quantitative method exists for relating microwave operating parameters (exposure time and power density) to thermal damage for different ore textures, mineralogies and thermo-mechanical properties.

Accordingly, this work attempts to better understand the effect of mineralogy, ore texture and microwave power delivery on microwave treatment of ores through numerical modelling and simulation. The work also attempts to provide guidelines regarding the design target and operating conditions for developing microwave cavities for industrial application.

The organization of the thesis is as follows: a review of the major experimental and theoretical studies carried out to date on microwave assisted comminution and liberation of minerals is presented in Chapter 2. This chapter aims to provide the reader with sufficient background to the study of microwave assisted comminution and to understand the intentions of the body of work presented in this thesis.

Chapter 3 discusses in general terms, the fundamental nature of microwave, how microwaves are generated, and their interactions with materials, the different microwave heating mechanisms and microwave system components. Brief notes concerning dielectric properties measurements, power density, penetration depth are also included in this chapter.

Chapter 4 discusses the most common strength properties of rocks, the tests used for estimating them, and the different failure criteria used in rock mechanics. These include uniaxial compressive strength, stress-strain properties in unixial compression and Brazilian tension test. The correlation between uniaxial compressive strength and ore breakage parameters is also presented. In the second part of the chapter, different numerical techniques currently in use in rock mechanics including finite difference, finite element, distinct element, boundary integral and hybrid methods are discussed.

Chapter 5 details the methodologies used to simulate thermal and mechanical behaviour and the specification of thermo-mechanical properties that are required to accurately describe thermal and mechanical behaviour of microwave treated ores using a continuum analysis based on the 2-D finite difference modelling software application, *FLAC V4.0*. In this chapter, the procedures for implementation of models in *FLAC*, the different constitutive models available and the specific application of each model are detailed. The chapter also discusses the methodologies used for modelling microwave heating, thermally induced stress and unconfined compressive strength test.

Chapter 6 discusses the results of different numerical simulations undertaken for investigating the effect of different variables on bulk strength reduction of microwave treated ore. The chapter details the studies designed to examine the effects of thermo-mechanical properties of constituent minerals, microwave absorbent phase grain size, microwave power delivery, absorbent phase modal area, and absorbent phase dissemination on bulk strength reduction of ores. Further, the effect of microwave treatment on mechanical state of an ore sample is examined in this chapter.

Chapter 7 presents a new method of characterizing damage in microwave treated ores using a continuum analysis. The method measures the damage around the grain boundary regions during the heating process. The method is used to quantify the damage induced in two microwave treated binary ores. The influence of power density on microwave treatment of ores is elucidated using the developed method. Construction of damage maps, which show damage as a function of power density and treatment time for different binary ores and ore

textures is carried out in this chapter. The effect of pulse repetition frequency on grain boundary damage is also examined.

The first part of Chapter 8 details the methodologies used to simulate a macroscopic behaviour of ore models and the specification of the microscopic properties that are required in the models to accurately describe mechanical and thermal behaviour of microwave treated ores using bonded-particle model (BPM). The calibration steps that were followed to obtain the required macroscopic properties of the ore models are also discussed. In the second part, the results of simulation of microwave-induced micro-cracks in the ore samples obtained using bonded-particle model are discussed. Damage maps, which show percentage of micro-cracks as a function of power density and exposure time for different binary ores are presented. At last, the results obtained from simulation of single particle compression of untreated and microwave treated ores are presented.

Chapter 9 is a summary of the conclusions drawn from the work performed. It presents the conclusions made from the result obtained using both continuum approach and bonded-particle model. The practical implication of the results on microwave assisted comminution and liberation of mineral are also addressed. The chapter also presents the scope for some future work.

Chapter 2

Literature Review

2.1 Introduction

Significant work has been undertaken to investigate the use of microwave energy in mineral processing. Despite the considerable effort that has been expended in understanding the concepts and principles of microwave treatment of ores, there are no industrial applications of the technology to date. This chapter reviews the major experimental and theoretical studies carried out to date on microwave assisted communition and liberation of minerals.

2.2 Experimental Studies

The first attempt to assess the heating rates of different minerals within a dielectric field, though qualitative in nature, was that carried out by Chen et al. (1984). These authors reported the result of heating forty minerals individually with microwave energy. As they had difficulty in measuring the accurate temperature during microwave irradiation, they did not report temperature instead they reported the microwave power input. The minerals samples were characterised before and after microwave heating. From the result of the study it was concluded that most silicate, carbonates and sulphates, some oxides and some sulphides were essentially transparent to microwave radiation. However, most sulphides, arsenides, sulphosalts and sulphoarsenides heated strongly.

Walkiewicz et al. (1988) later completed a more detailed qualitative study of microwave heating characteristics of various mineral and compound. All heating tests were conducted on a 25 g powdered sample per batch. All samples were irradiated in 1 kW, 2.45 GHz applicator. The temperature of the samples was monitored by employing a type K thermocouple an ungrounded tip sheathed in Inconel 702. The results obtained were similar to those of Chen et al. (1984). Highest temperatures were obtained for carbon and most of metal oxides. Most metal sulphides heated well

without any consistent pattern. Metal powder and some heavy metal halides also heated well, gangue minerals such as quartz, calcite and feldspar did not heat.

The study also reported an important observation that rapid heating of ores minerals in a microwave transparent matrix generated thermal stress of sufficient magnitude that can create microcrack along mineral boundaries. The study concluded that this kind of microcracking has a potential to improve grinding efficiency as well as leaching efficiency. Table 2-1 shows the results obtained for natural minerals.

Table 2-1: Effect of microwave heating on temperature of natural minerals (Walkiewicz et al., 1988)

Mineral	Chemical composition	Temperature (°C)	Time, min
Albite	$NaAlSi_3O_8$	82	7
Arizonite	$Fe_2O_3.TiO_2$	290	10
Chalcocite	Cu_2S	746	7
Chalcopyrite	$CuFeS_2$	920	1
Chromite	$FeCr_2O_4$	155	7
Cinnabar	HgS	144	8
Galena	PbS	956	7
Hematite	Fe_2O_3	182	7
Magnetite	Fe_3O_4	1258	2.75
Marble	$CaCO_3$	74	4.25
Molybdenite	MoS_2	192	7
Orpiment	As_2S_3	92	4.5
Orthoclase	$KAlSi_3O_8$	67	7
Pyrite	FeS_2	1019	6.76
Pyrrhotite	$Fe_{1-x}S$	886	1.75
Quartz	SiO_2	79	7
Sphalerite	ZnS	87	7
Tetrahedrite	$Cu_{12}Sb_4S_{13}$	151	7
Zircon	$ZrSiO_4$	52	7

McGill et al. (1988) reported the effect of power level on mineral heating rate. The sample minerals were powdered and exposed to various microwave power input ranging from 500 to 200 W. All tests were conducted on 25 g of sample. It was observed that an increase in microwave power led to an increase in the heating rate of the minerals while low loss minerals such as quartz and orthoclase did not heat effectively regardless of the applied power.

Chunpeng et al. (1990) also conducted a research to investigate the response of several oxides, sulphides and carbonate minerals to microwave irradiation. All tests were conducted on a 50 g powder sample per batch with a microwave power input of 500 W of 2.45 GHz frequency and constant exposure time (4 min). The results indicated that the majority of oxide and sulphide minerals heated well.

Walkiewicz et al. (1991) later demonstrated that the rapid heating of ores containing microwave energy absorbing minerals in a non-absorbing gangue matrix generated thermal stress. This thermal stress caused micro-crack along the mineral grain boundaries, as a result the ore became more amenable to grinding. In their study, iron ore samples were subjected to 3 kW, 2.45 GHz radiation and heated to average maximum temperatures between 840 and 940°C. S.E.M photomicrographs confirmed that fractures along grain boundaries and throughout the gangue matrix were occured. Standard Bond grindability tests showed that microwave preheating of the ores reduced the work index of iron ores by 10 to 24%. However, this improvement was not enough to compensate for the energy consumption of the microwave preheating.

Walkiewicz et al. (1993) studied the effect of temperature and power level on Bond work index. A Taconite feed material was heated to various temperature at 12 and 16 kW. Improved values of grindability were obtained at all power level which confirmed the hypothesis that microwave energy can induce thermal stress cracking. A comparison was also made between material heated to 880 and 197°C. It was found that ores heated to the lower temperature showed a considerable decrease in Bond work index and this significantly improved the cost effectiveness of microwave assisted grinding when compared to samples heated to 880°C.

Tavares and King (1996) investigated the effect of rapid microwave heating on single particle comminution of ores by using a device called Ultrafast Load Cell (UFLC).

The study was carried out on iron ore and taconite ore samples. The iron ore sample consisted of polycrystalline of hematite, magnetite and quartz. The taconite sample consisted of magnetite in a chert matrix. The authors used a low power multimode cavity operated at 2.45 GHz with a power range of 1 to 1.2 kW. The sample mass was about 10 grams. The effect of microwave and conventional thermal pre-treatment on the fragmentation pattern was assessed through examination of single particle breakage function. The results indicated that thermal pre-treatment (both conventional and microwave) improved breakage by producing a shift in the top of the breakage function to finer size without increasing significantly and even decreasing the proportion of fines. It was observed that the breakage functions of microwave treated ores were consistently finer than those of conventionally heated samples.

Harrison (1998) investigated the heating characteristics of twenty five minerals in a 650 W, 2.45 GHz microwave oven and classified them into three groups:

Group I: High heating rate (Common valuable ore mineral)

-Minimum temperature 175°C after 180 s

-Metalliferous ore minerals e.g. pyrite, galena, magnetite, pyrrhotite, bornite, chalcopyrite

Group II: Medium heating rate (some valuable ore mineral)

-Temperature varies 69 - 110°C after 180 s treatment

- Ore minerals e.g. ilimenite, hematite, cassiterite, bauxite

Group III: Low heating rate (silicates, carbonates and other typical gangue minerals)

-Maximum temperature 50°C after 180 s treatment

-Mainly gangue with some ore minerals e.g. quartz, feldspar, calcite, mica, barites, sphalerite, rutile.

Kingman et al. (1998) investigated the effect of microwave treatment on massive Norwegian. ilmenite ore. The results showed that considerable reductions in

comparative Bond work index could be achieved after microwave treatment. For instance, up to 90% reduction in Bond work index was achieved after treatment for 60 seconds at 2.6 kW. Significant increases in concentrate grade and recovery of valuable mineral were also demonstrated after a two stage magnetic separation process. It was concluded that short, high-power microwave treatments were most effective because over exposure of the sample led to reductions in downstream processing efficiency. This work was extended by Kingman and Rowson (2000) to examine the reason for possible increases in recovery of valuable minerals after microwave treatment. It was shown that increased recovery was not only due to increase in liberation but also due to the enhancement of the magnetic properties of the material.

Kingman et al. (2000a) carried out a study of the effect of mineralogy on the responses of ores to microwave radiation. Four different ores: massive ilmenite, refractory gold, carbonatite and massive sulphide were investigated. The work demonstrated that ores that have consistent mineralogy and contain a good absorber of microwave radiation in a transparent gangue matrix to be most responsive to microwave treatment while ores that contain small particles that are finely disseminated in discrete element respond poorly to microwave treatment in terms of reduction in required grinding energy. It was also concluded that the use of purpose built more efficient microwave heaters may make the microwave treatment of ores of certain mineralogy economic.

The influence of microwave treatment on flow sheet design has also been investigated by Kingman et al. (2000b). Rod mill feed from a South African copper plant was subjected to microwave treatment at various power levels for various exposure times. The comparative Bond work index determined for each samples was used to investigate the performance and design of the actual grinding for the ores. Using flow sheet modelling software, it was shown that an open circuit mill followed by a closed circuit ball mill could be replaced by a single open single circuit rod mill. However, it was concluded that the technical benefits were attractive but the economics were poor, as the reduction in work index was achieved at high microwave energy input. For instance, a microwave energy input of 130 kWh/t (microwave irradiation of 1 kg

sample at 2.6 kW for 180 seconds) was required to reduce the Bond work index from 13.1 to 2 kWh/t.

Vorster et al. (2001) investigated the effect of microwave treatment upon the processing of two types of Neves Corvo copper ores (a massive copper ore and a massive copper-zinc ore). Grindabliy tests were conducted on 500 g of the untreated samples and samples microwave treated at 2.6 kW for different exposure times. The results indicated a reduction in Bond work index of 70% after 90 s microwave exposure for the massive copper ore. For the massive copper-zinc ore that was water quenched after 90 s microwave exposure at 2.6 kW, a reduction in Bond work index of 65% was obtained. Process simulation on the package USIMPAC showed significant flowsheet changes were possible as a result of exposure to microwave radiation and the subsequent reduction in work index.

Kingman et al. (2004a) carried out a study to investigate the effect of applied microwave power level, optimisation of microwave energy transfer and microwave cavity type on the required comminution energy. Microwave power of 5, 7.5, 10, and 15 kW in single-mode and multimode cavity were applied to a lead-zinc ore of different particle sizes. Point load and drop weight tests were used to determine the strength of the ore after each type of microwave treatment. The results indicated that both cavity type and microwave power level had a significant influence on the reduction in strength of the ore. For the same power of 10 kW, a 5 s (an energy input of 13.9 kWh/t) treatment was needed to obtain a 50% reduction in strength in multimode cavity but only 0.5 s (an energy input of 1.39 kWh/t) was required for greater reduction in a single mode cavity. They concluded that microwave treatment of ores can be economical by using a single mode cavity capable of producing high electric field that is evenly distributed across the feed ore stream.

Kingman et al. (2004b) investigated in detail the comminution behaviour of ore treated at high microwave power for a short exposure time in a single mode cavity. A copper carbonitite ore samples were irradiated in a variable power inputs (3-15 kW). After microwave treatment; point load test, drop weight test, grindability test and QEM*SEM liberation data were used to characterise the comminution behaviour of the treated ore. The results of the tests indicated for the first time that significant changes can be achieved by using a microwave power inputs that is potentially

economic. The drop weight test showed a reduction in required breakage energy of 30%, grindability tests indicated that a reduction of 40% in specific breakage rate and QEM*SEM also showed that the liberation in the +500 μm size fraction increased over 100% using an energy input of less than 1 kWh/t.

Sahyoun et al. (2005) investigated the influence of microwave pre-treatment on copper floatation. Nine representatives 1 kg of copper carbonitite ore samples of rod mill feed were used. All samples were treated in a single-mode microwave cavity at power levels 5, 7.5,10 and 12 kW for exposure times of 0.1 and 0.5 s. After treatment the samples were ground in a steel rod mill. Then a 450 g of each sample was used for flotation in a 3 L Denver laboratory flotation cell. After flotation copper analysis was carried out using acid dissolution and atomic absorption spectroscopy. The result indicated that a higher initial recovery in the microwave treated samples for all power level and exposure time. It also showed that increasing microwave power and treatment time both improve the grade and recovery achieved. At lower power level the cumulative grade of the treated material was similar to that of untreated material. A simple economic analysis was also carried out by using the 4% increase in recovery obtained due to microwave treatment (without adding the energy saving from comminution) and the results indicated that a payback period time of less than 2 years required for the best scenario case where as 7-19 years of payback time needed for the worst scenario.

Olubambi et al. (2007) investigated the influences of microwave irradiation on the heating characteristics, breakage response, mineralogy and the mechanisms of dissolution in sulphuric acid and hydrochloric acid. The ore used for the study was a complex sulphide ore and it consisted of silica, siderite, ferrous sphalerite, galena, pyrite and covelite. 100 g each of the representative samples of the ore was treated in a kitchen type microwave oven for 5 to 11 min. Maximum power of 1100 W was used for the study. The results indicated that microwave heating at increased power and time had a positive effect on size reduction. Dissolution potentials were shifted to more negative values after microwave treatment, while dissolution currents, dissolution current densities, and dissolution rates were also increased. It was suggested that the increase in dissolution of the microwave treated samples was attributed to an increase in electrochemical sites resulting from an increase in the

number of cracks and increased pyrite phases which promoted galvanic interaction within the system.

Scott et al. (2008) investigated the effects of microwave treatment on the liberation spectrum of a rod-milled South African carbonatite ore based on quantitative mineralogical analysis. The ore was treated at microwave power of 10.5 kW for 0.5 s in a single mode microwave cavity in batches of 1 kg. The treated and untreated ore were subsequently grinded to 80%–800 μm. The microwave treated ore showed a significant increase in the amount of liberated copper minerals in the relatively coarse particle size range (106 to 300 μm). Similar significant shifts in the liberation spectra were noted for all the minerals in the ore. It was suggected that, as a result of microwave pretreatment, intergranular fracture was occurred between microwave susceptible and non-susceptible minerals, and also the fracture pattern was changed, which altered the size distribution of the gangue material.

2.3 Theoretical Studies

A number of theoretical studies have also been carried out on microwave treatment of ores. The first attempt to model the thermally induced stress when an ore subjected to microwave irradiation was that carried out by Salsman et al. (1996). These authors examined the feasibility of short pulsed microwave pre-treatment of ores using finite element numerical modelling to predict the thermo mechanical response of a single pyrite particle in a calcite matrix during microwave treatment. They predicated that a significant temperature differential would occur between the two phases and the resulting thermal stresses would exceed the strength of the materials. The simulation yielded promising results in terms of the magnitude of stresses developed when a short pulse of very high power densities (1×10^{12} W/m^3 for 40 ms and 1×10^{14} W/m^3 for 40 μs) were applied. They also suggested that the economy of microwave assisted grinding can be greatly improved by using very high power for a short period of time.

Whittles et al. (2003) investigated the influence of power density on strength reduction by using a finite difference numerical modelling. The simulations were carried on 15 mm × 30 mm size sample consisted of 10%, 1 mm^2 microwave absorbing pyrite in a calcite matrix. A specific volumetric heating rate was applied to the pyrite grains and the subsequent thermal expansion was modelled. No heat was

applied to the calcite matrix. A variable power density between 3×10^9 and 9×10^9 W/m^3 was used to represent the power density in a 2.6 kW, 2.45 GHz multimode microwave cavity. However, the method used for calculating the power densities was not mentioned. A power density of 1×10^{11} W/m^3 was assumed as a typical power density in a 15 kW, 2.45 GHz single mode cavity. The exposure times used for the simulations were between 1 and 30 s for the low power density and between 0.05 and 1 s for the high power density. After simulation of heating, uniaxial compressive strength tests were undertaken. The results showed that high power densities were vital to rapid stress generation within the ore matrix. Simulation of samples treated at multimode microwave cavity showed reduction in strength from 126 to 79 MPa in 30 s. However, simulations of samples treated at a power density of 1×10^{11} W/m^3 showed a reduction in strength from 126 to 57 MPa in 0.05 s. The authors suggested that higher stress were possible in the high power density (1×10^{11} W/m^3) case as there was less time for conduction between the microwave responsive and transparent phase.

Jones et al. (2005) later carried out a two dimensional finite-difference simulation to investigate in detail the thermal stress development and subsequent thermal damage when an ore exposed to high electric field microwave energy. The authors also examined the effect of power density and absorbent phase grain size on peak temperature attained by the simulated ore. The simulated mineral ore comprised of a pyrite grain in a calcite matrix. Simulations were carried out by varying the power densities between 1×10^8 and 1×10^{11} W/m^3 for different exposure times. The influence of particle size on the peak temperature attained also examined by using ten different particle size of microwave absorbent phase pyrite (50 μm - 500 μm). Simulation results indicated that the stress regime inside pyrite is compressive whereas outside the boundary shear and tensile stress are predominant. The peak temperature attained in the particle generally increased with particle size. From analysis of the stress regime, the authors suggested that intergranular fracture will be dominant for spherical particle, but for particle deviating from spherical, transgranular will be more prevalent.

The influence of microwave energy delivery method on strength reduction was also examined by Jones et al. (2007) using a two-dimensional finite difference thermo-

mechanical simulation. The model ore was comprised of a 1% pyrite particle randomly disseminated in a calcite matrix. The microwave heating of the absorbent phase was simulated by adding a volumetric power density in the particle. After heating, the strength of the ore was quantified by using simulation of unconfined compressive strength test. Lower power densities ranging from 1×10^9 - 1×10^{10} W/m^3 and higher power densities between 1×10^{13} and 1×10^{15} W/m^3 were used to represent the power densities that could be expected in continuous wave and pulsed wave equipment, respectively. The results indicated in general that higher strength reduction was obtained when the power density was very high and the exposure time was very short. The authors also suggested that future microwave equipment should be capable of producing power densities between 1×10^{10} and 1×10^{12} W/m^3 with exposure times between 0.002 and 0.2 s in order to have a significant strength reduction in the microwave treated ores.

Wang et al. (2008) studied the effect of microwave heating on thermal damage in a conceptual ore consisted of pyrite in a calcite matrix by using a thermal-based particle model. In the model, it was assumed that microwave energy input completely contributed to enhancing the repulsive bond strength between the contiguous particles and material's physical properties did not change during a successive heating process. The total particle size of the model material and the absorbent phase grain size were not reported. Simulations were performed using power densities of 1×10^9 and 1×10^{11} W/m^3 to describe the temperature profile, stress distribution and the fracture density within the model materials. The simulation results indicated a higher temperature gradient and thermal stress at the interface between the pyrite and calcite phases when the power density was high for the same exposure time. They also showed that the fracture density (the ratio of number of broken bonds to original number of bonds) increased as the microwave exposure time (energy input) increased. However, the effect of power density on temperature profile, stress distribution and fracture density for the same energy inputs was not investigated. It is apparent that if the exposure time is the same and the power density is high, the energy input to the material will be high.

2.4 Conclusions

Major experimental and theoretical studies on microwave assisted communition and liberation of minerals have been reviewed in the chapter. In general, most of studies have been exploratory in nature and have also been performed on a laboratory scale. However, results were very promising when they are compared to conventional technologies. The information presented in this chapter has shown that microwave treatment of ore minerals can indeed reduce the energy required in grinding and also increase liberation and recovery of minerals. However, there are no industrial applications of the technology.

In order to realize the potential benefits of microwave in mineral processing, much work remains to be done to scale up the process and system designs. The effects of mineralogy, thermo-mechanical properties, and ore textures on microwave treatment of ores have not been investigated either experimentally or theoretically. Further, it is noted that there are no good models for understanding the thermal and mechanical behaviour of microwave treated ores and there exist no predictive tools to forecast expected thermal damage (both bulk and local) in different ores (of different thermo-mechanical properties, ore textures) for a given microwave treatment condition (power density and exposure time).

It is most likely that the required design parameters (power density, energy input) for a microwave unit will be affected by mineralogy, ore texture and thermo-mechanical properties. Thus, the effects of these variables on the design target should be determined in order to scale up the technology for industrial application. It is noticeable that numerical modelling and simulation of the process by using different ore mineralogies and textures is of paramount importance.

Chapter 3
Microwave Fundamentals

3.1 Introduction

A basic understanding of microwaves and their interactions with materials is required in order to appreciate the potential benefits, as well as to understand the limitations, of microwave processing of ores. Accordingly, the aim of this chapter is to discuss in general terms, the fundamental nature of microwave, how microwaves are generated, their interactions with materials, the different microwave heating mechanisms and microwave system components. Further, brief notes concerning dielectric properties measurements, power density and penetration depth are presented.

3.2 Microwave

Microwaves are electromagnetic waves with wavelengths shorter than one meter and longer than one millimeter, or frequencies between 300 megahertz and 300 gigahertz (Figure 3.1). The initial surge in microwave technology development was driven by the military needs of the world war (Meredith, 1998). The tremendous effort that went into development of radar during World War II generated a great body of knowledge on the properties of microwaves and related technologies (Stein et al., 1994). From a commercial standpoint the microwave oven was first developed in 1951 when a large floor standing model was produced by the Raytheon company of North America (Osepchuck, 1984). For domestic purposes ovens become available in the early 1960's and from then a mass market was initiated.

In the past 40 years, the microwave oven has become an indispensable appliance in most kitchens. Faster cooking times and energy savings over conventional cooking methods are the main benefits (Meredith, 1998). Although the use of microwaves for cooking food is prevalent, the application of this technology to the processing of materials is a relatively new development. The use of microwave energy for

processing materials has the potential to offer similar advantages in reduced processing times and energy savings.

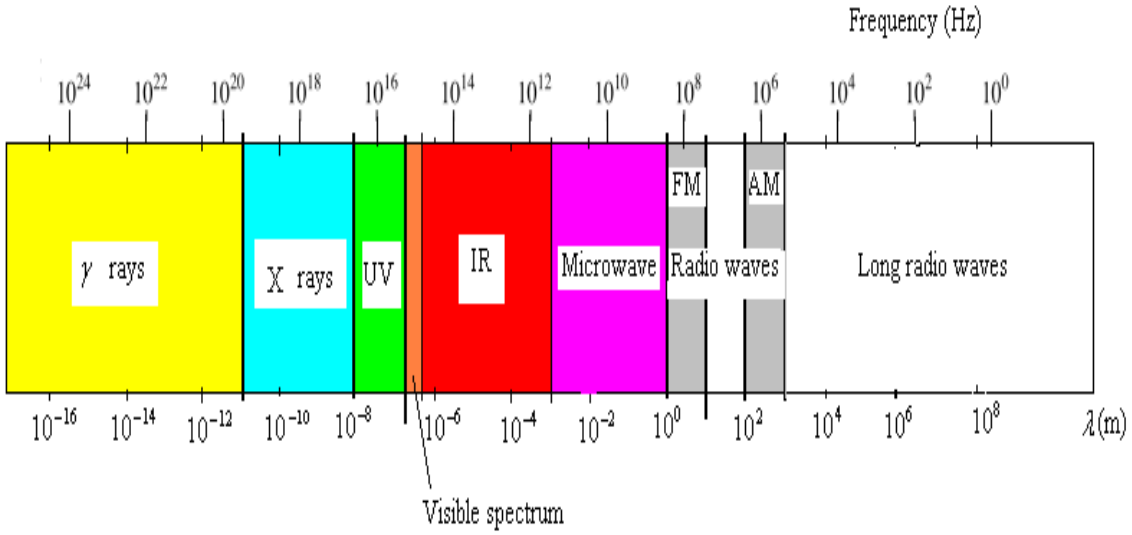

Figure 3.1: Electromagnetic spectrum and frequencies used in microwave

Microwaves have extensive application in the field of communication. However, the federal communication commission (FCC) has allocated certain frequencies for industrial, scientific, medical and instrumentation (ISMI) applications. The two most commonly used frequencies are 915 MHz (896 MHz in UK) and 2.45 GHz. Domestic microwave ovens are a familiar example operating at 2.45 GHz.

3.3 Microwave Heating

When an electric field interacts with a material various responses may take place. In conductors, electrons move freely in the material in response to the electric field and electric current results. However, microwave will be largely reflected from the surface and therefore they are not effectively heated by microwave (Haque, 1998). In insulator, electrons do not flow freely, but electronic reorientation or distortion of induced or permanent dipoles can give rise to heating (Stein et al., 1994). Materials which are excellent absorber of microwave energy are classified as dielectric. Thus, in

general, natural materials can be classified in to three: conductors, insulators (transparent) and dielectric (absorber).

3.3.1 Difference between Conventional and Microwave Heating

It is essential to understand the difference between conventional and microwave heating before discussing the potential advantages associated in using the microwave for material processing. In conventional thermal processing, energy is transferred to the material through convection, conduction, and radiation of heat from the surfaces of the material. In contrast, microwave energy is delivered directly to materials through molecular interaction with the electromagnetic field. In heat transfer, energy is transferred due to thermal gradients, but microwave heating is the conversion of electromagnetic energy to thermal energy.

Unlike conventional heating ovens, microwave ovens are very efficient in converting energy into heat in the workload. In a large industrial oven, the efficiency can be in the region of 95% and the conversion of electrical power into microwave power can have an efficiency of 85% (Meredith, 1998). In addition, a conventional oven has to be heated to a temperature substantially in excess of the required temperature in the workload; a microwave oven is normally heated to a temperature not greater than the required surface temperature of the workload. The radiation and the convection heat loss from the microwave oven are therefore significantly less because of its low temperature. Further, energy saving arises because a microwave oven has instantaneous control of power, which means that equilibrium condition are rapidly reestablished after a change, and start-up can be rapid. Very fast feed back control loops can be used to control process parameter accurately, leading to improved product quality (Meredith, 1998).

This difference in the way energy is delivered can result in many potential advantages to using microwaves for processing of materials. Since microwaves can penetrate materials and deposit energy, heat can be generated throughout the volume of the material. The transfer of energy does not rely on diffusion of heat from the surfaces, and it is possible to achieve rapid and uniform heating (Thostenson and Chou, 1999).

In addition to volumetric heating, energy transfer at a molecular level can have some additional advantages. Microwaves can be utilized for selective heating of materials.

The molecular structure affects the ability of the microwaves to interact with materials and transfer energy. When materials in contact have different dielectric properties, microwaves will selectively couple with the higher loss material. This phenomenon of selective heating can be used for a number of purposes including microwave assisted comminution and liberation of minerals.

Although direct heating by microwaves can offer advantages over conventional heat transfer, the different mechanism of energy transfer in microwave heating has also resulted in several new processing challenges. Because energy is transferred by the electromagnetic field, non-uniformity within the electromagnetic field will result in non-uniform heating. As materials are processed, they often undergo physical and structural transformations that affect the dielectric properties (Thostenson and Chou, 1999).

3.3.2 Microwave Heating Mechanism

Microwaves can be visualized as a high frequency oscillating electric (E) and magnetic (H) fields as shown in Figure 3.2. Anything that is put into this field, if it may be electrically or magnetically polarised at this oscillation frequency, will be affected.

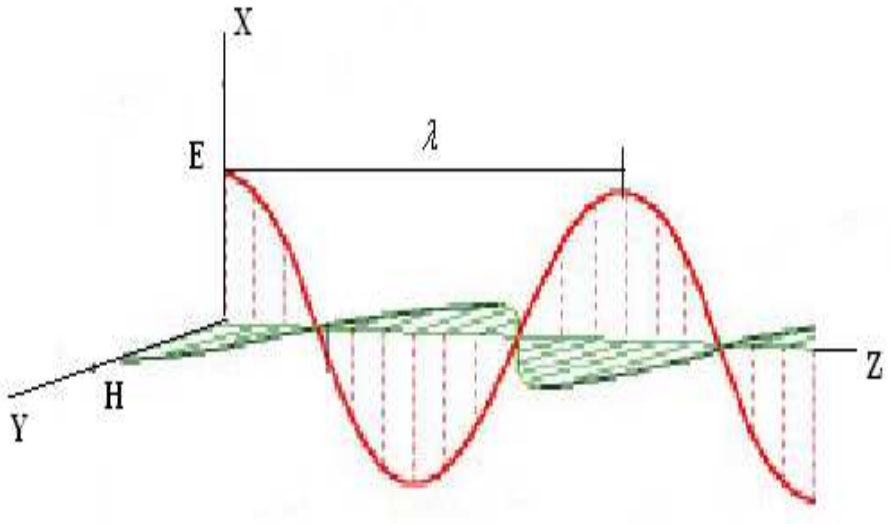

Figure 3.2: Electric and magnetic field in microwave

Three principal microwave heating mechanism exist (Whittaker, 1997):

1. Dipolar polarisation,
2. Conduction mechanisms
3. Interfacial polarisation

3.3.2.1 Dipolar Polarisation

Dipolar polarization is a polarization that is particular to polar molecules. In polar molecules, the different electronegativites of individual atoms results in the existence of a permanent electric dipole on the molecule (Figure 3.3). The dipole is sensitive to external electric fields, and will attempt to align with them by rotation, the energy for this rotation being provided by the field. This realignment is rapid for a free molecule, but in liquids instantaneous alignment is prohibited by the presence of other molecules (Whittaker, 1997). A limit is therefore placed on the ability of the dipole to respond to a field, which affects the behavior of the molecule with different frequencies of electric field.

Under low frequency irradiation, the dipole may react by aligning itself in phase with the electric field. Whilst some energy is gained by the molecule by this behavior, and some is also lost in collisions, the overall heating effect is small. Under the influence of a high frequency electric field, on the other hand, the dipoles do not have sufficient time to respond to the field, and so do not rotate. As no motion is induced in the molecules, no energy transfer takes place, and therefore, no heating (Whittaker, 1997).

Figure 3.3: Dipolar polarisation Schematic

Between these two extremes, at frequencies which are approximately those of the response times of the dipoles, is the microwave region. The microwave frequency is low enough that the dipoles have time to respond to the alternating field, and therefore to rotate, but high enough that the rotation does not precisely follow the field. As the dipole reorientates to align itself with the field, the field is already changing, and a phase difference exists between the orientation of the field and that of the dipole. This phase difference causes energy to be lost from the dipole in random collisions, and to give rise to dielectric heating.

3.3.2.2 Conduction Mechanisms

When the microwave irradiated sample is an electrical conductor, the charge carriers (electrons, ions, etc.) are moved through the material under the influence of the electric field resulting in a polarisation. These induced currents will cause heating in the sample due to any electrical resistance. For a very good conductor, complete polarisation may be achieved in approximately 10^{-18} seconds, indicating that under the influence of a 2.45 GHz microwave, the conducting electrons move precisely in phase with the field (Whittaker, 1997). When the conductivity of the material is very large (typical for metal-like material), the fields attenuate rapidly toward the interior of the sample due to skin effect.

The skin effect is the tendency of an alternating electric current (AC) to distribute itself within a conductor so that the current density near the surface of the conductor is greater than that at its core. That is, the electric current tends to flow at the "skin" of the conductor (Meredith, 1998). The skin effect involves the magnetic properties of the material. When a large current flows inside the sample due to a high conductivity, a combination of the magnetic filed with the current produces a force that pushes conducting electrons outward into a narrow area adjacent to the boundary. The extent of this skin-arm flow is called the skin depth, δ. Skin depth is defined as the distance into the sample at which the electric field is reduced to 1/e of the surface value. The following equation generally used to estimate the skin depth in a material (Stein et al., 1994).

$$\delta = \frac{1}{\sqrt{\pi \mu_o}} \sqrt{\frac{\rho'}{\mu_r f}} \qquad \textbf{3.1}$$

Where

δ = the skin depth (m)

$\mu_0 = 4\pi \times 10^{-7}$ (H/m)

μ_r = the relative permeability of the medium

ρ' = the resistivity of the medium (Ωm)

f = the frequency of the wave (Hz)

3.3.2.3 Interfacial Polarisation

Interfacial polarization is most easily viewed as a combination of the conduction and dipolar polarisation effects. This mechanism is important for systems comprised of conducting inclusions in a second, non-conducting material. An example would be a dispersion of metal particles in sulphur. Sulphur is microwave transparent and metals reflect microwaves yet, curiously, the combination forms an extremely good microwave absorbing material (Whittaker, 1997).

3.4 Microwave Systems

Microwave systems consist of three major components: the source, the transmission lines, and the applicator. The microwave source generates the electromagnetic radiation, and the transmission lines deliver the electromagnetic energy from the source to the applicator. In the applicator, the energy is either absorbed or reflected by the material.

3.4.1 Microwave Sources

Generation of electromagnetic radiation results from the acceleration of charge. To achieve the high power and frequencies required for microwave heating, most microwave sources are vacuum tubes (Stein et al., 1994). Some vacuum tubes that have been used for microwave heating include magnetrons, traveling wave tubes

(TWTs), klystrons, gyrotrons and power-grid tubes. Only magnetrons will be discussed here.

3.4.1.1 Magnetrons

These are the tubes used in conventional microwave ovens found in almost every home and in industrial ovens. The magnetron is the major player in a class of tubes termed ‘cross field’ so named because the basic interaction depends on electron motion in electric and magnetic field that are perpendicular to one another and thus ‘crossed’ (Stein et al., 1994). In Magnetron, a cylindrical electron emitter or a cathode is surrounded by a cylindrical structure, or anode, at high potential and capable of supporting microwave fields. Magnets are arranged to supply a magnetic field parallel to the axis and perpendicular to the anode cathode electric field. The interaction of electrons traveling in the cross field supplied by the anode causes a net energy transfer from the applied DC voltage to the microwave field. The interaction occurs continuously as the electron transverse the cathode anode region. The magnetron is the most efficient microwave tubes, with efficiencies of 90% having been achieved (Stein et al., 1994) with 70-80% efficiencies common.

The output power of the magnetron can be controlled through adjusting the period of operation or adjusting the cathode current or magnetic field strength. In home microwave ovens, the magnetron is operated at full power. During a specified time, the current is turned on and off for segments of the period, and the average power is reduced. This on/off type of control is often referred to as duty cycle control. If continuous microwave power is required, the output power of the magnetron tube can be varied by changing the current amplitude of the cathode or by changing the intensity of the magnetic field. This allows variable control of the microwave power within the range of the source (Thostenson and Chou, 1999).

3.4.2 Transmission Lines

The transmission lines couple the energy of the microwave source to the applicator. In low power systems, the transmission lines are often coaxial cables, which are similar to cables that are used on televisions. At high frequencies and output power, the losses that occur in coaxial cables are significant, and waveguides are often the transmission

line of choice in microwave heating systems. Waveguides are hollow tubes in which the electromagnetic waves propagate. The most commonly used cross-sections are rectangular (Thostenson and Chou., 1999).

Two modes of microwave propagation are possible in waveguides: transverse electric (TE) and transverse magnetic (TM). For the TE mode, the electric intensity in the direction of propagation is zero. For the TM mode the magnetic intensity in the direction of propagation is zero. Every mathematical solution of the electromagnetic wave in a rectangular waveguide can be decomposed into a linear combination of the TE and TM modes (Stein et al., 1994). The most common waveguide mode is the TE_{10} mode. The subscripts specify the mode of propagation, and the mode indicates the number of maxima and minima of each field in a waveguide. In addition to waveguides, there are several other transmission line components that are used for equipment protection, sensing purposes, and coupling microwaves with the material in the applicator (Thostenson and Chou., 1999).

3.4.3 Microwave Applicators

In simple term, microwave applicators are devices that are designed to heat a material by exposing it into a microwave field in a controlled environment. The objective is to cause a controlled interaction between the microwave energy and the material to occur under safe, reliable, repeatable, and economic operating conditions (Meredith, 1998). Applicator may be conveyor operated; batch or in case of indexing systems a combination of both. Microwave energy may also be combined inside the applicator with other energy sources, such as hot air, infrared and steam in order to achieve special results (Stein et al., 1994).

The design of the applicator is critical to microwave heating because the microwave energy is transferred to materials through the applicator. The temperature fields within the material undergoing microwave heating are inherently linked to the distribution of the electric fields within the applicator (Meredith, 1998). The most common microwave applicators are the travelling wave, multi-mode mode and single mode applicators and there are advantages and disadvantages in using them. They will be discussed in the following sections.

3.4.3.1 Multi-mode Applicators

Multi-mode applicators are the most common applicator types. They are capable of sustaining a number of high order modes at the same time. In multi-mode applicators, multiple field patterns are generated inside the cavity, which allows for uniform heating of larger materials (Metaxas and Meredith, 1983). An example of a multi-mode cavity is the home microwave oven. Microwave energy is introduced into a closed metal box, and with the help of a small rotating propeller called a mode stirrer, the microwave energy is scattered inside the oven, which uniformly heats the material as it comes into contact with the electric fields developed by the microwave energy.

Unlike the design of single mode applicators, which are designed based on solutions of the electromagnetic field equations for a given applicator geometry, the design of multi-mode applicators are often based on trial and error, experience, and intuition (Thostenson and Chou, 1999). To establish a reasonably uniform electric field strength throughout the cavity, it is desirable to excite as many of modes as possible (Stein et al., 1994).

Key features of multimode cavity include:

- Suitability for bulk processing application
- Oven dimensions that are often determined by product dimension
- Adaptability to batch or continuous product flow
- Performance that is less sensitive to product position or geometry.

Kingman (1998) carried out detailed mineralogical investigations into the effects of microwave treatment on various ores using multimode cavity systems. It was found that multimode cavity uses random heating patterns that created intense hotsopts within the samples. It was suggested that this type of microwave applicators were not ideal for treating minerals and ores.

3.4.3.2 Travelling Wave Applicators

These are microwave applicators in which power, fed into a chamber from the generator, is substantially absorbed by the workload with the residue being dissipated in an absorbing terminating load (Metaxas and Meredith, 1983). The microwave

power is gradually absorbed by the load as the travelling wave progresses along to the end of the applicator. Their efficiency depends on the dielectric properties of the load and its cross sectional area. They are used on continuous flow basis, usually with a conveyer belt. Travelling wave applicators are not suitable for materials of low loss because they become inconveniently long (Metaxas and Meredith, 1983).

3.4.3.3 Single-mode Applicators

In their simplest form, single-mode applicators consist of a section of waveguide operating at a frequency near cutoff (Stein et al., 1994). In the microwave applicator, theoretical analysis can be performed to describe the response of microwaves. Given the geometry of the applicator, it is often possible to solve the Maxwell equations analytically or numerically with the appropriate boundary conditions. The design of single mode applicators is based on solution of the Maxwell equations to support one resonant mode. Consequently, the size of single mode applicators is of the order of approximately one wavelength, and to maintain the resonant mode, these cavities require a microwave source that has little variation in the frequency output. Because the electromagnetic field can be determined using analytical or numerical techniques, the areas of high and low electromagnetic field are known, and single mode applicators have non-uniform, but predictable, electromagnetic field distributions (Stein et al., 1994). In general, single mode cavities have one “hot spot” where the microwave field strength is high (Thostenson and Chou., 1999).

Some advantages of single mode applicators are as follows:

- High electric fields are possible
- The applicators can operate in the standing or traveling wave configurations.
- Fields are well defined
- Fields can be matched to product geometry
- The applicators are useful for heating both low-loss and high-loss materials
- The applicator are compatible with continuous product flow
- High efficiency is possible

The main disadvantage of single mode applicators is that they are product specific rather than general purposes and in operation can be very sensitive to changes in product properties, geometry and position (Stein et al., 1994).

In general for the same power applied, a single mode cavity will establish much higher electric field strengths than a travelling wave or multi mode cavity and for this single mode cavity is most useful for treatment of low loss dielectric (Metaxas and Meredith, 1983).

Single mode cavity has been recently shown to be suitable for microwave treatment of ore. The results of the study carried out by Kingman et al. (2004 a,b) indicated for the first time that significant changes can be achieved by using a microwave power input that is potentially economic using single mode cavity.

3.5 Dielectric and Magnetic Properties

Energy is transferred to materials by interaction of the electromagnetic fields at the molecular level, and the dielectric properties eventually determine the effect of the electromagnetic field on the material. Thus, the physics of the microwave/materials interaction is of vital importance in microwave processing. The interaction of microwaves with molecular dipoles results in rotation of the dipoles, and energy is dissipated as heat from internal resistance to the rotation. Microwave propagation in materials depends on the dielectric and magnetic properties of the medium. The electromagnetic properties of a medium are characterized by complex permittivity (ε) and complex permeability (μ) where:

$$\varepsilon = \varepsilon' - j\varepsilon'' \qquad \textbf{3.2}$$

$$\mu = \mu' - j\mu'' \qquad \textbf{3.3}$$

Permittivity describes how an electric field affects and is affected by a dielectric medium, and is determined by the ability of a material to polarize in response to the field, and thereby reduce the total electric field inside the material. Thus, permittivity relates to a material's ability to transmit an electric field. The real component of the complex permittivity, ε' is commonly referred to as the dielectric constant or

permittivity while the imaginary part, ε'' is the dielectric loss factor. The dielectric constant, ε' characterizes the penetration of microwave into the material and the loss factor, ε'' indicates the material's ability to store the energy. Another commonly used term for expressing the dielectric response is the loss tangent where:-

$$\tan\delta = \frac{\varepsilon''}{\varepsilon'} \qquad \textbf{3.4}$$

The loss tangent tanδ is indicative of the ability of the material to convert absorbed energy into heat.

Permeability is the degree of magnetization of a material that responds linearly to an applied magnetic field. In SI units, permeability is measured in henries per meter (H/m), or newtons per ampere squared. Similarly the real and imaginary components of the complex permeability, μ' and μ'', are the permeability and the magnetic loss factor, respectively.

3.6 Dielectric Properties Measurements

Knowledge of dielectric data is essential in the design of the microwave heating systems because it enables estimates to be made of the power density dissipation and the associated electric-field stress. The dielectric properties of materials vary widely, not only with composition, but also with density, temperature and frequency (Meredith, 1998). As the dielectric properties govern the ability of materials to heat in microwave fields, the measurement of these properties as a function of temperature, frequency, or other relevant parameters is very important. Physical interaction mechanisms between electromagnetic field and material can be inferred from the characteristics behavior of the complex permittivity of materials as function of frequency and temperature (Stein et al., 1994).

Knowledge of the dielectric properties is also important in supporting numerical modeling and calculation of the absorbed power distribution (power density) in the samples heated using electromagnetic energy. Measurement of complex permittivity over a broad frequency band is required to completely characterize the dielectric properties of materials and to identify and characterize the various relaxation

processes (Meredith, 1998).The most common methods of dielectric measurement are transmission line, resonant cavity and free space method.

The most common popular measurement techniques for characterization of complex permittivity are transmission line methods. They provide broad band data from a single test, are relatively simple to form and do not require large sample sizes (Stein et al., 1994). In transmission line methods, complex scattering parameters (S-parameters) of a precisely machined sample placed in a coaxial line or rectangular waveguide are determined. Use of an automated network analyzer simplifies the measurements and the determination of S-parameters. Transmission-line methods are useful in that they show relaxation behaviour and transitions in permittivity with changes in frequency for the material being tested. However, there are disadvantages in using these methods. First, precise sample fit is critical, with air gaps causing significant errors. Material that are brittle or difficult to machine are especially troublesome. Second, elevated temperature measurements using transmission line methods are very difficult (Tinga, 1992).

Cavity perturbation methods have also been widely used to measure the complex permittivity of material at microwave frequencies. The basic assumption of this method is that the sample must be very small compared with the cavity itself, so that a frequency shift that is small compared with the resonant frequency of the empty cavity is produced by the insertion of the sample (Stein et al., 1994). The resonant frequency and Q of the cavity are determined and compared with empty cavity values. Cavity perturbation measurement can be highly accurate and are particularly advantageous in the determination of small loss tangent (Stein et al., 1994).

Free-space permittivity measurements are useful for accurate measurements at high frequency (above 40 GHz), for composite samples that have structural variations on relatively large scale compared with sample sizes required for other measurement techniques (Stein et al., 1994). For this method, a plate of the sample material is placed between a high-directivity transmitter and receiver horns. Samples are positioned at a given angle in the path of the incident beam and the transmission and reflection coefficients are measured by the two identical receiver horns suitably aligned with respect to the incident beam and the sample. The dielectric properties are then measured from the observed transmission and reflection (Stein et al., 1994).

3.7 Power Density

In microwave engineering, the amount of thermal energy deposited in to a material due to microwave heating is called power density and given by:

$$P_d = 2\pi f \varepsilon_o \varepsilon^{"} E_o^{\,2} + 2\pi f \mu_o \mu'' H_0^{\,2} \qquad \textbf{3.5}$$

Where P_d is the power density (W/m^3) , f is the frequency of the microwave radiation (Hz), ε_o is the permittivity of free space (8.854 × 10^{-12} F/m), ε'' is the dielectric loss factor, E_o is the magnitude of the electric field portion of the microwave radiation (V/m) , μ'' is the magnetic loss factor and H_0 is the magnetic field (A/m). The terms on the right side of the equation refer to electric and magnetic losses, respectively. For materials with no magnetic constituents the volumetric dissipation of power can be written as:-

$$P_d = 2\pi f \varepsilon_o \varepsilon^{"} E_o^{\,2} \qquad \textbf{3.6}$$

It can be seen that the power density dissipated in the workload is proportional to the frequency of operation. The power density is also proportional to the loss factor which depends on the frequency, temperature, composition and moistures content. The power density is also proportional to the square of the electric field (E_O). Further, it should be emphasized that determination of the electric field is not an easy matter, as it varies from point to point inside the applicator. Meredith (1998) mentioned the following reasons why the electric field is not uniform in microwave applicators:

a) the workload has boundary edges and corners, and its surface may be irregular, which causes field concentration by ‘fringing’

b) the workload may not be homogenous, with considerable variations in permittivity

c) Metal structures may be present within the heating chamber, especially with sharp edges (they should be ‘rounded’).

d) Dielectric structures may be present within the heating chamber to support the workload

e) There may be standing wave due to reflection within the heating oven

f) Attenuation of energy propagating into the workload may occur

g) Field concentration may exist adjacent to power injection points where the power flux density is high.

Due to the above reasons, estimating the power density in a material using Equation 3.6 is not straightforward. Consequently, numerical methods are normally used for estimating the power density range that can be expected for a given applicator geometry, dielectric properties, microwave power and frequency of operation.

Extensive experimental work and electromagnetic simulation have been carried out in Stellenbosch University, in the last ten years, for measuring the dielectric properties of monolithic and crushed ores samples and for estimating the power densities in real applicators. The results of a typical electromagnetic simulation in a tunnel applicator used for pilot scale treatment of crushed ores, using a 30 kW supply at 2.45 GHz, is shown in Figure 3-4.

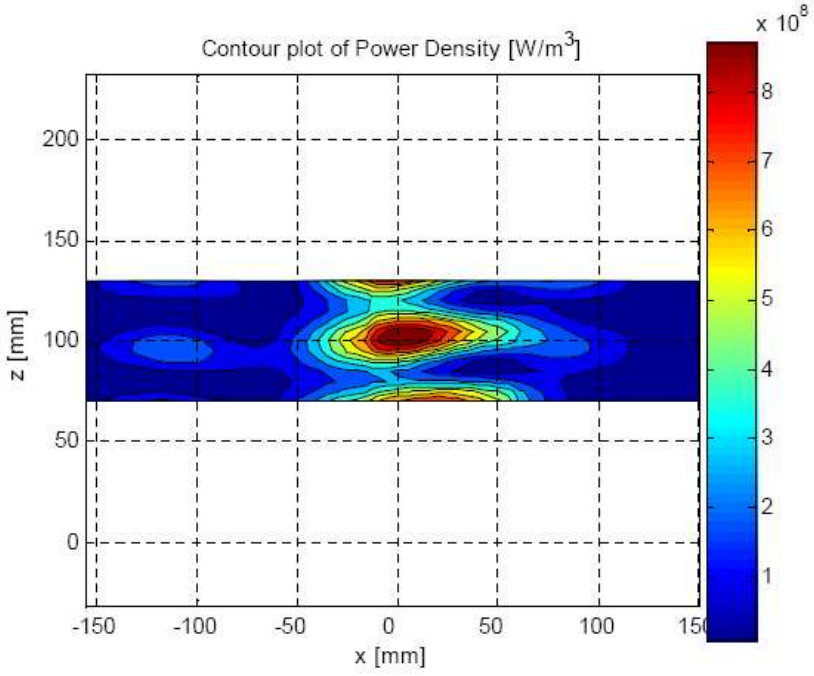

Figure 3.4: Typical electromagnetic simulation result showing power density variation inside an applicator (Marchand, 2008)

In this case, the bed of crushed ore was modeled as a solid homogeneous material with an effective bulk complex permittivity ε = 3.84- j0.28. The power densities shown in the figure were obtained by dividing the actual power densities by 0.1. In this way it is possible to correct for the homogenous assumption by assuming that the power is dissipated in only 10 vol.% of the workload (i.e. in this particular simulation it was assumed that the ore consists of 10% microwave absorbent minerals by volume).

As can be seen from the Figure 3-4, there is a significant variation of power densities inside the applicator. For example, for 30 kW supply used in this simulation, the power densities were in the range of $1 \times 10^8 - 1 \times 10^9$ W/m^3. However, it should be noted the power density inside an applicator is proportional to the power supply. Thus, it is possible to achieve higher power densities than this range by using high power microwave equipment. The power densities shown in the figure are typical of the conditions under which ores are currently being treated at pilot scale. Greater power densities are possible using high power pulsed equipment currently under industrial development. In this type of equipment peak pulse powers of the order of 1 MW can be obtained at pulse width of 1 μs. As the pulse width is increased, the peak pulse power decreases proportionally.

3.8 Penetration Depth

As a wave travels in to a dielectric-heating material, its amplitude diminishes owing to the absorption of power as heat in the material. In the absence of reflected waves in the material, the field intensity and its associated power flux density fall exponentially with distance from the surface (Meredith, 1998). Because the power absorbed in an elemental volume of material is proportional to the power flux density flowing through it, the power dissipation also falls exponentially from the surface.

The rate of decay of the power dissipation is a function of both the relative permittivity (ε') and the loss factor (ε''). The penetration depth, D_p (meter) is defined as the depth into the material at which the power flux has fallen to 1/e (0.368) of its surface value and is given as:-

$$D_p = \frac{\lambda_0}{2\pi\sqrt{2\varepsilon'\left\{\sqrt{1+\left(\frac{\varepsilon''}{\varepsilon'}\right)^2}-1\right\}}} \qquad \textbf{3.7}$$

Where λ_0 is the free space wavelength.

The penetration depth is a very important parameter for a workload because it gives an immediate first-order indication of the heat distribution within it (Meredith, 1998). Table 3-1 shows penetration depth of some minerals.

Table 3-1: Penetration depth of some minerals (Harrison, 1998)

Mineral	Penetration depth at 2.45 GHz (m)
Quartz	5.86
Hematite	0.21
Ilmenite	0.31
Chalcopyrite	0.33
Pyrite	0.11
Magnetite	0.06
Galena	0.84

As can be seen from the table, the penetration depth of most minerals is greater than 50 mm. Thus, as long as the particle size is less than the penetration depth, it is logical to assume that the absorbent mineral is evenly heated by the incoming microwave radiation i.e. volumetric heating assumption is reasonable for small particle size.

3.9 Conclusions

The fundamental nature of microwave, the different microwave heating mechanisms and microwave system components are discussed in the chapter. It has been noted that the ability of microwaves to couple energy directly to the microwave absorbent phases is the primary advantage of microwave processing as compared to conventional techniques. The volumetric heating ability of microwaves allows for more rapid, uniform heating, decreased processing time compared to conventional heating.

It has been noted that it is extremely difficult to precisely determine the power density in a dielectric due to variation of electric field within the applicator. However, estimation of the power density range that can be achieved in single mode and tunnel applicators for a given microwave power, dielectric properties, applicator geometry and frequency of operation is possible by utilizing numerical methods based on solutions of the electromagnetic field equations. It has also been noted that volumetric heating assumption is reasonable for small particle size.

Chapter 4

Rock Strength Testing and Modelling

4.1 Introduction

The mechanical properties of the intact rock are of primary importance in rock mechanics problems. Determination of the strength properties of the rock and the appropriate elastic constants is the principal step in any engineering design in rock. This chapter discusses the most common strength properties of rocks, the tests used for estimating them, and the different failure criteria used in rock mechanics. These include uniaxial compressive strength, stress-strain properties in uniaxial compression and Brazilian tension test. The correlation between uniaxial compressive strength and ore breakage parameters is also presented. In the last part of the chapter, different numerical techniques currently in use in rock mechanics including finite difference, finite element, distinct element, boundary integral and hybrid methods are briefly discussed.

4.2 Strength Properties of Rocks

The ability of a material to resist externally applied force is called its strength. In engineering practice, strength may be regarded as the force per unit area necessary to bring about rupture at given environmental conditions (Jumikis, 1979). The strength properties of rock are dependent upon the interaction between the crystals, particles and cementitious material of which it is composed and such as cracks, joints, bedding and minor faults as exist (Jaeger and Cook, 1969). The distribution of cracks, joint, bedding and faults is so variable that the mechanical properties of any large volume of rock influenced by such separations have little general evidence for any other large volume of rock. Therefore, the most basic mechanical properties of rock are those of a specimen of a size sufficient to contain a large number of constituent particles but small enough to exclude structural discontinuities, so that it posses homogenous properties (Jaeger and Cook, 1969).

Rock strength can be defined only when all the strength-governing factors such as rock environment, size of rock specimen, kind, intensity and duration of load, lateral confining pressure, temperature and failure criteria are known (Stagg and Zienkiewicz, 1968). The strength properties of a rock are also governed by the qualitative and quantitative mineral composition of the rock.

The strength of a rock may be established either experimentally by means of laboratory testing of intact rock specimens and /or by rock-testing in situ. The latter is performed because a rock may contain various kinds of rock imperfections and plane of slippage (Jumikis, 1979). There are two ways for the analysis of the strength of a rock: static and dynamic method. The static properties are computed from the stress-strain response of a representative specimen of the material subjected to a uniaxial loading. The dynamic method is based on non-destructive geophysical (seismic/acoustic) testing. It involves the measurement of compression and shear wave velocities of a known frequency wave, travelling through a representative sample of the rock material.

Important static laboratory-tested strength properties of rocks are: Compressive strength (Uniaxial or unconfined compressive strength and Triaxial compressive strength), Tensile strength, Direct shear strength, Bending or flexural strength and Torsion test. The details of each test are discussed in (Jaeger and Cook, 1969). Only unconfined compressive strength and tensile strength are discussed here.

4.3 Uniaxial Compressive Strength (UCS) Test

The uniaxial compressive strength test is generally known to be one of the most rigorous strength tests of a material. It is also the commonest method for studying the mechanical properties of rock (Jumikis, 1979). The uniaxial compressive strength test is performed on cylindrical or prismatic or cube rock specimens by compressing or loading them to failure (Brady and Brown, 1985). A length to diameter ratio from 2 - 2.5 is recommended to ensure a fairly uniform stress distribution in the sample and to increase the possibility of a failure plane being free to form without intersecting the resting head (Stagg and Zienkiewicz, 1968). The rock specimen usually fractures by axial, brittle splitting or fail in shear, depending up on the degree of the end constraints at the ends of the rock specimen offered by the platens of the testing

machine and the surface quality of the parallel ends of the rock specimen receiving the load (Jumikis, 1979). Upon failure of the rock specimen at the ultimate compressive stress σ, when the shear strength in its potential shear plane S-S is exhausted, the sheared-off parts slide past each other across the inclined S-S plane , i.e. the rock fractures or fail in shear (Jumikis, 1979).

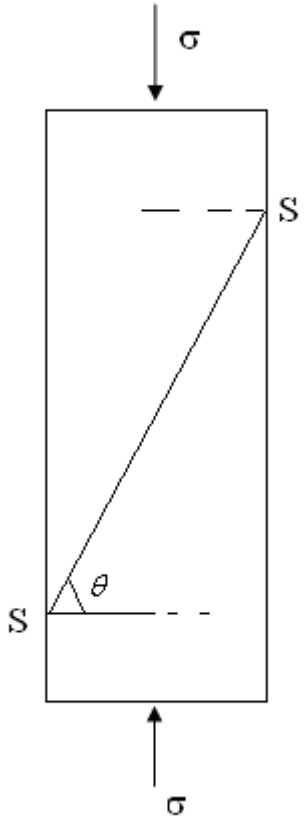

Figure 4.1: Failure of rock specimen in UCS test

The unconfined compression test results also render directly the unconfined shear strength τ and the test parameters ϕ and C commonly known as the angle of friction and cohesion, respectively as a function of rupture angle (θ). Friction on the rupture surface supports a considerable amount of axial stress. Cohesion may be regarded as the tangential strength (no-load strength).

The unconfined shear strength τ is expressed by Coulomb's shear strength equation:

$$\tau = \sigma_n \tan\phi + C \qquad \textbf{4.1}$$

Where

$$\sigma_n = \frac{\sigma_1}{2}\left(1 + \cos 2\theta\right) \qquad \textbf{4.2}$$

From geometry of Mohr's stress diagram, ϕ and θ can be related as:

$$2\theta = \pi/2 + \phi \qquad \textbf{4.3}$$

It is important to realize that the unconfined compressive strength is not an intrinsic material property. It strongly depends on the specimen geometry or the loading conditions used in the test.

4.4 Stress-strain Curve

The most common method of studying the mechanical properties of rocks is by axial compression of a circular cylinder. For any stress applied to the cylinder, the axial and lateral strains may be measured either by strain gauges attached to the cylinder or by measurement of displacements (Stagg and Zienkiewicz, 1968).The stress–strain curve is the graphical representation of the relationship between the stress, derived from measuring the load applied on the sample, and the strain, derived from measuring the deformation of the sample. The nature of the curve varies from material to material. Figure 4.2 shows a stress strain plot for the uniaxial compression of a cylindrical rock sample.

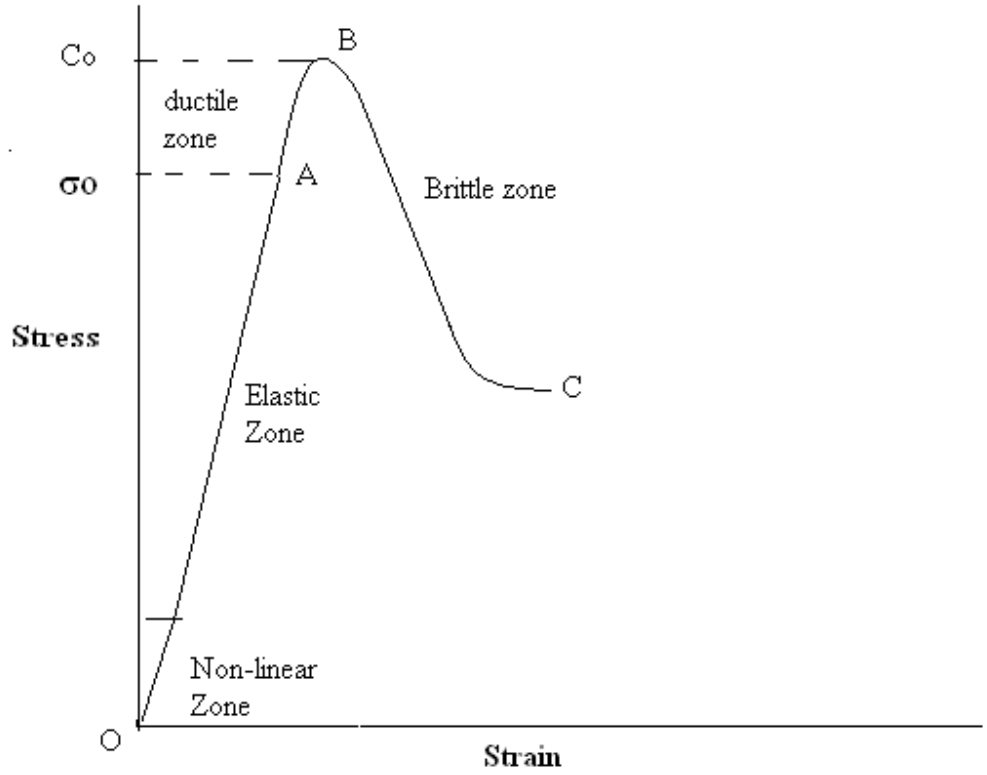

Figure 4.2: Stress-strain response for a cylindrical sample of rock under Uniaxial compression

The region OA is the elastic zone and the slope of a line in this region gives the Young's modulus. Point A is called the yield point. Between point A and B the rock continues to deform without losing its ability to resist load. This region is called the ductile region. Beyond point B, the ability of the material to resist load decreases with increasing deformation and the rock enters the brittle region. Thus, point B denotes the transition from ductile to brittle behaviour and the stress at this point defines the uniaxial compressive strength (UCS) of the material denoted as CO. Sudden failure of the material will then occur somewhere in the BC region of the graph. The UCS is the maximum force recorded at the point of ductile-brittle transition divided by the cross sectional area of the sample. Typical values of the UCS range from weak limestone at < 50 MPa to highly competent microcrystalline Hornfels at 450 MPa (Napier-Munn, 1996).

4.5 Brazilian Tension Test

Determination of the tensile strength by direct extension of a cylindrical specimen is very difficult and is not commonly made because a satisfactory means has not yet been devised to grip the specimen without introducing bending stresses (Stagg and Zienkiewicz, 1968). The most practical method of determining the direct tensile strength for engineering purposes is accomplished by attaching, with epoxy resin, metal end caps to cylindrical rock specimens which are then pulled in tension by wire cables or roller chain which is often difficult and time consuming. For this reason, despite the importance of the tensile strength of rock in practice and in connection with theories of failure, the tensile strength is most commonly measured by rapid indirect means (Jaeger and Cook, 1969). The most frequently used indirect method for determining the tensile strength of rock is the Brazilian tension test.

The Brazilian tension test (also known as the splitting tensile test) is widely used to evaluate the tensile strength of rocks, as it is easy to prepare and test specimen. Compression-induced extensional fracturing generated in this test is also more representative of the in situ loading and failure of rocks. In the Brazilian tension test, a circular disk placed between two platens is loaded in compression producing a nearly uniform tensile stress distribution normal to the loaded (vertical) diametrical plane, leading to the failure of the disk by splitting along the line of the diametrical loading (Rocco et al., 1999).

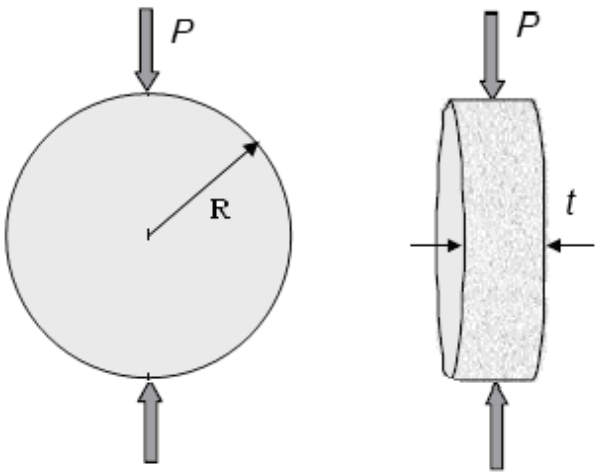

Figure 4.3: Brazilian test for indirect tensile strength

The indirect tensile strength of a disc sample (Figure 4.3) of radius R and thickness t, with known load at failure P is given by:-

$$\sigma_t = \frac{P}{\pi R t} \qquad \textbf{4.4}$$

For most engineering purposes, it is probably sufficiently accurate for most problems to assume a tensile strength of 5 - 10% of the uniaxial compressive strength of the rock (Stagg and Zienkiewicz, 1968). More accurate determination may not be justified because of the wide range of tensile strengths observed in a given suite of rock specimens. In addition, directional variation is very great in metamorphic rocks and in thinly bedded sedimentary rocks (Stagg and Zienkiewicz, 1968).

4.6 Rock Failure Criteria

The failure of solid materials can be divided into two groups depending on the failure characterises: brittle or ductile. For brittle failure, there is a sudden loss of strength once the peak (σ_{peak}) has been reached. Despite the fact the rock may break, there is often still a residual strength (σ_{res}), which refers to the maximum post-peak stress level that the material can sustain after substantial deformation has taken place (Brady and Brown, 1985). The yield limit (σ_{limit}) is the stress level at which departure from the elastic behaviour occurs and the plastic permanent deformation begins. For ductile failure, the loss of strength is not that sudden as for brittle behaviour and there is a small, or no, strength reduction when the yield limit is reached (Figure 4.4).

Failure of intact rock can often be classified as brittle. The harder igneous and some metamorphic rocks often fail in a brittle manner. Weak sedimentary intact rocks tend to fail in a more ductile manner (Edelbro, 2003).

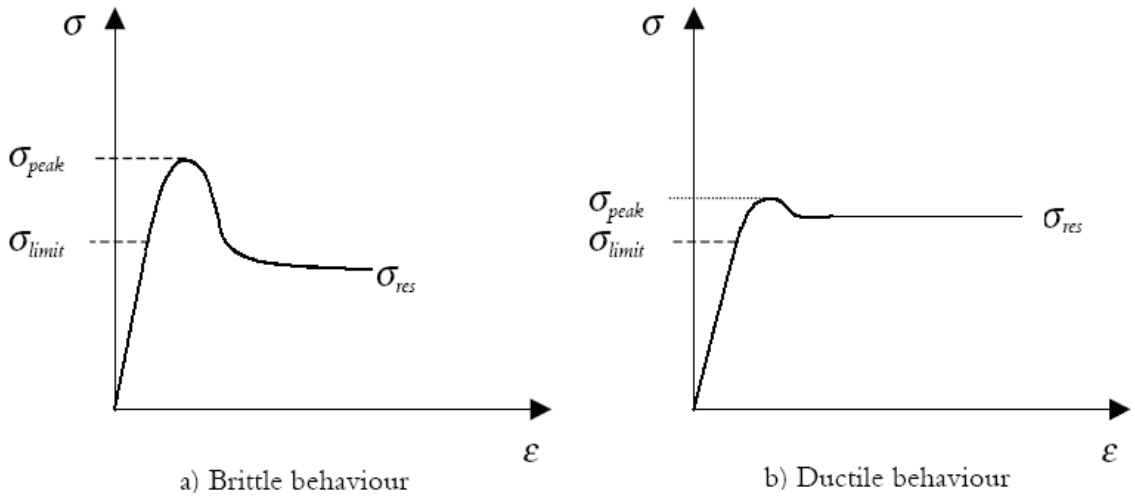

Figure 4.4: Stress- Strain curve for brittle (a) and ductile material (b)

4.6.1 Mohr-Coulomb Failure Criterion

In Mohr-Coulomb failure criterion, the rock strength is defined by the cohesive strength C and the angle of friction ϕ and which is written as:

$$\tau_s = C + \sigma_n \tan\phi \qquad \textbf{4.5}$$

Where

τ_s = the shear stress along the shear plane at failure

C = the cohesive strength of the rock

σ_n = the normal stress acting on the shear plane

ϕ = the friction angle of the shear plane

The equation above referred to as the Mohr-Coulomb criterion and is applied in rock mechanics for shear failure in rock, rock joints and rock masses (Edelbro, 2003). The Mohr-Coulomb criterion can also be expressed, in principal stresses, as

$$\sigma_1 / \sigma_3 = \frac{2c\cos\phi}{\sigma 3(1-\sin\phi)} + \frac{1+\sin\phi}{1-\sin\phi} \qquad \textbf{4.6}$$

Or in many case written as :

$$\sigma_1 = \sigma_c + k\sigma_3 \qquad \textbf{4.7}$$

Where k is the slope of the line relating σ_1 and σ_3. And σ_c is the uniaxial compressive strength. The Mohr-Coulomb criterion is linear but since rock can not sustain large tensile stresses, a tensile cut-off is often included. The values of the friction angle (ϕ) and the cohesion (C) can be calculated using Equations 4.8 and 4.9.

$$Sin\phi = k - 1/k + 1 \qquad \textbf{4.8}$$

$$C = \sigma_C \frac{(1-\sin\phi)}{2\cos\phi} \qquad \textbf{4.9}$$

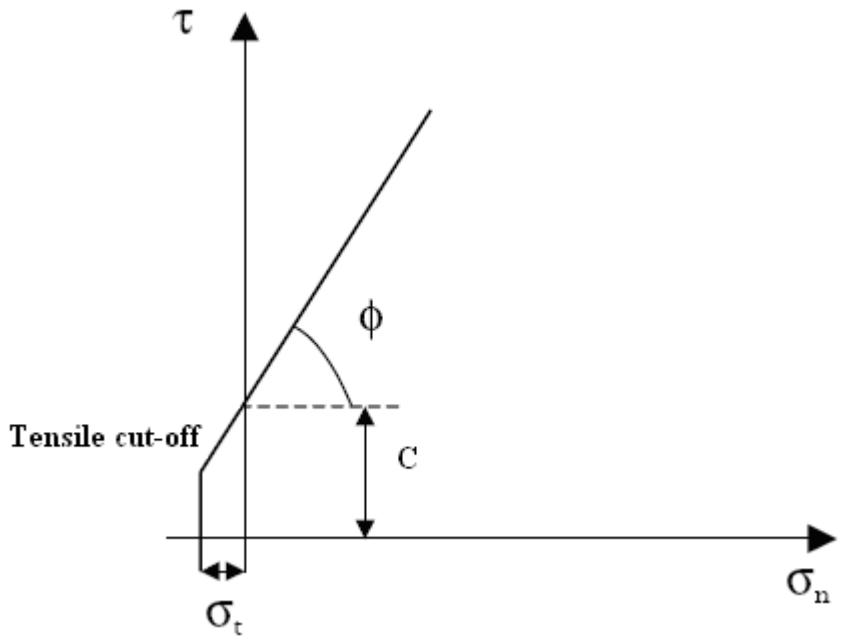

Figure 4.5: Mohr-Coulomb failure criterion in terms of normal and shear stresses

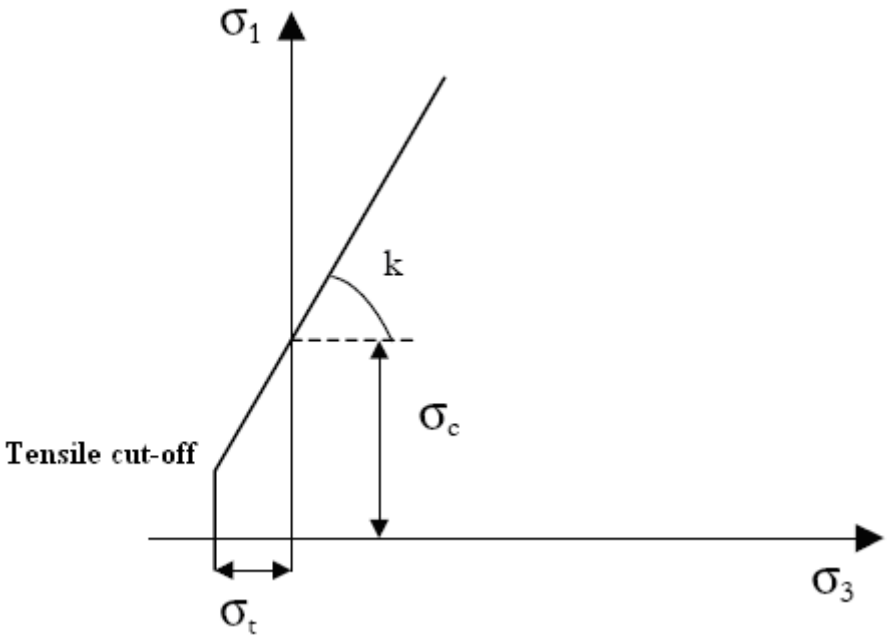

Figure 4.6: Mohr-Coulomb failure criterion in terms of principal stresses

4.6.2 Hoek-Brown Failure Criterion

The original Hoek-Brown failure criterion was developed for both intact rock and rock mass. Hoek and Brown (1980) found that the peak triaxial strength of a wide range of rock materials could be reasonably represented by the following equation:-

$$\sigma_1 = \sigma_3 + \sqrt{m\sigma_3\sigma_c + s\sigma_c^2} \qquad \textbf{4.10}$$

Where m and s are constant, which depend on the properties of the rock and on the extent to which it has been broken before being subjected to the stress σ_1 and σ_3. σ_c is the uniaxial compressive strength of the intact rock material. And σ_1 and σ_3 are the major and minor principal stress at failure.

The Hoek-Brown failure criterion is widely accepted and has been applied in a number of projects around the world.

4.6.3 Mohr-Coulomb Parameters from Hoek-Brown Failure Criterion

Most geotechnical softwares are written in terms of the Mohr-Coulomb failure criterion in which the rock strength is defined by the cohesive strength C and angle of friction, ϕ. There is no a direct relationship between the linear Mohr-Coulomb failure criterion and the non-linear Hoek-Brown criterion consequently the determination of the equivalent Mohr-Coulomb parameters (C and ϕ) for a rock that has been evaluated as a Hoek-Brown material was a difficult problem (Hoek et al., 2002). This problem was addressed in the 2002 edition of Hoek-Brown failure criterion and with the associated Window program called 'Roclab' which provides a convenient means of solving and plotting the equations presented in the paper. Hoek et al. (2002) found that the equivalent Mohr-Coulomb parameters for a material can be obtained by fitting an average linear relationship to the curve generated by the generalized Hoek-Brown criteria equation given below:-

$$\sigma_1^{'} = \sigma_3^{'} + \sigma_{ci}\left[m_b \frac{\sigma_3^{'}}{\sigma_{ci}} + s \right]^a \qquad \textbf{4.11}$$

Where m_b is a reduced value of the material constant m_i and is given by

$$m_b = m_i \exp\left[\frac{GSI - 100}{28 - 14D} \right] \qquad \textbf{4.12}$$

s and a are constants for rock mass given by the following relationship

$$s = \exp\left[\frac{GSI - 100}{9 - 3D} \right] \qquad \textbf{4.13}$$

$$a = \frac{1}{2} + \frac{1}{6}\left[e^{-GSI/15} - e^{-20/3} \right] \qquad \textbf{4.14}$$

Where D is a factor which depends upon the degree of disturbance (0-1) and GSI is the geological survey index (0-100). The estimation is done by fitting an average linear relationship to a curve generated by solving Equation (4.10) for a range of

minor principal stress values defined by $\sigma_t < \sigma_3 < \sigma'_{3max}$, as illustrated in Figure 4.7. The fitting process involves balancing the areas above and below the Mohr-Coulomb plot. This result in the following equations for angle of friction ϕ' and the cohesion strength c' :-

$$\phi' = \sin^{-1}\left[\frac{6am_b(s+m_b\sigma'_{3n})^{a-1}}{2(1+a)(2+a)+6am_b(s+m_b\sigma'_{3n})^{a-1}}\right] \quad \textbf{4.15}$$

$$c' = \frac{\sigma_{ci}\left[(1+2a)s+(1-a)m_b\sigma'_{3n}\right](s+m_b\sigma'_{3n})^{a-1}}{(1+a)(2+a)\sqrt{1+(6am_b(s+m_b\sigma'_{3n})^{a-1})/(1+a)(2+a)}} \quad \textbf{4.16}$$

Where

$$\sigma_{3n} = \sigma'_{3max}/\sigma_{ci} \quad \textbf{4.17}$$

The Mohr-Coulomb shear strength, τ_s , for a given normal stress σ_n, is then found by substitution of these values of c' and ϕ' into Equation 4.18:

$$\tau_s = c' + \sigma_n \tan\phi' \quad \textbf{4.18}$$

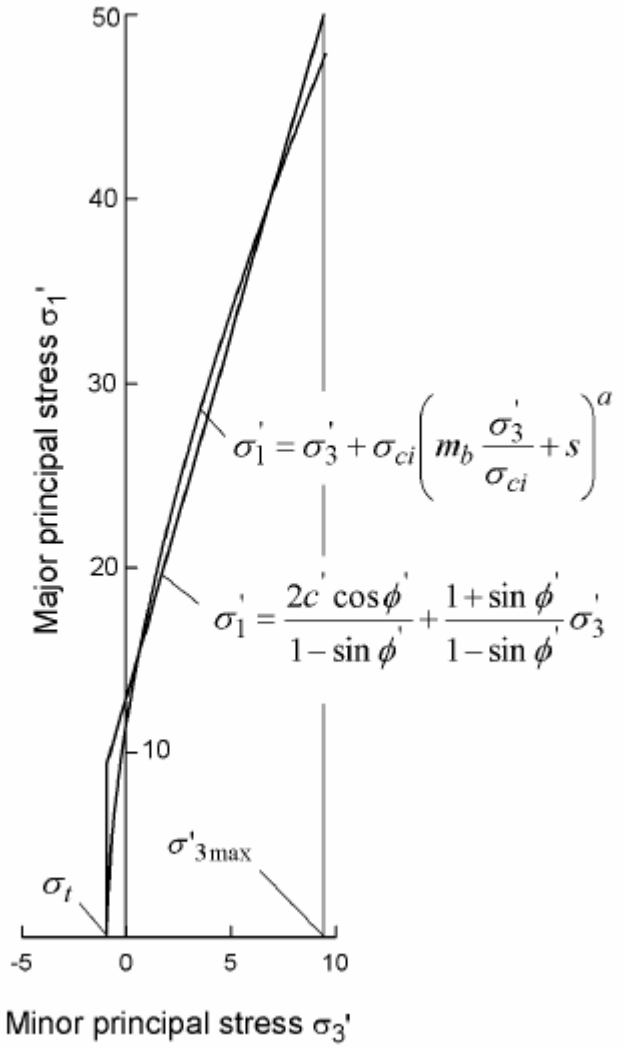

Figure 4.7: Relationship between major and minor principal stresses for Hoek-Brown and equivalent Mohr-Coulomb criteria

The equivalent plot in terms of the major and minor principal stresses is defined by:

$$\sigma_1' = \frac{2c'\cos\phi'}{1-\sin\phi'} + \frac{1+\sin\phi'}{1-\sin\phi'}\sigma_3' \qquad \textbf{4.19}$$

4.7 Other Methods of Rock Strength Testing

4.7.1 Point Load Test

The point load test is a fast and convenient way to determine the strength and fracture toughness of an ore. The point load index can be used to simultaneously characterise rock for blastability and comminution processes (JKMRC). Point load tests give a quick but reproducible method of determining uniaxial compressive strength of samples without the need for large amounts of sample preparation..

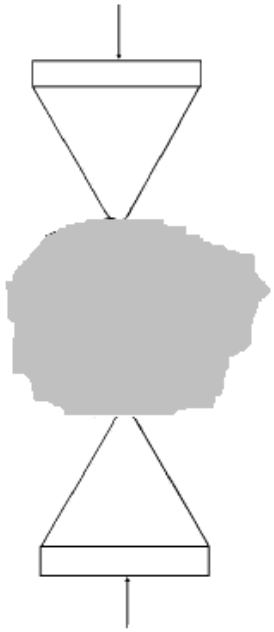

Figure 4.8: Point load testing

The test is very simple; a particle is measured and placed between a pair of specially shaped, hardened-steel tips (Figure 4-8). Force is then applied between the tips and the maximum force sustained by the particle is recorded. Several empirical equations have been developed to convert the test data to I_{s50} and then to an approximation of compressive strength (Hoek and Brown, 1980). The most common empirical equation is given in Equation 4.20.

$$I_{s50} = \left[\frac{\left(\frac{depth}{50} \right)^{0.45} \times force}{\left(\frac{4 \times width \times depth}{\pi} \right)} \right] \quad \textbf{4.20}$$

4.7.2 Drop Weight Test

Drop weight test is the most common method for assessing impact breakage characteristics of ores. The apparatus consists of a steel drop weight mounted on two guide rails and enclosed in Perspex as shown in Figure 4.9.

Figure 4.9: Drop weight testing device

The weight is released from a predetermined height by a pneumatic switch and falls under gravity to crush a single particle placed on a steel anvil. By changing the released height and/or the mass of the drop weight, a wide range of input energy can be produced. The standard drop weight device is fitted with a 20 kg mass, which can be extended to 50 kg. The range of drop height is between 0.05 and 1 m, which represents a wide operating energy range from 0.01 to 50 kWh/t (based on 10 to 50 mm particles) (Napier-Munn et al., 1996).

The results from the drop weight test provide an energy input size/product size relationship. This relationship is analyzed using a set of curves to describe the size distribution produced from breakage events of increasing size reduction or energy input. The analytical procedure is based on the assumption that product size distributions are a function of input energy or specific comminution energy (Ecs). To model the breakage process the JKMRC developed a method of relating energy to geometric size reduction.

The basic principle of the method is as follows. If a single particle is broken, the size distribution of the daughter particles may be considered as a √2 series and a cumulative size distribution graph plotted. The graph is then replotted after dividing the *x*-axis by the original particle size. A series of marker points are then used to describe the size distribution. These are defined as a percentage passing *t*, a fraction of the original particle size. Thus, t_2 is the percentage passing half of the original size, etc. The value of t_{10}, i.e., the amount passing 10% the original mean size, is used as a characteristic of size reduction and may be considered a fineness index (Napier-Munn et al., 1996). To make use of this technique, the marker points t_2, t_4, t_{25}, t_{50} and t_{75} are stored in matrix form against t_{10}. This information is then used to calculate the values of *A* and *b*, which are defined as the ore impact breakage parameters. *A* and *b* are related to E_{CS} and t_{10} by the following equation:-

$$t_{10} = A\left[1 - e^{(-b.E_{CS})}\right] \qquad \textbf{4.21}$$

In order to accurately predict future mine and mill production rates, knowledge of ore grindability is essential. For this reason, various researches were carried out to correlate the unconfined compressive strength of rock with ore grindablity, as it may be determined easily and at minimal cost. More researches were undertaken to examine potential relationships between UCS and Bond Work Index values (crushing, rod mill and ball mill). Broch and Franklin (1972) reported that for 50 mm diameter cores the uniaxial compressive strength is approximately equal to 24 times the point load index (Equation 4-22). They also developed a size correction chart so that core of various diameters could be used for strength determination.

$$\textbf{UCS} = 24\ \mathbf{I_{s50}} \qquad \textbf{4.22}$$

Bearman (1999) later showed that the point load index is related to mode 1 fracture toughness as:

$$K_{IC} = 0.209\ I_{s50} \qquad 4.23$$

The fracture toughness has also been shown to have a strong correlation with the breakage parameter A and b (Bearman et al, 1997). It was shown that:-

$$B = 2.2465 \times K_{IC}^{-1.6986} \qquad 4.24$$

$$A*b = 126.96 \times K_{IC}^{-1.8463} \qquad 4.25$$

By combing the above equations, it is possible to tabulate the impact breakage parameters for a given UCS value as shown in Table 4.1.

Table 4-1: Correlation of UCS and ore impact breakage parameters

UCS(MPa)	I_{s50}	K_{IC}	A×b	b	A
300.00	12.50	2.61	21.56	0.44	49.04
290.00	12.08	2.53	22.95	0.47	49.29
280.00	11.67	2.44	24.49	0.49	49.54
270.00	11.25	2.35	26.19	0.53	49.81
260.00	10.83	2.26	28.08	0.56	50.09
250.00	10.42	2.18	30.19	0.60	50.38
240.00	10.00	2.09	32.55	0.64	50.68
230.00	9.58	2.00	35.21	0.69	51.00
220.00	9.17	1.92	38.23	0.74	51.34
210.00	8.75	1.83	41.65	0.81	51.69
200.00	8.33	1.74	45.58	0.88	52.07
190.00	7.92	1.65	50.11	0.96	52.46
180.00	7.50	1.57	55.37	1.05	52.88
170.00	7.08	1.48	61.53	1.15	53.33
160.00	6.67	1.39	68.82	1.28	53.81
150.00	6.25	1.31	77.53	1.43	54.33
140.00	5.83	1.22	88.06	1.60	54.88
130.00	5.42	1.13	100.97	1.82	55.49
120.00	5.00	1.05	117.05	2.08	56.15
110.00	4.58	0.96	137.45	2.42	56.87
100.00	4.17	0.87	163.89	2.84	57.68
90.00	3.75	0.78	199.09	3.40	58.59
80.00	3.33	0.70	247.45	4.15	59.61
70.00	2.92	0.61	316.64	5.21	60.80
60.00	2.50	0.52	420.89	6.77	62.20

Once A and b are determined for a given UCS value; t_{10}, the percentage passing one tenth of the original particle size for a given specific comminution energy can be determined from the following equation:-

$$t_{10} = A\left[1 - e^{(-b.E_{CS})}\right] \qquad \textbf{4.26}$$

Where E_{CS} is the specific comminution energy (kWh/t)

4.7.3 Ore Abrasion Test

Ore abrasion parameter t_a is a measure of the resistance of the ore to abrasion. The standard abrasion test tumbles 3 kg of -55 + 38 mm particles for 10 minutes at 70% critical speed in a 305 mm by 305 mm laboratory mill fitted with 4×6 mm lifter bars (Napier-Munn et al., 1996). The resulting product is then sized and the t_{10} value for the product is determined. And t_a is defined as the 1/10 of t_{10}. t_a value is as low as 0.2 for very hard ores, to above 2 for very soft ores; a value of 0.88 is indicative of a medium resistance to abrasion (Napier-Munn et al., 1996).

In order to estimate the abrasion parameter from the impact breakage parameter A and b, a lower input energy of 0.118 kWh/t as suggested by (Napier-Munn et al., 1996) was used in Equation 4-26 to calculate t_{10} then the abrasion parameter was obtained as t_a = 1/10 of t_{10}. The abrasion parameter is correlated with the Bond work index (*WI*) though not strongly (Napier-Munn et al., 1996) as:

$$t_a = 19.7WI^{-1.34} \qquad \textbf{4.27}$$

From the information given above, it is possible to show the correlations between the different parameters as illustrated in Table 4.2.

Table 4-2: Correlations of UCS with Bond work index for E_{CS} = 0.118 kWh/t

UCS (MPa)	A×b	b	A	t_a	*WI*
300.00	21.56	0.44	49.04	0.25	26.18
290.00	22.95	0.47	49.29	0.26	25.02
280.00	24.49	0.49	49.54	0.28	23.87
270.00	26.19	0.53	49.81	0.30	22.73
260.00	28.08	0.56	50.09	0.32	21.61
250.00	30.19	0.60	50.38	0.34	20.51
240.00	32.55	0.64	50.68	0.37	19.42
230.00	35.21	0.69	51.00	0.40	18.36
220.00	38.23	0.74	51.34	0.43	17.31
210.00	41.65	0.81	51.69	0.47	16.27
200.00	45.58	0.88	52.07	0.51	15.26
190.00	50.11	0.96	52.46	0.56	14.27
180.00	55.37	1.05	52.88	0.61	13.30
170.00	61.53	1.15	53.33	0.68	12.35
160.00	68.82	1.28	53.81	0.75	11.42
150.00	77.53	1.43	54.33	0.84	10.51
140.00	88.06	1.60	54.88	0.95	9.63
130.00	100.97	1.82	55.49	1.07	8.78
120.00	117.05	2.08	56.15	1.22	7.95
110.00	137.45	2.42	56.87	1.41	7.15
100.00	163.89	2.84	57.68	1.64	6.38
90.00	199.09	3.40	58.59	1.94	5.65
80.00	247.45	4.15	59.61	2.31	4.95
70.00	316.64	5.21	60.80	2.79	4.30
60.00	420.89	6.77	62.20	3.42	3.69

4.8 Numerical Methods in Rock Mechanics

4.8.1 Introduction

Numerical methods have been extensively used in rock mechanics. They provide extremely powerful tools for analysis and design of engineering systems with complex factors that were not possible or very difficult with the use of the conventional methods.

Generally, numerical methods can be classified in to three categories: continuum method, discrete method and hybrid method. The choice of continuum or discrete methods depends on many problem-specific factors, and mainly on the problem scale and fracture system geometry (Jing, 2003). The continuum approach can be used if only a few fractures are present. The discrete approach is most suitable for moderately fractured rock where the number of fractures is too large for the continuum with fracture elements approach. There are no absolute advantages of one method over another (Jing and Hudson, 2002).

Different numerical techniques in rock mechanics including finite difference, finite element, distinct element, boundary integral and hybrid methods will be discussed briefly in the following sections.

4.8.2 Finite Difference Method (FDM)

Finite difference method is a numerical method for approximating the solutions to differential equations using finite difference equations to approximate derivatives. Differential equations are solved by dividing the domain into connected series of discrete points called nodes. These nodes are the sampling points for the solution and are linked using finite difference operators to the governing equations (Desai and Christian, 1977). It is not necessary to combine the element matrices into a large global stiffness matrix as in the finite element model. Instead, the finite difference method regenerates finite difference equations at each step. Derivatives of governing equations are replaced directly by algebraic expressions written in terms of field variables, e.g. stress or displacement, at discrete points in space (nodes).

The finite difference method allows one to follow a complicated loading path and highly non-linear behaviour without requiring the complex iterative procedure of a standard implicit code. Finite difference method can be used to discretize both time and space. It also provides easy error estimation techniques. It is particularly suitable for large, non-linear problem which may involve collapse or progressive failure (Jing and Hudson, 2002).

Finite difference method is difficult to use for irregular shape domain or for problems involving singularities, because the fine meshing required near the singularity cannot be easily reduced for the rest of the domain. The conventional finite difference method with regular grid systems does suffer from shortcomings, most of all in its inflexibility in dealing with fractures, complex boundary conditions and material heterogeneity.

FLAC is the most well known computer code for stress analysis for engineering problems using finite difference/finite volume method approach. It is the most popular numerical method in rock engineering with applications covering from all aspects of rock mechanics, e.g., slope stability, underground openings, coupled hydro-mechanical, coupled thermal-mechanical etc (Itasca, 2000).

4.8.3 Finite Element Method (FEM)

In the FEM, the system is modeled by a set of appropriate finite elements interconnected at points called nodes. Elements may have physical properties such as thickness, coefficient of thermal expansion, density, Young's modulus, shear modulus and Poisson's ratio. Finite element method is the most widely employed numerical method for rock mechanics and rock engineering. It does not require detailed programming experience to make efficient use of the finite element approach to problem solving in rock mechanics. However, familiarity with the fundamentals of the technique and with practical guidelines for generating reliable results is essential (Jing, 2003).

The formulation of finite element method is based on variational statement of the governing physics (Beer, 1983). Finite element method analysis constitutes three steps mainly, domain discretisation, local approximation and assemblage and solution of

global matrix equation. This method involves the representation of continuum as an assembly of elements which are connected at discrete points called nodes. The problem domain is divided into discrete elements of various shapes, e.g. triangles and quadrilaterals in two-dimension cases and tetrahedrons and bricks in three dimensions. All forces are assumed to be transmitted through the body by the forces that are set up at the nodes. Expressions for these nodal forces, which are essentially equivalent to forces acting between elements, are required to be established. Continuum problem is analyzed in terms of sets of nodal forces and displacements for the problem domain.

The displacement components within the finite elements are expressed in terms of nodal displacements. Derivation of these displacements describes strain in the element. The stiffness of the medium to this induced strain determines stress in the element. Total stress within an element can be found out by superimposition of initial and induced stresses. The matrix of each element describes the response characteristics of the elements. These coefficient matrices are based on minimization of total potential energy. The elemental stiffness matrices are assembled to give the global stiffness matrix which is related to global force and displacement. As the number of elements in a problem domain tends to infinity, this is equivalent to solving differential equation.

Finite element method suffers limitations when simulating fracture problems mainly due to the limitation of small element size, continuous remeshing with fracture growth, conformable fracture path and element edges (Jing and Hudson, 2002). However to overcome this limitation, discontinuous shape functions (Wan, 1990) are used for implicit simulation of fracture initiation and growth through bifurcation theory. Disadvantage of this method is that considerable time is required in preparing input data for a typical problem. This is particularly crucial in 3D problems and has led to the development of sophisticated mesh generation programs which eliminate much of the tedium involved in data preparation (Sheppard, 1988).

Finite element method is computationally expensive. A large number of simultaneous equations must be solved to obtain a solution. If the problem is non-linear, the computation time increases enormously because the sets of simultaneous equations must be solved a number of times.

4.8.4 Boundary Element Method (BEM)

The boundary element method is a numerical computational method of solving linear partial differential equations which have been formulated as integral equations. The integral equation may be regarded as an exact solution of the governing partial differential equation. The boundary element method attempts to use the given boundary conditions to fit boundary values into the integral equation, rather than values throughout the space defined by a partial differential equation.

The boundary element method requires the discretisation of the domain and, if necessary the boundaries between the regions with different properties. For two-dimensional situations line elements at the boundary represent the problem, while for three-dimensional problems, surface elements are required (Beer, 1983). Thus, the dimensionality of the problem is reduced by one. This is particularly attractive as the amount of data required to describe the problem is greatly reduced as compared to finite element method. Due to the boundary element methods advantage in reducing model dimensions, 3D application using the displacement discontinuity method for stress analysis has become efficient (Jing and Hudson, 2002).

However, the computational algorithm is not so straightforward. In boundary element method, a system of simultaneous equations in terms of unknowns associated with nodes of the surface elements is solved. Boundary integral equation method solves linear boundary value problems with known green function solutions. Green's function solution and the governing differential system are used to formulate boundary value problems as an equivalent surface integral. Boundary element method can be direct or indirect depending upon the different mathematical approach, but for either of them to be practical it is necessary to be able to compute economically a function of two points in space known as the fundamental or basic singular solution. Both of these two methods in their simplest form fail if two surfaces in space such as crack are modeled (Jing, 2003).

Although boundary element method has been used in complex rock mechanics problems involving non-linear constitutive equations and number of materials, this method of analysis is particularly efficient in homogeneous, linear elastic problems in three dimensions (Jing and Hudson, 2002). Advantage of this method is reduced in

complex non-linear material laws with sets of materials because the surface needs to be discretised wherever there is change of material properties, and hence the preparation of input data becomes more complicated. Matrices of the equations in this method are not symmetric and banded as in finite element method. Though the number of equations to be solved is less, the computation time is not reduced by the same amount.

4.8.5 Distinct Element Method (DEM)

Distinct element method is one of the most rapidly developing areas of computational mechanics with a broad variety of applications in rock mechanics. The term distinct element method is a family of numerical methods for computing the motion of a large number of particles. The fundamental assumption of the method is that the material consists of separate, discrete particles. These particles may have different shapes and properties. The method was initially developed in 1979 by Cundall and Strack.

In the distinct element method, the interaction of the particles is treated as a dynamic process with states of equilibrium developing whenever the internal forces balance. The contact forces and displacements of a stressed assembly of particles are found by tracing the movements of the individual particles. Movements result from the propagation through the particle system of disturbances caused by specified wall and particle motion. This is a dynamic process in which the speed of propagation depends on the physical properties of the discrete system. The dynamic behaviour is represented numerically by an explicit time steeping algorithm, using a central-difference scheme to integrate velocities and accelerations. The distinct element method is based upon the idea that time step chosen may be so small that, during a single time step, disturbances cannot propagate from any particle further than its immediate neighbours (Cundall, 2001).

The distinct element method utilizes the breakage of individually structural unit or bonds to directly represent damage whereas continuum–based modelling represents damage indirectly through empirical relation.

Distinct element technique method is capable of analyzing multiple interacting deformable continuous, discontinuous or fracturing bodies undergoing large

displacements and rotations. Dynamic equilibrium equation is solved for each body subjected to boundary interaction forces. There is no restriction on where one element may make contact with another, and nodes may interact with nodes or nodes with element faces. Forces generated between the contacting elements can be made to obey various interacting laws depending upon the physical nature of simulation.

The main advantage of distinct element method is its capability to simulate the fracture process which is not possible in the continuum approaches. UDEC, 3DEC PFC and ESyS-Particle are the most popular computer codes used to perform static as well as dynamic analysis using the distinct element method.

4.8.6 Hybrid Methods

Hybrid methods combine different methods to take advantages of each method while avoiding many of its disadvantages (Jing and Hudson, 2002). Finite element method/ distinct element method is used for non-linear or fractured near fields where explicit representation of the fracture is needed. Boundary element method is used for simulating far field rocks as equivalent elastic continuum. Hence, the hybrids of these methods provide numerical technique for effective representation of the effects of the far field to the near field rocks (Jing and Hudson, 2002).

The use of hybrid methods in rock mechanics has many benefits. However, ensuring continuity conditions in the interface between regions of different models is often very difficult. This is particularly significant when different material assumptions (e.g. modeling different minerals in an ore) are made (Jing, 2003).

4.9 Conclusions

The most common strength properties of rocks, the tests used for estimating them, and the different failure criteria used in rock mechanics have been discussed in the chapter. It has also been shown that by combining different correlations, it is possible to obtain a relation between uniaxial compressive strength, ore breakage parameters and Bond work index.

Various numerical methods in rock mechanics have also been discussed in the chapter. It is noted that there have been major progresses in numerical methods in solving rock mechanics problems over the last decades. However, due to the inherent nature of rock containing fractures and inhomogeneity, numerical modeling of rock is demanding.

It has been noted that the choice of continuum or discrete methods depends on the problem scale and fracture system geometry. The continuum approach is suitable if only a few fractures are present. The discrete approach is most suitable for modelling moderately fractured rock and fracture process. This suggests that it is advantageous to use both continuum and discrete methods for better understanding of microwave treatment of ore. For instance, continuum analysis can provide the distribution of stresses inside an ore for a given microwave treatment condition easily and with less computational time. Hence, it can be used for understanding the effects of different variables on microwave treatment of ores. The discrete element method can be used for better understanding of microwave induced micro-cracks and crack patterns for different treatment conditions.

It has also been noted that it is not possible to completely validate numerical models by experiments in rock mechanics due to the assumptions in mathematical models and complexities like existing cracks, faults, grain boundary strength in rock. Further, some of the input parameters are not usually measured and availability of these data is generally poor. However, numerical models can be successfully used for corroborating hypotheses, elucidating discrepancies, supporting design decisions and guiding further study.

Chapter 5

Numerical Methodology for Continuum Analysis

5.1 Introduction

This chapter details the methodologies used to simulate thermal and mechanical behaviour and the specification of thermo-mechanical properties that are required to accurately describe thermal and mechanical behaviour of microwave treated ores using a continuum analysis based on the 2-D finite difference modelling software application, *FLAC V4.0*. The first section serves as an introduction to *FLAC*. In section 5-3, the procedures for implementation of models in *FLAC* are detailed; this section also discusses the different constitutive models available and the specific application of each model. Selection of minerals and geometrical construction are discussed in section 5-4 and 5-5. Sections 5-6 to 5-8 detail the procedures followed for modelling microwave heating, thermally induced stress and unconfined compressive strength test.

5.2 *FLAC* (Fast Lagrangian Analysis of Continua)

FLAC (Fast Lagrangian Analysis of Continua) is a two-dimensional explicit finite difference program for modelling soil, rock and structural behaviour. The program simulates the behaviour of materials that may undergo plastic flow when their yield limits are reached (Itasca, 2000).

FLAC has been chosen as a suitable commercially available code for the purpose of understanding microwave treatment of ores, as it allows thermal–mechanical analysis by combining the thermal option with the mechanical calculation. *FLAC* has been previously used to successfully model microwave heating of binary ore and the thermal stress development (e.g. Whittles et al., 2003; Jones et al., 2005). The thermal-mechanical coupling in *FLAC* is one-way: temperature change may induce a mechanical stress change as a function of the thermal-expansion coefficient. Mechanical changes in the body, however, do not result in temperature change or changes to thermal properties.

In *FLAC*, materials are represented by zones, which for, a grid that is adjusted by the user to fit the shape of the object to be modelled. Each zone behaves according to a prescribed linear or nonlinear stress/strain law in response to the applied forces or boundary restraints. *FLAC* also contains the powerful built-in-programming language *FISH* (short for *FLACish*).

FISH enables the user to define new variables and functions. It is a compiler; programs entered via a *FLAC* data file are translated into a list of instructions stored in *FLAC*'s memory space; these are executed whenever a *FISH* function is invoked. *FISH* was developed to do things with *FLAC* that were either difficult or impossible with the existing code. For instance, it was possible to write the thermal properties of minerals as a function of temperature and to incorporate it to the model, which was apparently required for obtaining the temperature profile inside an ore for a given treatment condition (e.g. Jones, 2004).

FLAC can be operated as either a menu-driven or command-driven computer program. The menu-driven mode provides easy-to-use access to *FLAC* operation by generating and applying all the input required for a *FLAC* simulation, in response to point and click operations. The menu-driven mode is particularly important for plotting temperature profiles and the material mechanical state (whether it reaches yield or not) for a given microwave power density and exposure time.

5.3 Implementation of Model

5.3.1 Finite Difference Grid Generation

The fist step in any modelling problem involves construction of the geometry of the physical domain being analyzed. In *FLAC*, this is done by construction of the finite difference grid. Grid generation involves the shaping of the row and column grid to fit the shape of the physical domain. A grid is defined by specifying the number of zones "i" desired in the horizontal (x) direction, and the number of zones "j" in the vertical (y) direction. The grid is organized in a row and column fashion. Any zone in the grid uniquely identified by a pair of i,j indices. Similarly, each grid point is identified by a pair of i,j indices. It can be noted that if there are p zones in the x-direction and q

zones in the y-direction, then there will be p +1 grid points in the x-direction and q +1 grid points in the y-direction.

It should be noted that a balance must be struck between the accuracy required and the solution speed when selecting the number of zones for a model. The calculation speed to reach a solution varies directly as a function of the number of zones. Figure 5-1 shows typical grid generated in a 10×20 mm model.

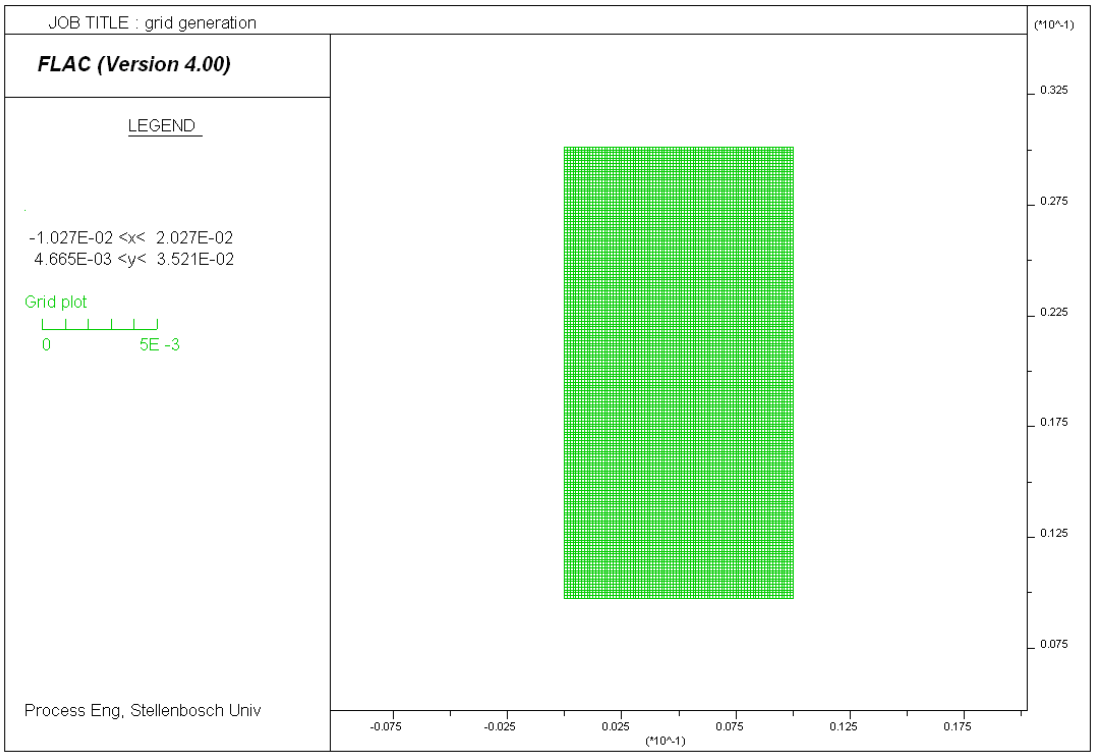

Figure 5.1: Grid generation in *FLAC*

5.3.2 Assigning Constitutive Models and Material Properties

Once the grid generation is complete, one or more material models and associated properties must be assigned to all zones in the model. *FLAC* has ten built-in material models but these models can be put in to three main groups:

1) Null model
2) Elastic model
3) Plastic model

An overview of the constitutive models available in *FLAC* is presented below.

5.3.2.1 Null Model

Null model represents material which is excavated or removed from the model. The stresses within a null zone are set to zero; no body forces acts on these zones. The null material may be changed to a different material model to a later stage of the simulation (Itasca, 2000).

5.3.2.2 Elastic Model

The models in this group are characterized by reversible deformations upon unloading; the stress-strain laws are linear and path-independent. It includes the elastic, isotropic model and elastic transversely isotropic model.

a) ***Elastic, isotropic model***

This model provides the simplest representation of material behaviour. It is valid for homogenous, isotropic, continuous materials that exhibit linear stress-strain behaviour with no hysteresis on unloading.

b) ***Elastic, transversely isotropic model***

This model gives the ability to simulate layered elastic media in which there are distinctly elastic moduli in directions normal and parallel to the layers.

The material properties that should be assigned for the elastic model are:

1) density
2) bulk modulus
3) shear modulus

5.3.2.3 Plastic Model Group

The plastic models involve some degree of permanent, path dependent deformations (failure); as a consequence of the non-linearity of the stress-strain relations (Itasca, 2000). The difference models are characterized by their yielding function, hardening/softening functions and flow rule. The yield functions for each model define the stress combination for which plastic flow takes place. The plastic flow formulation in *FLAC* rests on basic assumptions from plasticity theory that the total

strain increment may be decomposed in to elastic and plastic parts, with the elastic part contributing to the stress increment by means of an elastic law.

Some of the plastic models are discussed below,

a) Drucker-Prager model

This model may be useful to model soft clays with low friction angles; however, this model is not generally recommended for application to geologic materials. It is included in *FLAC* to permit comparison with other numerical program results (Itasca, 2000).

b) Mohr-Coulomb model

The Mohr-Coulomb model is the conventional model to represent shear failure in soils and rocks. The failure envelope for this model corresponds to a Mohr-Coulomb criterion (shear yield function) with tensile cut-off (tensile yield function).

For Mohr-Coulomb plasticity model, the required properties are:

1) density
2) bulk modulus
3) shear modulus
4) friction angle
5) cohesion
6) dilation angle; and
7) tensile strength

c) Ubiquitous-joint model

The ubiquitous-joint model is an anisotropic plasticity model that includes weak planes of specific orientation embedded in a Mohr-Coulomb solid. This is specifically used for modeling thinly laminated material exhibiting strength anisotropy (e.g., slate)

d) Strain-hardening/softening model

This model has been previously used and proven to be suitable for modelling the thermally induced damage (Whittles et al., 2003; Jones, 2004, Jones et al., 2007). The model is based on the *FLAC* Mohr-Coulomb model. The difference, however, lies in the possibility that the cohesion, friction, dilation and tensile strength may harden or soften after the onset of the plastic yield. In the Mohr-Coulomb model, those properties are assumed to remain constant. Here, it is possible to define the cohesion, friction and dilation as piecewise-linear functions of a hardening parameter measuring the plastic shear strain.

The initiation of material hardening or softening is commonly a gradual process once plastic yield begins. At failure, deformation becomes more and more inelastic as a result of micro-cracking in concrete and rock and particle sliding in soil. This also leads to degradation of strength in these materials and the initiation of shear bands (Itasca, 2000). The strain hardening/softening model allows representation of nonlinear material softening and hardening behaviour based on prescribed variations of the Mohr-Coulomb model properties (cohesion, friction, tensile strength) as a function of plastic strain.

Figure 5.2 shows one-dimensional strain softening model. As can be seen, the curve is linear to the point of yield; in that range the strain is elastic only: $e = e^e$. After yield, the total strain is composed of elastic and plastic parts: $e = e^e + e^p$.

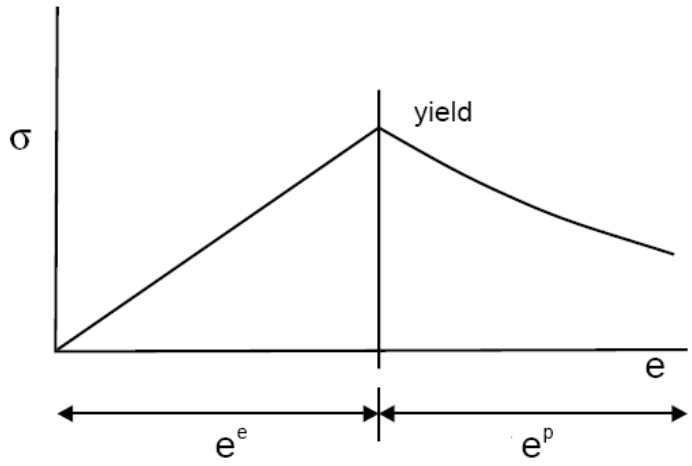

Figure 5.2: One dimensional strain- stress curve with strain softening

5.4 Selection of Microwave Absorbent and Transparent Minerals

As has been discussed in Chapter 4, it is not possible to completely validate numerical models by experiments in rock mechanics due to the assumptions in mathematical models and complexities like fracture and grain boundary in rock. This study also focused on better understanding of the effects of different variables on microwave treatment of ores, not on modelling a specific ore. Accordingly, the study was carried out by constructing different conceptual ore models.

To date, all theoretical studies of microwave treatment of ores were carried out using pyrite as a microwave absorber and calcite as a transparent matrix (Salesman et al., 1997; Whittles et al., 2003; Jones et al., 2005; Jones et al., 2007; Wang et al., 2008). This is mainly due to the fact that most of the studies were carried out only to elucidate the extent of microwave induced stresses for different microwave treatment conditions. The effects of mineralogy and ore texture have not been investigated.

In this study, four additional minerals have been examined. These were galena and magnetite as microwave absorbers and dolomite and quartz as transparent matrices. The selection of minerals was based on absorption of microwave (high/good and low/poor) and availability of thermo-mechanical properties. Magnetite, galena and pyrite were chosen, as they are known to be a good absorber of microwave energy (Walkiewicz et al., 1988) and their thermal and mechanical properties are also known.

Calcite, dolomite and quartz were also selected as transparent matrices, as they are common gangue minerals found in many ores, their thermal and mechanical properties are known and they are also known to be non-responsive to microwave (Walkiewicz et al., 1988; Kingman et al., 2004). The construction of the ore models were then made by disseminating one absorbing mineral in a transparent matrix.

The following binary ores were modelled:

1) Pyrite-Calcite	4) Magnetite-Calcite	7) Galena-Calcite
2) Pyrite-Dolomite	5) Magnetite-Dolomite	8) Galena-Dolomite
3) Pyrite-Quartz	6) Magnetite-Quartz	9) Galena-Quartz

5.5 Geometrical Construction

The maximum ore particle size that can be treated in a microwave system varies according to the internal dimension of the microwave cavity. The maximum diameter of a single-mode microwave cavity is limited by the frequency of operation (refer Chapter 3). Depending on the feed size, the required applicator size dimension can be increased by using lower ISM frequencies of operation, e.g. 915 or 433 MHz (Bradshaw et al., 2007). Currently, the maximum ore particle size that can be treated in the 2.45 GHz tunnel applicator, which is being used for experimentation is about 31.5 mm. It is apparent that the particle size of the models should be less than this size. Accordingly, for all conceptual binary ores, total particle size of 10 mm $\times$ 20 mm was used. The aspect ratio was based on the requirement for a standard UCS test as has been discussed in Chapter 4

A fine resolution was adapted in order to ensure that the rapidly changing temperature and the stress fields that were anticipated to occur around the grain boundary could be accurately captured by the model. Selection of the zone size was also based on numerical stability and computational time. A zone size of 0.125 mm was chosen after running simulations using different zone sizes. This was done by comparing the stress-strain curves obtained at each zone size and also the computational times required. It was not possible to model real fine-grained ores, for which the grain size would be less than 0.05 mm, as the computational time for such cases was inconveniently long. Each binary ore was assigned a composition of 10% microwave absorbing and 90% transparent minerals by area. This composition was deemed to be typical composition of common sulphide ores[1].

To examine the effect of grain size of the microwave absorbent phase on microwave treatment of the ores, three different textures were simulated for each binary ore by randomly disseminating different sizes, square and rectangular shaped, microwave absorber grains in the transparent matrix. These textures were used to represent coarse-grained (>1000 μm)**,** medium-grained (250 μm - 1000 μm) and fine-grained texture (<250 μm). A texture parameter has also been used for identifying the grain

[1] This was obtained from MLA analysis of the ores treated in the AMIRA P879A project, and thus represents a typical mineralogy of industrial interest.

size distribution. This texture parameter was derived by modifying the King's texture characterisation equation (King, 1991) in to two dimensional forms and defined as:

$$\varphi = S^{AB} X / g_A \qquad \textbf{5.1}$$

Where S^{AB} is interphase length per unit area of phase B (absorber), X is total Particle size (equivalent diameter of a circle), g_A is area fraction of phase B(absorber) and φ is the texture parameter.

In addition to the different absorbent grain sizes, in order to include the shape effect to the direction of the loading, three different shapes of grain were used. These were: rectangle, horizontal to the direction of loading; rectangle, vertical to the direction of loading and square. It was not possible to generate other shapes such as circle and polygon randomly, as they distorted the zone and created a 'bad geometry' such that the modeling cannot proceed further. This is in fact one of the main drawbacks of using continuum approach. The maximum and minimum grain sizes that were possible to generate randomly in a 10 mm × 20 mm matrix were determined after making simulations with different grain sizes. The maximum grain size was found to be 2 mm and the minimum was 0.125 mm. Typical textures with their respective texture parameters are shown in Figure 5-3, note that each texture contains 10% microwave absorbing mineral (black colour) by area:-

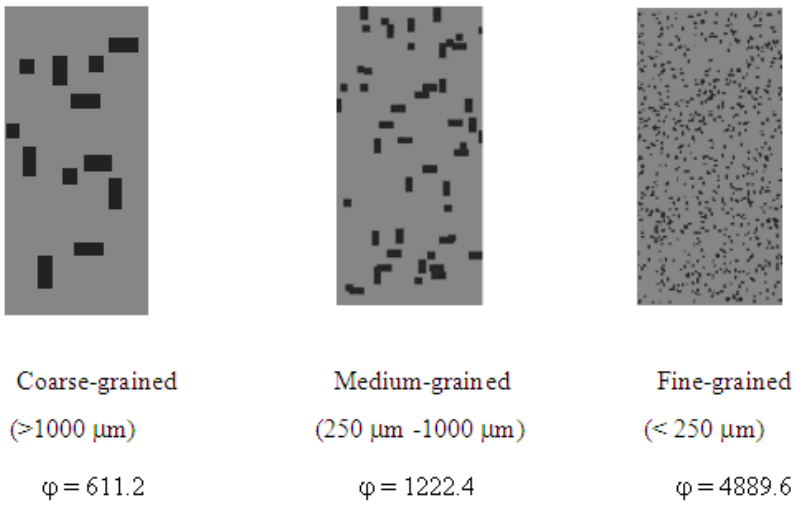

Figure 5.3: Representation of different size microwave absorbent grains in a transparent matrix

5.6 Power Density Specification in *FLAC*

As has been discussed in Chapter 3, it is extremely difficult to precisely determine the power density in the absorbing mineral grain due to variation of electric field within the applicator (refer section 3-7). However, for a given microwave power, effective dielectric properties, applicator geometry and frequency of operation, the power density range within the applicator can be estimated using electromagnetic simulation (e.g. Bradshaw et al., 2007). In this study, power densities ranging from 1×10^7 to 1×10^{11} W/m^3 were used. These values were obtained from electromagnetic simulations and deemed to be the power densities achievable in current and future microwave applicators (Bradshaw et al., 2007; Bradshaw et al., 2009).

It was also assumed that the absorbing phase is evenly heated by the incoming microwave and the power density is zero in the transparent phase. Although this is recognized as a bit simplistic approach it was considered that the models would still elucidate the major characteristics of microwave-induced damage (e.g. Salesman et al., 1997; Whittles et al., 2003; Jones, 2004). Typical *FISH* code used for specifying the power density in the absorbent phase is shown in Table 5-1.

Table 5-1: *FISH* code used for specifying power density in the absorbent phase

```
def source
loop i(1,horcoor)                    , search all zones
loop j(pbplone,ptminone)
if density(i,j)=7597 then      ,apply volumetric heat in the absorbent phase (Galena)
command
interior source 5e8 i=i j=j    ;  Pd=5e8 W/m3
end_command
end_if
end_loop
end_loop
end
source                         , Execute
```

5.7 Thermal Model

In *FLAC*, the differential expression of the energy balance has the following form:-

$$-q_{i,i} + q_v = \rho C_P \frac{\partial T}{\partial t} \qquad \textbf{5.2}$$

Where $q_{ii} = -\nabla.(\lambda \nabla T)$ **5.3**

q_v is the volumetric heat intensity in (W/m^3) which is equated to the power density inside the material, λ is thermal conductivity (W/m.K), ρ is the density of the material (kg/m^3) and C_p is the specific heat capacity (J/kg.K).

The external boundaries of the transparent matrices were assumed to be thermally insulated. More realistic boundary conditions should also take into account convection and radiation. However, in this study, these were considered to be secondary importance, as the microwave exposure times were very short. Accordingly, convection and radiation were not incorporated into the model. The initial temperatures of the ore models were set to be 10°C to represent the temperature of untreated ores in laboratory.

The heat conduction equation in two dimensions can be written as:

$$\frac{\partial^2 T}{\partial x^2} + \frac{\partial^2 T}{\partial y^2} + \frac{q_v}{\lambda} = \frac{\rho C_P}{\lambda} \frac{\partial T}{\partial t} \qquad \textbf{5.4}$$

The finite difference equation for a node i, j is obtained by applying conservation of energy to a control volume about the nodal volume. Since the actual direction of heat flow is often unknown, it is generally formulated by assuming that all heat flow is into the node.

The finite difference approximations of the derivatives in space and time are given as:

$$\frac{\partial^2 T}{\partial x^2} = \frac{T^n_{i-1,j} - 2T^n_{i,j} + T^n_{i+1,j}}{(\Delta x)^2} \qquad \textbf{5.5}$$

$$\frac{\partial^2 T}{\partial y^2} = \frac{T_{i,j-1}^n - 2T_{i,j}^n + T_{i,j+1}^n}{(\Delta y)^2} \quad \textbf{5.6}$$

$$\frac{\partial T}{\partial t} = \frac{T_{i,j}^{n+1} - T_{i,j}^n}{\Delta t} \quad \textbf{5.7}$$

Where superscript n is used to denote the time dependence of the temperature T and Δx and Δy indicate the zone dimension in x and y direction, respectively.

Substituting Equations 5.5 to 5.7 in Equation 5.4 and rearranging for $\Delta x = \Delta y$ (square zone) gives:

$$T_{i,j}^{n+1} = T_{i,j}^n + \frac{\Delta t \lambda_{i,j}}{\rho_{i,j} C_{p_{i,j}} (\Delta x)^2} \left(T_{i-1,j}^n + T_{i+1,j}^n + T_{i,j-1}^n + T_{i,j+1}^n - 4T_{i,j}^n \right) + \frac{q_{V_{i,j}} \Delta t}{\rho_{i,j} C_{p_{i,j}}} \quad \textbf{5.8}$$

And substituting $q_v = P_d$, where P_d = microwave power density within the material (W/m^3) gives**:-**

$$T_{i,j}^{n+1} = T_{i,j}^n + \frac{\Delta t \lambda_{i,j}}{\rho_{i,j} C_{p_{i,j}} (\Delta x)^2} \left(T_{i-1,j}^n + T_{i+1,j}^n + T_{i,j-1}^n + T_{i,j+1}^n - 4T_{i,j}^n \right) + \frac{P_{d_{i,j}} \Delta t}{\rho_{i,j} C_{p_{i,j}}} \quad \textbf{5.9}$$

And the temperature rise for a Δt time increment is then obtained as:-

$$\Delta T_{i,j} = T_{i,j}^{n+1} - T_{i,j}^n = \frac{\Delta t \lambda_{i,j}}{\rho_{i,j} C_{p_{i,j}} (\Delta x)^2} \left(T_{i-1,j}^n + T_{i+1,j}^n + T_{i,j-1}^n + T_{i,j+1}^n - 4T_{i,j}^n \right) + \frac{P_{d_{i,j}} \Delta t}{\rho_{i,j} C_{p_{i,j}}} \quad \textbf{5.10}$$

The transient temperature distribution inside the material as a function of time during the heating process can then be obtained by solving Equation 5.10 using intervals of Δt until the specified time is reached.

It is apparent that the temperature rise within the mineral ore is strongly dependent on the applied power density, the exposure time and its thermal properties. It is emphasised, however, that the extent of the effects that these variables have on the microwave-induced damage was unclear so far.

5.8 Mechanical Model

FLAC allows thermal–mechanical analysis by combining the thermal option with the mechanical calculation. All the features of thermal calculation, including transient and steady state heat transfer and thermal solution are available in a thermal-mechanical calculation. The thermal-mechanical coupling is provided by the influence of temperature change on the volumetric change of a zone. The thermally induced strain after heating is given by:-

$$\varepsilon_{i,j} = \alpha_{ij} \Delta T_{ij} \qquad \textbf{5.11}$$

Where

ε_{ij} is the strain in zone i,j.

α_{ij} is the thermal expansion coefficient (1/K)

ΔT_{ij} is the temperature change in zone i,j .

And the thermally induced stress within a zone for isotropic elastic behaviour then determined by Hoek's law as:-

$$\sigma_{i.j} = \frac{\varepsilon_{i,j} E_{i,j}}{(1 - 2\nu_{i.j})} \qquad \textbf{5.12}$$

Where $\sigma_{i,j}$ is the isotropic thermally induced stress within the zone i,j, $E_{i,j}$ is the Young's modulus of zone i, j and $\nu_{i,j}$ is the Poisson's ratio of zone i,j.

All material models in *FLAC*, except for the transversely-isotropic elastic model, assume an isotropic material behavior in the elastic range described by two elastic constants: bulk modulus (*K*) and shear modulus (*G*). The elastic constants, *K* and *G*, are used in *FLAC* rather than Young's modulus, *E*, and Poisson's ratio, *v*, because it is believed that bulk and shear moduli correspond to more fundamental aspects of material behavior than do Young's modulus and Poisson's ratio (Itasca, 2000).

The elastic constants are related by the following equations:-

$$K = \frac{E}{3(1-2\nu)} \qquad \textbf{5.13}$$

$$G = \frac{E}{2(1+\nu)} \qquad \textbf{5.14}$$

The Mohr-Coulomb strain softening was used as a failure criterion (refer section 5.3). The strain softening model is a particular form of Mohr-Coulomb model in which some of the zones yielding parameters (cohesion, friction, tensile strength) can be modified after the onset of plasticity and it utilizes three phases. The initial phase is the elastic phase and its limiting strain is calculated by using elasticity and the compressive strength of the material. The second phase is the strain softening which is a reduction in strength as a function of strain. And the last phase is the perfect plastic deformation phase in which the material properties are at residual strength value. The rock strength in Mohr-Coulomb criterion is defined by the cohesive strength C and the angle of friction ϕ according to the following equation:-

$$\tau_s = C + \sigma_n \tan\phi \qquad \textbf{5.15}$$

Where τ_s is the shear strength of the material and σ_n is the normal stress acting on the shear plane. Since rock can not sustain large tensile stress, a tensile cut-off was also included in the criterion.

5.9 Properties Data

5.9.1 Densities and Specific Heat Capacities

The densities of the minerals were obtained from Bass (1995). The specific heat capacity of mineral varies with temperature and the values reported by Knacke et al (1991) were used. Table 5.2 shows the densities and specific heat capacities of the minerals.

Table 5-2: Densities and Specific heat capacities

Mineral	Density	Specific heat capacity (J/kg.K)		
	(kg/m^3)	298 K	500 K	1000 K
Pyrite	5016	517.08	600.42	683.83
Magnetite	5206	654.22	829.81	865.65
Galena	7597	208.95	215.23	234.94
Quartz	2648	740.50	991.17	1167.17
Calcite	2712	817.70	1051.00	1238.50
Dolomite	3795	838.40	1013.60	1263.00

The heat capacities were approximated by using two linear portions in order to incorporate them in *FLAC* and the results are shown in Table 5-3.

Table 5-3: Specific heat capacities of minerals approximated by two linear portions

Minerals	Temperature	Specific heat capacity (J/kg.K)
Magnetite	T < 500 K	$C_p = 0.8690T + 395.26$
	T ≥ 500 K	$C_p = 0.0713T + 794.12$
Pyrite	T < 500 K	$C_p = 0.4126T + 394.13$
	T ≥ 500 K	$C_p = 0.1668T + 517.01$
Galena	T < 500 K	$C_p = 0.0311T + 199.68$
	T ≥ 500 K	$C_p = 0.0394T + 195.52$
Quartz	T < 500 K	$C_p = 1.2410T + 370.70$
	T ≥ 500 K	$C_p = 0.3520T + 815.17$
Calcite	T < 500 K	$C_p = 1.1550T + 473.51$
	T ≥ 500 K	$C_p = 0.3750T + 863.50$
Dolomite	T < 500 K	$C_p = 0.8670T + 580.04$
	T ≥ 500 K	$C_p = 0.5000T + 763.63$

The *FISH* code used to specify specific heat capacity as a function of temperature is shown in Table 5-4.

Table 5-4: *FISH* code used to specify specific heat capacity as a function of temperature for dolomite

```
if density(i,j) =3795 and
if (temp(i,j)+273) < 500 then
spec_heat(i,j)=(0.867*(temp(i,j)+273))+580.04
end_if
end_if
if density(i,j) =3795 and
if (temp(i,j)+273) >= 500 then
spec_heat(i,j)=(0.5*(temp(i,j)+273))+763.63
end_if
end_if
```

5.9.2 Thermal Conductivities

The thermal conductivities of minerals are often available for room temperature condition only even though they are required at elevated temperature. For this purpose some empirical relationships have been proposed for extrapolation on the basis of the data measured at elevated temperature. It is emphasized, however, that there is no real substitute for individual measurement. The most reasonable and general empirical relation for thermal conductivity of a mineral (λ (T)) as a function of λ (25) is that proposed by Sass et al. (1992). The empirical relation proposed by these authors is shown below:-

$$\lambda(T) = \frac{\lambda(0)}{1.007 + T.\left(0.0036 - \frac{0.0072}{\lambda(0)}\right)} \qquad \textbf{5.16}$$

Where T = temperature in °C

$$\lambda(0) = \lambda(25).\left[1.007 + 25.\left(0.0037 - \frac{0.0074}{\lambda(25)}\right)\right] \qquad \textbf{5.17}$$

Equation 5.16 is derived from the classical experimental data set of Birch and Clark (1940), who measured thermal conductivity as a function of temperature in the range 0 – 200°C and higher on 38 samples from a different types of rocks including volcanic, metamorphic, plutonic and sedimentary rocks. The thermal conductivities of many minerals at normal temperature (25 – 35°C) are reported by Diment and Pratt (1988).

Table 5-5: Thermal conductivities at room temperature (Diment and Pratt, 1988)

Mineral	Thermal conductivity (W/m.K)
Pyrite	23.15
Magnetite	4.61
Galena	2.76
Quartz	6.15
Calcite	3.16
Dolomite	4.78

The data in Table 5-5 were then inserted in Equation 5-17 for estimation at higher temperature. The estimated values are tabulated in Table 5-6.

Table 5-6: Thermal conductivities as a function of temperature

Mineral	Thermal conductivity (W/m.K)		
	298 K	773 K	1273 K
Pyrite	23.15	9.48	5.85
Magnetite	4.61	2.37	1.57
Galena	2.76	1.85	1.37
Quartz	6.15	2.92	1.87
Calcite	3.16	1.92	1.36
Dolomite	4.78	2.65	1.72

The thermal conductivities of the minerals were written again as a function of temperature by using two linear portions in order to input them in *FLAC*. The

equations and typical *FISH* code used for specifying the conductivity as a function of temperature are shown in Table 5-7 and 5-8, respectively.

Table 5-7: Thermal conductivities of minerals approximated by two linear portions

Minerals	Temperature	Thermal conductivity(λ) (W/m.K)
Magnetite	T < 500°C	$\lambda(T) = -0.0047T + 4.73$
	T ≥ 500°C	$\lambda(T) = -0.0016T + 3.17$
Pyrite	T < 500°C	$\lambda(T) = -0.0294T + 24.18$
	T ≥ 500°C	$\lambda(T) = -0.0073T + 13.11$
Galena	T < 500°C	$\lambda(T) = -0.0020T + 2.83$
	T ≥ 500°C	$\lambda(T) = -0.0010T + 2.33$
Quartz	T < 500°C	$\lambda(T) = -0.0068T + 6.32$
	T ≥ 500°C	$\lambda(T) = -0.0021T + 3.97$
Calcite	T < 500°C	$\lambda(T) = -0.0026T + 3.22$
	T ≥ 500°C	$\lambda(T) = -0.0011T + 2.48$
Dolomite	T < 500°C	$\lambda(T) = -0.0045T + 4.89$
	T ≥ 500°C	$\lambda(T) = -0.0019T + 3.58$

Table 5-8: *FISH* code used to specify thermal conductivity as a function of temperature for dolomite

```
if density(i,j) =3795 and
if temp(i,j) < 500 then
conductivity(i,j)= ((temp(i,j))*(-0.0045))+4.89
end_if
end_if
if density(i,j) =3795 and
if temp(i,j) >= 500 then
conductivity(i,j)= ((temp(i,j))*(-0.0019))+ 3.58
end_if
end_if
```

5.9.3 Thermal Expansion Coefficient

Thermal expansion coefficient also varies with temperature. The values reported by Clark et al. (1966) were used and are shown in Table 5-9.

Table 5-9: Thermal expansion coefficient as a function of temperature

Mineral	**Thermal expansion coefficient (1/K)(10^{-6})**			
	373 K	**473 K**	**673 K**	**873 K**
Pyrite	27.3	29.3	33.9	-
Magnetite	26.5	28.5	34.9	41.5
Galena	61.2	61.0	63.2	66.8
Quartz	45.0	43.3	49.7	77.9
Calcite	13.1	15.8	20.1	24.0
Dolomite	18.4	21.5	26.6	31.4

The thermal expansion coefficients were also approximated by two linear portions and the results and typical *FISH* code used are shown in Table 5-10 and 5-11.

Table 5-10: Thermal expansion coefficients of minerals approximated by two linear portions

Minerals	Temperature	Thermal expansion coefficient(α) (1/K)(10^{-6})
Magnetite	T < 673 K	$\alpha = 0.0280T + 16.056$
	T ≥ 673 K	$\alpha = 0.0330T + 12.691$
Pyrite	T < 473 K	$\alpha = 0.0200T + 19.840$
	T ≥ 473 K	$\alpha = 0.0230T + 18.421$
Galena	T < 673 K	$\alpha = 0.0067T + 58.710$
	T ≥ 673 K	$\alpha = 0.0180T + 51.091$
Quartz	T < 673 K	$\alpha = 0.0157T + 39.156$
	T ≥ 673 K	$\alpha = 0.1410T - 45.193$
Calcite	T < 673 K	$\alpha = 0.0233T + 4.398$
	T ≥ 673 K	$\alpha = 0.0195T + 6.975$
Dolomite	T < 673 K	$\alpha = 0.0274T + 8.210$
	T ≥ 673 K	$\alpha = 0.0237T + 10.691$

Table 5-11: *FISH* code used to specify thermal expansion coefficient as a function of temperature for dolomite

```
if density(i,j) =3795 and
if (temp(i,j)+273) < 673 then
thexp(i,j)=((0.0274*(temp(i,j)+273))+8.210)*1e-6
end_if
end_if
if density(i,j) =3795 and
if (temp(i,j)+273) >= 673 then
thexp(i,j)=((0.0237*(temp(i,j)+273))+10.691)*1e-6
end_if
end_if
```

5.9.4 Bulk Modulus

The bulk modulus (*K*) of a substance measures the substance's resistance to uniform compression. It is defined as the pressure increase needed to affect a given relative decrease in volume. The bulk modulus *K* can be formally defined by the equation:

$$K = -V\frac{\partial P}{\partial V} \qquad \textbf{5.18}$$

Where P is pressure, V is volume, and $\partial P/\partial V$ denotes the partial derivative of pressure with respect to volume. The Bulk moduli of the minerals were obtained from Bass (1995) and the values have been tabulated in Table 5.12.

Table 5-12: Bulk moduli of minerals

Mineral	Bulk modulus (GPa)
Pyrite	142.7
Magnetite	161.0
Galena	58.6
Quartz	37.8
Calcite	73.3
Dolomite	94.5

5.9.5 Shear Modulus

Shear modulus or modulus of rigidity, denoted by *G*, and is defined as the ratio of shear stress to the shear strain. Shear moduli of the minerals were obtained from Bass (1995) and the values have been tabulated in Table 5.13.

Table 5-13: Shear moduli of minerals

Mineral	Shear modulus (GPa)
Pyrite	125.7
Magnetite	91.4
Galena	31.9
Quartz	44.3
Calcite	32.0
Dolomite	45.7

5.9.6 Mohr-Coulomb Strength Parameters

The Mohr-Coulomb Strength Parameters of the ores were determined by using the software package, 'RocLab', which has been developed as an associated Windows program in the 2002 edition of the Hoek-Brown failure criteria (Hoek et al., 2002). The software is normally used for obtaining the equivalent Mohr-Coulomb parameters, namely cohesive strength and friction angle for a rock that has been evaluated as a Hoek-Brown material. The input data required for an intact and undisturbed rock are the unconfined compressive strength and the material constant (m). Unconfined compressive strength values of 263 MPa, 144 MPa and 105.5 MPa were used for quartz, calcite and dolomite ores, respectively, which are typical strength of quartzite, strong limestone and dolomite rock (Lama and Vutukuri, 1978). The Material constants were obtained from the software itself and these were 20, 12 and 9 for quartzite, limestone and dolomite rock respectively. Typical results from 'RocLab' are shown in Figures 5.4 - 5.6.

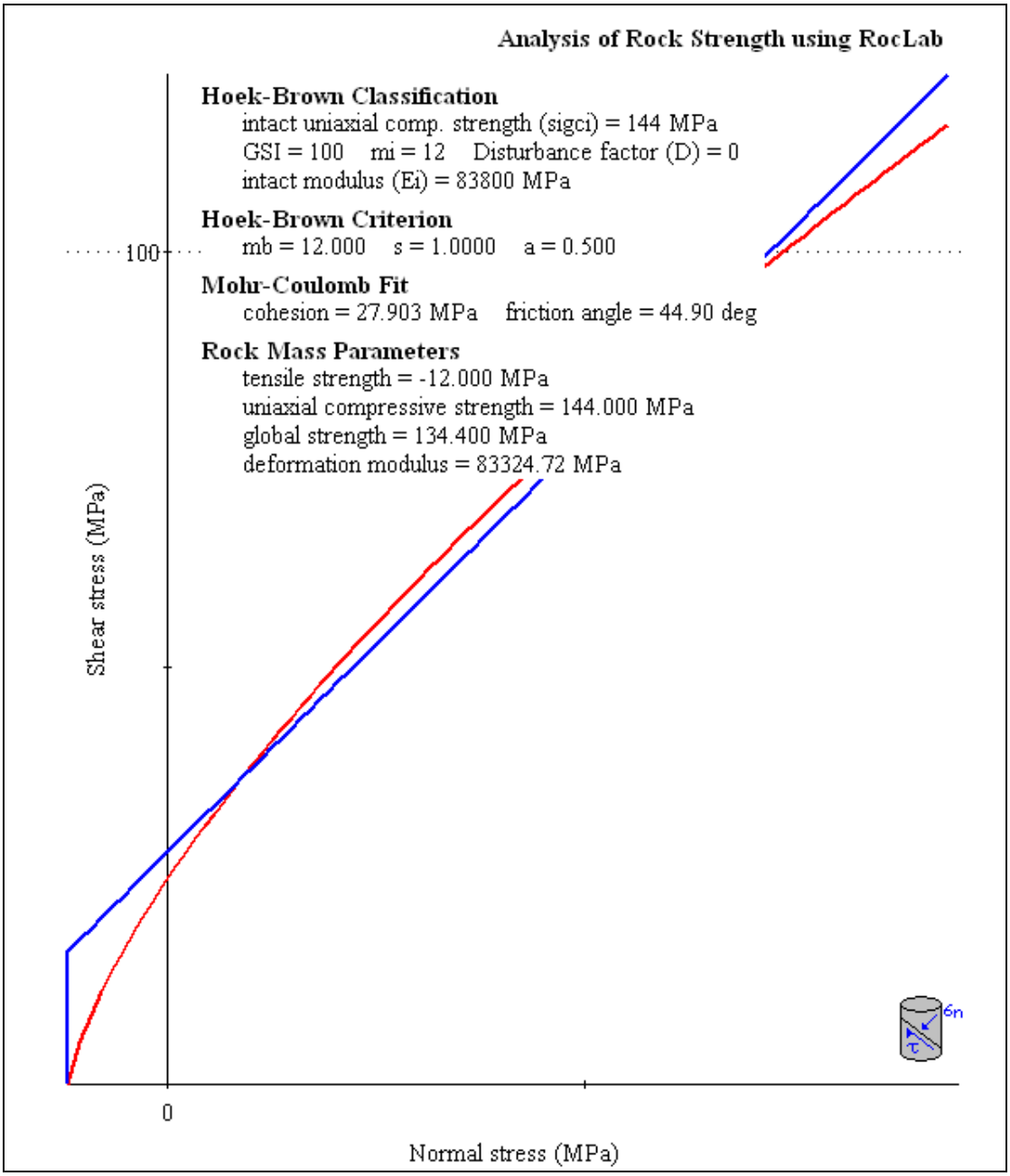

Figure 5.4: Estimation of Mohr-Coulomb strength parameters for calcite ore (RocLab)

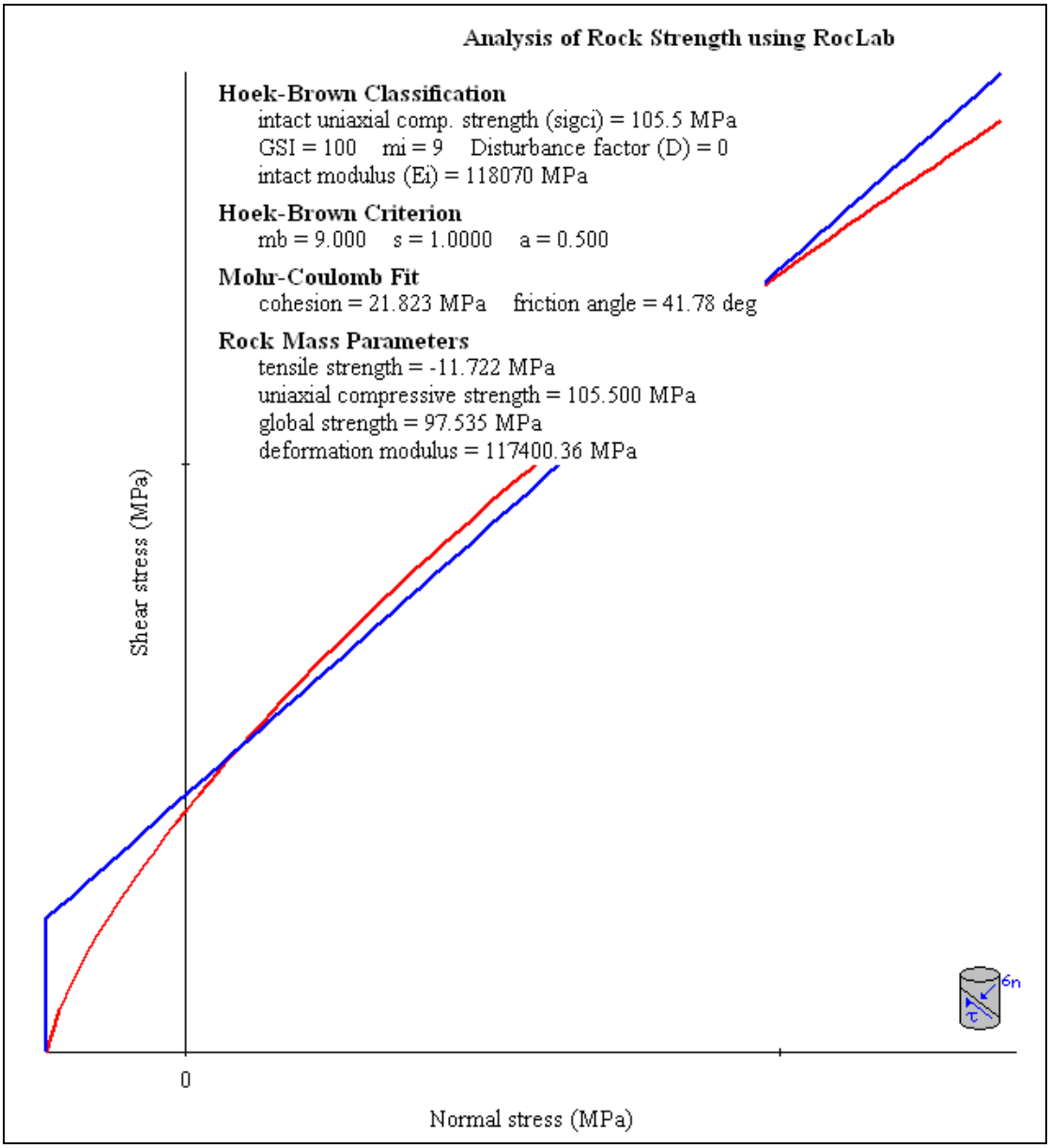

Figure 5.5: Estimation of Mohr-Coulomb strength parameters for dolomite ore (RocLab)

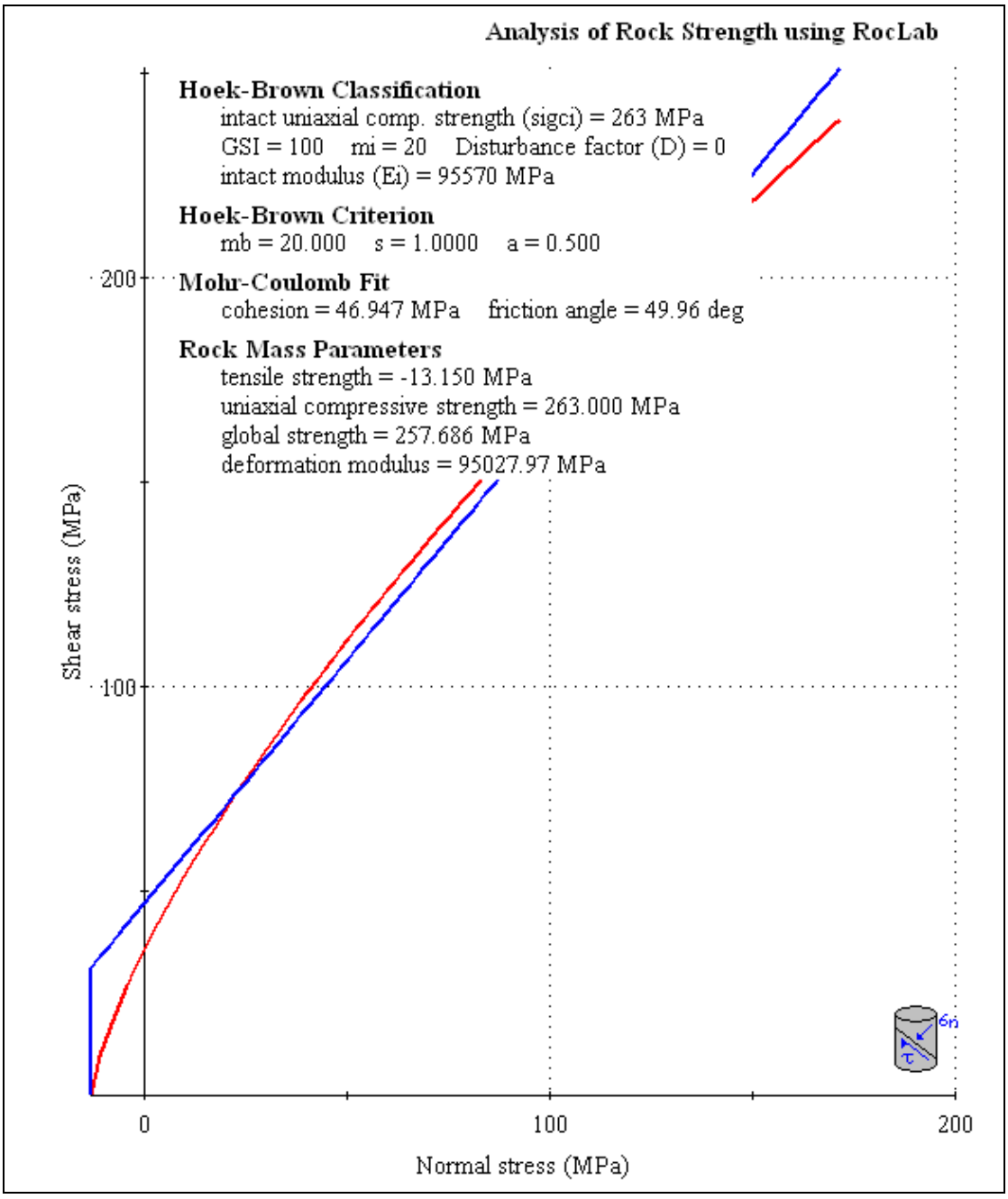

Figure 5.6: Estimation of Mohr-Coulomb strength parameters for quartz ore (RocLab)

5.9.7 Strain Softening

In *FLAC*, it is possible to define the cohesion, friction and tensile strength variation as a function of the plastic portion of the strain. Softening behaviours for the cohesion, friction in terms of the shear strain could be given in the form of tables. Each table contains pairs of values: one for the parameter and one for the property value. Softening of the tensile strength is described in a similar manner using the plastic tensile strain. In *FLAC*, it is assumed that the property varies linearly between two consecutive parameter entries in the table. At the initiation of tensile failure, the tensile strength of a material will generally drop to zero (Itasca, 2000). The tensile strength of the ores was deemed to fall to 0.1% after 0.1% tensile strain and the cohesion was specified to fall to 10% after 1% shear strain. The Peak strength (obtained from the previous section) and the residual strength for each matrix are shown in Tables 5-14 and 5-15. In practice, softening parameters must be calibrated for each specific analysis with values that are generally back-calculated from result of laboratory triaxial tests, which is usually an iterative process.

Table 5-14: Peak strength

Mineral	Cohesive strength (MPa)	Tensile strength (MPa)	Friction angle (°)
Quartz	46.95	13.15	50
Calcite	27.90	12.00	45
Dolomite	21.80	11.70	42

Table 5-15: Residual strength after 1% strain

Mineral	Cohesive strength (MPa)	Tensile strength (MPa)	Friction angle (°)
Quartz	4.69	0	50
Calcite	2.79	0	45
Dolomite	2.18	0	42

The *FISH* code used for specifying the strain softening properties is also shown in Table 5-16.

Table 5-16: *FISH* code used for modelling strain softening for calcite

```
model ss
prop fric 45 tens 12e6 coh 27.9e6  i=1,horcoor j=pbplone,ptminone
prop ttab=1 ctab=2 i=1,horcoor j=pbplone,ptminone
table 1 0,12e6 0.001,0.12e6
table 2 0,27.9e6 0.01,2.79e6
group 'User: calcite' region horcoor horcoor
prop den=2712 bulk=7.33e10 shear=3.2e10 group 'User: calcite'
prop fric 45 tens 12e6 coh 27.9e6 group 'User: calcite'
```

Thus, it is now possible to simulate microwave heating of binary ores and observe the temperature profile for a particular treatment condition. The following figures show typical temperature profiles observed for the ores after microwave treatment. The full simulation code used for modelling microwave heating of a binary ore is shown in Appendix B.

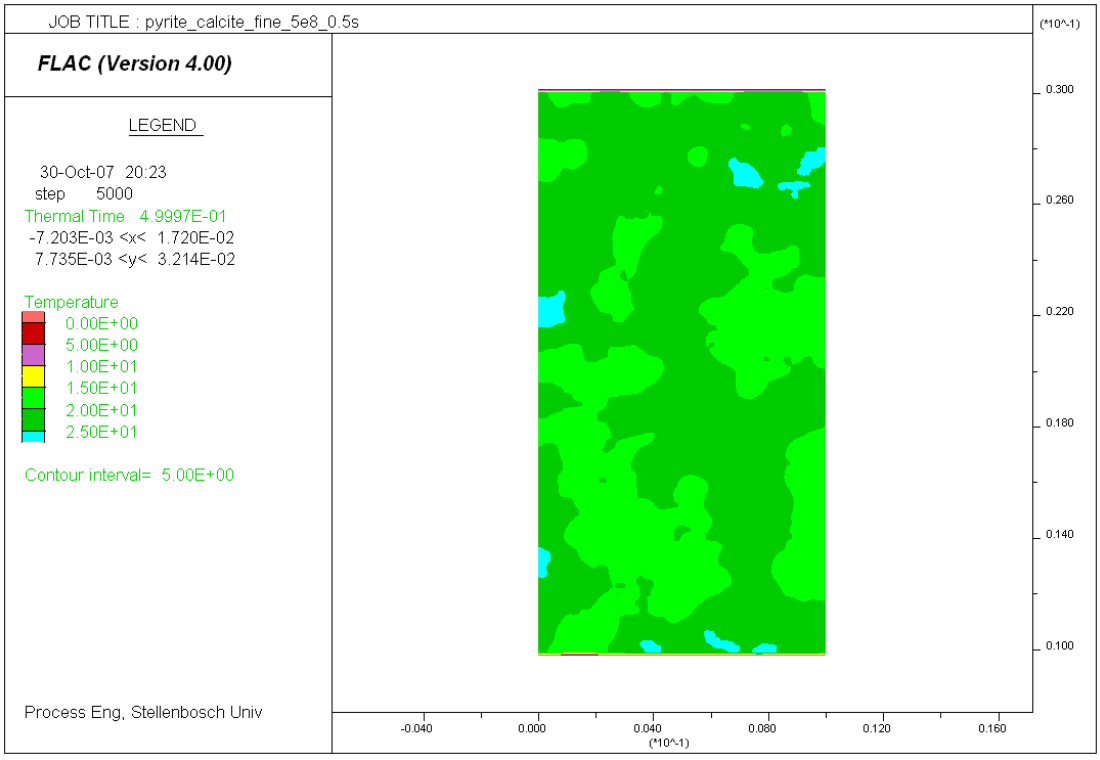

Figure 5.7: Temperature profile in fine-grained pyrite-calcite, treated at P_d = 5E8 W/m^3, t = 0.5 s , Max Temperature = 25°C

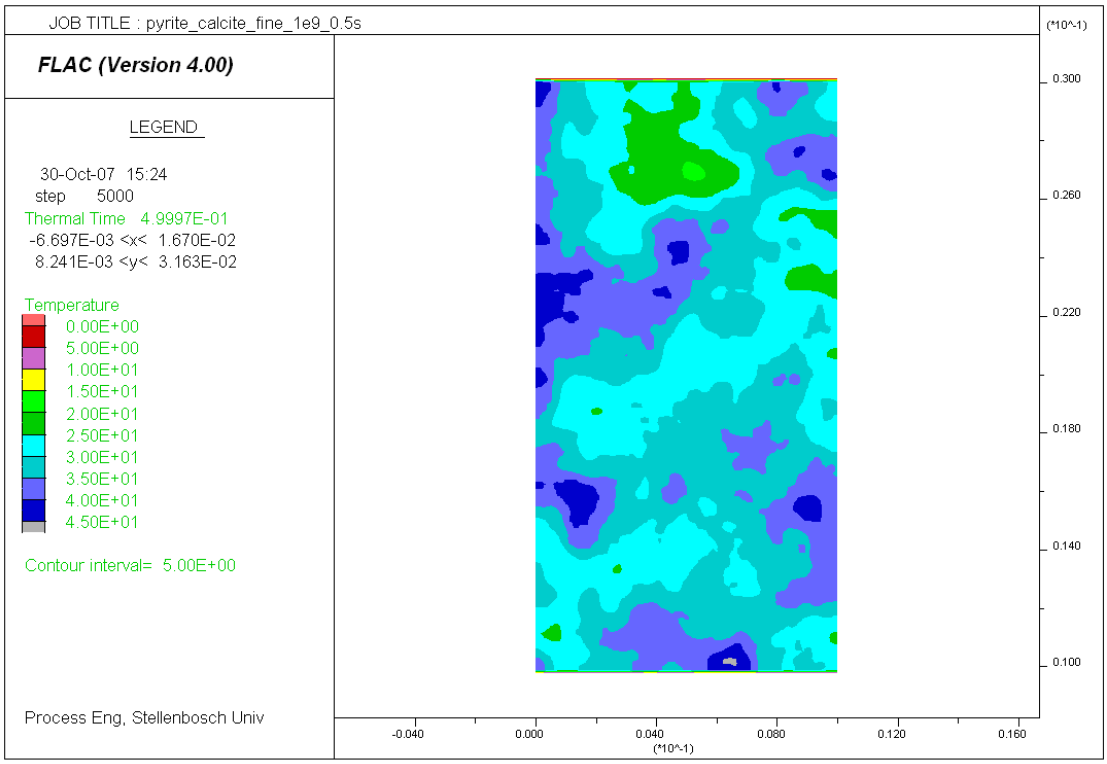

Figure 5.8: Temperature profile in fine-grained pyrite-calcite, treated at P_d =1E9 W/m^3, t = 0.5 s, Max Temperature = 45°C

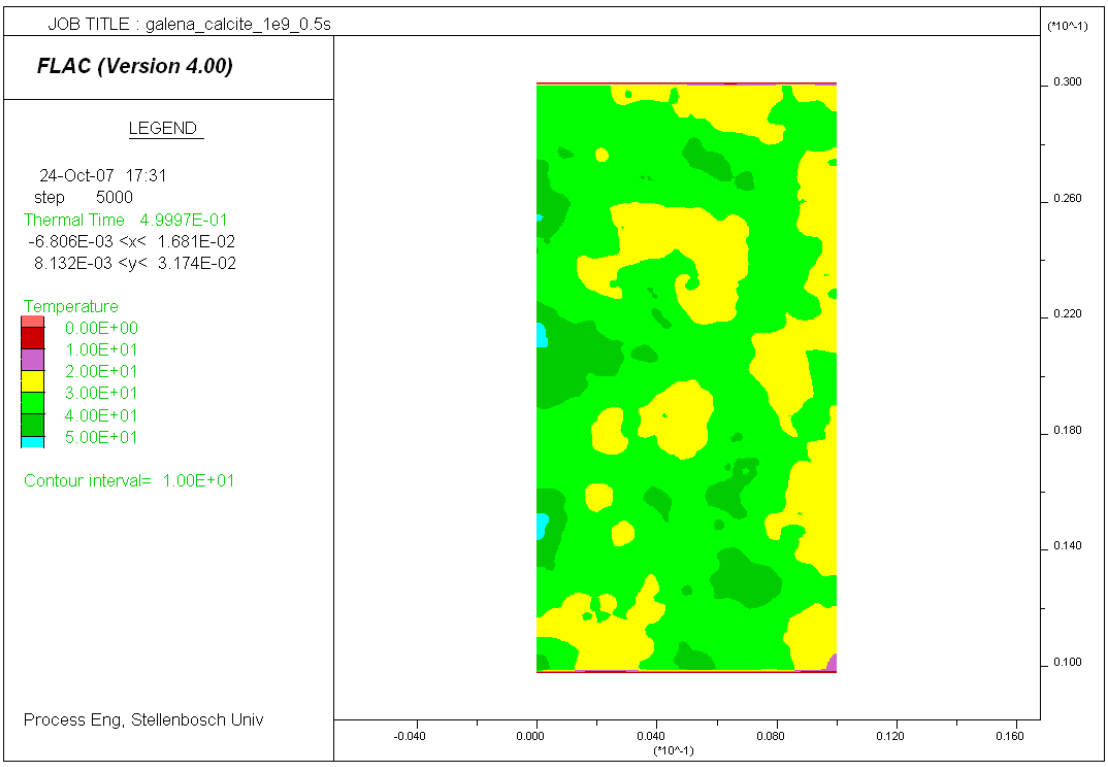

Figure 5.9: Temperature profile in fine-grained galena-calcite, treated at P_d = 1E9 W/m^3, t = 0.5 s, Max Temperature = 50°C

5.10 Simulation of Unconfined Compressive Strength Test

The effect of the microwave treatment on strength reduction of the ores was predicted by the simulation of the unconfined compressive strength test on the thermally damaged models. The uniaxial compressive strength test was chosen, as it is the commonest method for studying the mechanical properties of rock and it is possible to correlate it with ore breakage parameters (refer Chapter 4).

The simulation for unconfined compressive strength test was made by modelling two steel platens above and below the samples as per the normal arrangement in standard test. The loading rate should be set sufficiently slow enough to ensure the sample remains in quasi-static equilibrium throughout the test. After running simulation with different loading rates, a velocity of 5×10^{-9} m/step was found to be slow enough for the ore models considered and provide typical strain rate used for testing rock strength in experiments. The velocity was applied at the top and the bottom platens to compress the samples. It is well known that the strain-rate affects the unconfined compressive strength of rock; thus, this velocity was fixed for testing the untreated and microwave treated materials. The steel was modelled as an isotropic elastic material with a bulk modulus specified as 210 GPa and shear modulus specified as 81 GPa. The contact between the steel and the rock was represented by a spring-dashpot type interface.

To monitor the load deformation relationship within the samples during testing, history files were generated from the average stress conditions at the top and bottom boundaries. The models were run for a total of 40000 steps which was well above the values at which the materials reached their unconfined compressive strength. The complete simulation code (*FISH*) used for unconfined compressive strength test is shown in Appendix C. On average a computational time of 3 hours was required to complete one simulation.

Typical fracture patterns of an untreated ore after loading are shown in Figures 5-10 and 5-11. The rock specimen fractures by brittle splitting and fail in shear, which is in complete agreement with real experiment (refer Chapter 4). Typical results of stress-strain curve obtained from the simulation were also shown in Figures 5-12 and 5-13.

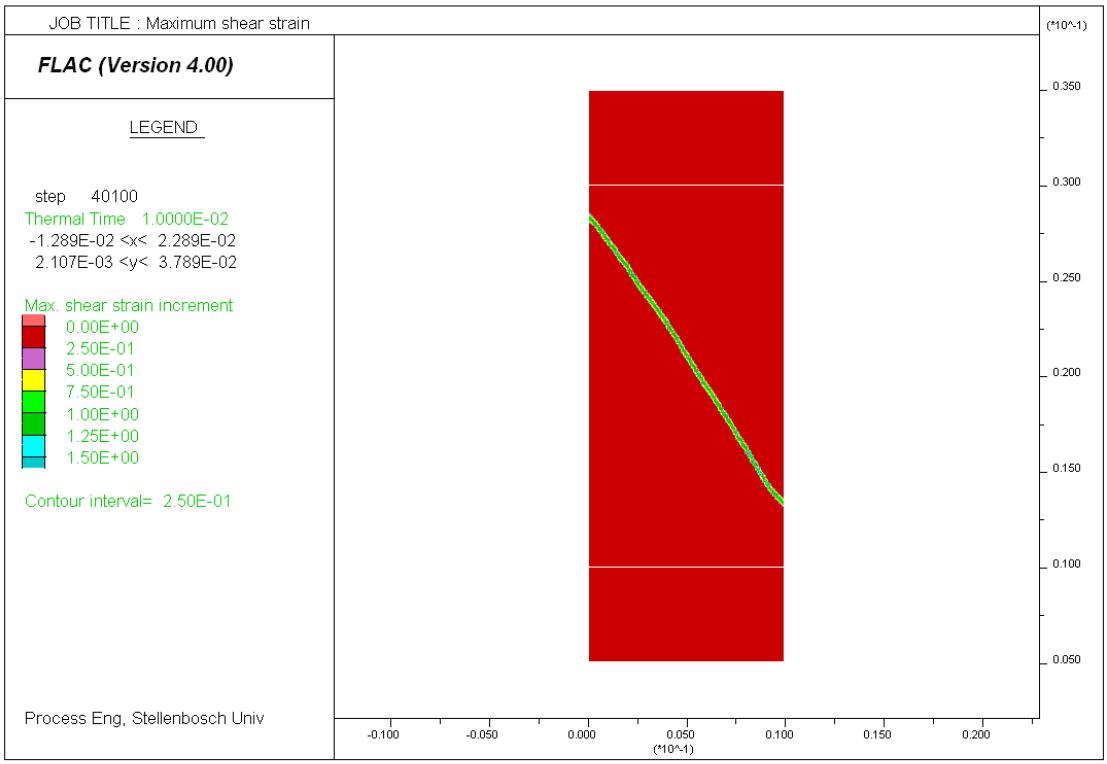

Figure 5.10: Maximum shear strain contour after loading (note the steel platens above and below the sample)

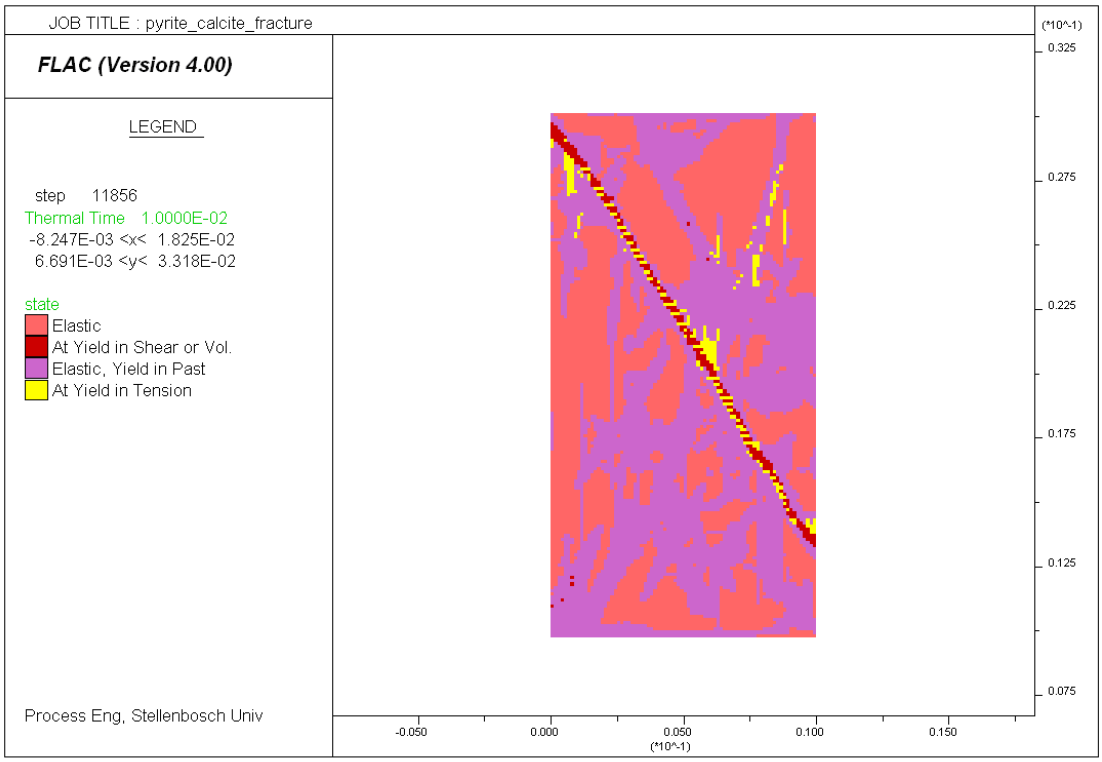

Figure 5.11: Mechanical state of a material after loading

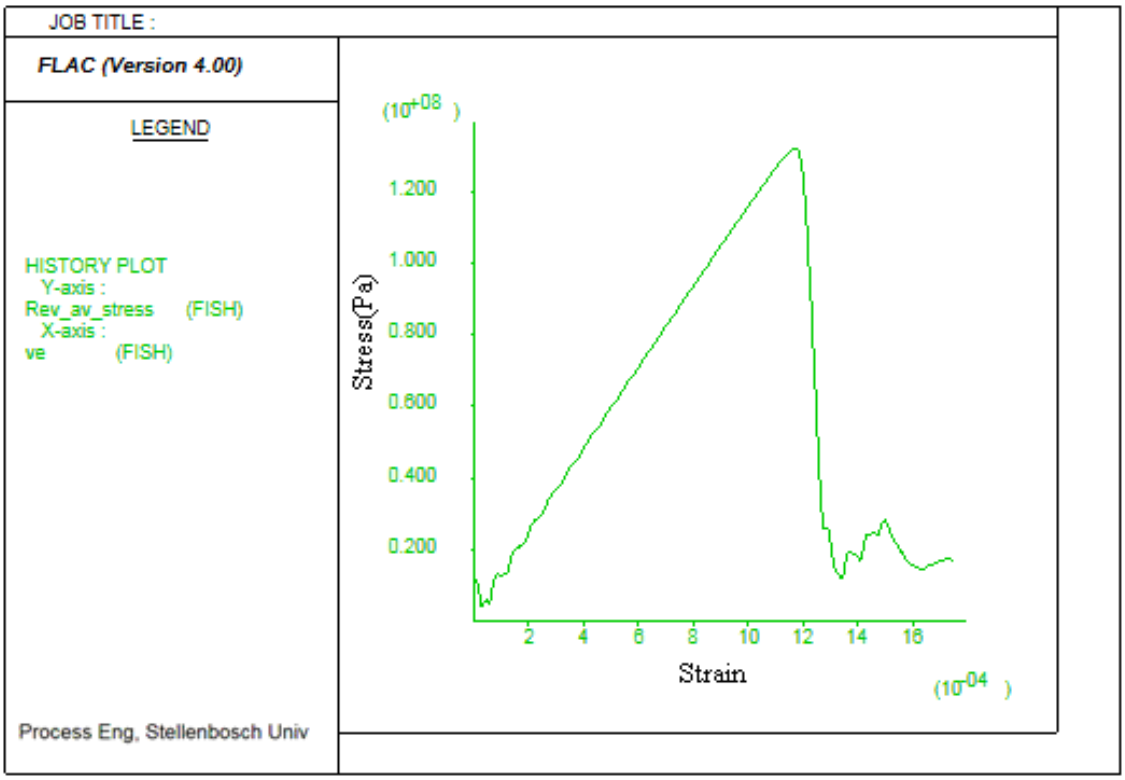

Figure 5.12: Typical strain-stress curve for calcite ore

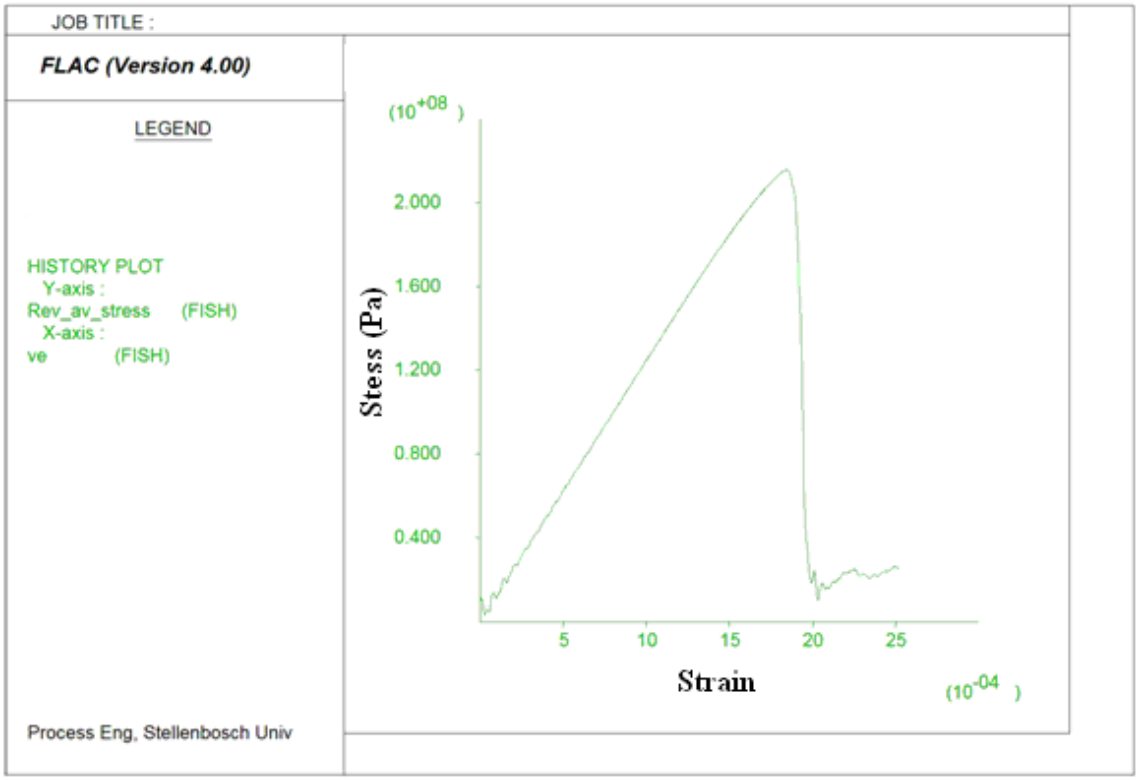

Figure 5.13: Typical strain-stress curve for quartz ore

5.11 Conclusions

The methodologies used to simulate thermal and mechanical behaviour and the specification of the constitutive thermal and mechanical models that are required in *FLAC* have been discussed in the chapter. The thermal and mechanical properties for each mineral and the *FISH* codes used for specifying the properties have also been tabulated. The procedure for applying power density in *FLAC*, hence, modelling microwave heating, has been detailed. The model used for simulation of unconfined compressive strength test is also presented. It is now possible to carry out different numerical experiments and to investigate the effects of different variables on microwave treatment of ores. The results obtained from different numerical experiments will be discussed in Chapter 6.

Chapter 6

Results of Bulk Strength Simulation

6.1 Introduction

This chapter discusses the results of different simulations undertaken for investigating the effect of different variables on bulk strength reduction of microwave treated ores. The first section details a study designed to examine the effect of thermo-mechanical properties of mineral constituents on strength reduction of ores. The second section examines the effect of microwave absorbent phase grain size. In the third section, the effect of power density for a narrow range is investigated. The effect of absorbent phase modal area and dissemination are also presented in the fourth and fifth section, respectively. In the sixth section, the effect of microwave treatment on the mechanical state of an ore sample is examined.

6.2 Effect of Thermo-mechanical Properties on Strength Reduction

6.2.1 Introduction

This section details the study carried out for investigating the effect of thermo-mechanical properties of minerals on strength reduction of ores. A total of nine different binary ore models were constructed. Next, a series of simulations of microwave heating, thermal damage and unconfined compressive strength test were carried out to illustrate the effects of thermo-mechanical properties of both the microwave absorbent phase and the transparent matrix on strength reduction of the ores.

6.2.2 Methodology

The methodologies used for construction of the ore models and for modelling microwave heating and unconfined compressive strength test were all detailed in Chapter 5. In this study, the conceptual ores were exposed to heating at power densities of 1×10^9 W/m^3 and 5×10^8 W/m^3 for exposure times of 0.5 to 10 s. One simulation was carried out by exposing nine different coarse-grained ores to

microwave at power density of 1×10^9 W/m^3. Another simulation was also undertaken by changing the power density and the texture of the ores. The effect of thermo-mechanical properties was then investigated by comparing the strength reduction of the ores for the same texture and microwave treatment condition.

6.2.3 Results of Coarse-grained Binary Ores

The results of the unconfined compressive strength tests of coarse-grained binary ores treated at power density of 1×10^9 W/m^3 and at different exposure times are tabulated in Table 6-1.

Table 6-1: Unconfined compressive strength of binary ores, coarse-grained texture (φ= 611.2), treated at $P_d = 1 \times 10^9$ W/m^3

Binary ores	UCS (untreated) (MPa)	UCS 0.5 s (MPa)	UCS 1 s (MPa)	UCS 2 s (MPa)	UCS 5 s (MPa)	UCS 8 s (MPa)	UCS 10 s (MPa)
Galena-Quartz	231.5	191.5	135.0	99.5	51.0	47.0	47.0
Galena-Calcite	140.0	91.5	84.0	77.5	62.0	42.5	38.0
Galena-Dolomite	104.5	85.0	72.0	67.0	56.5	46.5	43.0
Pyrite-Calcite	127.0	126.0	106.5	93.5	67.5	49.5	40.5
Pyrite-Quartz	201.0	201.0	178.5	131.5	52.5	46.5	46.0
Pyrite-Dolomite	106.5	101.0	97.0	90.0	67.5	52.0	48.0
Magnetite-Calcite	128.5	127.5	120.0	101.0	64.5	45.0	42.0
Magnetite-Quartz	200.5	200.5	193.0	136.0	55.0	49.0	47.0
Magnetite-Dolomite	107.0	100.0	95.0	87.5	71.0	50.0	47.0

6.2.3.1 Effect of Absorbent Phase's Thermo-mechanical Properties

The results in Table 6-1 are plotted in Figures 6-1, 6-5 and 6-6 to illustrate the effect of microwave absorber's thermo-mechanical properties on strength reduction of ores. Figure 6-1 shows the percentage reductions in strength of different coarse-grained quartz ores (consist of different microwave absorbent minerals). As can be seen, there was a significant variation in strength reductions for the same texture and treatment condition. The reduction in strength obtained for galena-quartz was much higher than that obtained for the other quartz ores at all exposure times. For instance, a reduction of 17.2% was obtained at 0.5 s for galena-quartz whilst there were no strength reductions in pyrite-quartz and magnetite-quartz ores. The temperature profiles inside the ores after 0.5 s are also shown in Figures 6-2 to 6-4. As can be seen, the maximum temperature obtained for galena-quartz was significantly high. A maximum temperature up to 100°C was obtained for galena-quartz whilst the maximum temperatures for the other ores were below 60°C.

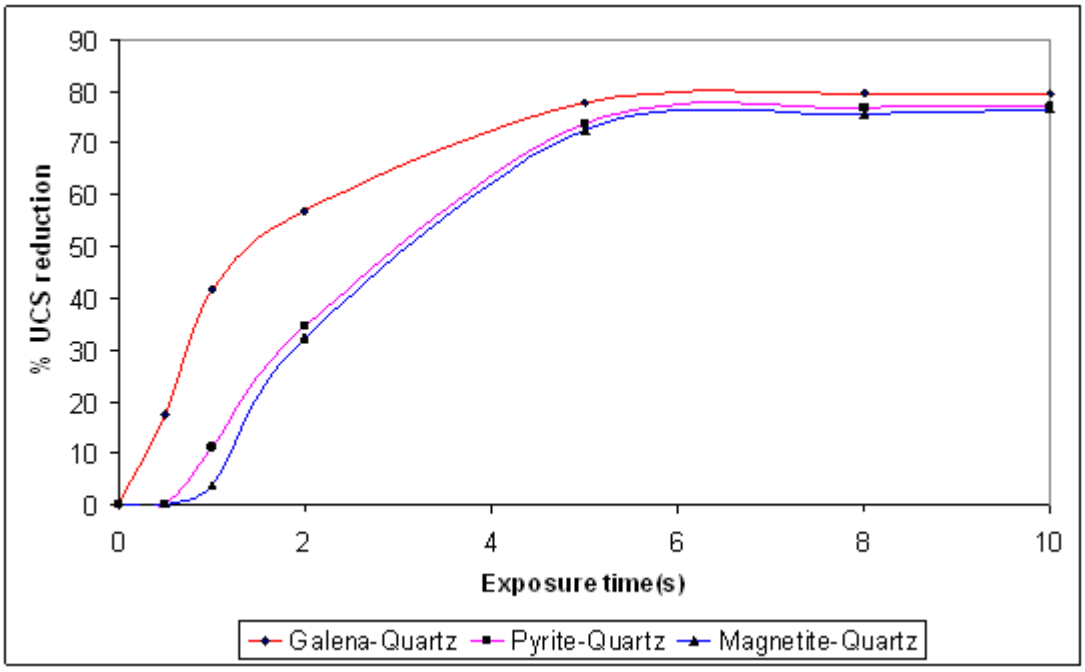

Figure 6.1: Strength reduction of quartz ores, coarse-grained (φ = 611.2), $P_d = 1 \times 10^9$ W/m^3

As has been discussed in Chapter 5, the thermally induced stresses in an ore are directly proportional to the rise in temperature. Further, the thermal expansion coefficient of galena is much higher than that of magnetite and pyrite. It can also be seen that the difference in strength reductions between magnetite-quartz and pyrite-quartz was very small at all exposure times. The maximum temperature rise obtained for the two ores were also relatively similar. After 5 s, the strength reductions were almost the same for the three ores once they attained the maximum strength reduction. Increasing the exposure time beyond 5 s did not change the strength reductions of the ores. It can be said that there is a point for a given mineralogy and power density beyond which no further reduction in strength would be obtained by increasing the exposure time.

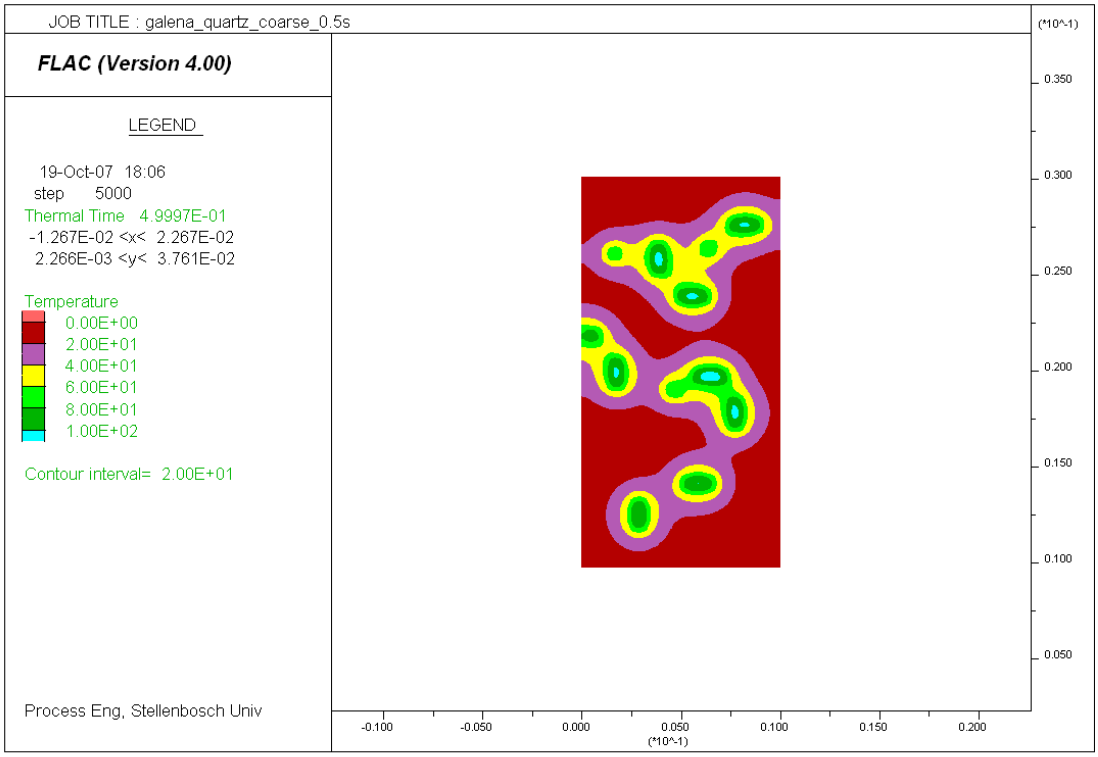

Figure 6.2: Temperature profile in galena-quartz , coarse-grained (φ = 611.2), treated at $P_d = 1 \times 10^9$ W/m^3 for t = 0.5 s

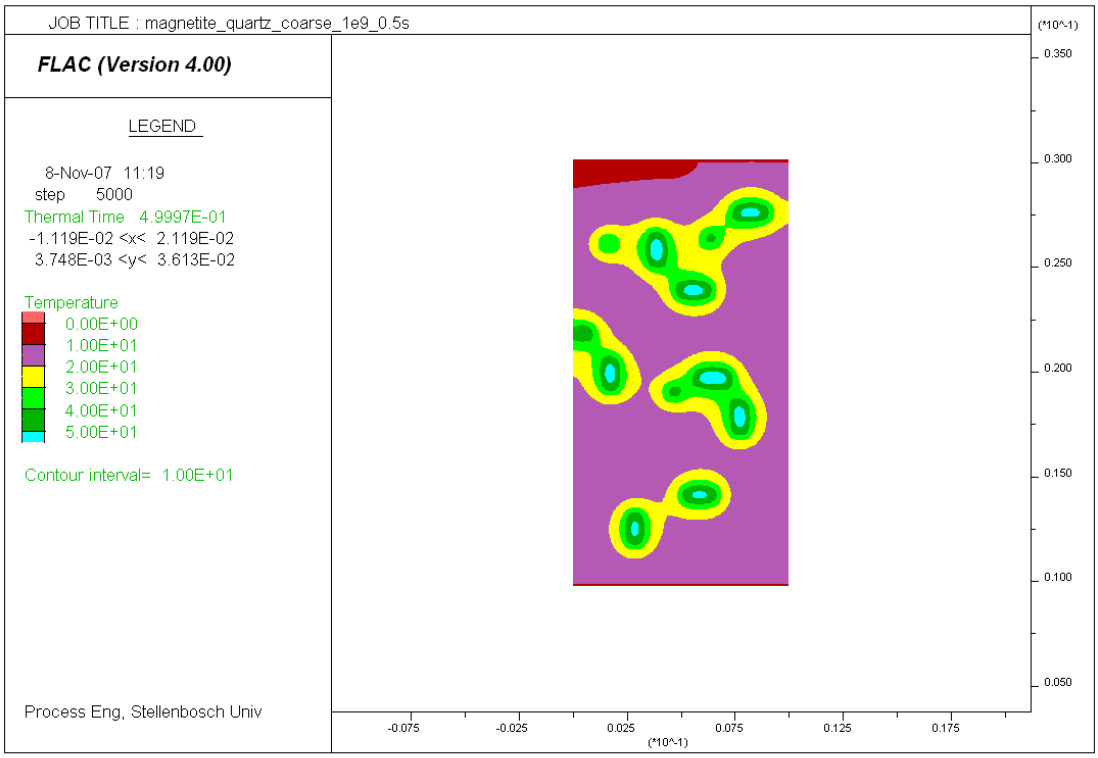

Figure 6.3: Temperature profile in magnetite-quartz, coarse-grained (φ = 611.2), treated at $P_d = 1 \times 10^9$ W/m^3 for t = 0.5 s

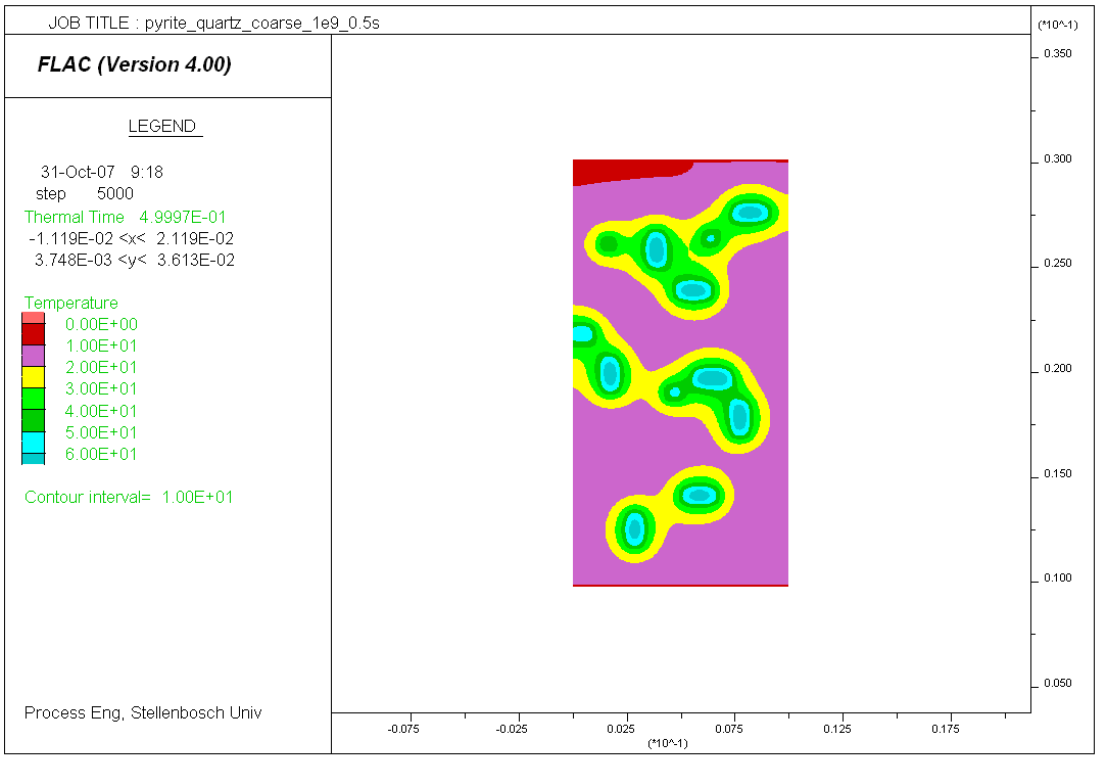

Figure 6.4: Temperature profile in pyrite-quartz, coarse-grained (φ = 611.2), treated at $P_d = 1 \times 10^9$ W/m^3 for t = 0.5 s

Figure 6-5 shows the effect of microwave absorbent phase's thermo-mechanical properties on strength reduction of calcite ores. Here again, the strength reduction obtained for galena-calcite was much higher than that obtained for pyrite-calcite and magnetite-calcite ores at all exposure times. Galena-calcite achieved much higher strength reduction in particular below 2 s. For instance, a 40% reduction in strength was obtained at 1 s for galena-calcite whereas only 16% and 6.6% reductions were obtained at this time for pyrite-calcite and magnetite-calcite ore, respectively. The effect on strength reduction of dolomite ores is also shown in Figure 6-6. Higher reduction here also was attained by galena-dolomite ores than pyrite-dolomite and magnetite-dolomite. Once again, it should be noted that the difference in strength reductions between pyrite-dolomite and magnetite-dolomite was very small. In general, binary ores that contain galena as microwave absorber attained the highest reductions in strength and similar strength reductions were obtained for magnetite and pyrite ores.

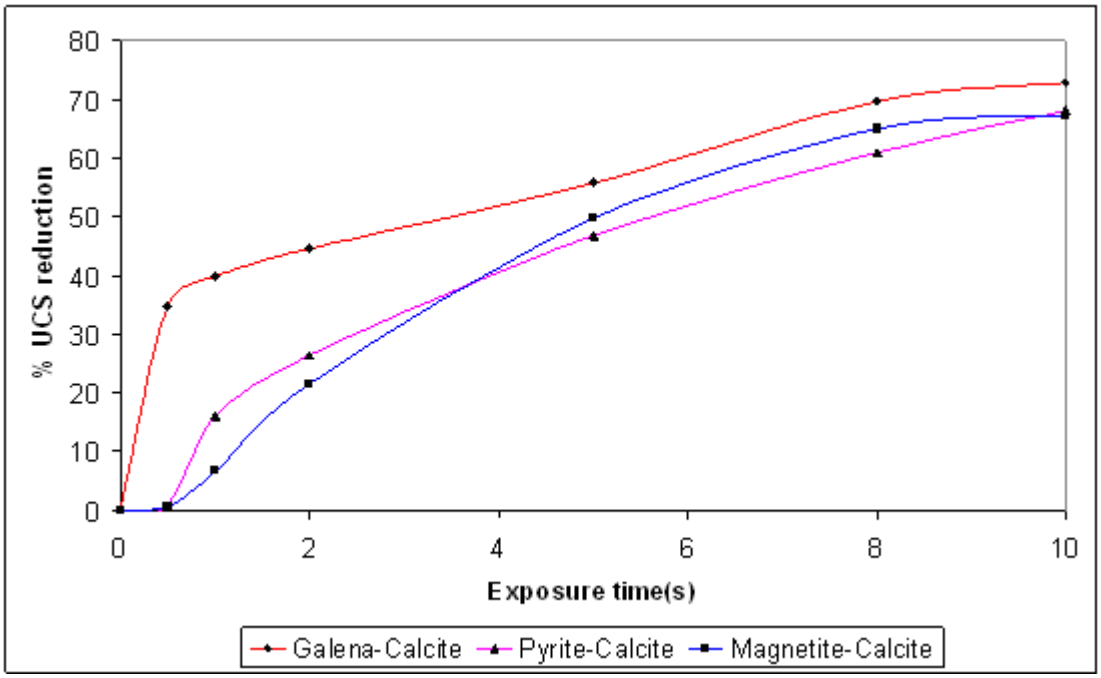

Figure 6.5: Strength reduction of calcite ores, coarse-grained (φ = 611.2), $P_d = 1 \times 10^9$ W/m^3

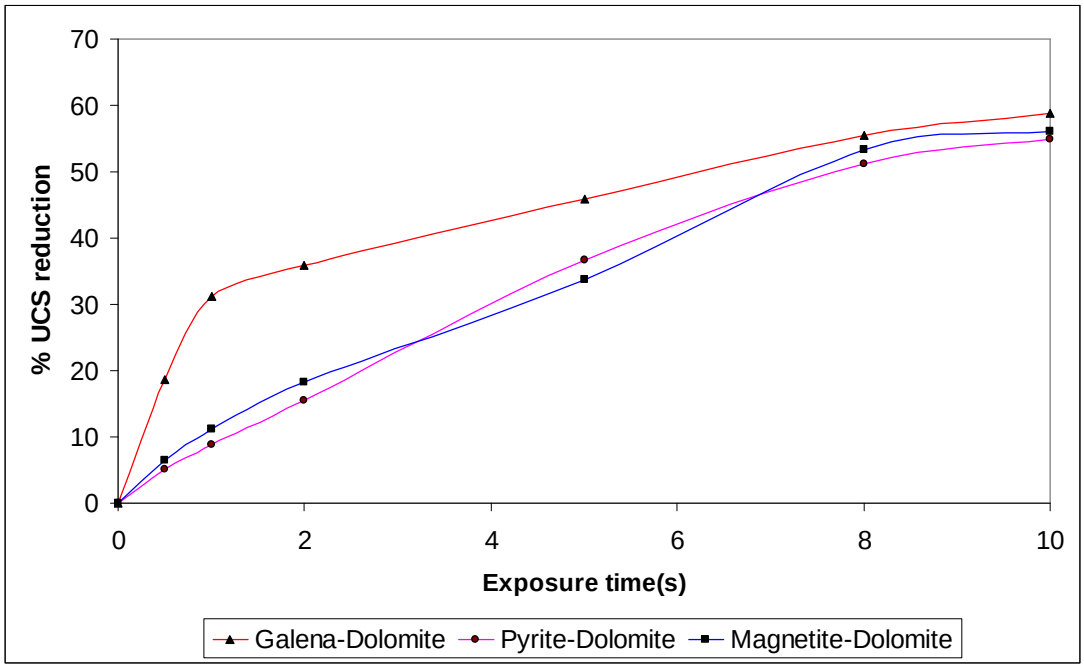

Figure 6.6: Strength reduction of dolomite ores, coarse-grained (φ = 611.2), $P_d = 1 \times 10^9$ W/m^3

6.2.3.2 Effect of Transparent Phase's Thermo-mechanical Properties

Figures 6-7, 6-11 and 6-12 show the effect of thermo-mechanical properties of the transparent phase on strength reduction of the ores. Figure 6-7 shows the effect on strength reduction of galena ores. It can be seen that there was a significant difference in strength reductions between different galena ores. The reduction in strength obtained for galena-calcite was higher below 1 s. However, after 1 s, a much higher strength reduction was attained by galena-quartz. For example, at 2 s, the reduction in galena-quartz was 57% whilst 44.6% and 35.8% reductions were obtained in galena-calcite and galena-dolomite, respectively. The temperature profiles inside the ores after microwave treatment for 2 s are also shown in Figures 6-8 to 6-10. As can be seen, the maximum temperatures obtained for all ores were between 175 and 200°C. It appears that the thermal properties of the transparent phase did not have a significant effect on the maximum temperature attained by the ores.

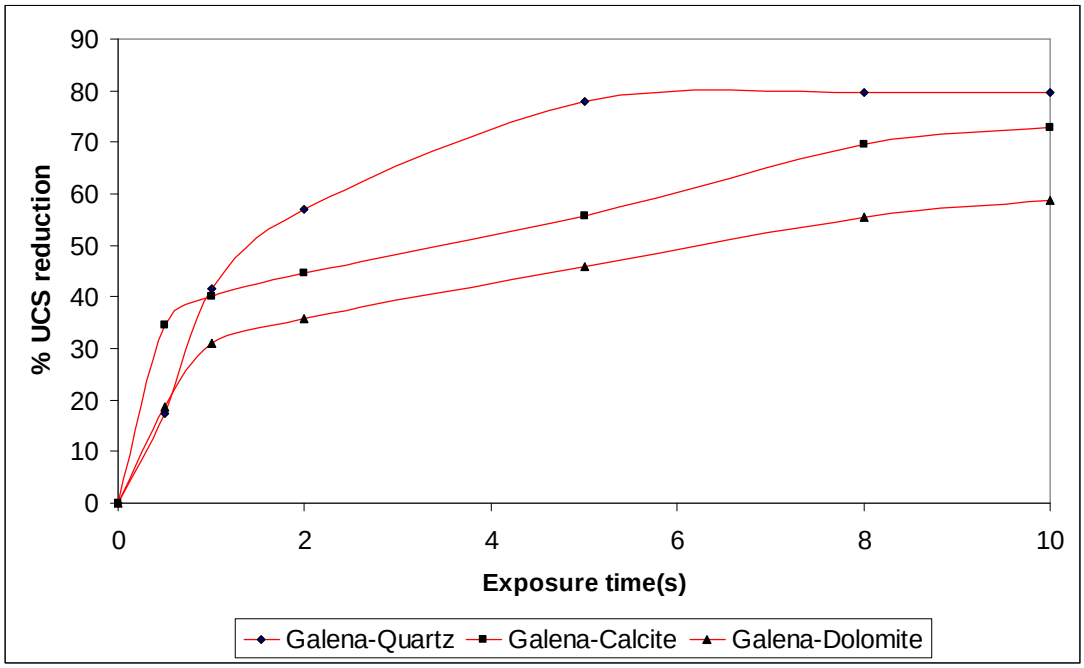

Figure 6.7: Strength reduction of galena ores, coarse-grained (φ = 611.2), $P_d = 1 \times 10^9$ W/m^3

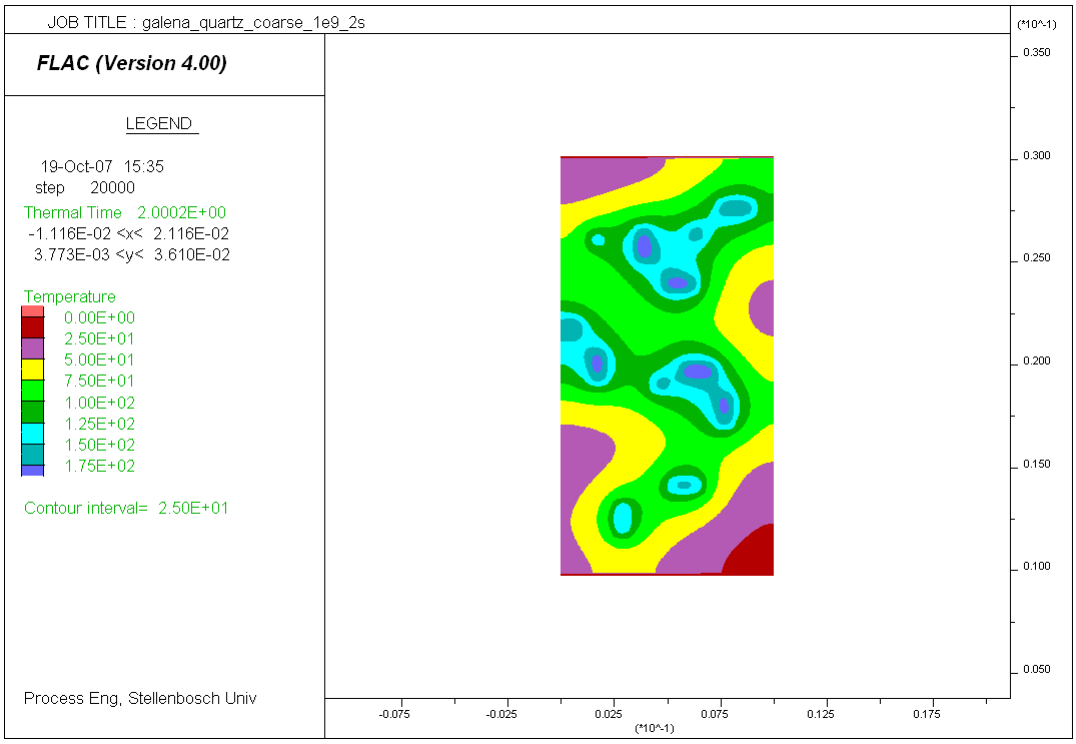

Figure 6.8: Temperature profile in galena-quartz treated at $P_d = 1 \times 10^9$ W/m^3 for t = 2 s

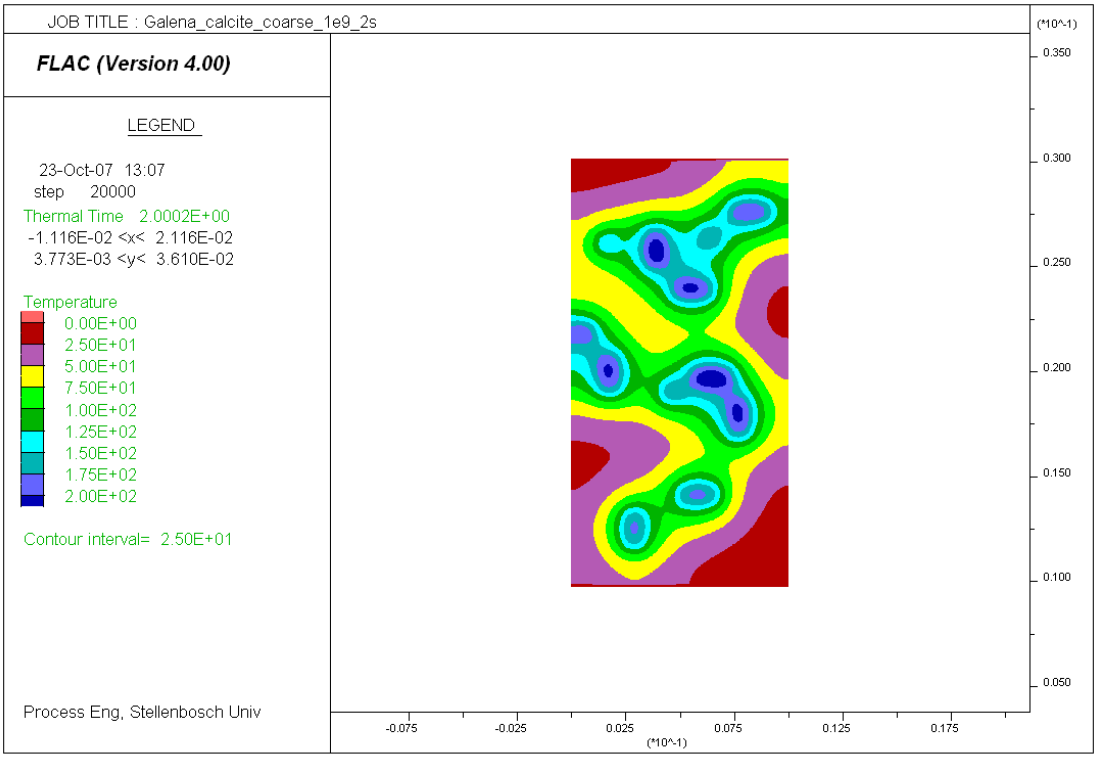

Figure 6.9: Temperature profile in galena-calcite treated at $P_d = 1 \times 10^9$ W/m^3 for t = 2 s

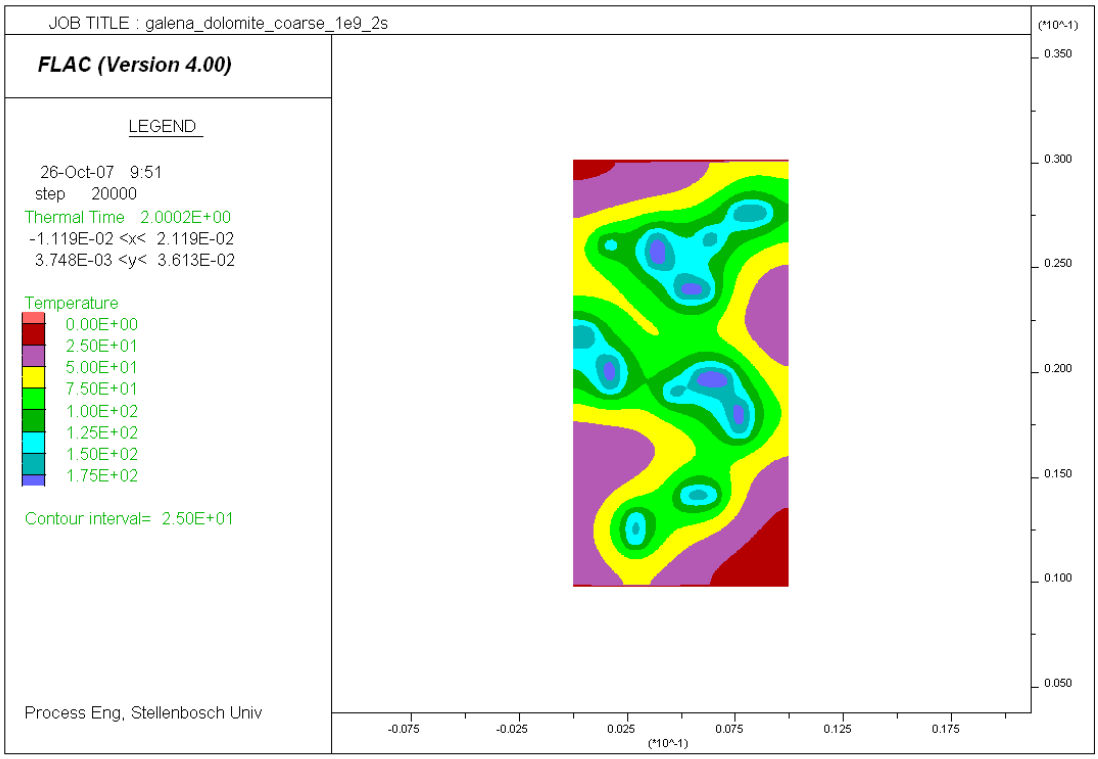

Figure 6.10: Temperature profile in galena-dolomite treated at $P_d = 1 \times 10^9$ W/m^3 for t = 2 s

Figure 6-11 shows the effect of thermo-mechanical properties of the transparent phase on strength reduction of pyrite ores. Again, it can be seen that there was a considerable difference in strength reductions between different pyrite ores. The strength reduction obtained for pyrite-quartz was much higher than that obtained for pyrite-calcite and pyrite-dolomite. For example, at 5 s, the reduction in strength was 73.8% in pyrite-quartz while 46.8% and 36.6% reductions were obtained for pyrite-calcite and pyrite-dolomite ores, respectively. The effect on strength reductions of magnetite ores is also shown in Figure 6-12. As can be seen, the difference in strength reductions was very small below 2 s. However, after 2 s, highest reductions in strength were obtained for magnetite-quartz while the lowest reductions were obtained for magnetite-dolomite. For instance, at 5 s, the reduction in strength attained by magnetite-quartz was 72.5% whilst 49.8% and 33.6% reductions were obtained for magnetite-calcite and magnetite-dolomite, respectively.

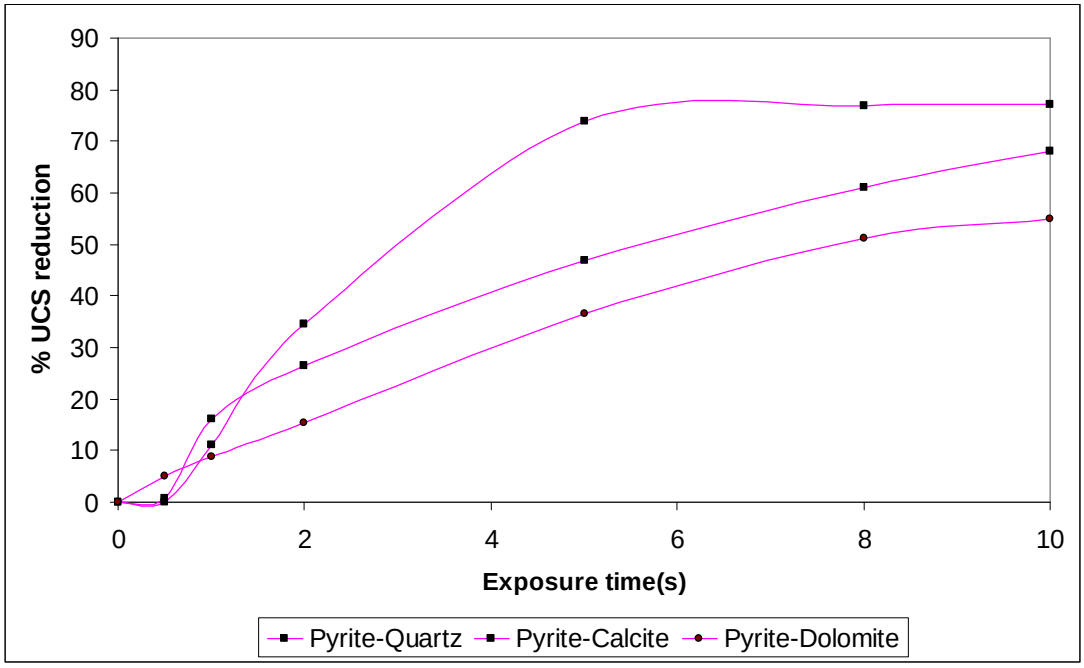

Figure 6.11: Strength reduction of pyrite ores, coarse-grained (φ = 611.2), $P_d = 1 \times 10^9$ W/m^3

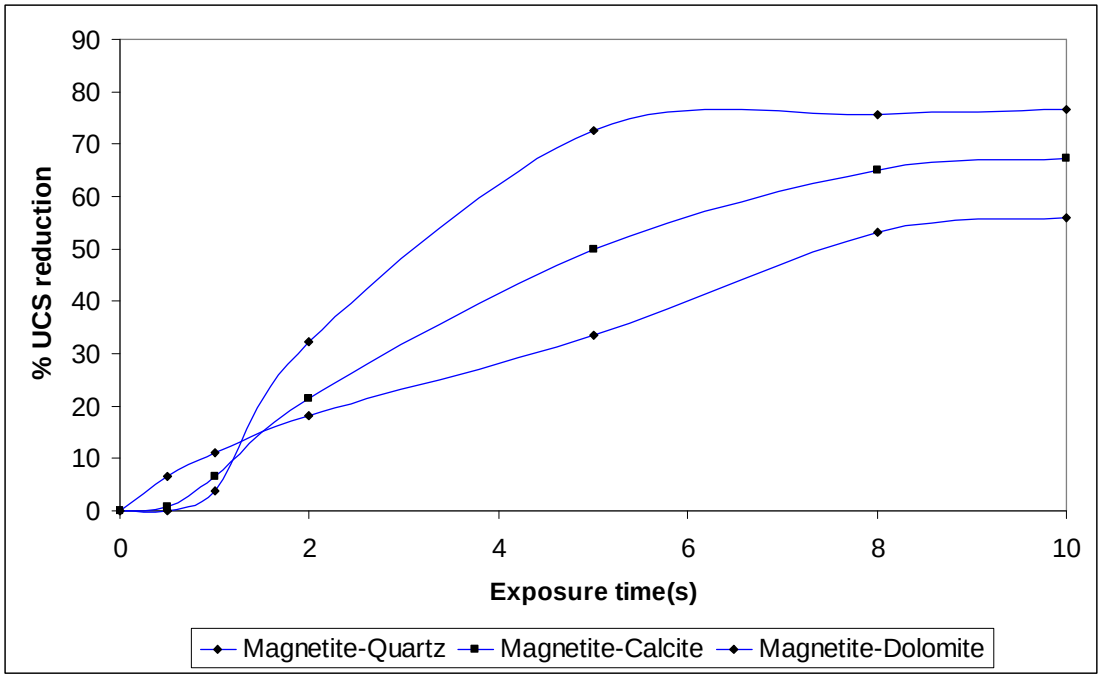

Figure 6.12: Strength reduction of magnetite ores, coarse-grained (φ = 611.2), $P_d = 1 \times 10^9$ W/m^3

6.2.4 Results of Fine-grained Binary Ores

In order to verify whether the trends that were seen in the previous section would be repeated when the texture and power density are varied, another simulation was carried out by changing the power density value and the texture of the ores. For this case, the power density was lowered to 5×10^8 W/m^3 and fine-grained binary ores were used. The simulation results obtained are shown in Table 6-2.

Table 6-2: Unconfined compressive strength of binary ores, fine-grained texture (φ = 4889.6), treated at $P_d = 5 \times 10^8$ W/m^3

Binary ores	UCS (untreated) (MPa)	UCS 0.5 s (MPa)	UCS 1 s (MPa)	UCS 2 s (MPa)	UCS 5 s (MPa)	UCS 8 s (MPa)	UCS 10 s (MPa)
Galena-Quartz	234.0	234.0	234.0	234.0	144.0	72.5	51.5
Galena-Calcite	140.0	140.0	139.0	137.0	104.5	84.0	82.0
Galena-Dolomite	104.5	104.5	104.5	103.5	89.5	83.0	73.5
Pyrite-Calcite	135.5	135.5	135.5	133.5	128.5	112.0	99.5
Pyrite-Quartz	222.5	222.5	222.5	222.0	161.0	84.5	57.0
Pyrite-Dolomite	108.0	108.0	108.0	107.5	102.5	93.0	88.0
Magnetite-Calcite	136.0	136.0	136.0	134.0	128.0	114.5	102.0
Magnetite-Quartz	220.0	220.0	220.0	216.5	159.0	95.0	57.0
Magnetite- Dolomite	107.5	107.5	107.5	107.0	103.0	94.0	89.5

6.2.4.1 Effect of Absorbent Phase's Thermo-mechanical Properties

The results in Table 6-2 are plotted in Figures 6-13, 6-14 and 6-15 to illustrate the effect of thermo-mechanical properties of the microwave absorbing mineral on the strength reduction of fine-grained ores. Figure 6-13 shows the effect on the strength reduction of fine-grained quartz ores. It can be seen that there were no reductions in strength for all ores up to 2 s. However, after 2 s, a higher strength reductions were obtained for galena-quartz at all exposure times. For example, a 39% reduction was obtained for galena-quartz at 5 s whilst only 28% reduction was obtained for pyrite-quartz and magnetite-quartz ores. Figure 6-11 shows the effect of microwave absorber's thermo-mechanical properties on strength reduction of fine-grained calcite ores. The general trend shown by quartz ores were also repeated by calcite ores i.e. below 2 s, there was little damage while beyond 2 s a much higher strength reduction was obtained for galena-calcite. For instance, at 8 s, the strength reduction obtained for galena-calcite was 40% while the reductions in strength of pyrite-calcite and magnetite-calcite were below 20%.

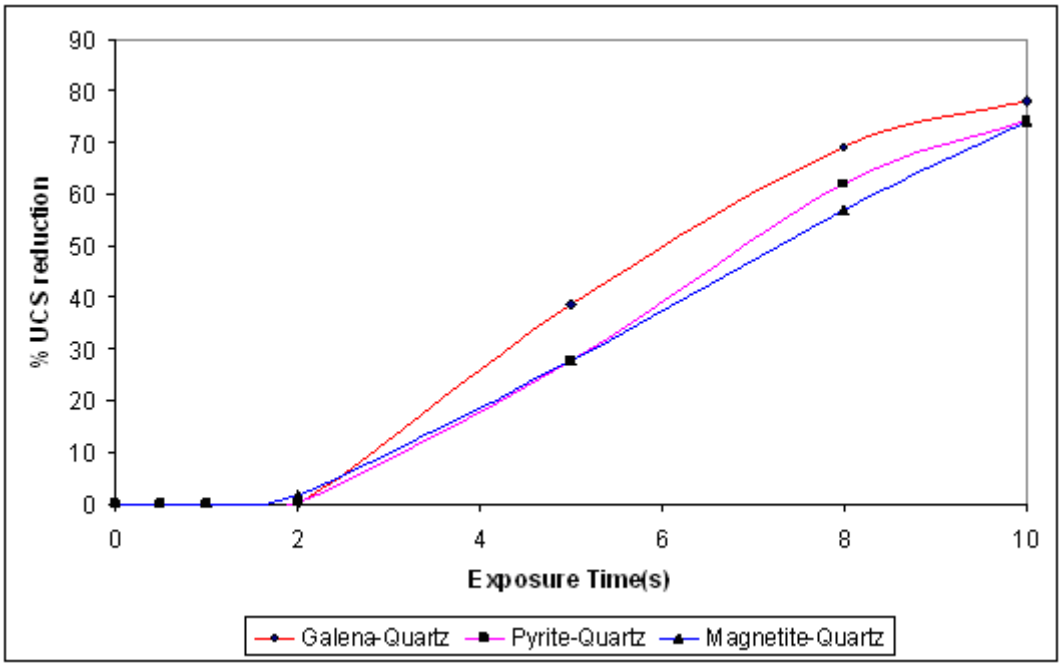

Figure 6.13: Strength reduction of quartz ores, fine-grained (φ = 4889.6), $P_d = 5 \times 10^8$ W/m^3

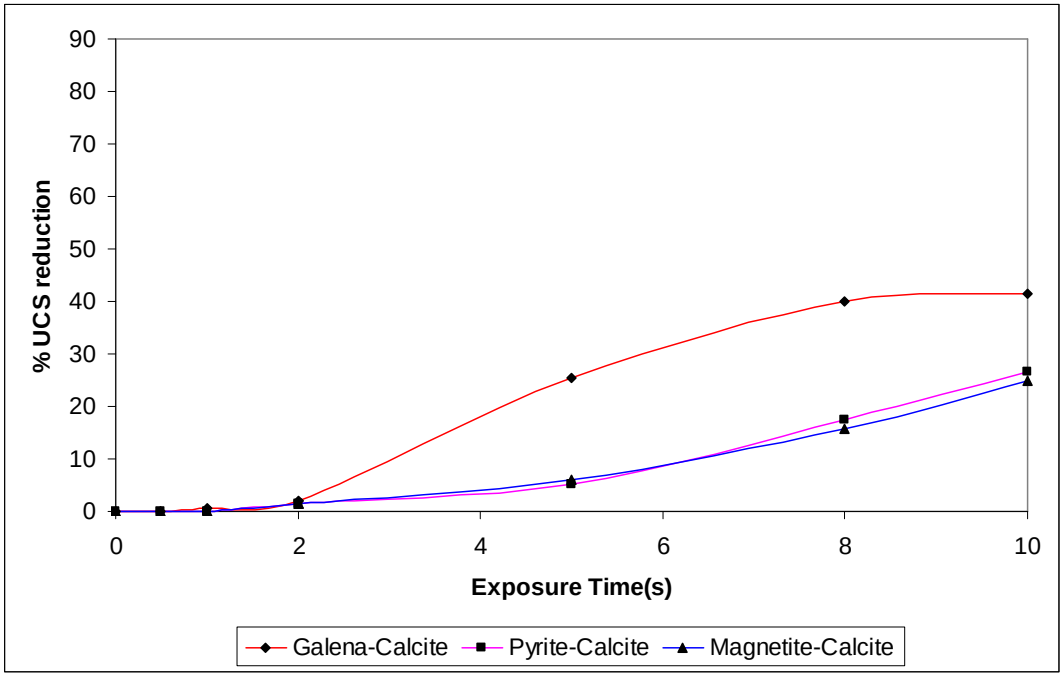

Figure 6.14: Strength reduction of calcite ores, fine-grained (φ = 4889.6), $P_d = 5 \times 10^8$ W/m^3

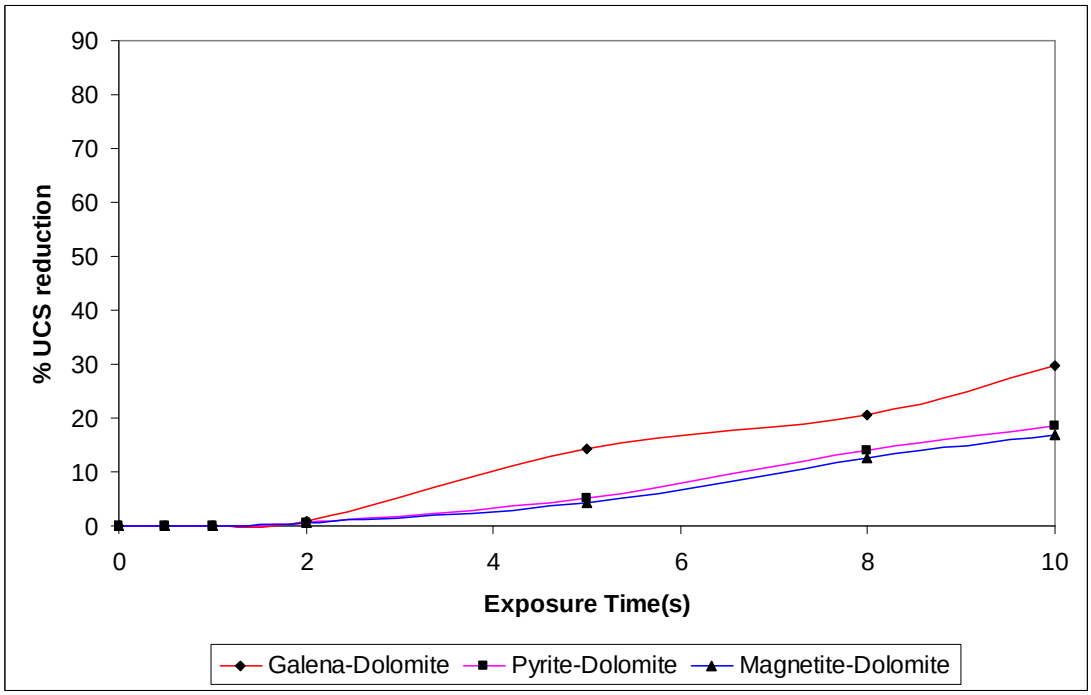

Figure 6.15: Strength reduction of dolomite ores, fine-grained (φ = 4889.6), $P_d = 5 \times 10^8$ W/m^3

The effect on strength reduction of fine-grained dolomite ores is also shown in Figure 6-15. As can be seen, the maximum strength reduction obtained here was about 30% which was obtained for galena-dolomite treated for 10 s. Here also the pattern seen in calcite and quartz ores was repeated. It can also be noted that the differences in strength reductions between pyrite-dolomite and magnetite-dolomite were very small at all exposure times.

6.2.4.2 Effect of Transparent Phase's Thermo-mechanical Properties

Figures 6-16, 6-17 and 6-18 show the effect of the thermo-mechanical properties of the transparent phase on strength reduction of fine-grained ores. As can be seen from Figure 6-16, there was a considerable difference between strength reductions obtained for different fine-grained galena ores. The highest strength reduction was obtained for galena-quartz ore while the lowest was obtained for galena-dolomite at all exposure times. For example, at 8 s, the reduction was 69% in galena-quartz, 40% in galena-calcite and 20% in galena-dolomite.

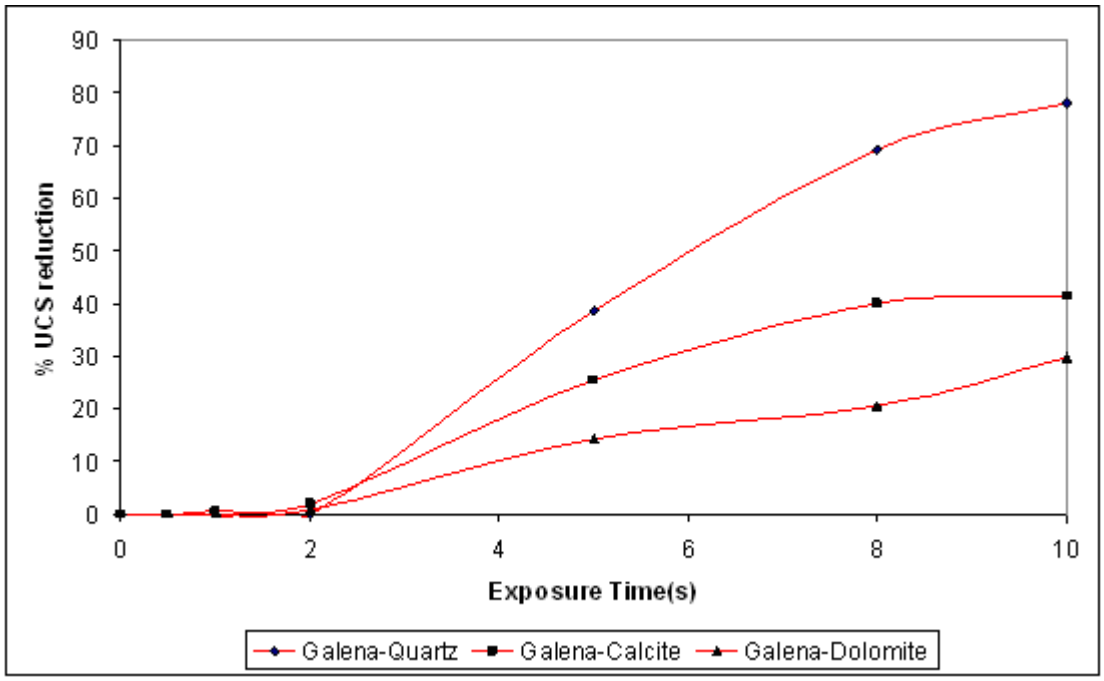

Figure 6.16: Strength reduction of galena ores, fine-grained (φ = 4889.6), $P_d = 5 \times 10^8$ W/m^3

The effect of thermo-mechanical properties of the transparent phase on strength reduction of fine-grained pyrite ores is also shown in Figure 6-17. As can be seen, the strength reduction obtained for pyrite-quartz was much higher compared to that obtained for pyrite-calcite and pyrite-dolomite ores. For example, at 5 s, the strength reduction of pyrite-quartz was 27.6% while the strength reduction of pyrite-calcite and pyrite-dolomite were 5.2% and 5.1%, respectively. Figure 6-18 shows the effect on strength reduction of magnetite ores. It can be seen that the general trend shown by galena and pyrite ores was also repeated for magnetite ores. For example, the strength reduction at 10 s was 74.1% in magnetite-quartz, 25% in magnetite-calcite and 16.7% in magnetite-dolomite.

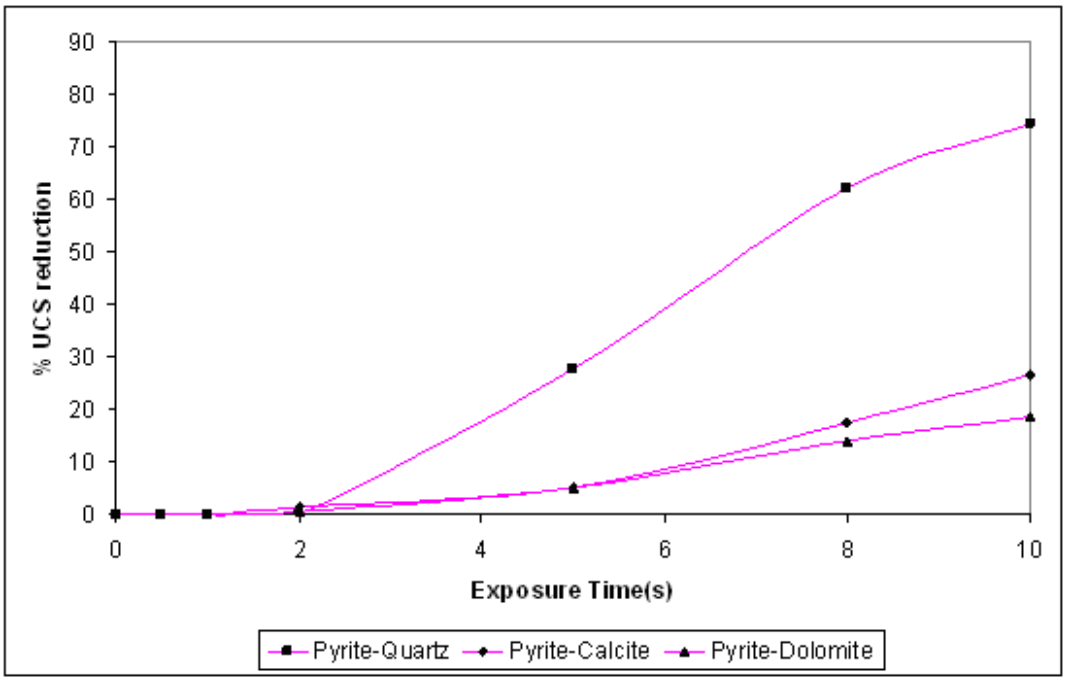

Figure 6.17: Strength reduction of pyrite ores, fine-grained (φ = 4889.6), $P_d = 5 \times 10^8$ W/m^3

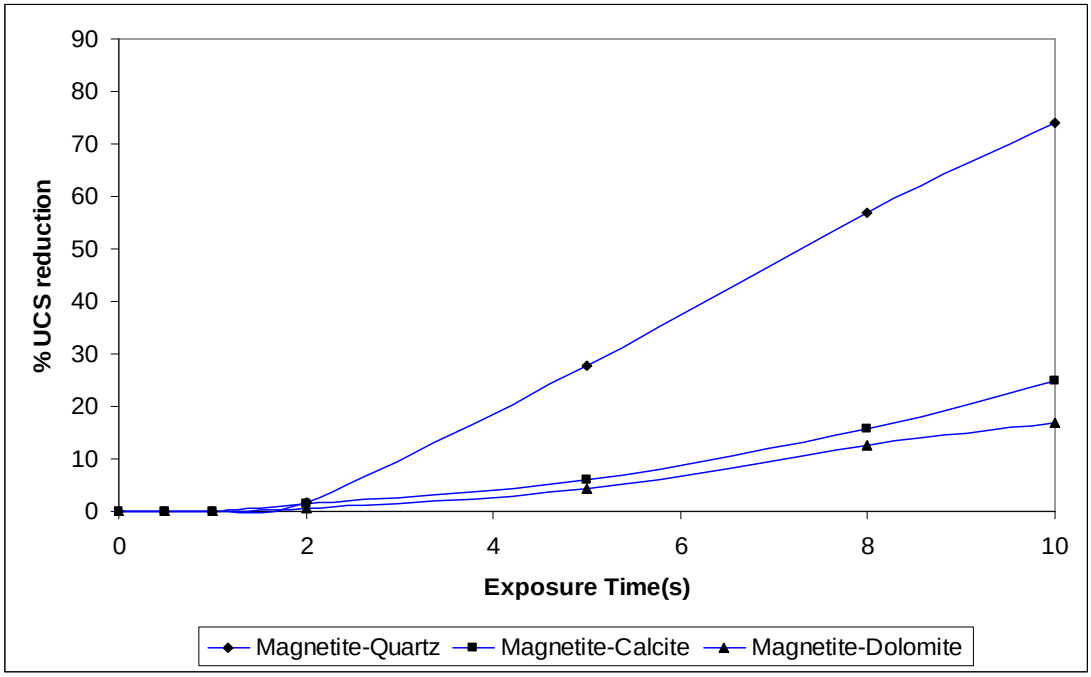

Figure 6.18: Strength reduction of magnetite ores, fine-grained (φ= 4889.6), $P_d = 5 \times 10^8$ W/m^3

6.2.5 Discussion and Summary

It has been shown that binary ores containing galena as the microwave absorber attained the highest reductions in strength. This can be explained by looking the thermal properties in Tables 5.2, 5.6 and 5.9. From Table 5.2, it can be seen that even though the density of galena is higher than that of magnetite and pyrite (1.4 and 1.5 times), its specific heat capacity is 2.79 and 3.85 times lower than that of magnetite and pyrite, respectively. This means that for the same power density and exposure time, the temperature rise in galena was higher (refer Figures 6-2 to 6-4).

Another property that is very important in thermal stress development consequently in strength reduction is the thermal expansion coefficient. As can be seen from Table 5-9, the thermal expansion coefficient of galena is 2 and 2.1 times that of pyrite and magnetite, respectively. This implies that even for the same temperature rise, the strain developed in galena would be 2 and 2.1 times that of pyrite and magnetite, respectively.

It can be seen from Tables 5-11 and 5-12 that the bulk and shear modulus of galena are much lower than those of pyrite and magnetite. It is known that a higher bulk and shear modulus of the microwave absorbing mineral will result in higher stresses being generated per unit strain. However, the strength reduction obtained for pyrite and magnetite ore were lower than that of galena ore. Thus, it can be said that the effect of thermal properties of the microwave absorbent phase was much higher than the effect of its mechanical properties on strength reduction of the ores.

As was shown in Chapter 5, the thermo-mechanical properties of pyrite and magnetite are somewhat similar except that pyrite has a much higher thermal conductivity value than magnetite. High thermal conductivity of the microwave absorbing mineral will increase the conduction heat loss and as a consequence, decrease the thermally induced stresses. However, since the microwave exposure times were short, the influence of thermal conductivity was not that significant compared to the effect of other thermal properties such as specific heat capacity and density. The temperature profiles obtained for the two ores also confirmed this situation. As a result, pyrite and magnetite ores achieved similar strength reductions regardless of a considerable thermal conductivity difference. Nonetheless, it is suggested that if the exposure times were very long and the power density was very low, higher strength reductions would be expected in magnetite than pyrite ores.

It has also been shown that the effect of the thermo-mechanical properties of the transparent minerals have also a significant effect on the strength reduction. Highest reductions in strength in general were obtained for quartz ores and the lowest were obtained for dolomite ores. The strength reductions obtained for calcite ores were between that of quartz ores and dolomite ores at all power densities and ore textures. Looking the properties of the transparent minerals, it can be seen that there is a significant difference between unconfined compressive strengths of the ores. The unconfined compressive strengths of the quartz ores were 2 - 2.5 times that of dolomite and 1.25 - 1.5 times that of calcite. Thus, for quartz ores, the transparent mineral (matrix) is very strong and it is suggested that this would facilitate fracture during thermal expansion of the heated phase.

From Table 5-9, it can be seen that the thermal expansion coefficient of quartz is 2.5 - 3 times higher than that of calcite and dolomite. Based on only the thermal expansion

coefficient difference between the microwave absorbing and the transparent minerals, one could expect for example that the strength reduction in galena-quartz would be lower than in galena-dolomite, as the thermal expansion coefficient difference is higher in galena-dolomite. But a much higher reduction was obtained for galena-quartz. Thus, it can be said that the effect of hardness difference between microwave absorber and transparent minerals is more significant than the effect of thermal expansion coefficient difference on bulk strength reduction. However, it was also seen that below 1 s coarse-grained calcite ores achieved relatively higher strength reduction than coarse-grained quartz ores. It is suggested that the high thermal expansion coefficient of quartz (the transparent matrix) might also have a contribution for the increase in bulk damage after 1 s.

6.2.6 Conclusions

This section has examined the effect of thermo-mechanical properties of minerals on strength reduction when binary ores subjected to microwave radiation. It has been shown that the thermo-mechanical properties of both the microwave absorbing and microwave transparent minerals have a strong influence on strength reduction. It was shown that in general the thermal properties of the microwave absorbing mineral and the mechanical properties of the transparent matrix have the most significant effect on the strength reduction. Binary ores containing a microwave absorbing mineral that has a high thermal expansion coefficient in a strong transparent matrix achieved higher reductions in strength.

6.3 Effect of Absorbent Phase Grain Size on Strength Reduction of Microwave Treated Ores

6.3.1 Introduction

This section details the study undertaken for investigating the effect of grain size of the microwave absorbent phase on unconfined compressive strength reduction of microwave treated ores. Simulation of microwave heating, thermal damage and unconfined compressive strength tests were carried out for two binary ores, each having three different textures (coarse, medium and fine-grained). The effect of absorbent phase grain size was then examined by comparing the reduction in strength of the ores for the same microwave treatment condition.

6.3.2 Methodology

Based on the results from the previous section, two binary ores namely, galena-quartz and magnetite-dolomite were selected for the study. The two ores were chosen as they attained the highest and the lowest strength reduction than any other binary ores. Three different textures were constructed for each binary ore. The method for constructing different textures was already discussed in Chapter 5 and it will not be repeated here. Typical ore textures are shown in Figure 6-19 again for clarity, note that all ore textures contain 10% of microwave absorbing and 90% transparent mineral by volume. The conceptual ores were then exposed to microwave heating at power densities of 1×10^9 W/m^3 and 5×10^8 W/m^3 for 0.5 to 10 s. After heating, the ores were subjected to unconfined compressive strength test and the strength reduction of each ore at each treatment condition was recorded.

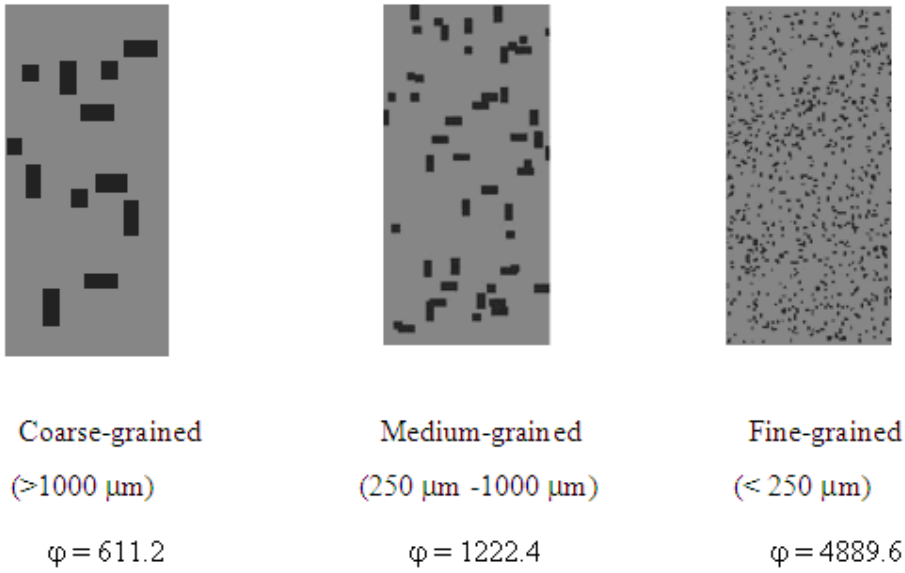

Figure 6.19: Representation of different textures

6.3.3 Results and Discussion

The results of the unconfined compressive strength tests for galena-quartz treated at microwave power $P_d = 1 \times 10^9$ W/m^3 are shown in Table 6-3 and the reductions in strength are also shown in Figure 6-20. It can be seen from Table 6-3 that as the texture parameter φ increases (as the grain size decreases), the damage incurred in the samples become smaller. For example, a reduction of 17.28% was obtained for the coarse-grained ore at 0.5 s while there were no reductions at this time for both the medium-grained and fine-grained textures. The amount of energy required to achieve the same strength reduction as the coarse-grained ore was also considerably high for the fine-grained one. For example, it can be seen that it required an energy input of 1×10^9 J/m^3 to reduce the unconfined compressive strength of coarse-grained galena-quartz ($\varphi = 611.2$) by 41% but more than 3×10^9 J/m^3 was needed to achieve the same reduction for the fine-grained ones ($\varphi = 4889.6$).

Table 6-3: Unconfined compressive strength of galena-quartz ore, treated at P_d = 1 x 10^9 W/m^3

Texture parameter (φ)	UCS (untreated) (MPa)	UCS 0.5 s (MPa)	UCS 1 s (MPa)	UCS 2 s (MPa)	UCS 5 s (MPa)	UCS 8 s (MPa)	UCS 10 s (MPa)
611.2	231.5	191.5	135.0	99.5	51.0	47.0	47.0
1222.4	224.5	224.5	171.0	112.0	52.0	47.0	47.0
4889.6	232.0	232.0	232.0	176.0	54.0	47.0	47.0

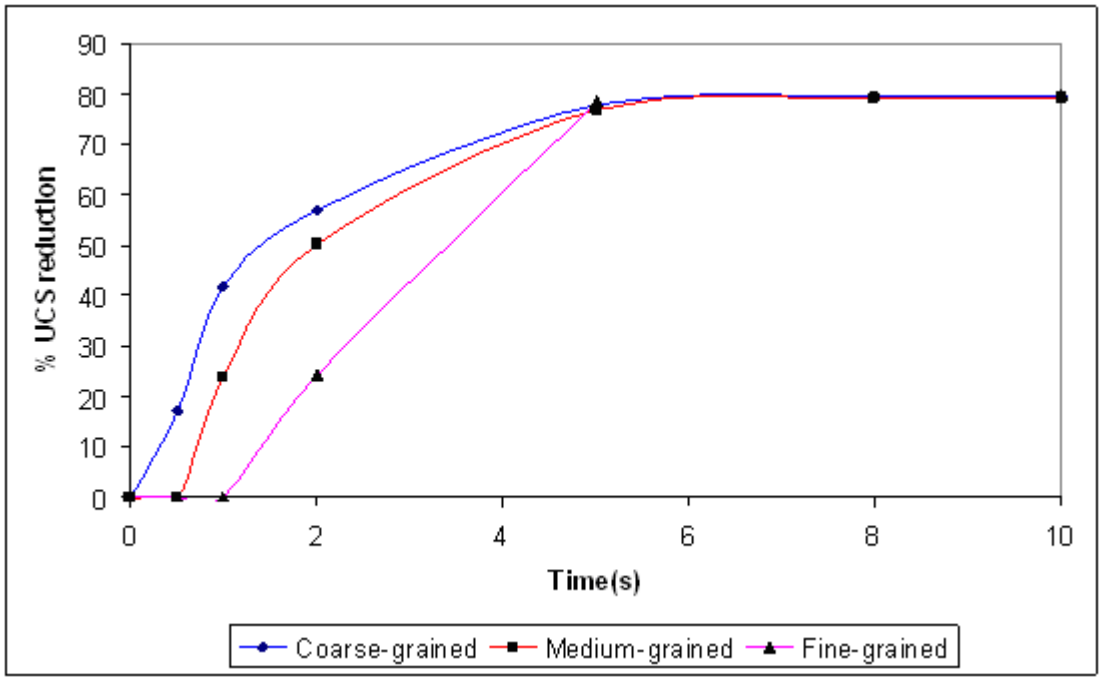

Figure 6.20: Strength reduction of galena-quartz ore, P_d = 1 × 10^9 W/m^3

The possible reason for this can be explained by looking the temperature profiles inside the ores for the same treatment condition. Figures 6-21 to 6-23 show the

temperature profiles obtained for different textures after 1 s microwave treatment. As can be seen, maximum temperature of 150°C was achieved by the coarse-grained ore while the maximum temperatures obtained for medium grained and fine–grained ore were 125 and 80°C, respectively. It is evident that the fine-grained and medium-grained ores lost heat by conduction more rapidly. Further, the temperature gradients for the coarse-grained were much higher around the grain boundary. This is most likely due to the increase in heat transfer area (surface area to volume ratio) between the microwave absorbent mineral and transparent matrix as the grain size decreases. It is apparent that if the rise in temperature inside the ore is low, then the thermally induced stresses will also be low (refer Chapter 5). Thus, the damage induced in the medium grained and fine grained ores were smaller for the same treatment condition.

The difference in reduction of unconfined compressive strengths of the ores became smaller as the exposure time increased and finally all ores achieved the maximum strength reduction. However, it should be noted that the coarse-grained ore achieved a considerable (> 40%) strength reduction in a shorter exposure time (< 1 s).

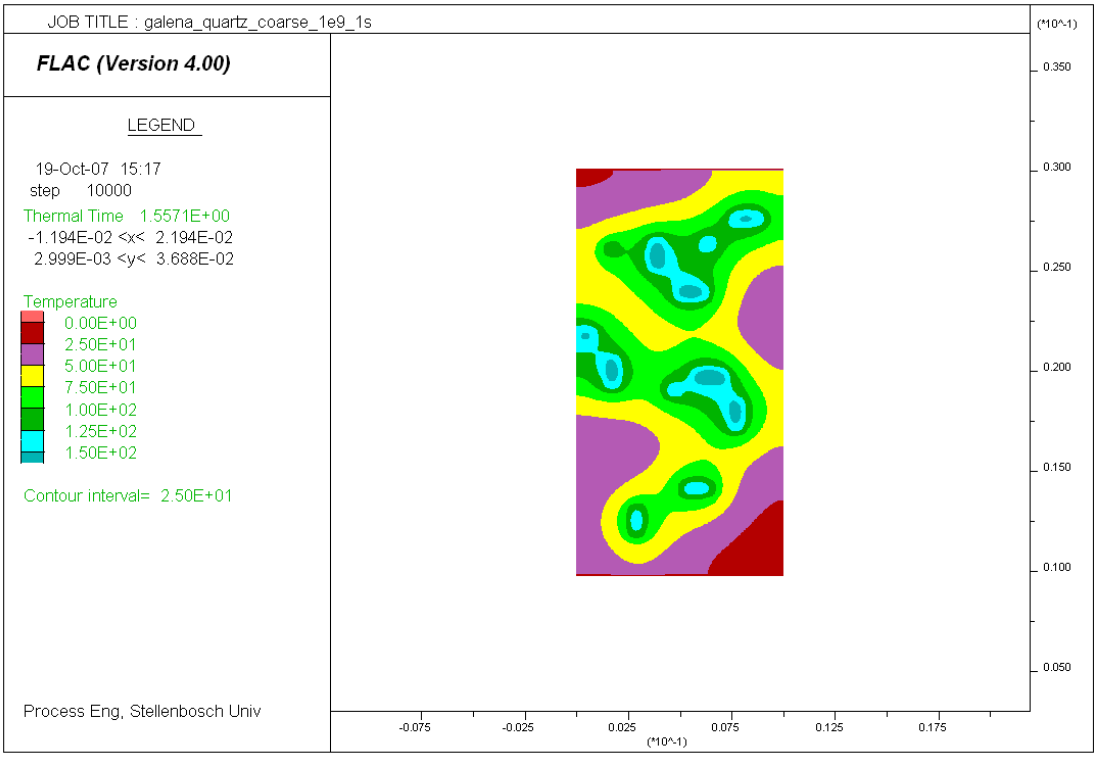

Figure 6.21: Temperature profile in galena-quartz, coarse-grained, treated at $P_d = 1 \times 10^9$ W/m^3 for t = 1 s

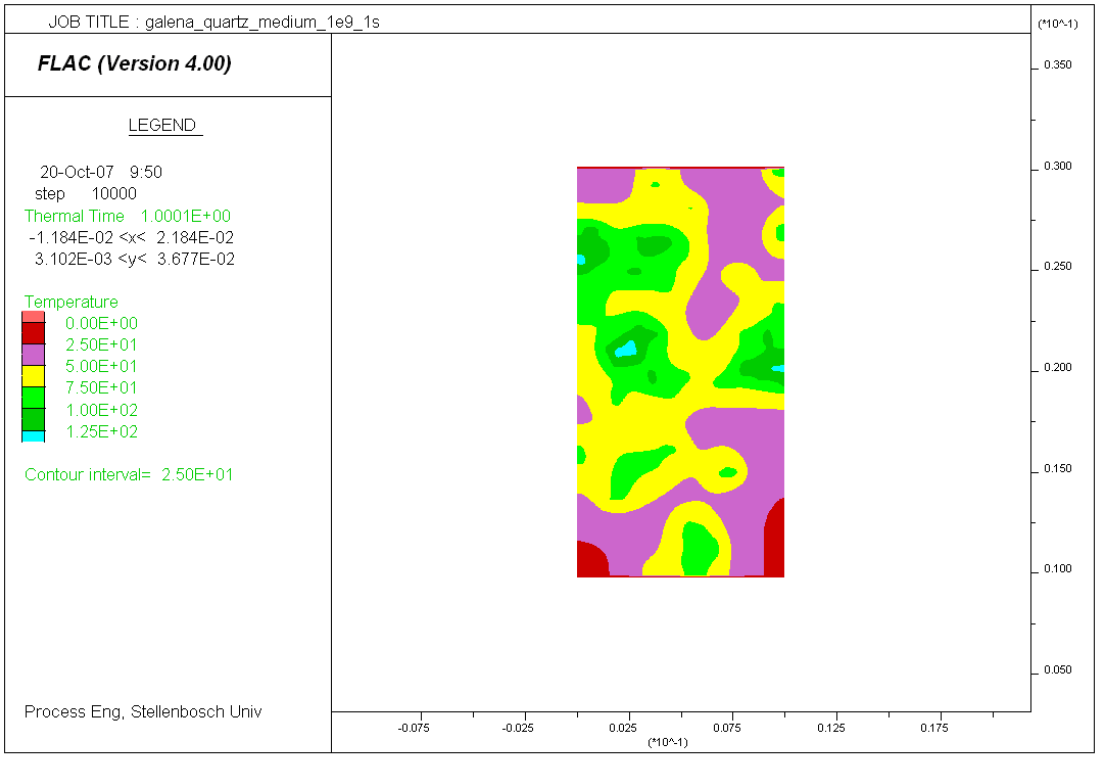

Figure 6.22: Temperature profile in galena-quartz, medium-grained, treated at $P_d = 1 \times 10^9$ W/m^3 for t = 1 s

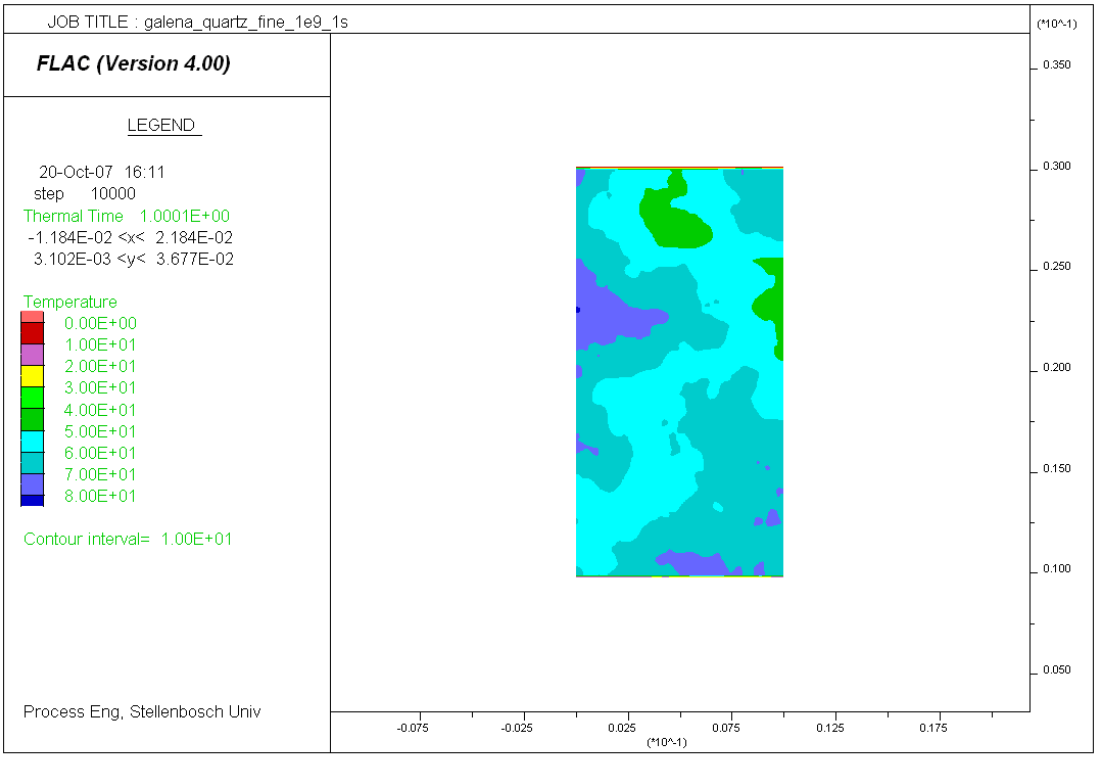

Figure 6.23: Temperature profile in galena-quartz, fine-grained, treated at $P_d = 1 \times 10^9$ W/m^3 for t = 1 s

Table 6-4 and Figure 6-24 show the results of the unconfined compressive strength test of galena-quartz ores treated at $P_d = 5 \times 10^8$ W/m^3. As it would be expected, the reductions in strength obtained here were lower than the result obtained from the previous simulation because of the power density difference. But here also the pattern is repeated, i.e. higher strength reduction was obtained for coarse-grained ore than medium-grained and fine-grained ore. As can be seen, more than 70% reduction in strength was obtained at 5 s for coarse-grained ore while the reduction in fine-grained ones was below 40%.

Table 6-4: Unconfined compressive strength of galena-quartz ore, treated at $P_d = 5 \times 10^8$ W/m^3

Texture parameter (φ)	UCS (untreated) (MPa)	UCS 0.5 s (MPa)	UCS 1 s (MPa)	UCS 2 s (MPa)	UCS 5 s (MPa)	UCS 8 s (MPa)	UCS 10 s (MPa)
611.2	236.0	236.0	209.0	135.0	68.0	52.5	51.5
1222.4	230.0	230.0	230.0	221.0	106.5	63.0	52.0
4889.6	234.0	234.0	234.0	234.0	144.0	72.5	52.5

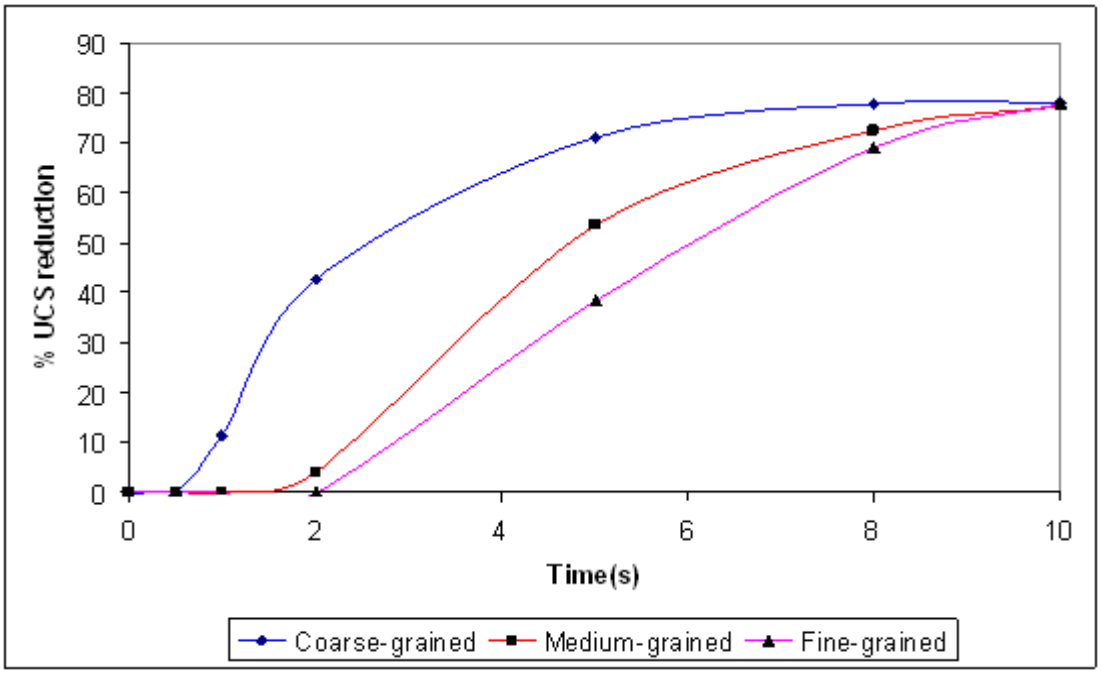

Figure 6.24: Strength reduction of galena-quartz ore treated at $P_d = 5 \times 10^8$ W/m^3

The results of unconfined compressive strength test for magnetite-dolomite treated at microwave power at $P_d = 1 \times 10^9$ W/m^3 are shown in Table 6-5 and Figure 6-25. It can be seen that the general trend shown by galena-quartz was also repeated by magnetite-dolomite i.e., highest reductions in strength were obtained for coarse-grained texture and the lowest obtained for the fine-grained ones at all exposure times. For example, the reductions obtained at 5 s were 33.6% for the coarse-grained, 23.8% for the medium-grained and 18.1% for the fine-grained ore.

Table 6-5: Unconfined compressive strength of magnetite-dolomite ore, treated at P_d = 1 $\times 10^9$ W/m^3

Texture parameter (φ)	UCS (untreated) (MPa)	UCS 0.5 s (MPa)	UCS 1 s (MPa)	UCS 2 s (MPa)	UCS 5 s (MPa)	UCS 8 s (MPa)	UCS 10 s (MPa)
611.2	107.0	100.0	95.0	87.5	71.0	50.0	47.0
1222.4	107.0	106.0	103.5	99.0	81.5	57.0	49.5
4889.6	107.5	107.0	105.5	104.0	88.0	66.0	55.0

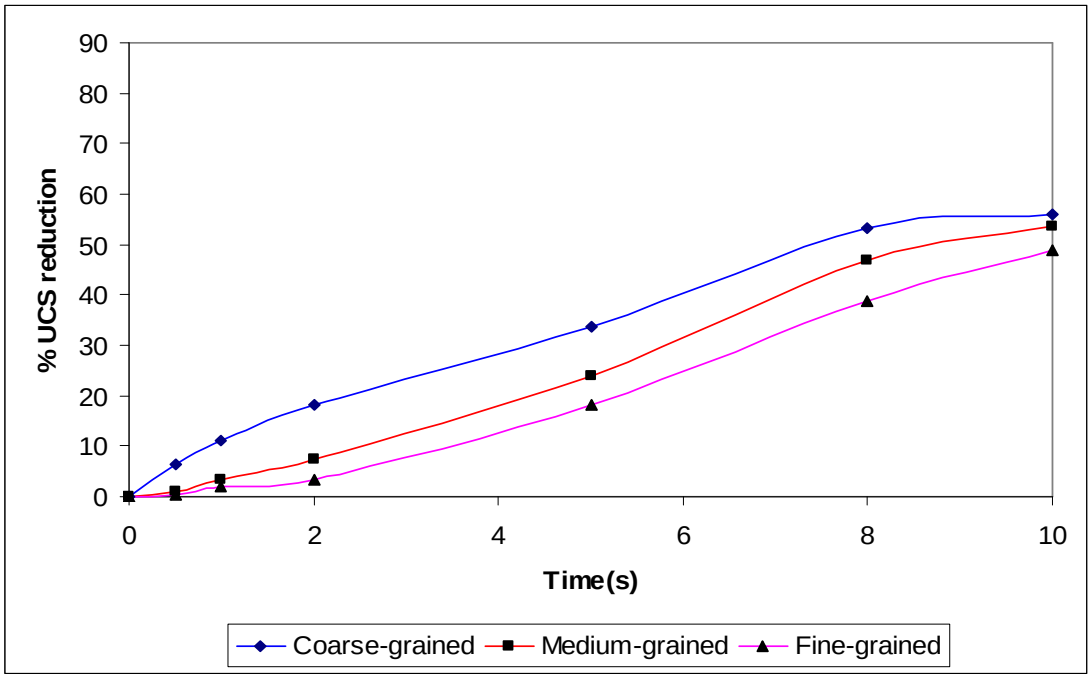

Figure 6.25: Strength reduction of magnetite-dolomite ore, treated at $P_d = 1 \times 10^9$ W/m^3

Table 6-6: Unconfined compressive strength of magnetite-dolomite ore, treated at P_d = 5 $\times 10^8$ W/m^3

Texture parameter (φ)	UCS (untreated) (MPa)	UCS 0.5 s (MPa)	UCS 1 s (MPa)	UCS 2 s (MPa)	UCS 5 s (MPa)	UCS 8 s (MPa)	UCS 10 s (MPa)
611.2	106.5	105.0	104.5	97.5	92.0	83.0	73.0
1222.4	107.0	107.0	105.5	104.0	95.0	88.0	83.5
4889.6	107.5	107.5	107.5	107.0	103.0	94.0	89.5

Table 6-6 shows the results of the unconfined compressive strength test of magnetite-dolomite treated at 5×10^8 W/m^3. The reductions in strength are also shown in Figure 6-26. Here also, highest reduction in strength was obtained for coarse-grained magnetite-dolomite and lowest reduction was obtained for fine-grained one at all exposure times. For instance, at 10 s, the reductions were 16.7% for the fine-grained, 22% for the medium-grained and 31.5% for the coarse-grained one. It is evident that for the same energy input of 5×10^9 J/m^3 the reduction in strength attained by coarse-grained magnetite-dolomite was twice than that of fine-grained one.

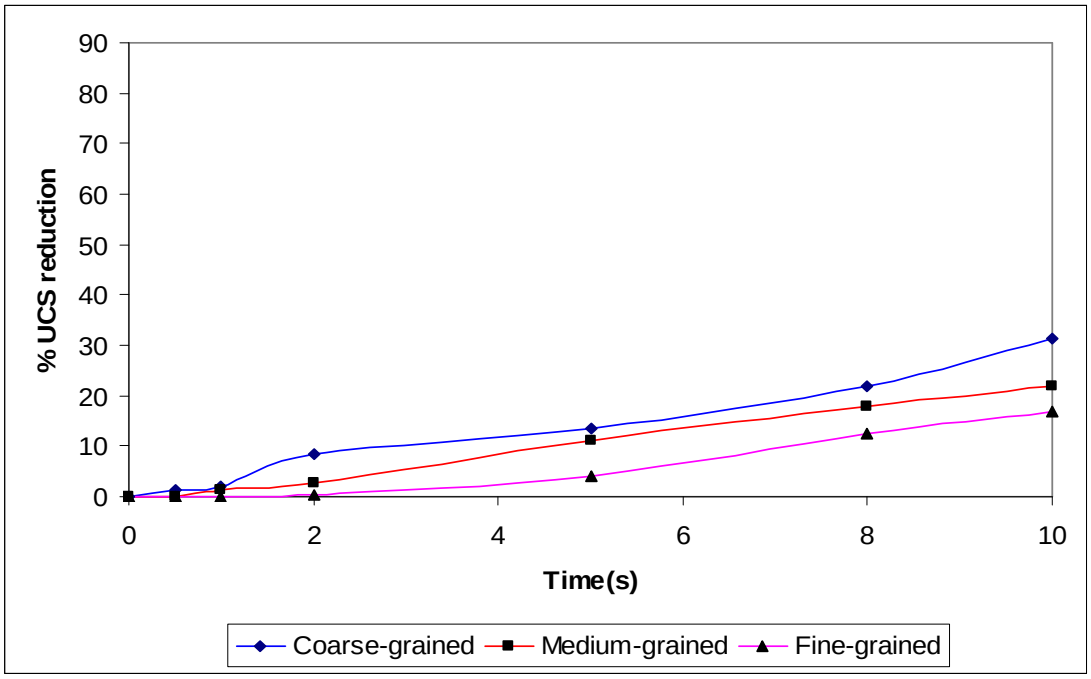

Figure 6.26: Strength reduction of magnetite-dolomite ore, treated at $P_d = 5 \times 10^8$ W/m^3

6.3.4 Conclusions

This section has examined the effect of grain size of microwave absorbent phase on bulk strength reduction when binary ores exposed to microwave radiation. It has been shown that binary ores with coarse-grained texture achieved the highest reductions in strength while lowest reductions in strength were obtained for fine-grained texture for all binary ores. The following reasons are suggested for this: firstly, larger microwave absorbing grains would create larger stresses during thermal expansion, thus, increasing fracture. Secondly, it can be seen that for the same percentage of the microwave absorbent phase (10%), the heat transfer area (surface area to volume ratio) between the microwave absorbent phase and transparent matrix in the fine-grained is much higher than in the medium-grained and coarse-grained ores as indicated by the texture parameter. Thus, the fine-grained ores will loss heat by conduction more rapidly during heating (refer the temperature profiles in Figures 6-21 to 6-21). This will significantly decrease the temperature gradient and consequently, reduce the thermally induced stresses.

6.4 Influence of Power Density on Strength Reduction of Microwave Treated Ores

6.4.1 Introduction

This section investigates the influence of power density on unconfined strength reduction of microwave treated ores. It has been previously shown that power density has a significant effect on microwave treatment of ore (e.g. Whittles et al., 2003; Jones et al., 2007). It was shown that by increasing the power density, significantly greater stresses could be created for much lower energy inputs. Previous simulation work by Jones et al. (2007) indicated that higher strength reduction in strength was obtained when the power density was very high and the exposure time was very short for the same energy inputs. However, the power densities values used on that study were between 1×10^9 and 1×10^{15} W/m^3. The intention in that study was to examine the effect of using future very high power pulsed microwave equipment on microwave treatment of ores. Hence, the power density range was greater than that is likely to be achievable in practice, either as a result of limitations in available technology or because of the likelihood of dielectric breakdown at the electric field strengths required. In this study, the effect of power density on the strength reduction of ores for a narrow power density range is investigated.

6.4.2 Methodology

Here again, two binary ores, namely galena-quartz and magnetite-dolomite were used for the study. In addition, two different textures (coarse-grained and fine-grained) were also simulated for each binary ore. Further, studying the effect of power density for a narrow range would provide useful data for designing the required applicator as there is variation in electric field inside the applicator (refer Chapter 3). As was discussed previously, due to non-uniformity of the electric field, there would be a power density variation inside the applicator. Accordingly, simulations were carried out for the two binary ores by varying the power density from 5×10^8 to 1×10^9 W/m^3. Again, this power density range was assumed to be typical of the power density range achievable using a 30 kW, 2.45 GHz supply in either a single mode applicator or

continuous treatment applicator and further, within the range of values obtained from electromagnetic simulations performed elsewhere.

6.4.3 Results and Discussion

Figure 6-27 shows the results of simulations of unconfined compressive strength tests of coarse-grained galena-quartz. The percentage reduction in strength as a function of power density is also shown in Figure 6-28. It can be seen that even for the narrow power density range examined; the results indicated that strength reduction is strongly dependent on power density. This can be noticed by looking the strength reduction obtained at the same energy inputs. It can be seen from Figure 6-28 that 17.5% strength reduction was achieved at $P_d = 1 \times 10^9$ W/m^3, 0.5 s while the strength reduction at $P_d = 5 \times 10^8$ W/m^3, 1 s was about 10%. After 5 s, the strength reductions obtained at different power densities were almost the same, as the ore reached its maximum strength reduction. However, it should be noted that at $P_d = 1 \times 10^9$ W/m^3 the maximum strength reduction was achieved at shorter exposure time. It is evident that a small change in the power density had a significant effect on the strength reduction of the ore.

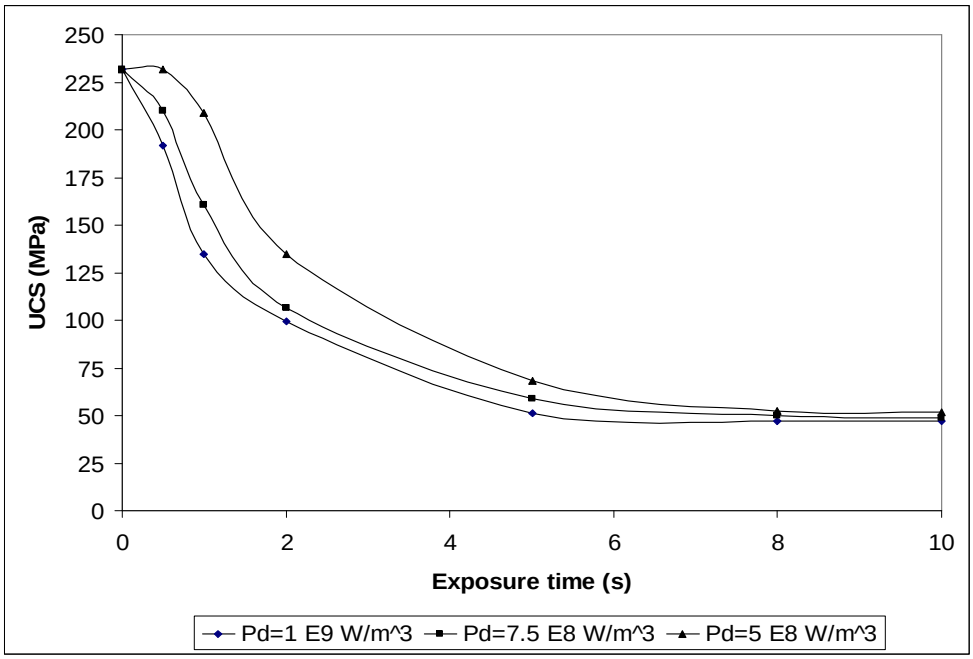

Figure 6.27: Unconfined compressive strength of coarse galena-quartz ore, treated at different power densities

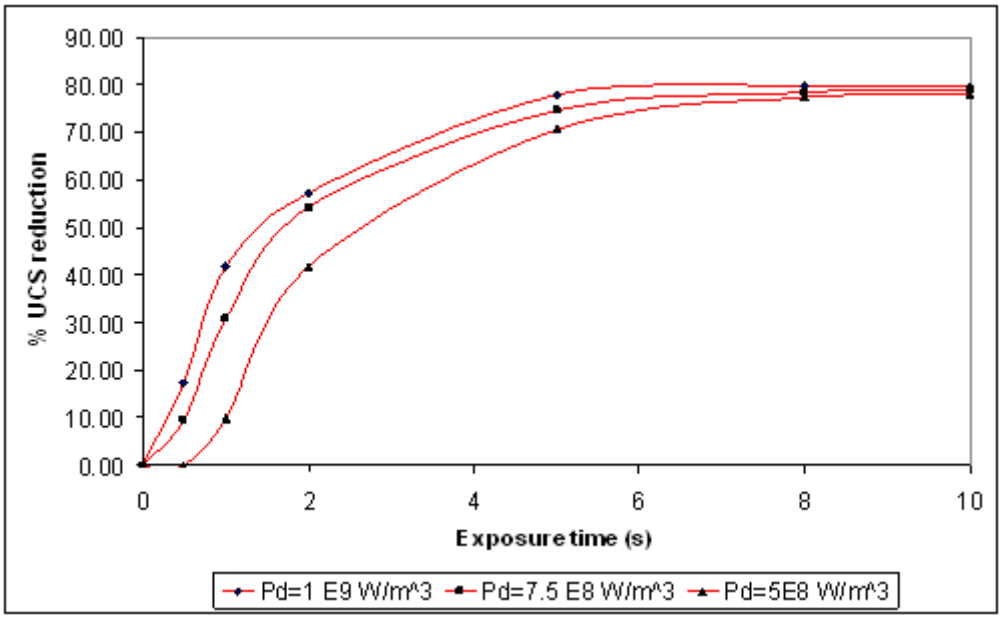

Figure 6.28: Reduction in strength of coarse-grained galena-quartz ore

Figure 6-29 shows the result of simulation of UCS tests of fine-grained galena-quartz. The percentage reduction in strength is also shown in Table 6-7. As can be seen, there were no strength reductions at all power densities below 1 s. However, after 1 s, the pattern seen in the coarse-grained ore was repeated, i.e. higher strength reduction was obtained when the power density was high for the same energy input. For example, it can be seen that at 2 s, more than 24% strength reduction was achieved using power density of 1×10^9 W/m^3 while no strength reduction was obtained at $P_d = 5 \times 10^8$ W/m^3 and less than 5% strength reduction was achieved at $P_d = 7.5 \times 10^8$ W/m^3. Here also, it is evident that once the ore reached the maximum strength reduction, increasing the exposure time did not make any significant change in strength. The possible reason for this has already been discussed in Section 6.1 and is not repeated here.

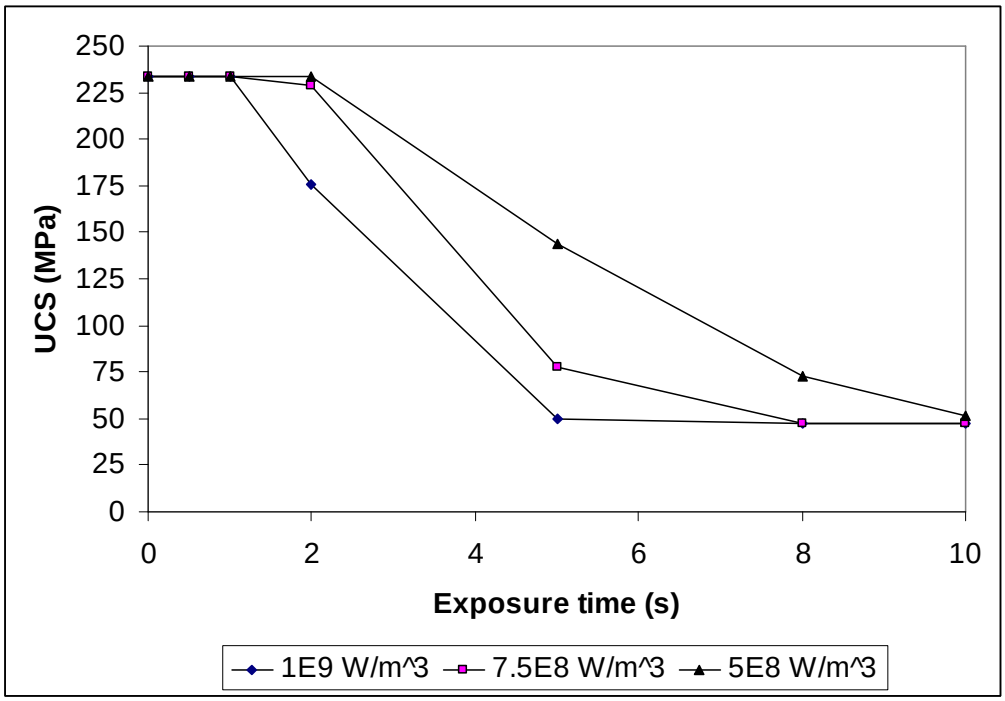

Figure 6.29: Unconfined compressive strength of fine-grained galena-quartz, treated at different power densities

Table 6-7: Strength reduction of fine-grained galena-quartz, treated at different power densities

Power density (W/m^3)	**(untreated) (%)**	**0.5 s (%)**	**1 s (%)**	**2 s (%)**	**5 s (%)**	**8 s (%)**	**10 s (%)**
1×10^9	0.00	0.00	0.85	24.79	78.63	79.91	79.91
7.5×10^8	0.00	0.00	0.00	2.14	66.88	79.70	79.91
5×10^8	0.00	0.00	0.00	0.00	38.46	69.02	77.99

In Table 6-8, the results of unconfined compressive strength tests of coarse-grained magnetite-dolomite are shown. Figure 6-30 also shows the percentage strength reductions as a function of power density. It can be seen that for this ore also power density had a considerable effect on strength reduction. However, for this ore the maximum strength reduction was not obtained below 10 s. This is in fact due to its less amenability to microwave treatment as discussed in section 6-1. Nonetheless, here also it can be noted that it is still advantageous to operate at higher power density. For instance, for the same energy input of 5×10^9 J/m^3, the strength reduction obtained at power density of 1×10^9 W/m^3 was 33.6% while 31.8% was obtained at power density of 5×10^8 W/m^3. The increase in strength reduction for the higher power density case for the same energy input can be explained by looking the temperature profiles in Figures 6-31 and 6-32. As can be seen, for the higher power density case, a relatively higher maximum temperature was obtained but more importantly the temperature gradients were higher around the grain boundary regions. Thus, this would increase the thermally induced stresses and the damage incurred in the sample. It can be noted that increasing the exposure time beyond 10 s for this ore could increase the strength reduction, as the maximum strength reduction has not been yet reached, especially for the lower power density case. However, this would significantly increase the energy cost and thus, would not be economical.

Table 6-8: Unconfined compressive strength of coarse-grained magnetite-dolomite treated at different power densities

Power density (W/m^3)	UCS (untreated) (MPa)	UCS 0.5 s (MPa)	UCS 1 s (MPa)	UCS 2 s (MPa)	UCS 5 s (MPa)	UCS 8 s (MPa)	UCS 10 s (MPa)
1×10^9	107.0	100.0	95.0	87.5	71.0	50.0	47.0
7.5×10^8	107.0	101.5	100.0	96.0	86.0	65.5	54.5
5×10^8	107.0	105.0	104.5	97.5	92.0	83.0	73.0

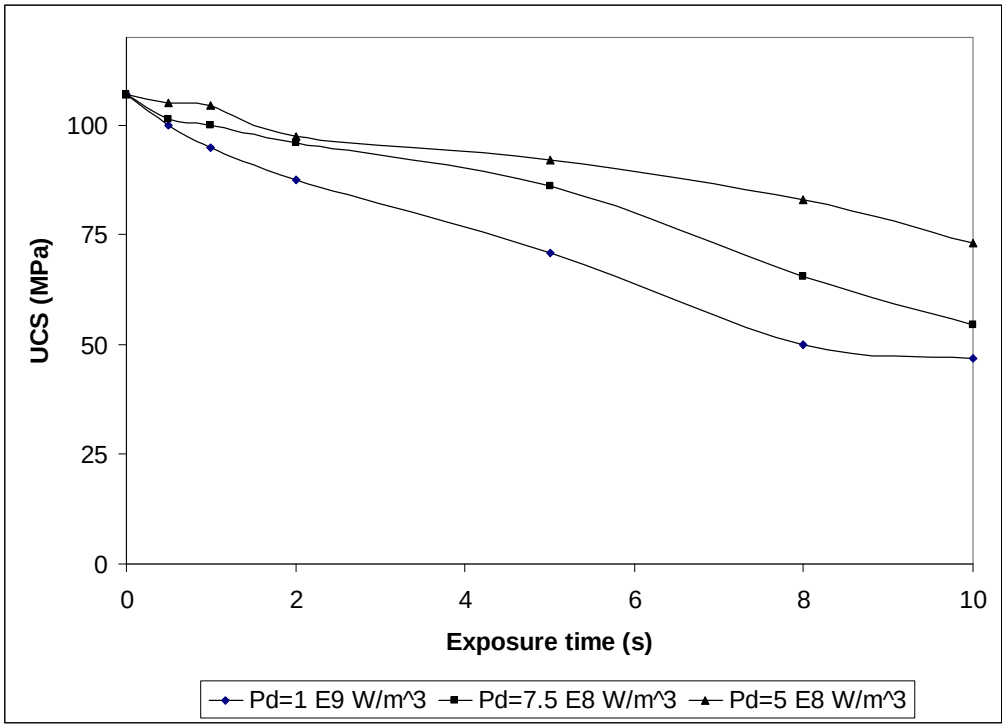

Figure 6.30: Unconfined compressive strength of coarse-grained magnetite-dolomite

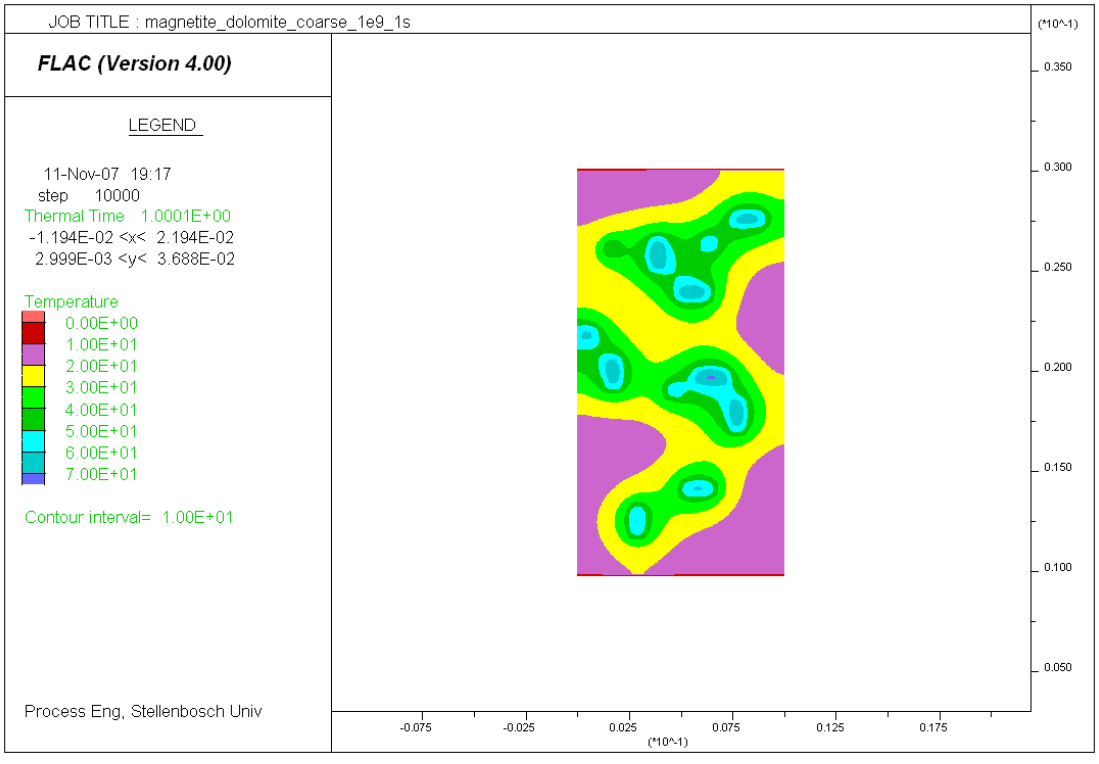

Figure 6.31: Temperature profile in coarse-grained magnetite-dolomite, treated at P_d = 1 $\times 10^9$ W/m^3 for t = 1 s

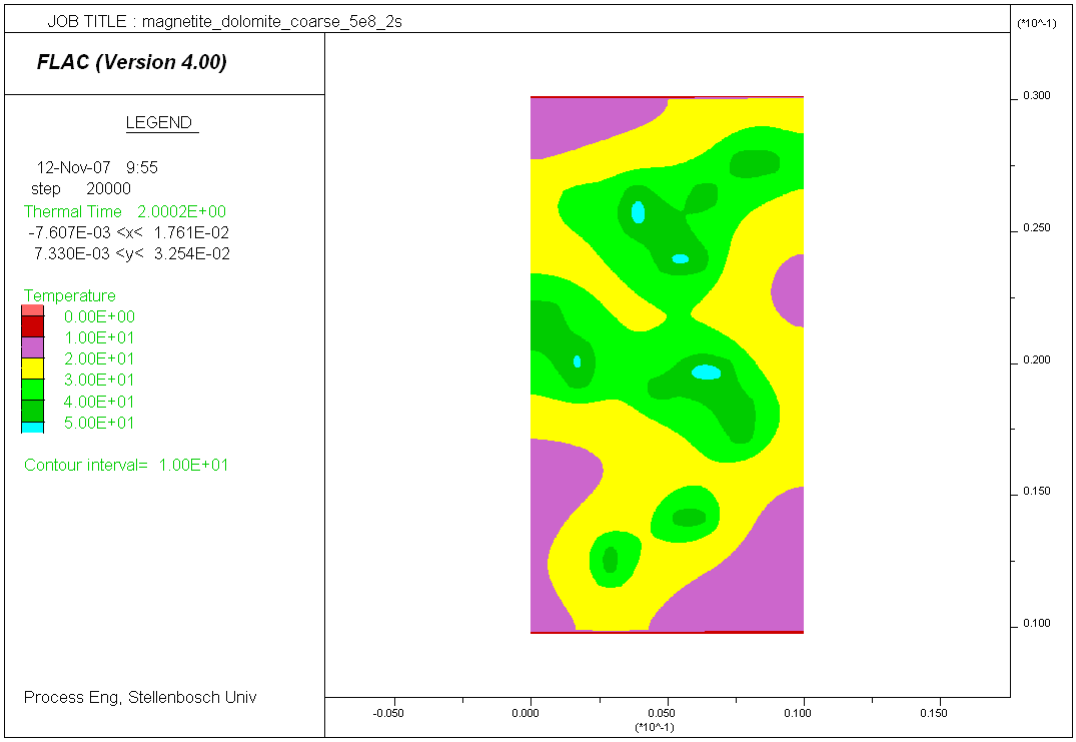

Figure 6.32: Temperature profile in coarse-grained magnetite-dolomite, treated at P_d = 5 $\times 10^8$ W/m^3 for t = 2 s

Figure 6-33 shows the results of simulation obtained for fine-grained magnetite-dolomite treated at different power densities. Here also the trend is repeated, i.e. higher strength reduction was obtained when the power density was high for the same energy inputs. Although the strength reductions obtained here were relatively low, they still indicated that it is beneficial in terms of energy cost to operate at higher power density. For instance, at 1×10^9 W/m^3 and 1 s the strength reduced by 2.5 MPa while at 5×10^8 W/m^3 and 2 s the strength decreased only by 0.5 MPa. The simulation results obtained for different binary ores in general indicated that the effect of power density was significant even for the narrow power density range.

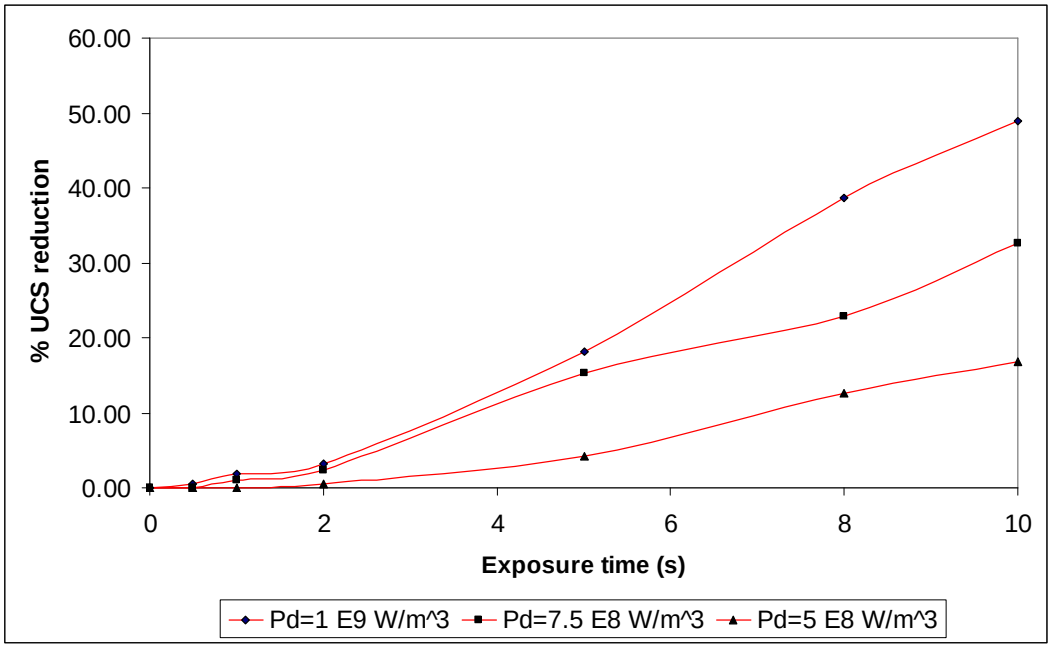

Figure 6.33: Reduction in strength of fine-grained magnetite-dolomite ore (φ= 4889.6), treated at different power densities

6.4.4 Conclusions

The influence of power density on unconfined compressive strength reduction of different microwave treated ores was investigated for a narrow range. It has been shown that strength reduction of microwave treated ores strongly depends on the applied power density. It was illustrated that by increasing the power density dissipated in the absorbent phase, a higher bulk strength reduction of ore could be achieved for the same energy input. The practical implication of the results of this study is that any microwave applicators intended to be used for microwave treatment of ores should be designed both for high power density and uniform treatment (electric field) as much as possible, as it has been shown a slight difference in power density can cause a significant variation on the damage incurred in the particles.

6.5 Influence of Absorbent Phase Modal Area on Strength Reduction of Microwave Treated Ores

6.5.1 Introduction

Thus far, all simulations were carried out by using a composition of 10% microwave absorbent phase and 90% transparent matrix assuming this to be a typical composition of common ores. However, it was necessary to show how the strength reduction of ores affected by the composition of the heated phase. Accordingly, this section details a study designed to examine the influence of microwave absorbent phase modal area on strength reduction of ores.

6.5.2 Methodology

Two fine-grained binary ores, namely galena-quartz and magnetite-dolomite were used for the study. Four different textures having absorbent phase modal areas of 5, 10, 20, and 50% were constructed for each binary ore by disseminating the absorbent phase randomly in the transparent phase according to the required composition. The textures are shown in Figure 6-34 for clarity. One simulation was carried out by varying the percentage of microwave absorbent phase in a single binary ore using the same power density. For this case, all ores were exposed to microwave heating at a fixed power density of 1×10^9 W/m^3 for 0.5, 1, 2, 5, 8, 10 s. Another simulation was undertaken by varying the percentage of the absorbent phase while fixing the energy input; hence, different power densities were used. In both simulations, the ores were subjected to unconfined compressive strength testing after heating.

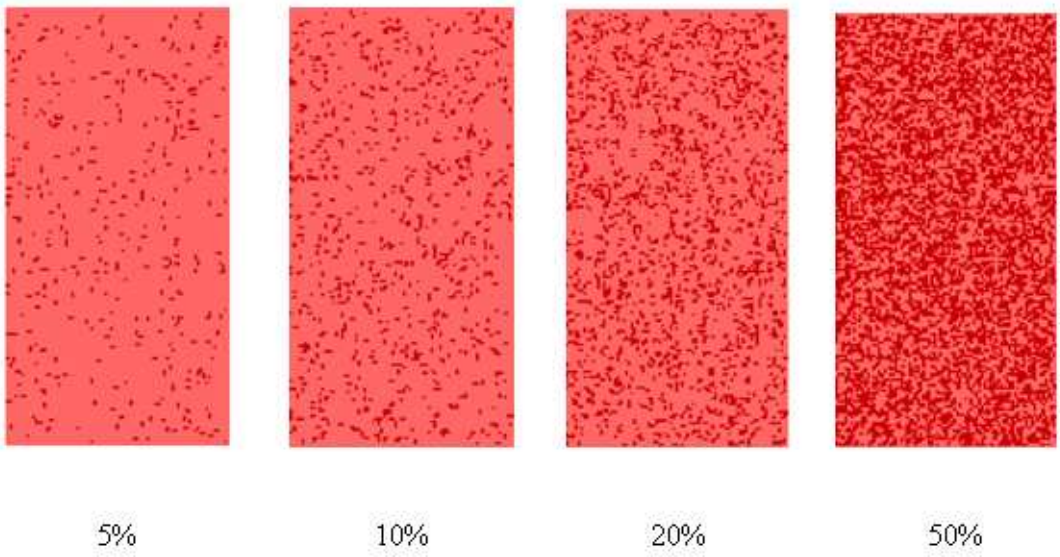

Figure 6.34: Representation of binary ores with different microwave absorbent phase modal areas

6.5.3 Results and Discussion

The results of simulation of unconfined compressive strength tests obtained for galena-quartz treated at fixed power density are shown in Table 6-9 and Figure 6-35. It can be seen that a much more rapid strength reduction was obtained when the absorbent modal area was high. For instance, at 0.5 s, 68.6% strength reduction was achieved by the ore with 50% absorbent modal area while no strength reductions were obtained for the ores with 20, 10 and 5% modal area. Further, at 1 s the strength reduction for 50 and 20% absorbent area were 80.7 and 26.8%, respectively while no strength reductions were obtained for the ores with 10 and 5% absorbent modal area.

However, it should be noted that as the absorbent modal area increases for the same power density, the energy input to the ores becomes higher. The temperature profiles results shown in Figures 6-36 to 6-39 also confirmed this situation. Thus, theoretically the results obtained were as expected.

Table 6-9: UCS of galena-quartz of different absorbent modal areas, treated at P_d = 1 × 10^9 W/m^3

Absorbent phase modal area (%)	UCS (untreated) (MPa)	UCS 0.5 s (MPa)	UCS 1 s (MPa)	UCS 2 s (MPa)	UCS 5 s (MPa)	UCS 8 s (MPa)	UCS 10 s (MPa)
5	232.5	232.5	232.5	232.5	144.5	76.5	50.5
10	232.0	232.0	232.0	176.0	50.0	46.5	46.5
20	235.0	235.0	172.0	65.0	46.5	46.5	46.5
50	240.5	75.5	46.5	46.5	46.5	46.5	46.5

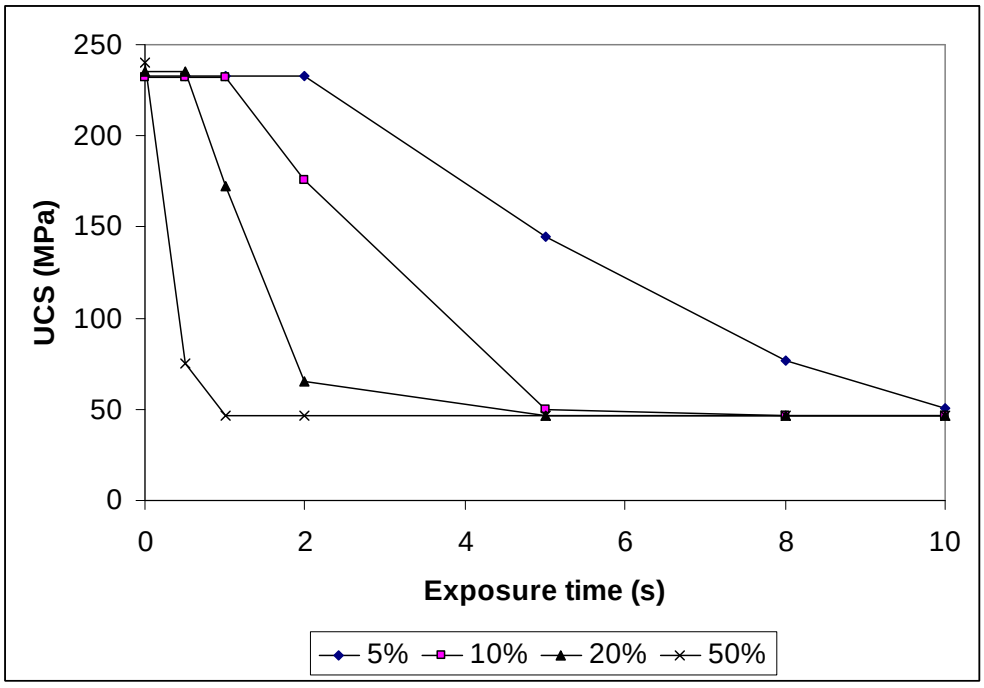

Figure 6.35: UCS of galena-quartz of different absorbent modal areas, treated at P_d = 1 × 10^9 W/m^3

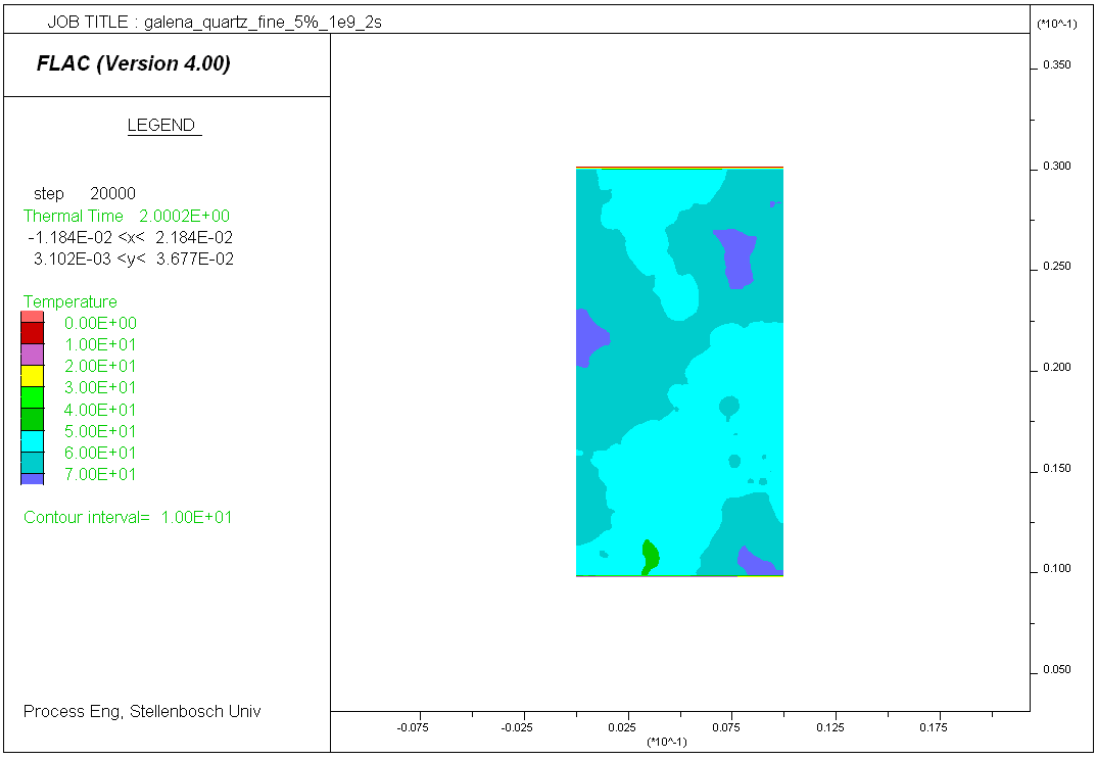

Figure 6.36: Temperature profile in galena-quartz, fine-grained, 5% absorbent phase, treated at $P_d = 1 \times 10^9$ W/m^3 for t = 2 s

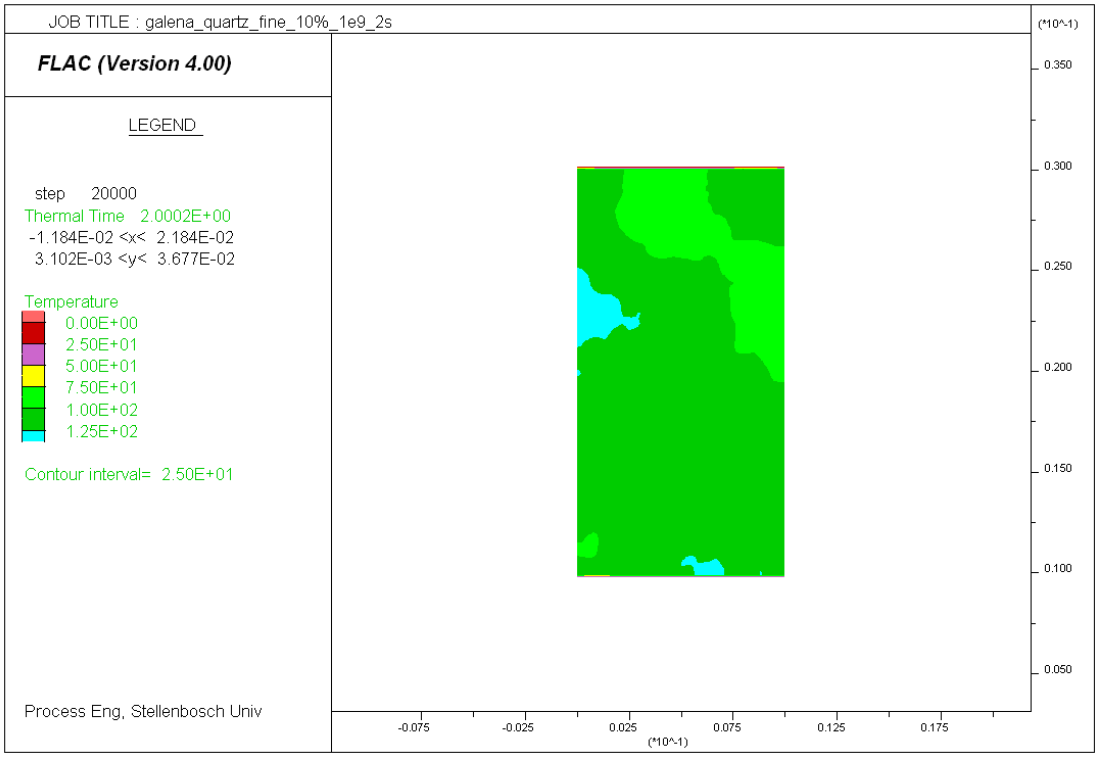

Figure 6.37: Temperature profile in galena-quartz, fine-grained, 5% absorbent phase, treated at $P_d = 1 \times 10^9$ W/m^3 for t = 2 s

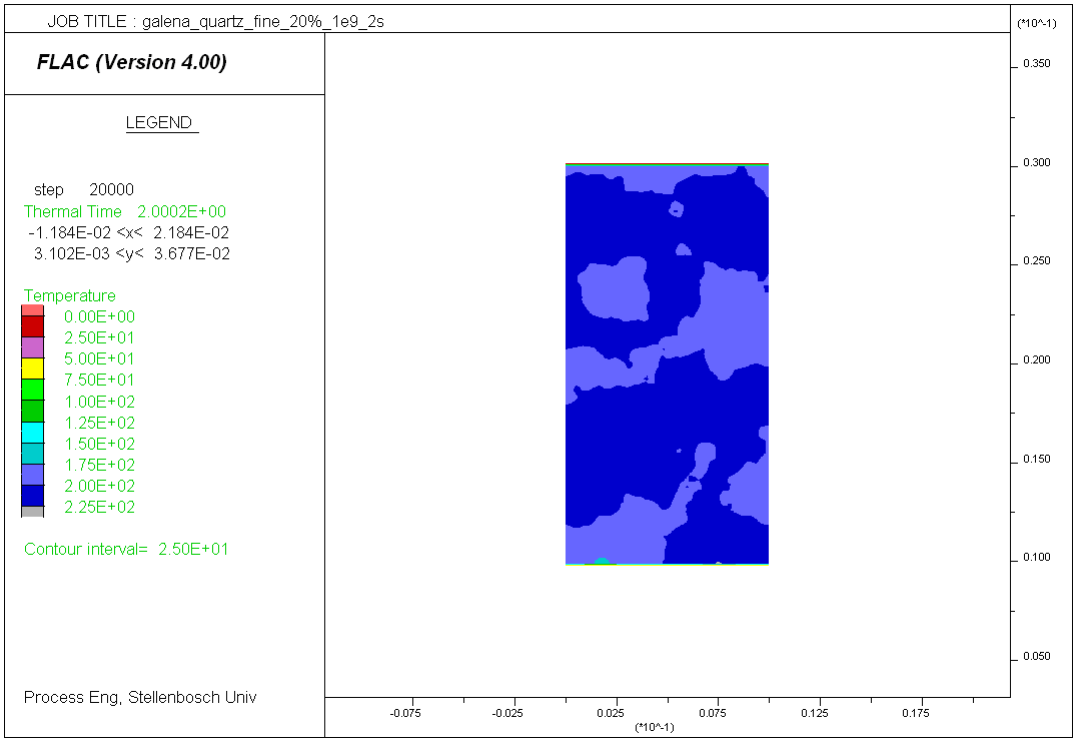

Figure 6.38: Temperature profile in galena-quartz, fine-grained, 20% absorbent phase, treated at $P_d = 1 \times 10^9$ W/m^3 for t = 2 s

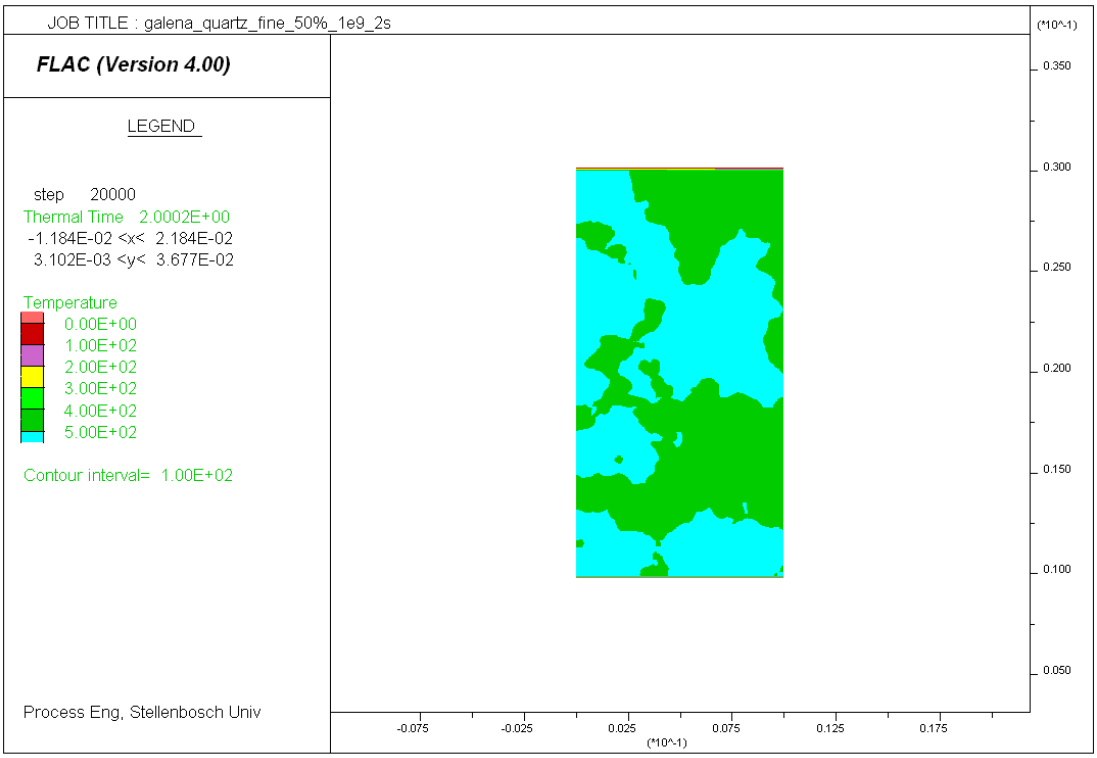

Figure 6.39: Temperature profile in galena-quartz, fine-grained, 50% absorbent phase, treated at $P_d = 1 \times 10^9$ W/m^3 for t = 2 s

Table 6-10 and Figure 6-40 show the result of simulation of unconfined compressive strength tests for magnetite dolomite of different textures treated at the same power density. It can be seen that the trend observed for galena-quartz is also repeated here, i.e. as the absorbent modal area increases, the strength reduction becomes higher. However, the extents of strength reductions were not the same. For instance, at 0.5 s, only 10.6% strength reduction was obtained for magnetite-dolomite with 50% absorbent modal area. Nonetheless, the results still clearly show that higher strength reduction was achieved when the absorbent phase modal area was higher.

It can be noted that depending on the mineralogy and texture of the ore a certain energy input per unit volume of the ore should be dissipated in order to obtain a significant strength reduction. For instance, for the magnetite-dolomite ore considered here with 50% absorbent modal area the energy input needed was 2.5×10^8 J/m^3 of the ore (5×10^8 J/m^3 of the absorbent phase).

Table 6-10: UCS of magnetite-dolomite of different absorbent modal area, treated at P_d = 1×10^9 W/m^3

Absorbent phase modal area (%)	UCS (untreated) (MPa)	UCS 0.5 s (MPa)	UCS 1 s (MPa)	UCS 2 s (MPa)	UCS 5 s (MPa)	UCS 8 s (MPa)	UCS 10 s (MPa)
5	106.5	106.5	106.5	106.5	103.5	97.5	91.0
10	107.5	107.5	105.5	104.0	88.0	66.0	55.0
20	109.5	106.5	96.5	89.0	54.0	32.0	31.0
50	103.5	92.5	80.0	48.5	29.5	29.5	29.5

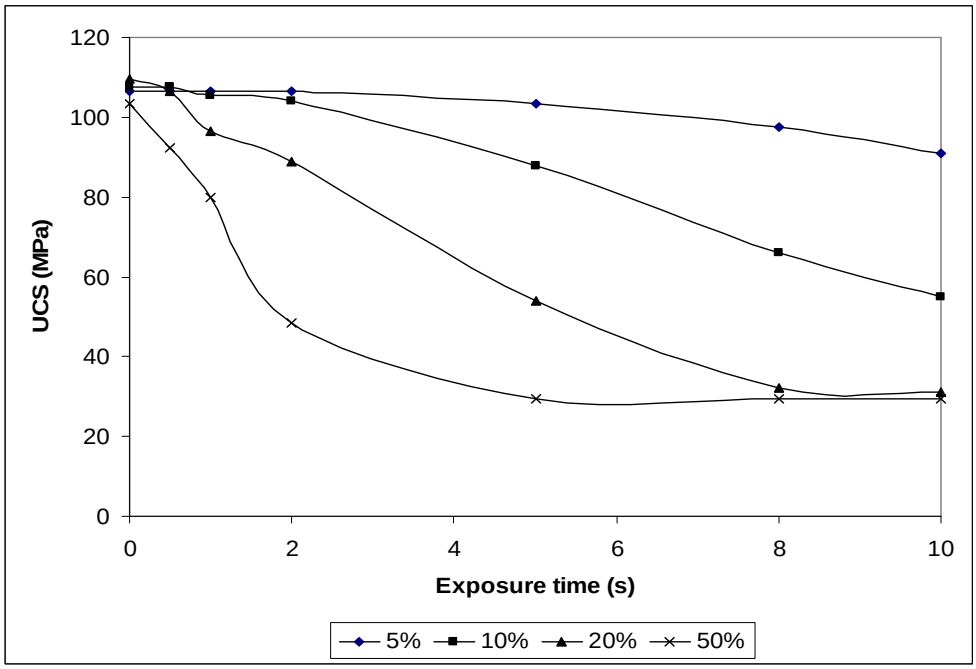

Figure 6.40: UCS of magnetite-dolomite of different absorbent modal areas, treated at $P_d = 1 \times 10^9$ W/m^3

The simulation results obtained by fixing the energy input while varying the absorbent phase modal area for galena-quartz are shown in Table 6-11 and Figure 6-41. As can be seen, there were no strength reductions in all textures up to 2 s. However, after 2 s, significant strength reductions were observed in all ores. It can be seen that for the same energy input, the ore with 50% absorbent modal area achieved much higher strength reduction than the other ores. This would suggest that there is a direct relation between strength reduction and absorbent modal area percentage. However, a relatively higher strength reduction was obtained for the ore with 5% absorbent phase modal area than the ore with 10%.

Table 6-11: UCS of galena-quartz of different absorbent modal areas, treated at the same energy input

Power density (W/m^3)	Absorbent phase modal area (%)	UCS (untreated) (MPa)	UCS 0.5 s (MPa)	UCS 1 s (MPa)	UCS 2 s (MPa)	UCS 3 s (MPa)	UCS 4 s (MPa)	UCS 5 s (MPa)
2×10^9	5	236.0	236.0	236.0	161.0	100.5	60.0	47.0
1×10^9	10	232.0	232.0	232.0	176.0	107.0	70.5	50.0
5×10^8	20	236.0	236.0	236.0	149.0	86.5	62.0	48.0
2×10^8	50	240.0	240.0	240.0	141.0	55.0	50.0	46.5

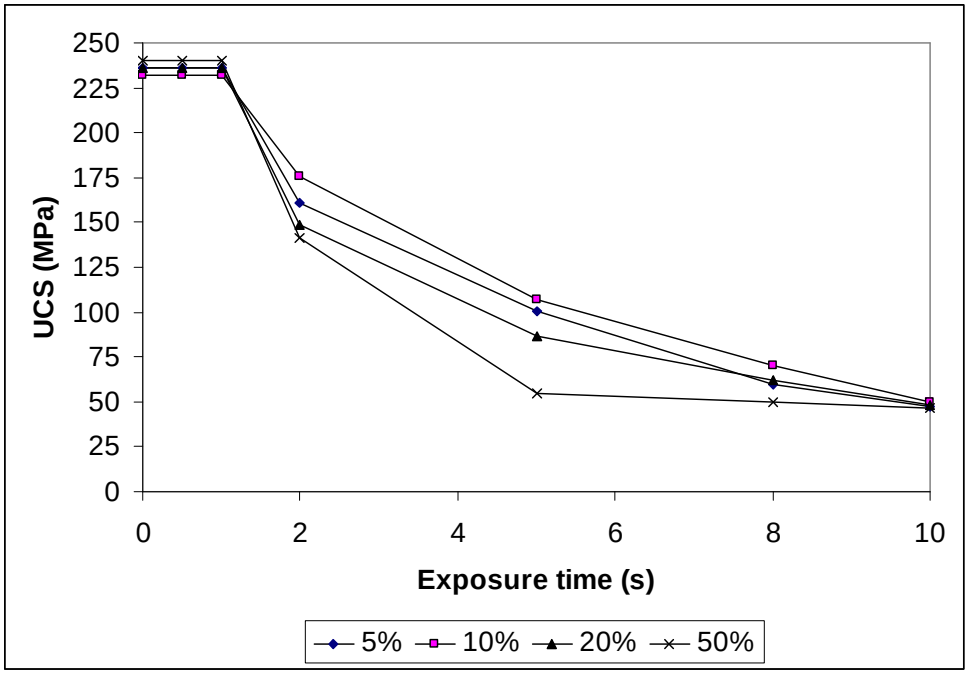

Figure 6.41: UCS reduction of galena-calcite of different absorbent modal areas for the same energy input

Table 6-12 and Figure 6-42 show the result of simulations of magnetite-dolomite when the energy input was fixed and the absorbent modal area was varied. As can be seen, there were no any significant difference in strength reductions of the ores with absorbent modal area of 5, 10 and 20%. However, for the ore with 50% absorbent modal area a slightly higher strength reduction was obtained at all exposure times.

In general, the results suggest a direct relation between absorbent modal area and strength reduction even for the same energy inputs. However, a more detail investigation is needed in order to obtain a full understanding of the effect, particularly when the absorbent modal area is below 10%.

Table 6-12: UCS of magnetite-dolomite of different absorbent modal areas, treated at the same energy input

Power density (W/m^3)	**Absorbent phase modal area (%)**	**UCS (untreated) (MPa)**	**UCS 0.5 s (MPa)**	**UCS 1 s (MPa)**	**UCS 2 s (MPa)**	**UCS 5 s (MPa)**	**UCS 8 s (MPa)**	**UCS 10 s (MPa)**
2×10^9	5	107.0	107.0	104.5	102.5	88.0	67.0	56.0
1×10^9	10	107.5	107.5	105.5	104.0	88.0	66.0	55.0
5×10^8	20	109.5	109.5	108.0	103.5	86.5	66.0	54.5
2×10^8	50	103.0	103.0	101.5	95.5	79.5	62.5	49.0

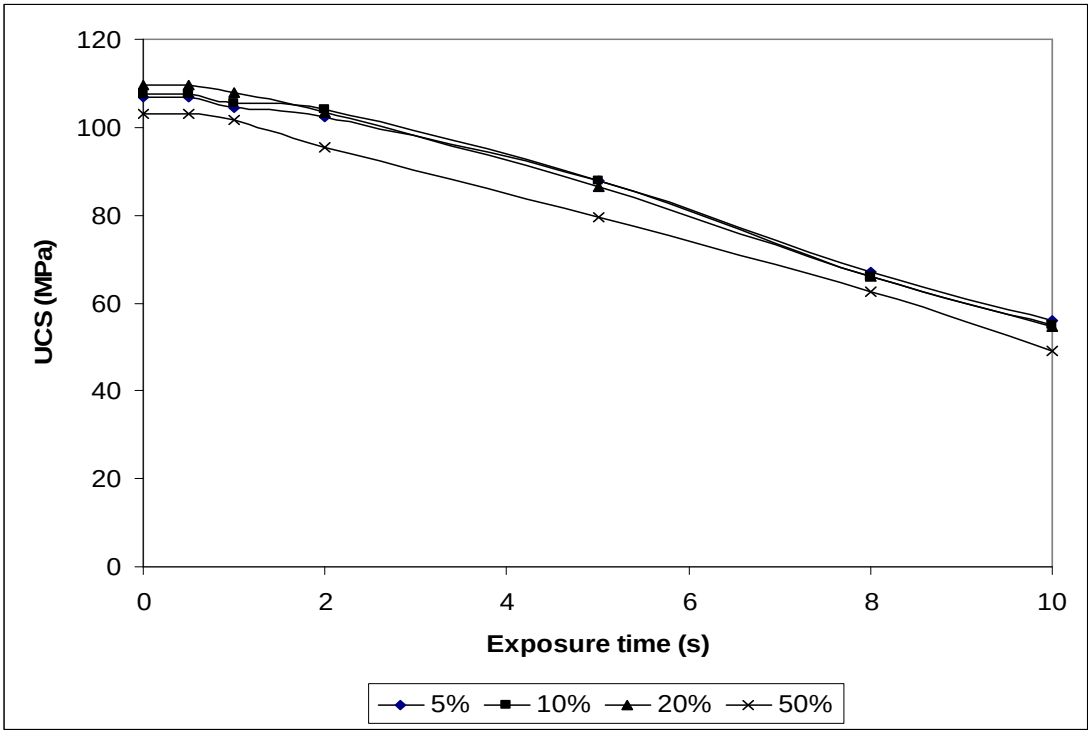

Figure 6.42: UCS reduction of magnetite-dolomite of different absorbent modal areas for the same energy input

6.5.4 Conclusions

The effect of absorbent phase modal area on strength reduction of microwave treated ores was investigated for two cases. The results obtained by fixing the power density indicated a higher strength reduction for the ores with higher absorbent modal area. However, it should be noted that as the absorbent modal area increases for the same power density, the energy input to the ore becomes higher. The results obtained by fixing the energy input also indicated in general a relatively higher strength reduction for the ore with high absorbent modal area.

In a real applicator, for a fixed microwave power and mineralogy, the power density dissipated in the ore sample depends on the fraction of absorbent phase. It is apparent that for the same electromagnetic properties, higher power density will be dissipated in the ore with smaller fraction of absorbent phase. However, as the fraction of the absorbent phase decreases for the same mineralogy, the effective loss factor of the ore will reduce, which lowers the power density.

6.6 Influence of Absorbent Phase Dissemination on Strength Reduction of Microwave Treated Ores

6.6.1 Introduction

It has been previously suggested that the degree of dissemination of the absorbent phase in an ore has an influence on the extent of damage incurred in microwave treated ore (Kingman et al., 2000). However, quantification of this effect exclusively by experiment is very difficult. Accordingly, this section details the study carried out for investigating the effect of microwave absorbent phase dissemination on strength reduction of ores. The simulation results obtained for three different textures (low to high dissemination), each having the same absorbent modal area and treated at the same condition are presented.

6.6.2 Methodology

Different textures were constructed by placing four 1 mm absorbent grains (galena for galena-quartz and magnetite for magnetite-dolomite) in the transparent matrix at different positions. The first ore consisted of four absorbent grains, which were placed with 1 mm horizontal difference and 2 mm vertical difference. The second ore also consisted of four absorbent grains, which were placed at 2 mm horizontal difference and 4 mm vertical difference. The last ore (highly disseminated case) consisted also four absorbent grains but they were placed in 4 mm horizontal difference and 8 mm vertical difference. The total particle size for all ores was 10×20 mm. The ores are shown in Figure 6-32 for clarity.

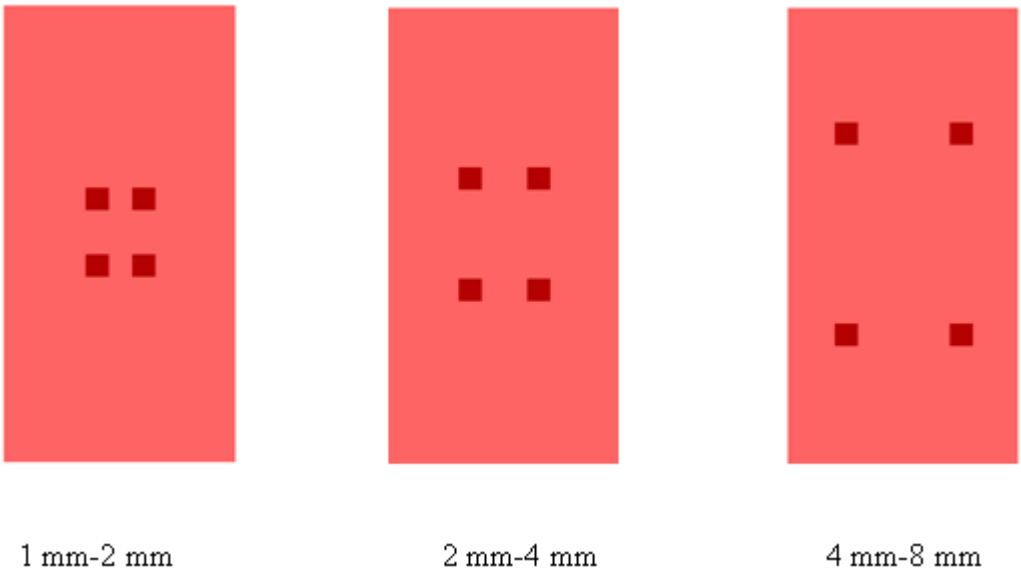

Figure 6.43: Representation of binary ore with different absorbent phase disseminations

The ores were then exposed to microwave heating at power density of 1×10^9 W/m^3 for 0.5 s to 10 s. After heating, the ores were subjected to an unconfined compressive strength test. A similar simulation was also repeated for magnetite-dolomite ore.

6.6.3 Results and Discussion

The results of simulation of unconfined compressive strength test obtained for galena-quartz are shown in Table 6-13 and Figure 6-44. The percentage reductions in strength are also shown in Figure 6-45. It can be seen that there were no strength reductions for all textures up to 2 s. However, after 2 s, a much higher strength reduction was obtained for the ore with poorly disseminated heated phase (1 mm - 2 mm difference). For instance, at 5 s, 43% strength reduction was obtained for the poorly disseminated case while there was no strength reduction for the highly disseminated case. The trend is repeated at all exposure times. It is apparent that a higher energy input is needed for the highly disseminated case in order to obtain a significant strength reduction even if it was composed of the same minerals and also had the same absorbent modal area.

Table 6-13: Strength of galena-quartz for different absorbent phase disseminations, treated at $P_d = 1 \times 10^9$ W/m^3

Dissemination (mm)		UCS (untreated)	UCS 0.5 s	UCS 1 s	UCS 2 s	UCS 5 s	UCS 8 s	UCS 10 s
X	Y	(MPa)	(MPa)	(MPa)	(MPa)	(MPa)	(MPa)	(MPa)
1	2	234.0	234.0	234.0	206.5	133.0	112.0	89.0
2	4	230.0	230.0	230.0	230.0	191.0	141.5	124.0
4	8	222.5	222.5	222.5	222.5	222.5	188.0	156.5

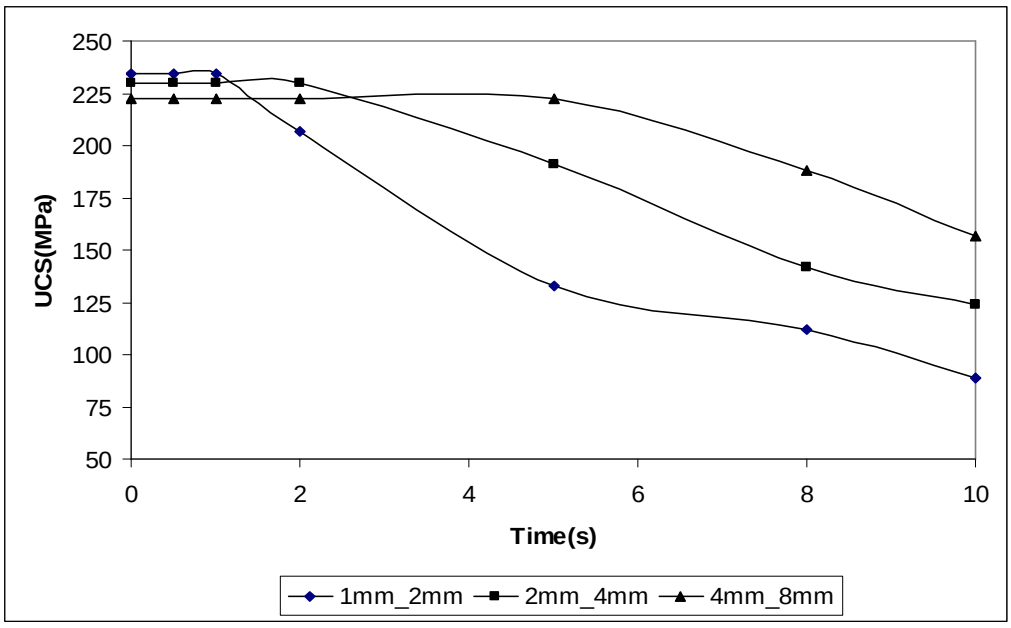

Figure 6.44: UCS of galena-quartz for different absorbent phase disseminations, treated at $P_d = 1 \times 10^9$ W/m^3

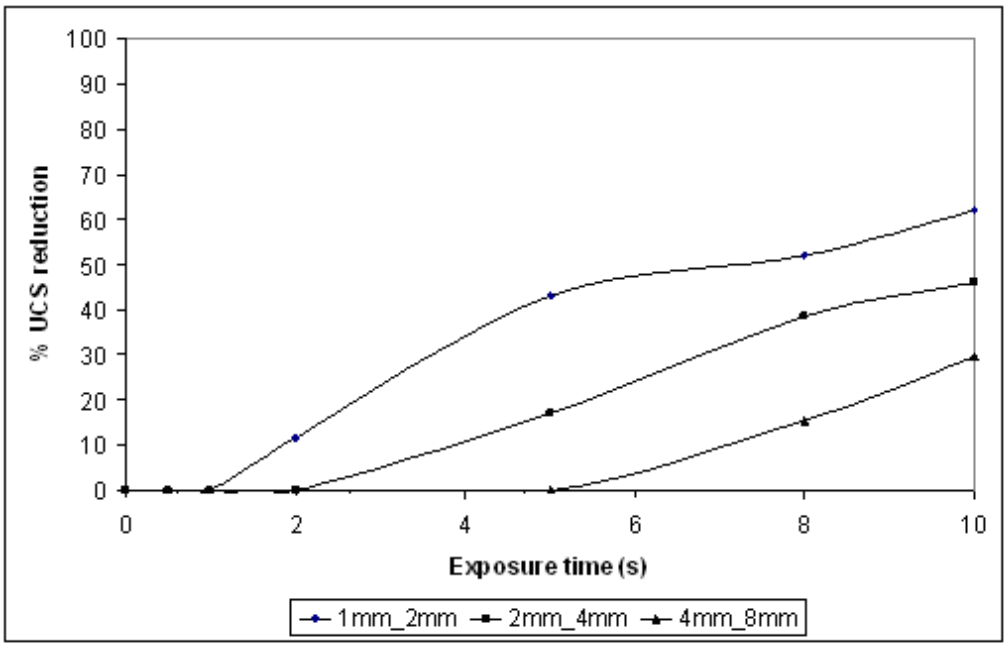

Figure 6.45: Reduction in strength of galena-quartz for different absorbent phase disseminations, treated at $P_d = 1 \times 10^9$ W/m^3

The possible reason for this is that when the microwave absorbent grains are far way from each other, they would lose heat more rapidly to the adjacent transparent matrix. In other words, they will not retain heat longer like the one with poor dissemination. This can be also confirmed by looking at the temperature profiles obtained for the ores. As can be seen from Figures 6-46 to 6-48, the maximum temperature achieved by the ore with poorly disseminated absorbent phase was higher. Further, it can be seen that the temperature gradients were much higher around the grain boundary for the ore with poorly disseminated heated phase. As a result, a greater thermally induced stresses will occur in the ore with poorly disseminated heated phase, which will result in a higher strength reduction.

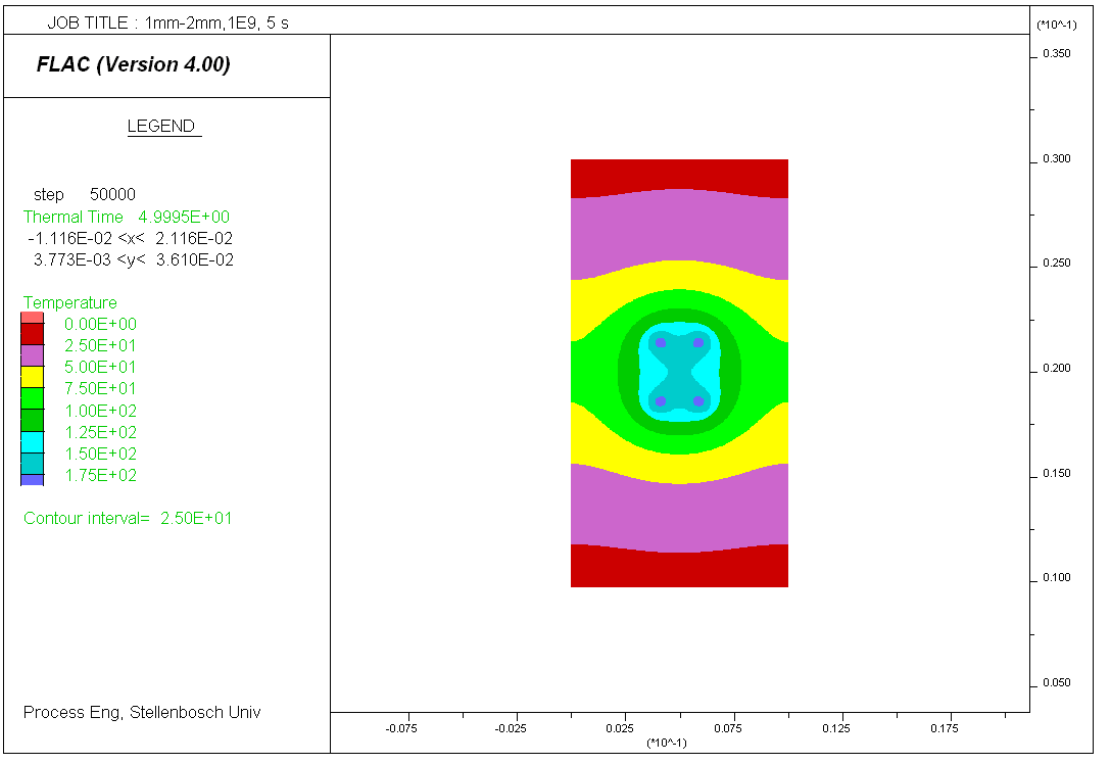

Figure 6.46: Temperature profile in galena-quartz for poorly disseminated case (1 mm - 2 mm) treated at $P_d = 1 \times 10^9$ W/m^3 for 5 s

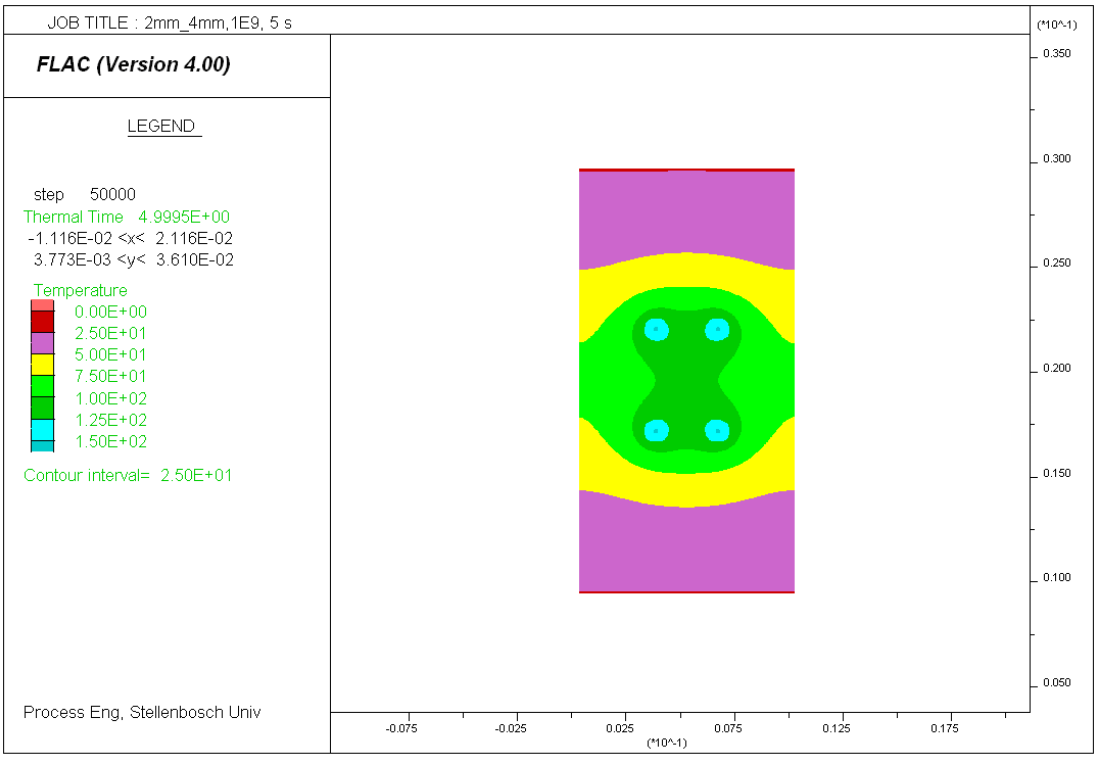

Figure 6.47: Temperature profile in galena-quartz for fairly disseminated case (2 mm - 4 mm) treated at $P_d = 1 \times 10^9$ W/m^3 for 5 s

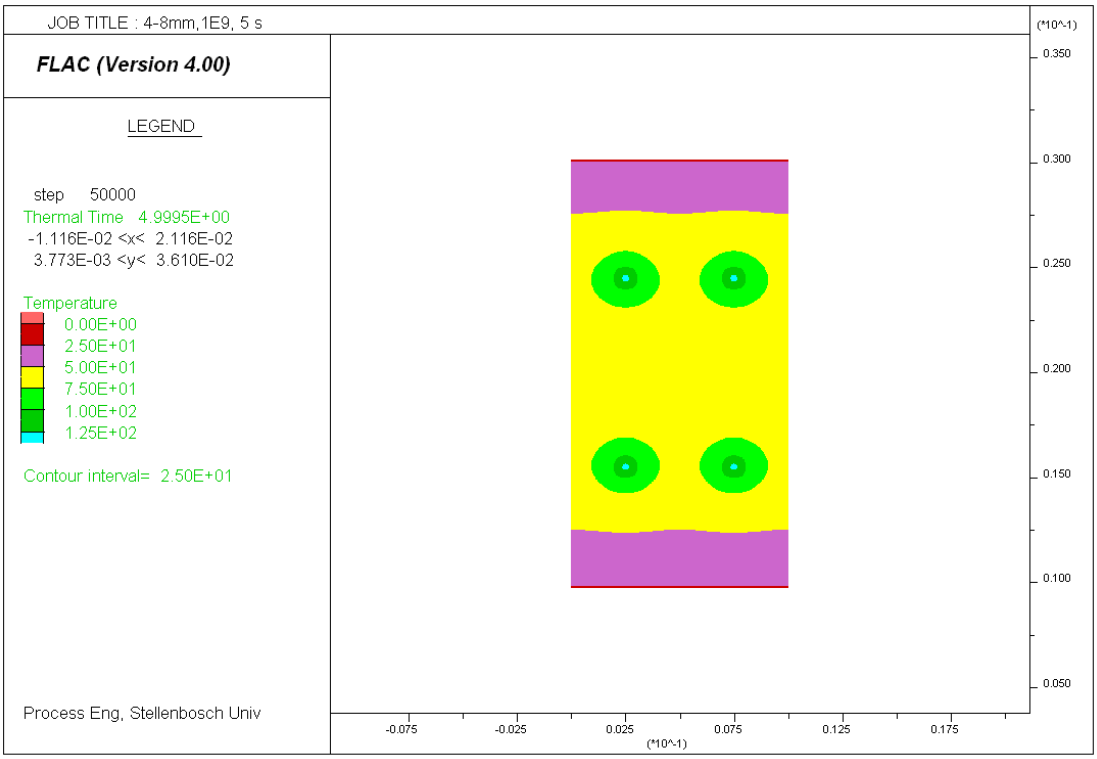

Figure 6.48: Temperature profile in galena-quartz for highly disseminated case (4 mm - 8 mm) treated at $P_d = 1 \times 10^9$ W/m^3 for 5 s

Table 6-14 shows the result of simulation of magnetite-dolomite ore. As can be seen, higher strength reduction here also obtained for ore with poorly disseminated heated phase. For instance, at 10 s, 12.5% strength reduction was obtained for the poorly disseminated case while only 2.5% was obtained for the highly disseminated case.

In general the results indicated that for the same microwave absorbent phase modal area, microwave treatment condition and mineralogy; strength reduction of ore strongly depends on the degree of dissemination of the absorbent (heated) phase in the ore. Binary ores consisted of poorly disseminated absorbent phase achieved much higher strength reduction.

Table 6-14: Strength of magnetite-dolomite for different absorbent phase disseminations treated at $P_d = 1 \times 10^9$ W/m^3

Dissemination (mm)		UCS (untreated)	UCS 0.5 s	UCS 1 s	UCS 2 s	UCS 5 s	UCS 8 s	UCS 10 s
X	Y	(MPa)	(MPa)	(MPa)	(MPa)	(MPa)	(MPa)	(MPa)
1	2	107.0	107.0	107.0	104.5	104.0	97.5	93.5
2	4	107.0	107.0	107.0	106.5	105.5	103.0	98.5
4	8	107.0	107.0	107.0	107.0	106	105.0	104.5

6.6.4 Conclusions

The influence of microwave absorbent phase dissemination on strength reduction of microwave treated ores was examined. It has been shown that for the same mineralogy, absorbent modal area, power density and energy input; strength reduction of ores strongly depends on absorbent phase dissemination. It was shown that ore with poorly disseminated absorbent phase achieved much higher strength reduction while the lowest strength reduction was obtained for the ore with highly disseminated heated phase.

6.7 Effect of Microwave Heating on Mechanical State of an Ore

6.7.1 Introduction

This section details the study undertaken for investigating the effect of microwave treatment on mechanical state of an ore. Investigation of the mechanical state of microwave treated ore was necessary, as the exposure times that were obtained from the UCS simulation, in which a reduction in strength occurred, were very large compared to that were needed for a significant improvement in liberation in experiment[2]. In a typical experiment using 15 kW microwave power, at 2.45 GHz single mode cavity, a significant increase in liberation was observed at exposure time as short as 0.1 s (Kingman et al., 2004). However, in the UCS simulation, an exposure time greater than 2 s was needed for significant strength reduction. Accordingly, the effect of microwave treatment on the mechanical state of the simulated ore particle was examined in order to increase the sensitivity of the simulation and to determine whether UCS is an adequate descriptor of liberation behaviour.

6.7.2 Methodology

Continuum analysis was carried out to understand the patterns of stresses generated inside an ore subjected to microwave at different exposure times. Although continuum analysis does not allow visualization of crack propagation, it provides the distribution of stresses inside an ore for a given microwave treatment condition. The ore used for the study was a medium-grained galena-calcite. The texture is shown in Figure 6-49. The ore was treated at power density of $P_d = 5 \times 10^8$ W/m^3. This power density was assumed to be typical power density in a 15 kW microwave power, 2.45 GHz, single mode cavity currently used for experimentation. The exposure time was started from zero and increased gradually and the mechanical state of the ore at each exposure time was examined. In addition, the unconfined compressive strength of the ore at each mechanical state was also recorded.

[2] These experiments are part of the AMIRA P 879 A Microwave Assisted Comminution and Liberation Project 2007-2009, but are commercially sensitive and may not be reported here.

FLAC indicates the mechanical state of a material by using four different colours. The available states and the specific colours that are used for indicating them are given below:

State	Colours
Elastic	salmon pink
At yield in tension	yellow
At yield in shear or volume	dark red
Elastic, yield in past	purple

“Elastic” corresponds to the state of the intact material without any damage and is indicated by salmon pink colour.

Regions of the material “at yield in tension” or ”at yield in shear or volume” are indicated by yellow and dark red colour, respectively.

“Elastic, yield in past” corresponds to regions where the material has been at yield previously but the stresses at the moment are below the original yield strength of the material and it is indicated by purple colour.

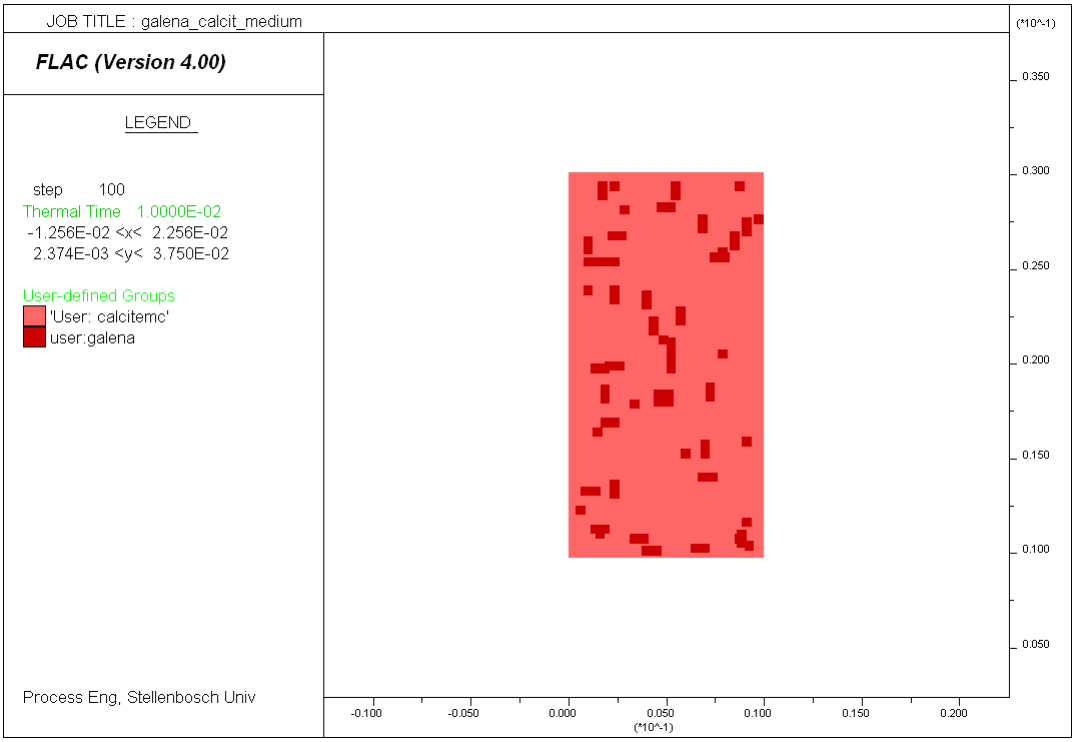

Figure 6.49: Representation of galena-calcite ore, showing the different mineral phases

6.7.3 Results and discussion

Figure 6-50 shows the mechanical state of the ore before microwave treatment. As can be seen, the ore was elastic through out the volume as indicated by salmon pink colour. Figure 6-51 shows the mechanical state of the ore after subjecting it to microwave irradiation for 0.05 s. It can be seen that some of the regions in the vicinity of the grain boundary has been yielded and tensile failure starts to occur even at this short exposure time. Increasing the exposure time to 0.1 s and then to 0.2 s gave rise to a substantial damage as shown in Figures 6-52 and 6-53. This indicates that the thermally induced stresses at these treatment conditions were greater than the tensile strength of the material and are sufficiently large to cause micro-fractures. The mechanical states for the longer exposure times (> 0.5 s) are also shown in Figures 6.54 - 6.57. As can be seen, as the exposure time increases, the region of damage spreads to the bulk of the material. Tensile and shear damage were observed both in the absorbent phase and in the transparent matrix at long exposure times. The unconfined strength of the material at each mechanical state was also recorded and shown in Table 6-15 and Figure 6-58.

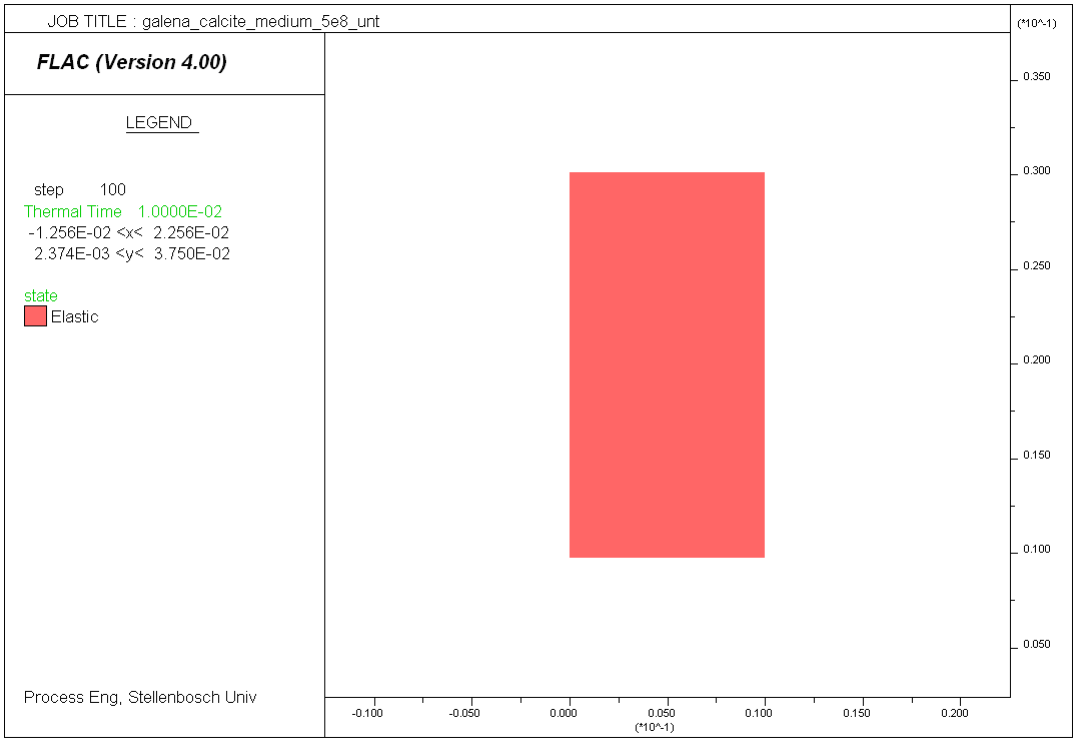

Figure 6.50: Mechanical state of galena-calcite, untreated

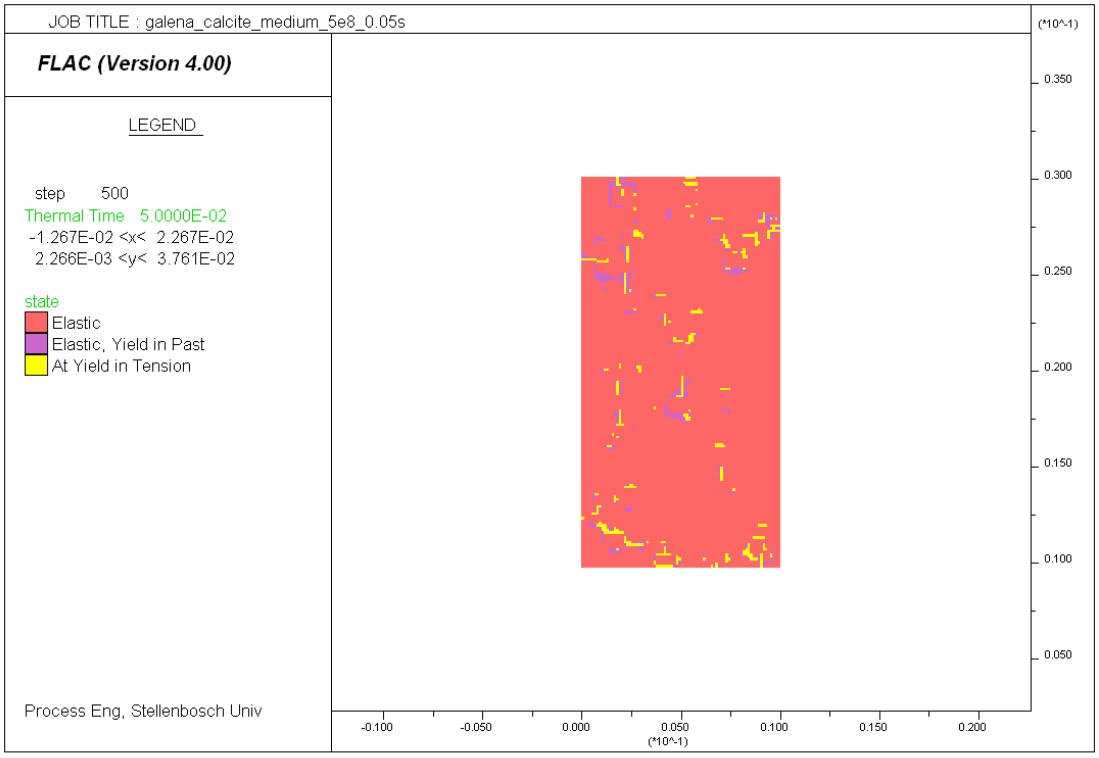

Figure 6.51: Mechanical state of galena-calcite, treated at $P_d = 5 \times 10^8$ W/m^3 for 0.05 s

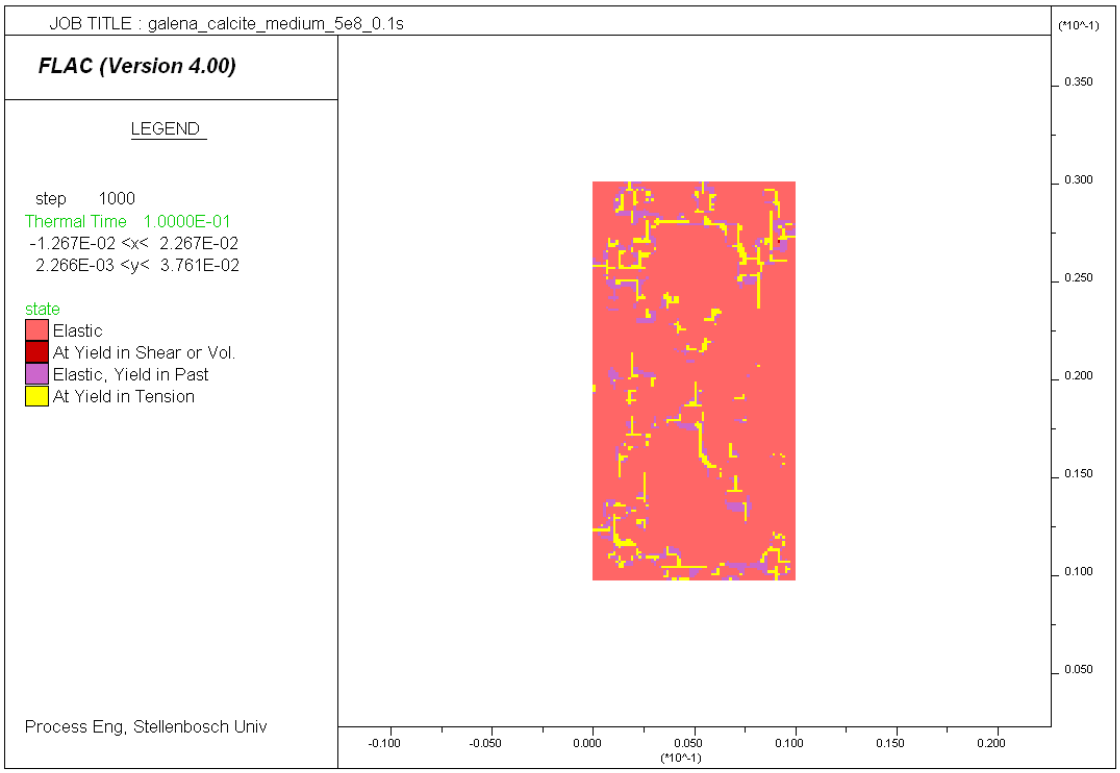

Figure 6.52: Mechanical state of galena-calcite, treated $P_d = 5 \times 10^8$ W/m^3 for 0.1 s

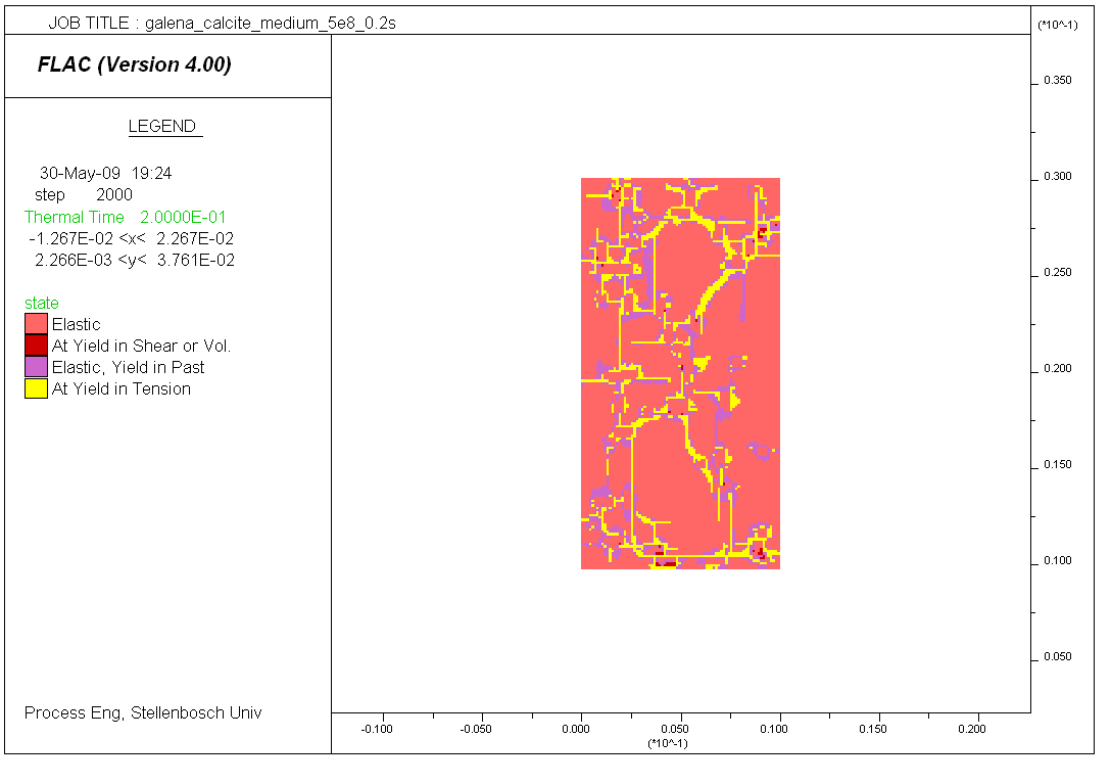

Figure 6.53: Mechanical state of galena-calcite, treated at $P_d = 5 \times 10^8$ W/m^3 for 0.2 s

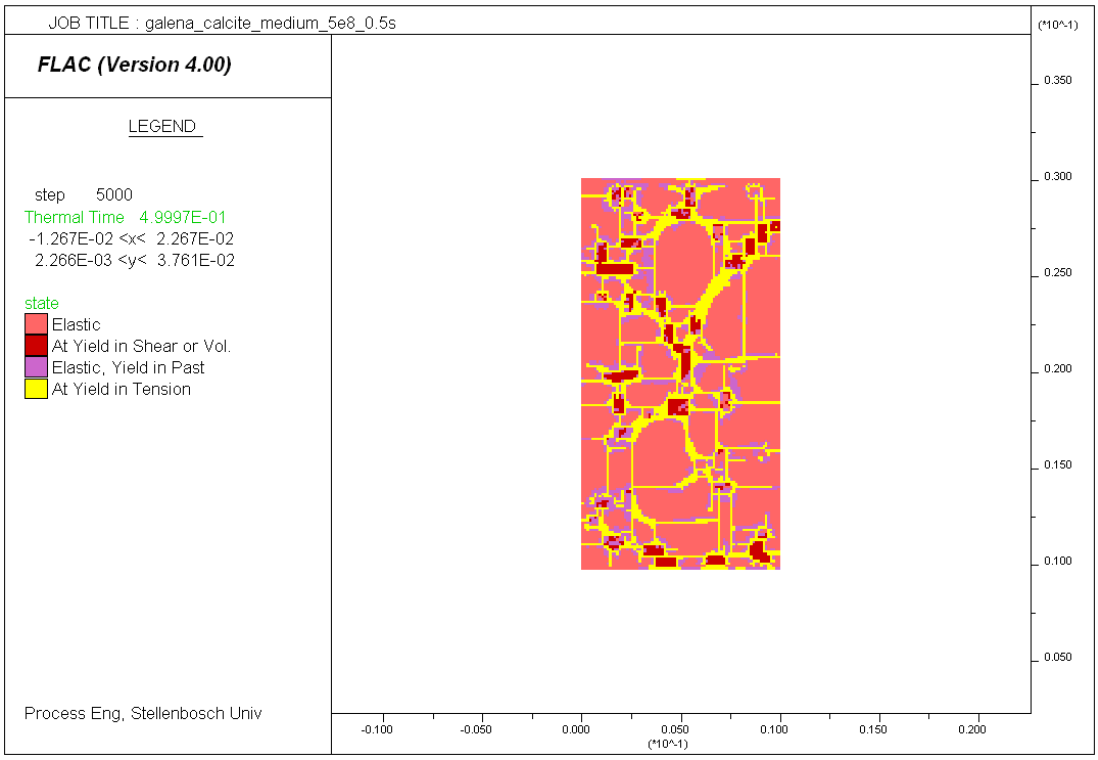

Figure 6.54: Mechanical state of galena-calcite, treated at $P_d = 5 \times 10^8$ W/m^3 for 0.5 s

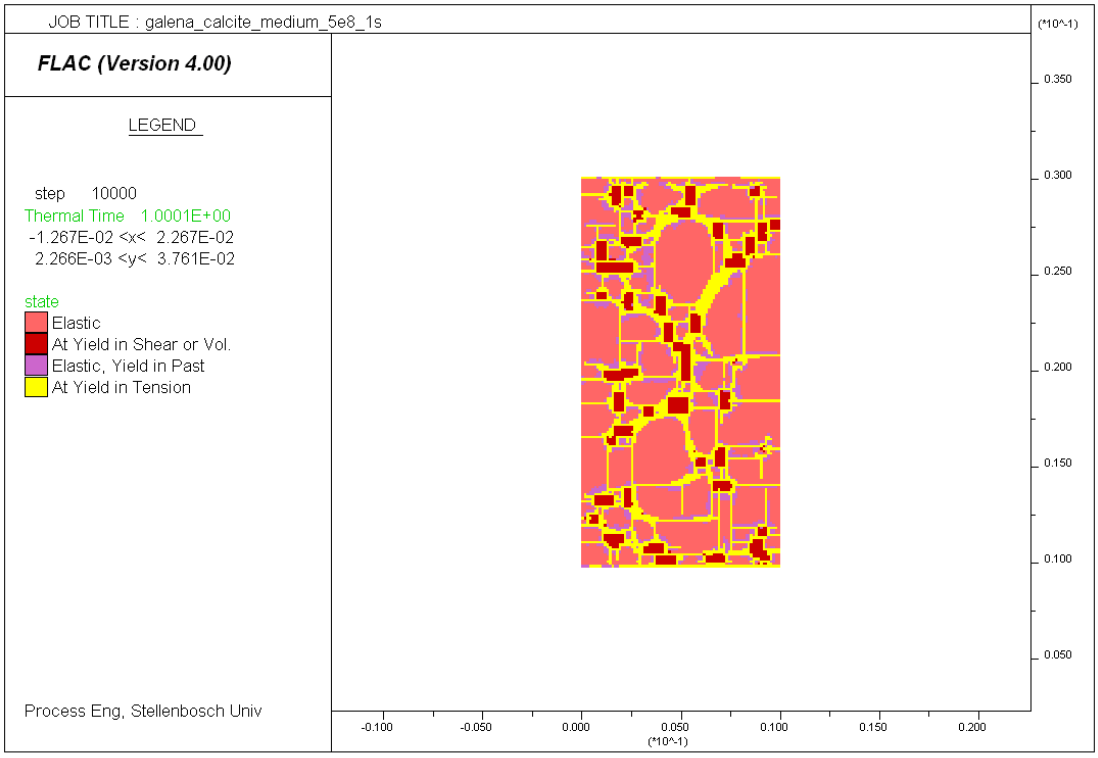

Figure 6.55: Mechanical state of galena-calcite, treated at $P_d = 5 \times 10^8$ W/m^3 for 1 s

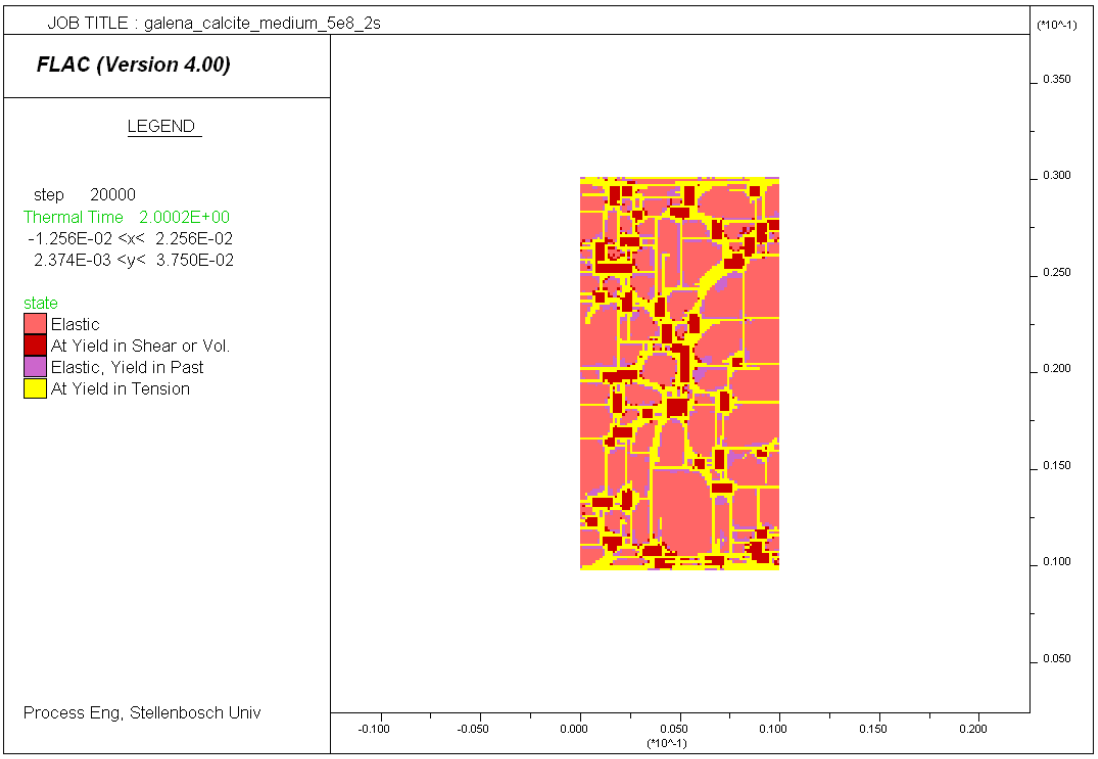

Figure 6.56: Mechanical state of galena-calcite, treated at $P_d = 5 \times 10^8$ W/m^3 for 2 s

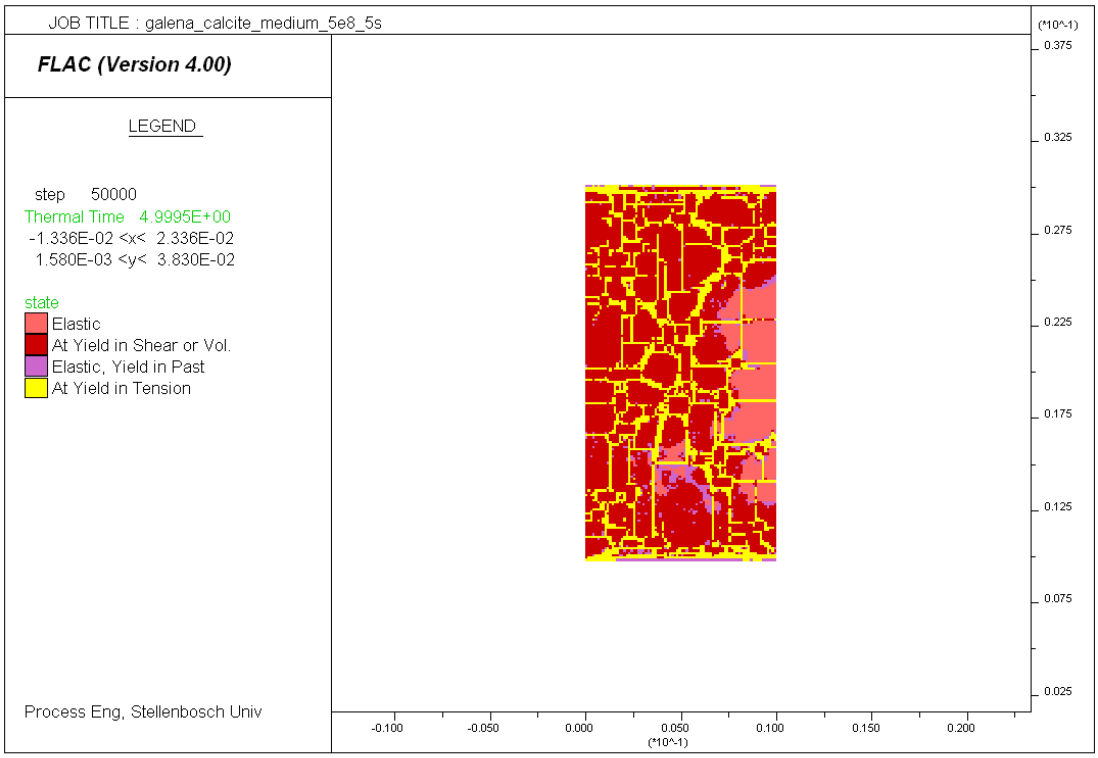

Figure 6.57: Mechanical state of galena-calcite , treated at $P_d = 5 \times 10^8$ W/m^3 for 5 s

Table 6-15: Unconfined compressive strength of galena-calcite treated at $P_d = 5 \times 10^8$ W/m^3 for different exposure times

UCS (untreated) (MPa)	UCS 0.05 s (MPa)	UCS 0.1 s (MPa)	UCS 0.2 s (MPa)	UCS 0.5 s (MPa)	UCS 1 s (MPa)	UCS 2 s (MPa	UCS 5 s (MPa)
139.0	139.0	139.0	139.0	137.5	130.0	112.0	76.5

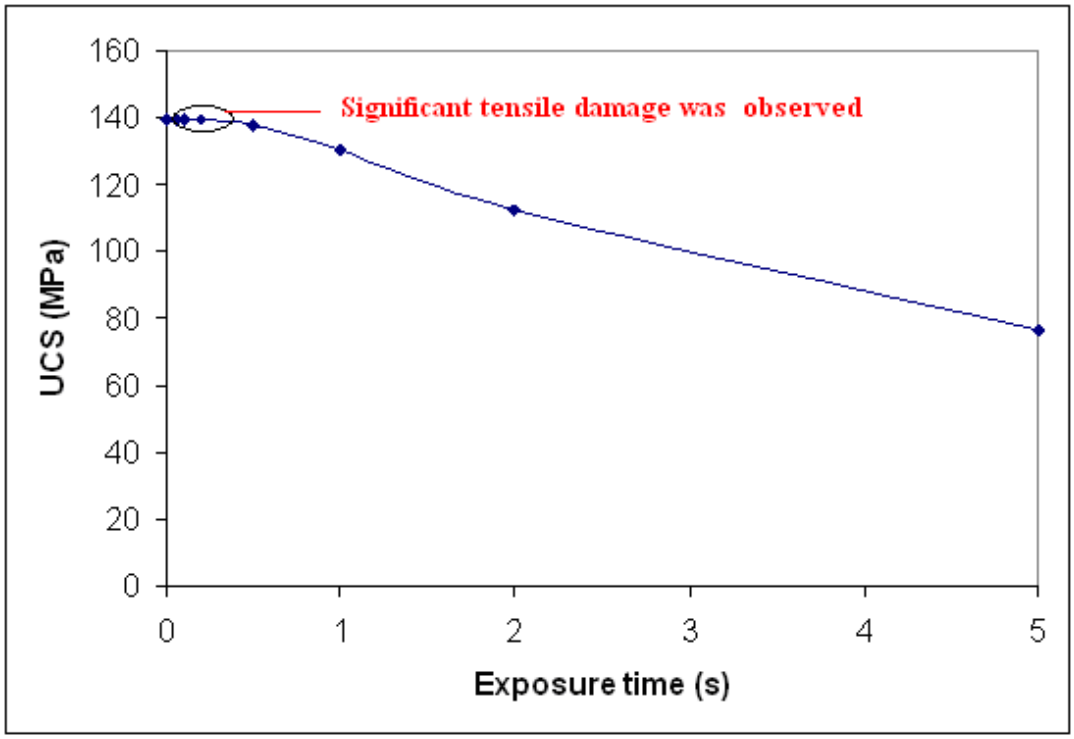

Figure 6.58: Unconfined compressive strength versus microwave treatment time

It can be seen from Table 6-15 and Figure 6-58 that there was no change in the unconfined compressive strength of the ore up to 0.5 s even though a significant tensile damage was observed when we look at the mechanical state of the material. Significant change in unconfined compressive strength was observed only after 1 s where tensile and shear damage occurred throughout the bulk of the sample. It appears that unconfined compressive strength of the material was less sensitive to the micro-fractures that existed in the vicinity of the grain boundary. This leads to the requirement of a new method of quantifying damage in ore samples after microwave treatment which is more sensitive to damage around grain boundary. This will be examined in Chapter 7.

6.7.4 Conclusions

The effect of microwave treatment on the mechanical state of an ore sample was examined. And it was compared with the effect of microwave treatment on unconfined compressive strength reduction. It was observed that even if a significant tensile damage occurred in the vicinity of the grain boundary at exposure times as short as 0.05 s, there was no change in the unconfined compressive strength of the ore. Significant reduction in unconfined compressive strength of the ore was observed only at longer exposure time (> 1 s) where tensile and shear damage occurred throughout the bulk of the sample. It appears that unconfined compressive strength of the material is less sensitive to microwave induced micro-fractures; hence, a poor descriptor of liberation behaviour.

The practical implication of the results is that comparison of microwave treated and untreated ore should be made in terms of liberation of valuable minerals instead of bulk strength measures such as Point load and UCS. This is due to the fact that a considerable improvement in liberation for the microwave treated one may be obtained without a significant change in the bulk strength of the ore as clearly indicated in the simulations.

Chapter 7
Quantifying Damage around Grain Boundaries

7.1 Development of New Method for Quantifying Damage around Grain Boundaries

7.1.1 Introduction

To date, most theoretical studies on microwave treatment of ores were investigated by comparing the unconfined compressive strength of treated and untreated ore (Whittles et al., 2003; Jones et al., 2007). However, it is well known that UCS is a bulk measure of strength and does not indicate the local damage around the grain boundary, which is more important when mineral liberation is the processing goal. Simulation work in the previous chapter indicated that under UCS test conditions, localized stresses at the grain boundaries of microwave treated ore could be observed which exceeded the strength of the material (refer section 6-7). These stresses are indicative of localized failure in the grain boundary regions. However, it was only once significant stresses developed throughout the bulk of the sample that noticeable reduction in UCS occurred. This leads to the requirement of a new method of quantifying damage in the ore samples after microwave treatment.

This chapter addresses this issue by presenting a new method of characterizing damage in microwave treated ores. The method measures the damage around the grain boundary regions during the heating process. The developed method is used to quantify the damage induced in two microwave treated binary ores.

7.1.2 Numerical Methodology

Two binary ore models, namely galena-calcite and magnetite-dolomite were constructed. The selection was based on the simulation results from the previous chapter. Galena-calcite was selected as it was shown to be the most amenable binary ore in the short time (< 1 s) and magnetite-dolomite was chosen as it showed relatively poor response to microwave treatment compared to other binary ores. It

should be noted that the responses observed from the simulations were only associated with thermo-mechanical properties of the constituent minerals and they do not indicate the true responses of real ores for which the electromagnetic properties will also have a significant effect.

7.1.2.1 Geometrical Construction of Ore Models

The construction of the ore models was made by randomly disseminating one microwave absorbing mineral in a transparent matrix. For both binary ores, the total particle size was fixed as 15 mm × 15 mm, typical of the particle size likely to be treated in practice, and a zone size of 0.125 mm was used. The conceptual ores here also were assigned a composition of 10% of microwave absorbing mineral and 90% transparent matrix by volume. For each binary ore, two different textures were simulated: coarse-grained (grain size = 1 - 2.5 mm)**,** and 'fine-grained' (grain size = 0.125 - 0.25 mm). Real fine-grained ores, for which the grain size would be less than 0.05 mm, were not modelled, as the computational time for such cases was inconveniently long.

After disseminating the absorbing minerals in the transparent matrices, the zones immediately surrounding the absorbing grain were identified and grouped as 'grain boundary regions'. It should be noted that accurate representation of the actual grain boundary is not possible, as the grain boundary regions are on too small a length scale to resolve computationally. Typical coarse-grained and fine-grained ores with grain boundary regions are shown in Figures 7-1 to 7-4.

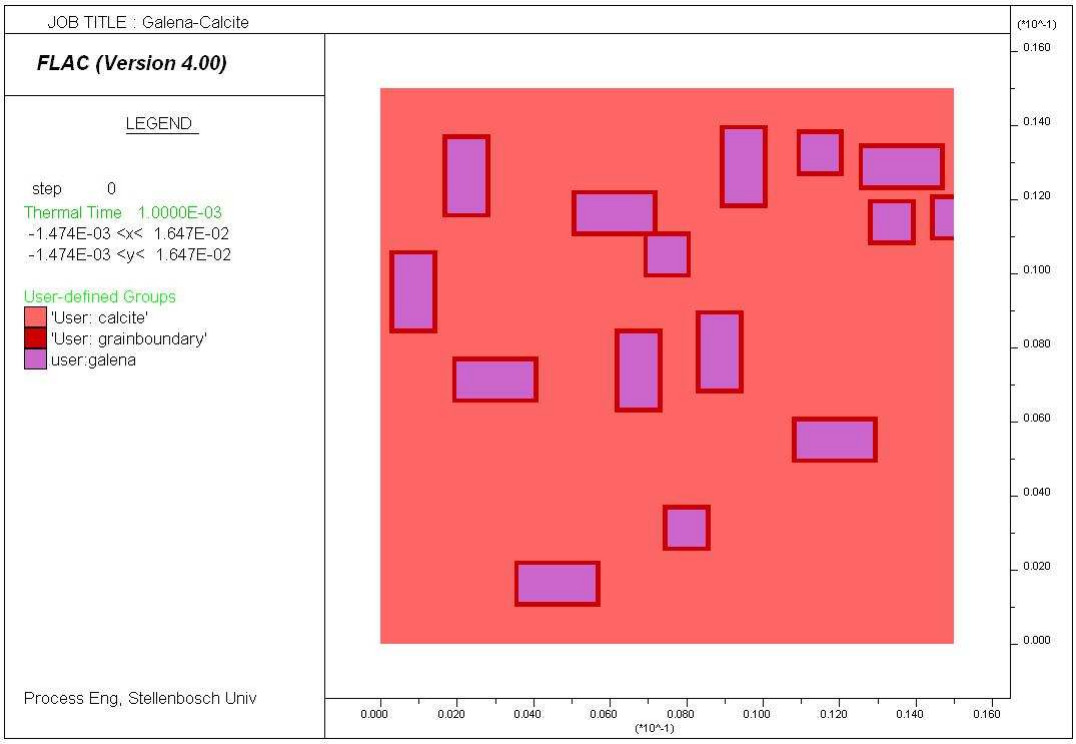

Figure 7.1: Representation of coarse-grained galena-calcite with grain boundary regions

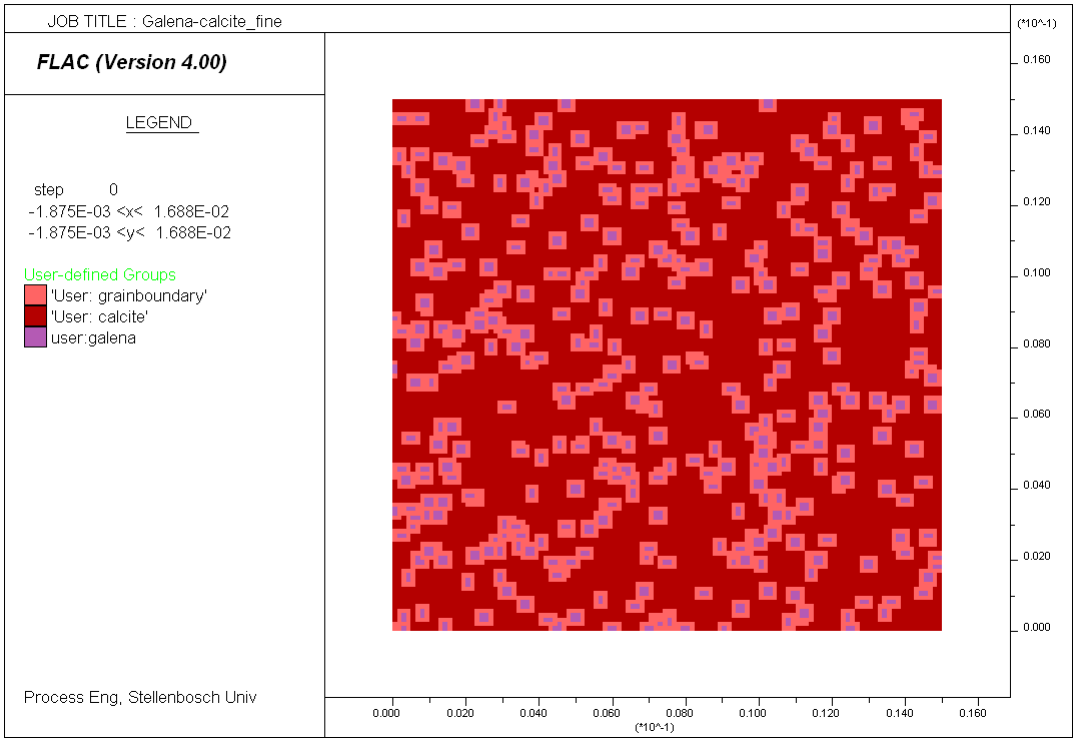

Figure 7.2: Representation of fine-grained galena-calcite with grain boundary regions

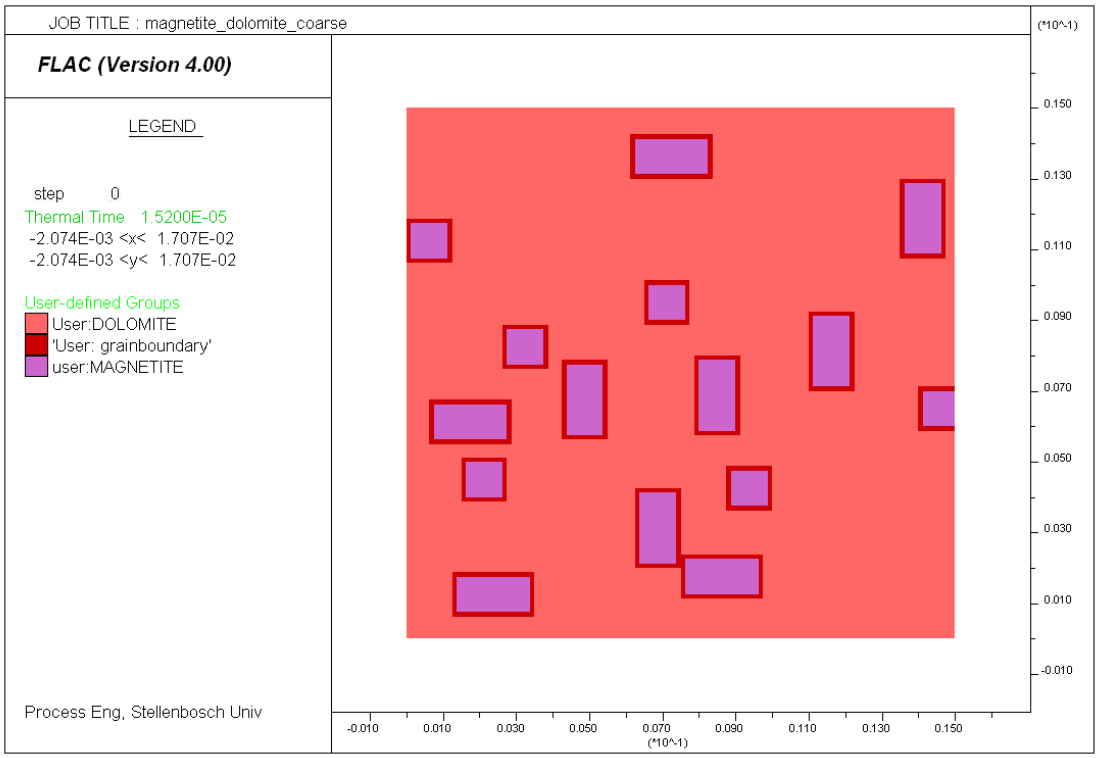

Figure 7.3: Representation of coarse-grained magnetite-dolomite with grain boundary regions

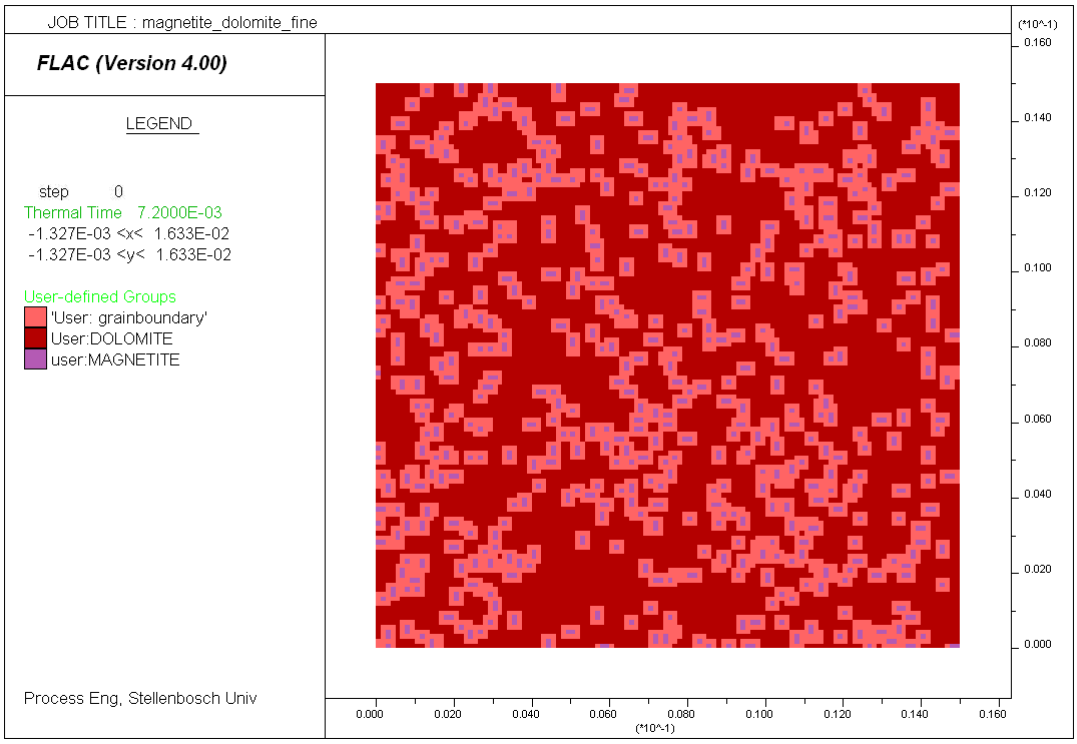

Figure 7.4: Representation of fine-grained magnetite-dolomite with grain boundary regions

7.1.2.2 Quantifying Damage

Previous simulation work by Salsman et al. (1996) and Jones et al. (2005) demonstrated that rapid microwave heating of ore containing a microwave absorbing mineral in a non-absorbing gangue matrix can generate thermal stresses high enough to exceed its strength. It is logical to assume that if the regions in which these stresses exceeded the strength of the material could be quantified, it would be possible to measure the damage induced around the grain boundaries. This is the focus of the present method.

In present method, the zones which make up the grain boundary regions as shown in Figures 7-1 to 7-4 were examined during the heating process. A code was written using *FLAC*'s inbuilt computer programming language, *FISH*, which counts the number of these grain boundary zones in which the stress had exceeded the tensile strength of the material. It was observed from simulation that the type of failure around the grain boundary region is predominately tensile and failure in shear occurs only after a long exposure time. This agrees with the fundamental aspect of brittle failure, that the formation of tensile cracks precedes failure in shear (Lama and Vutukuri, 1978).

Previous simulation studies have also shown that the matrix will be in tension during thermal expansion of the absorbent phase and tensile stresses that exceed the strength of the material will be induced around the grain boundary (Salsman et al., 1996; Whittles et al., 2003; Jones et al., 2005). Thus, by counting the zones at which the tensile stress exceeds the tensile strength of the material, it is possible to infer the amount of fracture which could be induced around the grain boundaries during the heating process.

7.1.2.3 Power Density and Exposure time

Simulations were performed using two different power densities. One simulation was done with power density of 1×10^{10} W/m^3 which is expected to be achievable in future pulsed equipment[3]. Another simulation was performed using power density of 1×10^{9} W/m^3 to represent the power density in 30 kW source, 2.45 GHz applicator

[3] In equipment under development in the AMIRA P 879 A project, millisecond pulses of the order of several hundred kilowatts can be generated with a range of pulse repetition frequencies

currently used for experimentation. These power densities have been established by consideration of measured net input power, sample mass and mass fraction of the microwave absorbing phase.The exposure times for each power density were started from zero and increased until a significant damage was observed.

7.1.3 Results and Discussion

Figure 7-5 shows the mechanical state of coarse-grained galena-calcite ore before microwave treatment. As can be seen, the ore was elastic through out the volume. Figures 7-6 and 7-7 show the temperature profile and the mechanical state of the ore, respectively after subjecting it to microwave treatment at a power density of 1×10^{10} W/m^3 for 0.75 ms. It can be seen that tensile failure starts to occur around the grain boundary region even when the temperature gradient across the grain boundary is of the order 5°C. It is important to note that it is not the absolute temperature which is important in microwave treatment of ores, but it is the temperature gradient between the absorbent and the transparent minerals. Thus, it was possible to induce stresses which were greater than the strength of the material with out significantly increasing the absolute temperature of the material. The damage at this time was 36.6%. This means that the tensile stresses in the 36.6% of the grain boundary zones exceeded the tensile strength of the material (12 MPa). Increasing the exposure time gave rise to a substantial damage as shown in Figures 7-9 and 7-11. It was observed that zones of damage were frequently rectilinear and aligned with the finite difference grid. This is most likely due the shape of the finite difference zones being square; however, for a random shape of zones, it is expected that such preferential orientation would be lost.

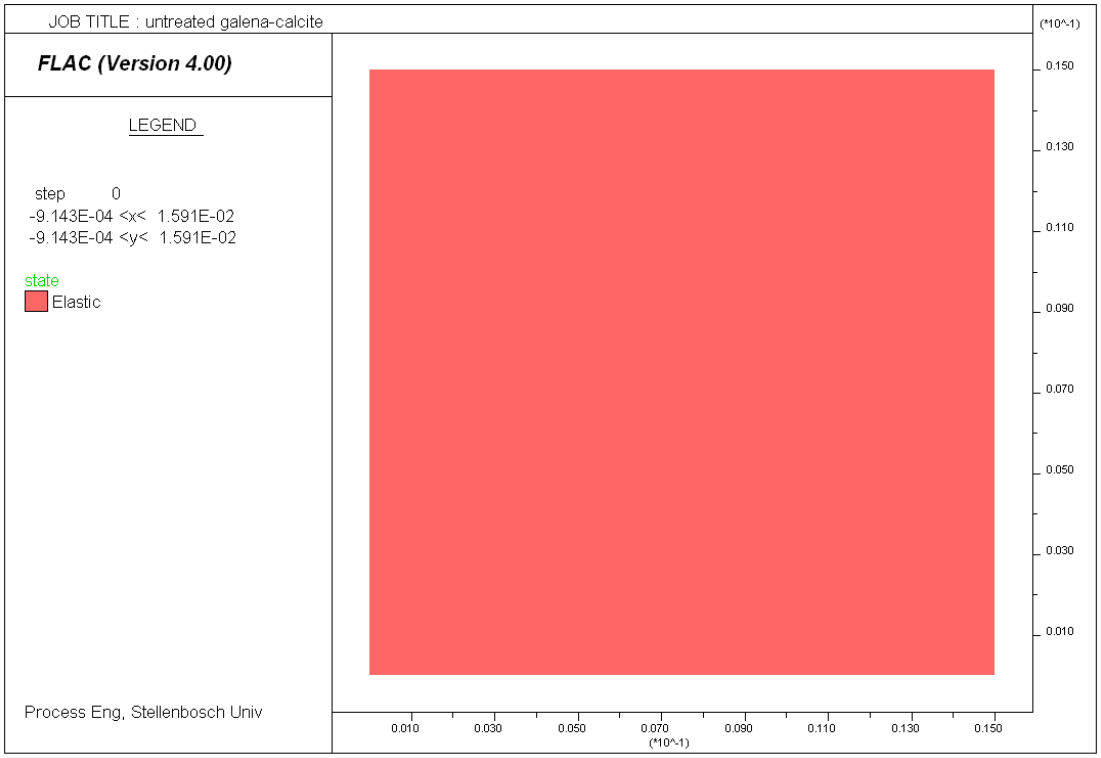

Figure 7.5: Mechanical State of coarse-grained galena-calcite, untreated, Damage = 0 %

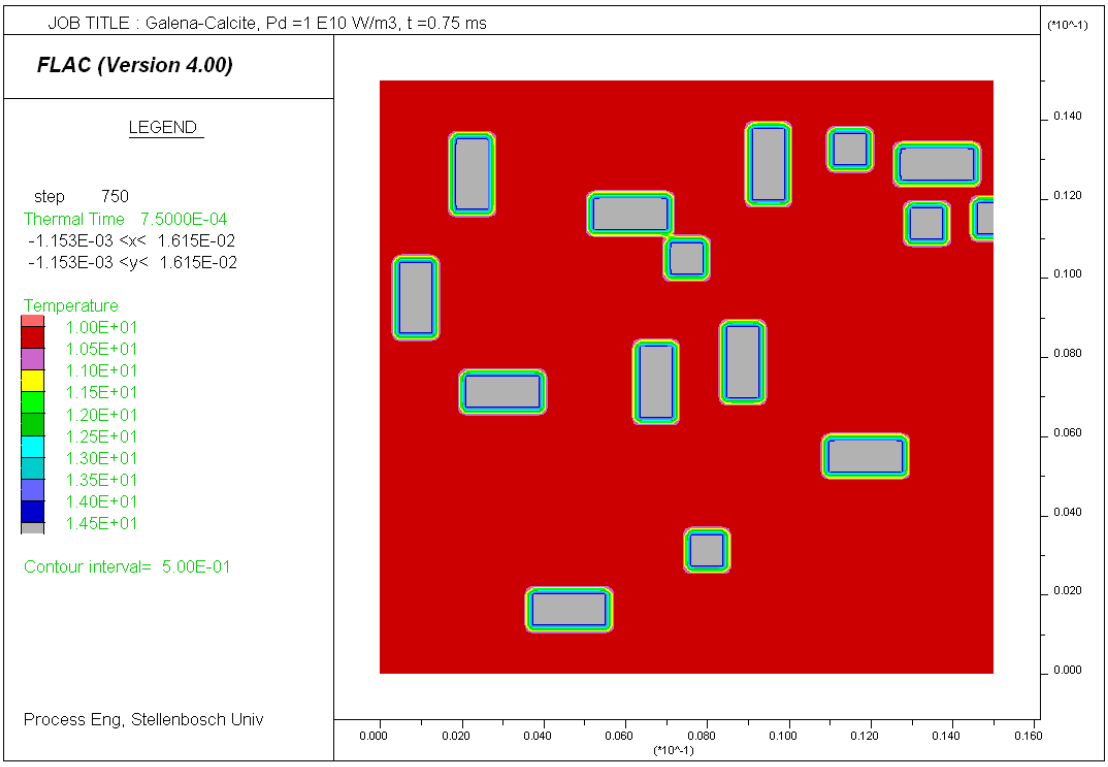

Figure 7.6: Temperature profile in coarse grained galena-calcite treated at $P_d = 1 \times 10^{10}$ W/m^3 for 0.75 ms

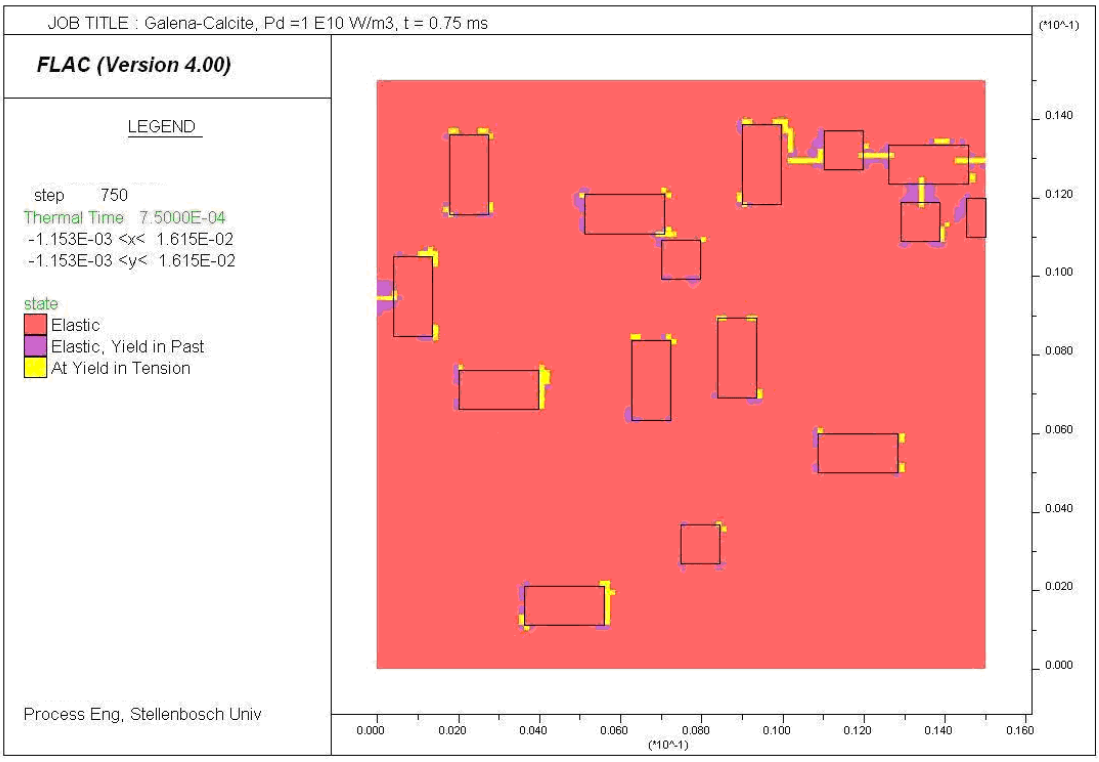

Figure 7.7: Mechanical state of coarse-grained galena-calcite treated at $P_d = 1 \times 10^{10}$ W/m^3 for 0.75 ms, Damage = 36.6%

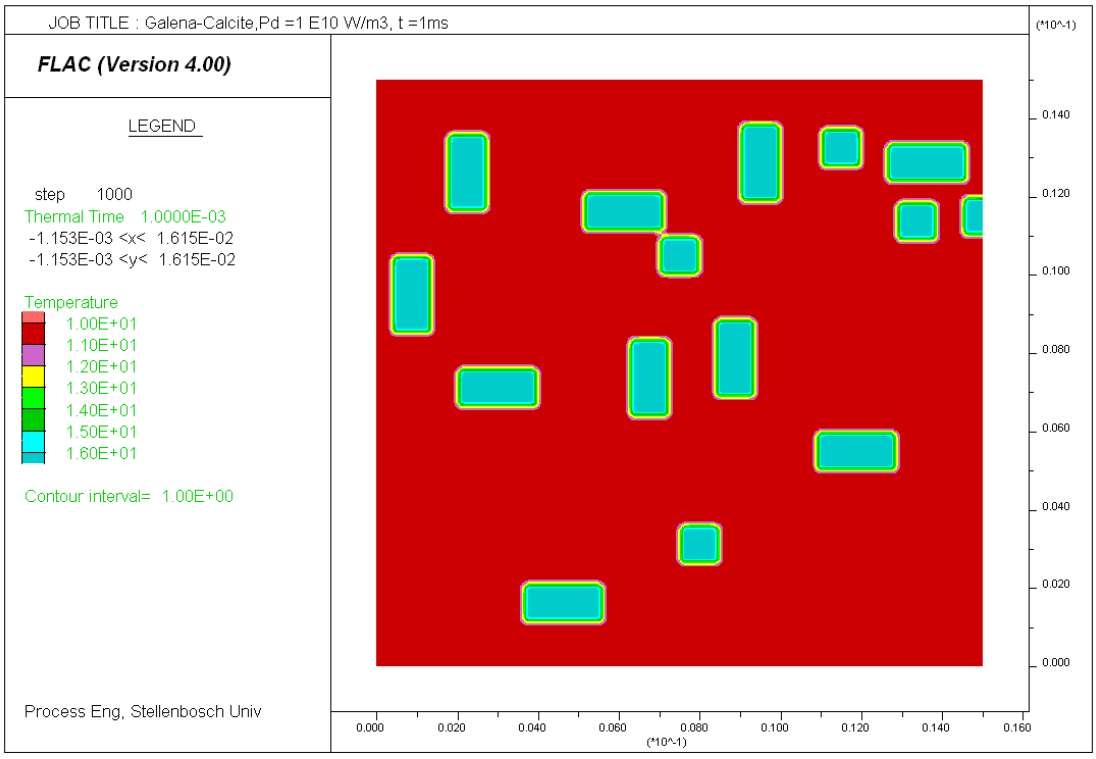

Figure 7.8: Temperature profile in coarse grained galena-calcite treated $P_d = 1 \times 10^{10}$ W/m^3 for 1 ms

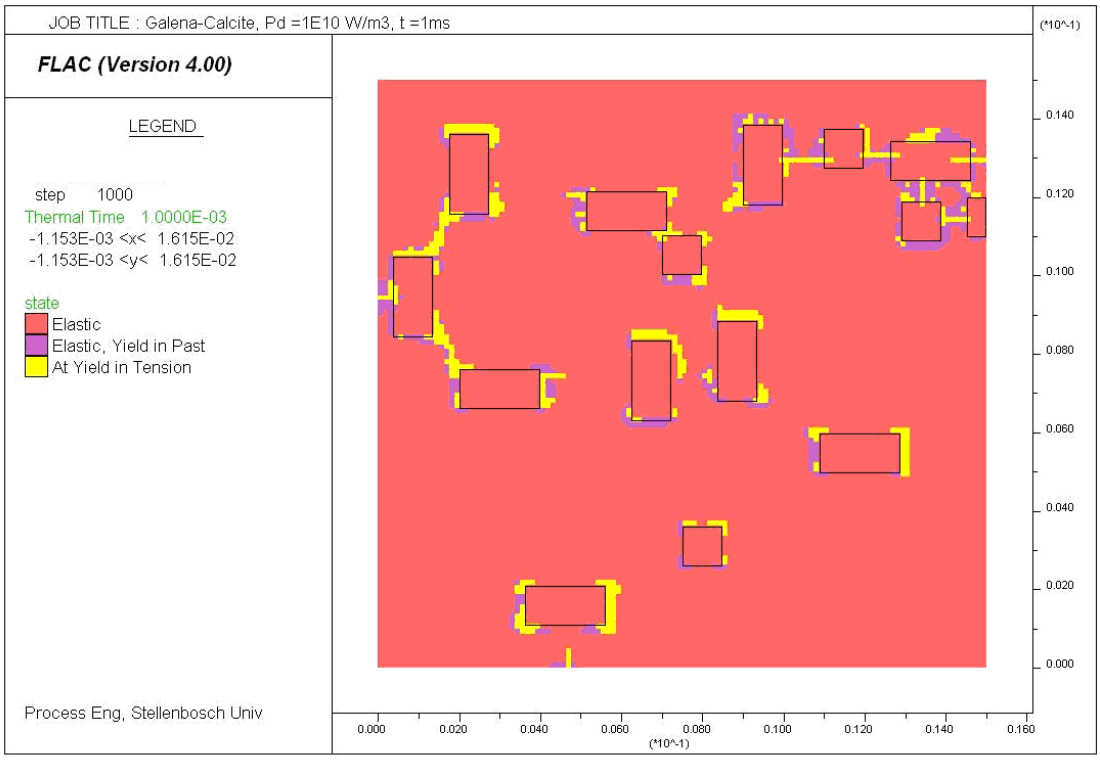

Figure 7.9: Mechanical state of coarse-grained galena-calcite treated at $P_d = 1 \times 10^{10}$ W/m^3 for 1 ms, Damage = 74.3%

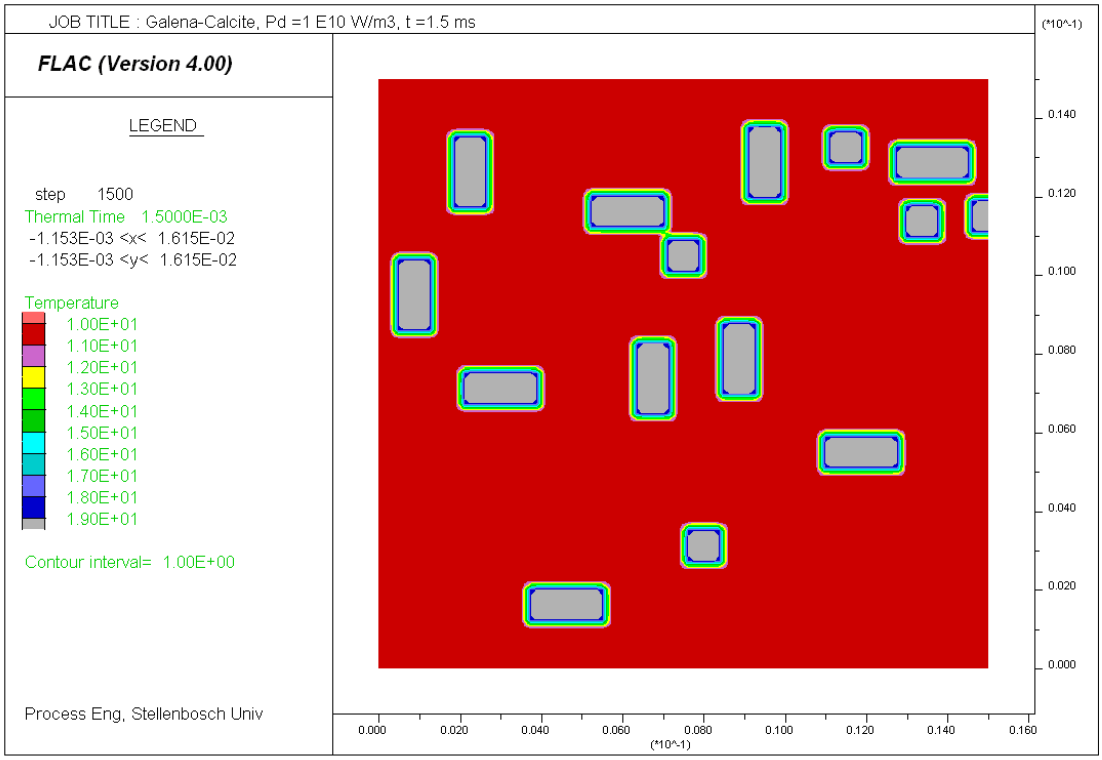

Figure 7.10: Temperature profile in coarse grained galena-calcite treated at $P_d = 1 \times 10^{10}$ W/m^3 for 1.5 ms

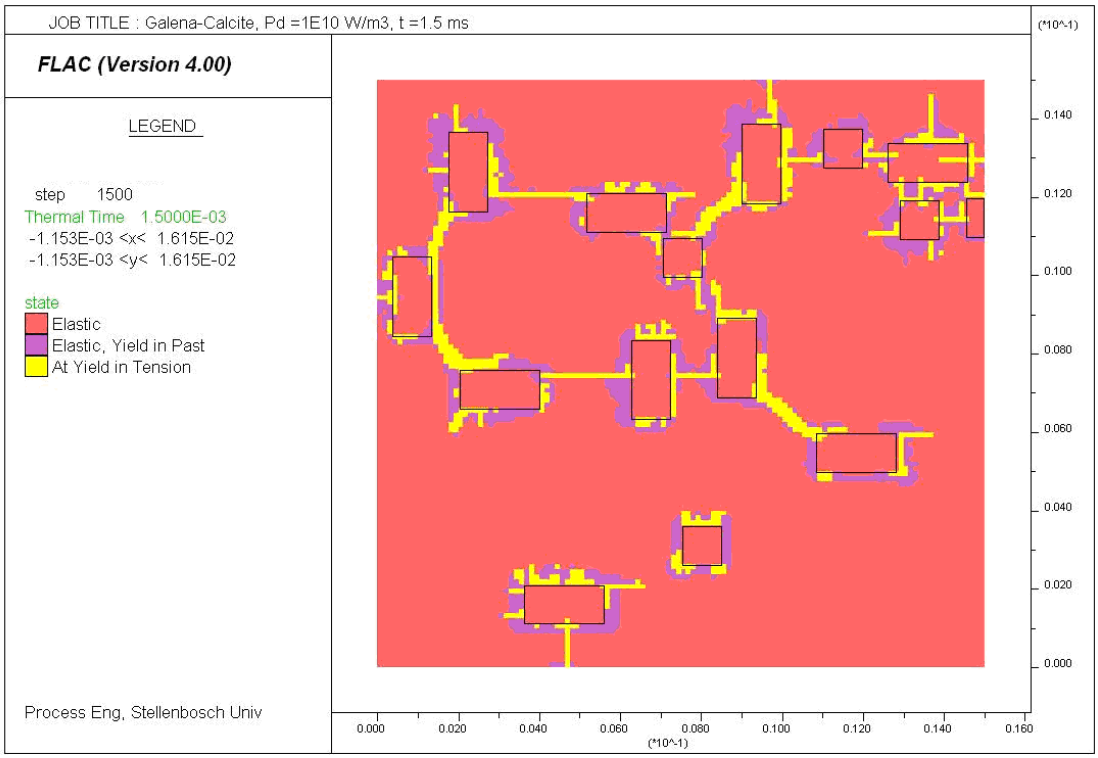

Figure 7.11: Mechanical state of coarse-grained galena-calcite treated at $P_d = 1 \times 10^{10}$ W/m^3 for 1.5 ms, Damage = 97.8%

Figure 7-12 shows the damage as a function of exposure time. It can be seen that as the exposure time is increased, the damage incurred in the sample becomes higher. It took approximately 1.75 ms in order to damage the entire grain boundary region. It should also be noted that most of the damage occurred between 0.5 and 1.5 ms. This suggests that there is an optimum exposure time range for a known power density at which the benefit of microwave irradiation of a specific ore is at a maximum.

Figure 7-13 shows the results when the power density was lowered to 1×10^9 W/m^3. As would be expected, the damage was diminished for the same energy inputs. For instance, at 1×10^{10} W/m^3 and 0.001 s the amount of grain boundary damage was 74.3% while at 1×10^9 W/m^3 and 0.01 s the damage was less than 50%. It has been previously shown that if the power density is low and the exposure time is high, the conduction heat loss from the absorbent phase would be higher. And this would result in a lower temperature gradient between the two phases (Salsman et al., 1997;

Whittles et al., 2003; Jones et al., 2007). Previous simulation work by Salsman et al., (1997) also showed a relatively flat temperature profile around the grain boundary region when the power density was lowered.

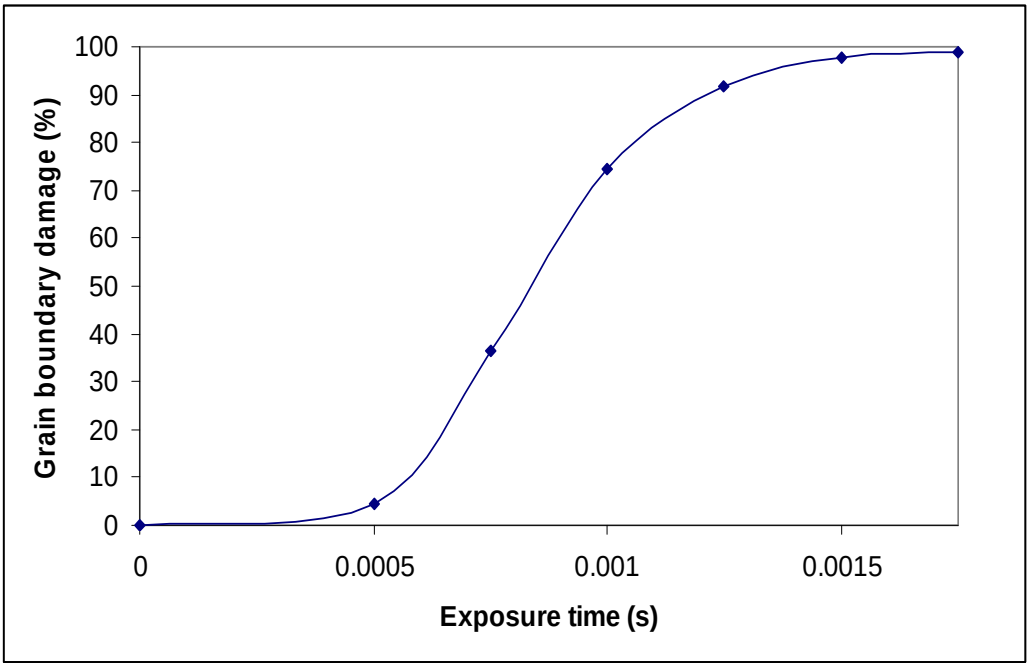

Figure 7.12: Damage around grain boundary regions of coarse-grained galena-calcite treated at $P_d = 1 \times 10^{10}$ W/m^3

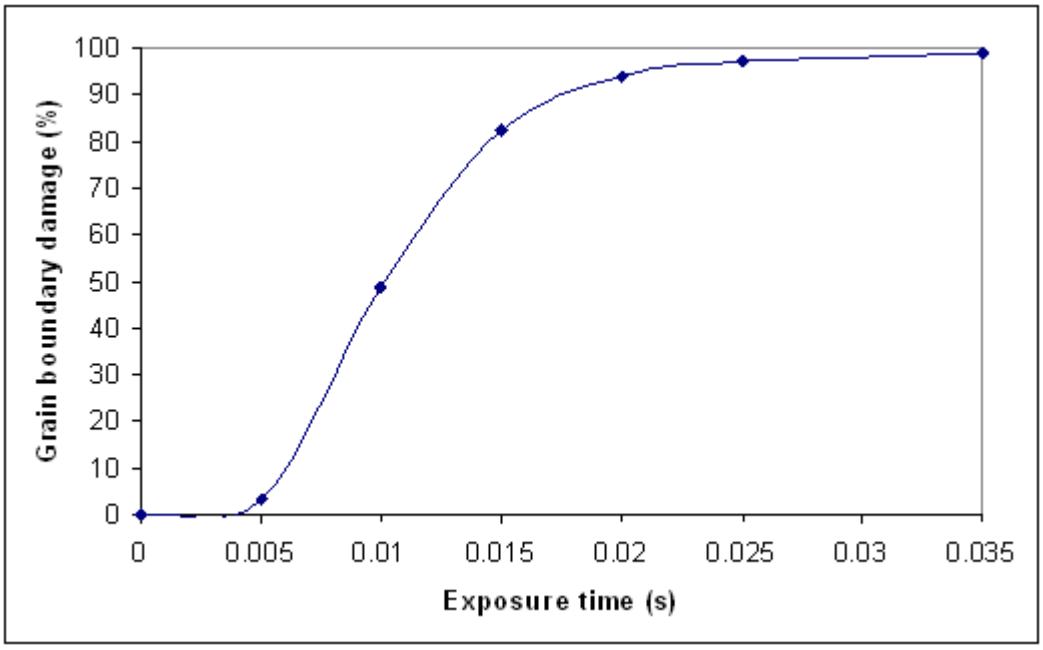

Figure 7.13: Damage around grain boundary regions of coarse-grained galena-calcite treated at $P_d = 1 \times 10^{9}$ W/m^3

Figures 7-14 and 7-15 show the results of simulation for fine-grained galena-calcite. It is evident that as the grain size decreases, the damage incurred in the samples becomes lower. This suggests that a higher energy input is required if it is desired to have the same damage as for a coarse grained ore. For instance, if one operates at a power density of 1×10^{10} W/m^3, an energy input of 2.5×10^7 J/m^3 is required to obtain a 30% grain boundary damage whilst less than 7.5×10^6 J/m^3 is needed to achieve the same damage in coarse-grained one. The reasons for the higher energy input requirement for the fine-grained ores were previously discussed in section 6-2 and will not be repeated here.

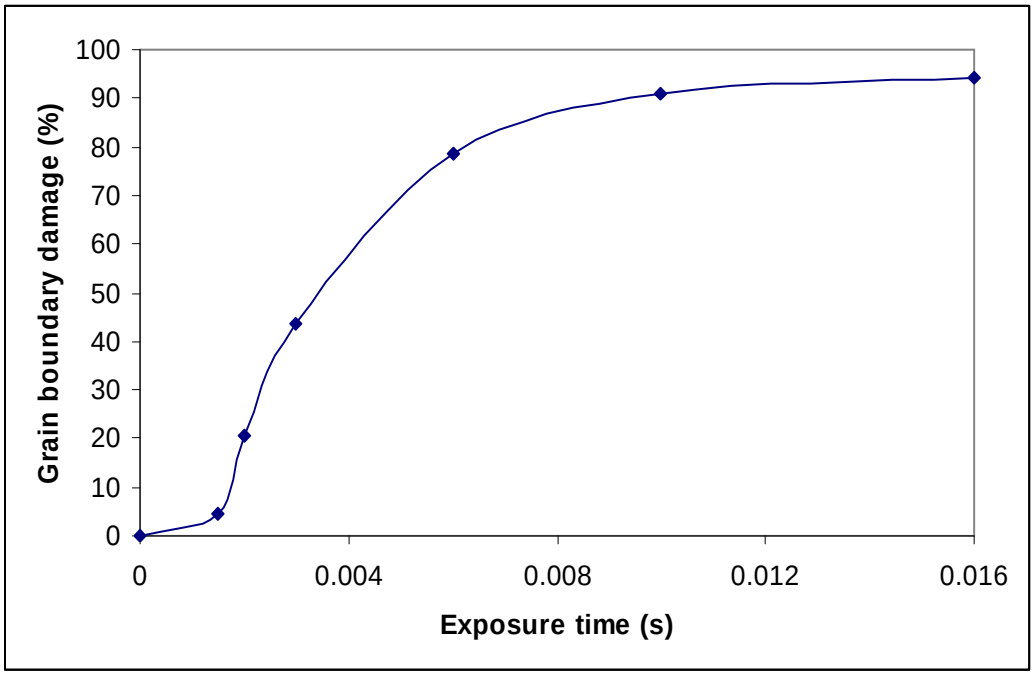

Figure 7.14: Damage around grain boundary regions of fine-grained galena-calcite treated at $P_d = 1 \times 10^{10}$ W/m^3

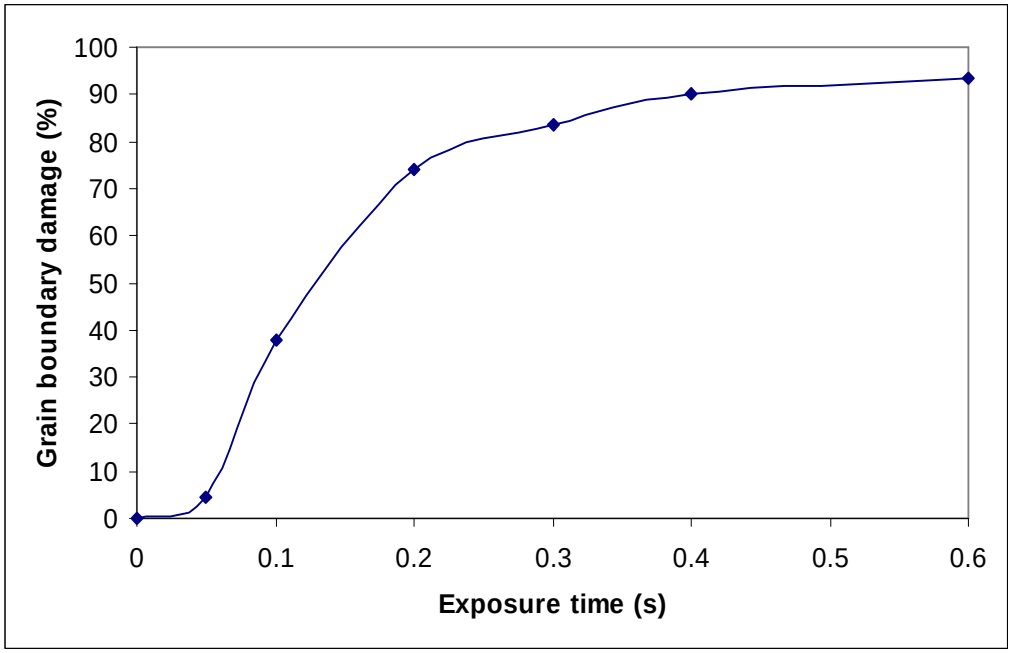

Figure 7.15: Damage around grain boundary regions of fine-grained galena-calcite treated at $P_d = 1 \times 10^9$ W/m^3

The results obtained for coarse grained magnetite-dolomite ore are shown in Figures 7-16 and 7-17. It can be seen that for this ore, there is a substantial difference between operating at 1×10^{10} W/m^3 and 1×10^9 W/m^3. Increasing the power density decreases the required energy input considerably. For example, if it is desired to obtain 90% grain boundary damage, it would require an energy input of 1.5×10^8 J/m^3 at power density of 1×10^9 W/m^3. However, if the power density were increased to 1×10^{10} W/m^3, the required energy input would only be 4×10^7 J/m^3. The practical implication of this is that it would be cheaper in terms of energy to operate at higher powers and shorter times.

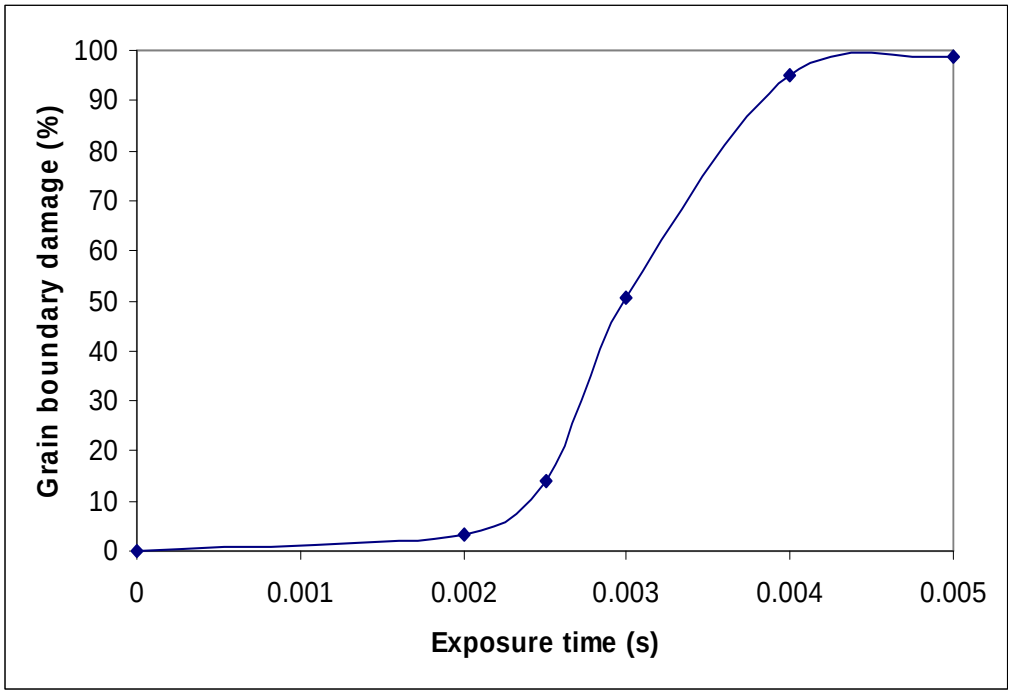

Figure 7.16: Damage around grain boundary regions of coarse-grained magnetite-dolomite treated at $P_d = 1 \times 10^{10}$ W/m^3

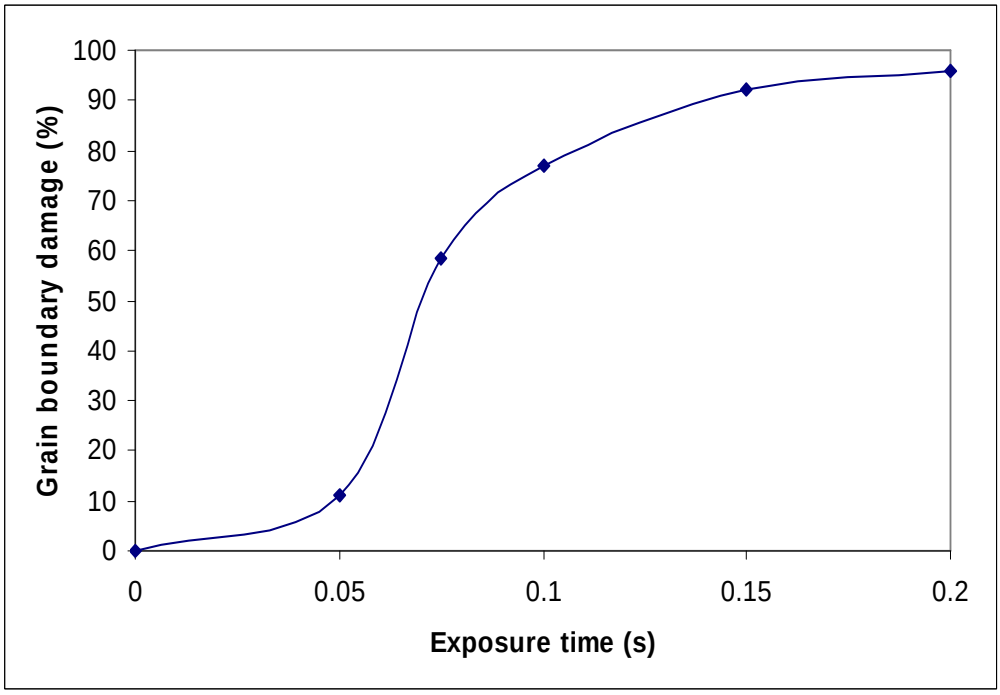

Figure 7.17: Damage around grain boundary regions of coarse-grained magnetite-dolomite treated at $P_d = 1 \times 10^{9}$ W/m^3

Figures 7-18 and 7-19 show the result of simulation of fine-grained magnetite-dolomite ore. As can be seen, the pattern observed for galena-calcite is repeated, i.e. the damage decreases considerably as the grain-size is decreased. It indicates that a higher energy input is needed than that required for the coarse-grained one in order to have the same damage. It is also evident that there is a considerable difference between operating at 1×10^{10} W/m^3 and 1×10^{9} W/m^3.

It can be seen from Figure 7-19 that increasing the exposure time beyond 0.6 s did not cause any significant increase in grain boundary damage. It is evident that higher power density is required in addition to higher energy input in order to achieve significant damage in the ore. This suggests that for a given mineralogy and ore texture there is a power density level below which no further increase in grain boundary damage is possible by increasing exposure time. The possible reason for this is that a longer exposure time increases the conduction heat loss from the absorbent phase into the surrounding transparent matrix. This would decrease the temperature gradient between the two phases. As a consequence, the damage incurred at the grain boundary would be diminished.

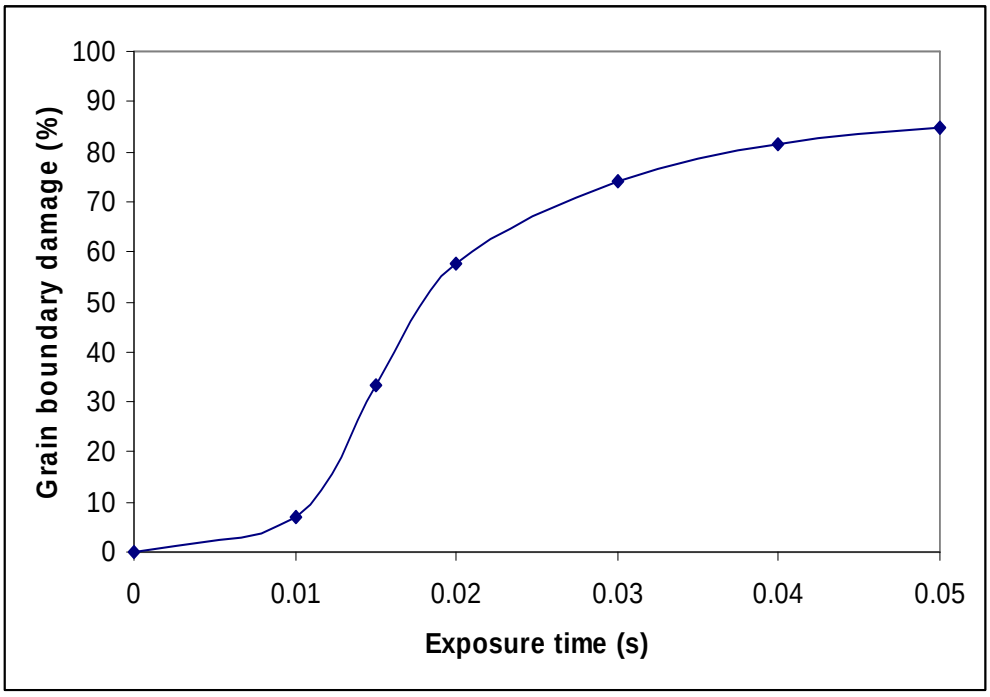

Figure 7.18: Damage around grain boundary regions of fine-grained magnetite-dolomite treated at $P_d = 1 \times 10^{10}$ W/m^3

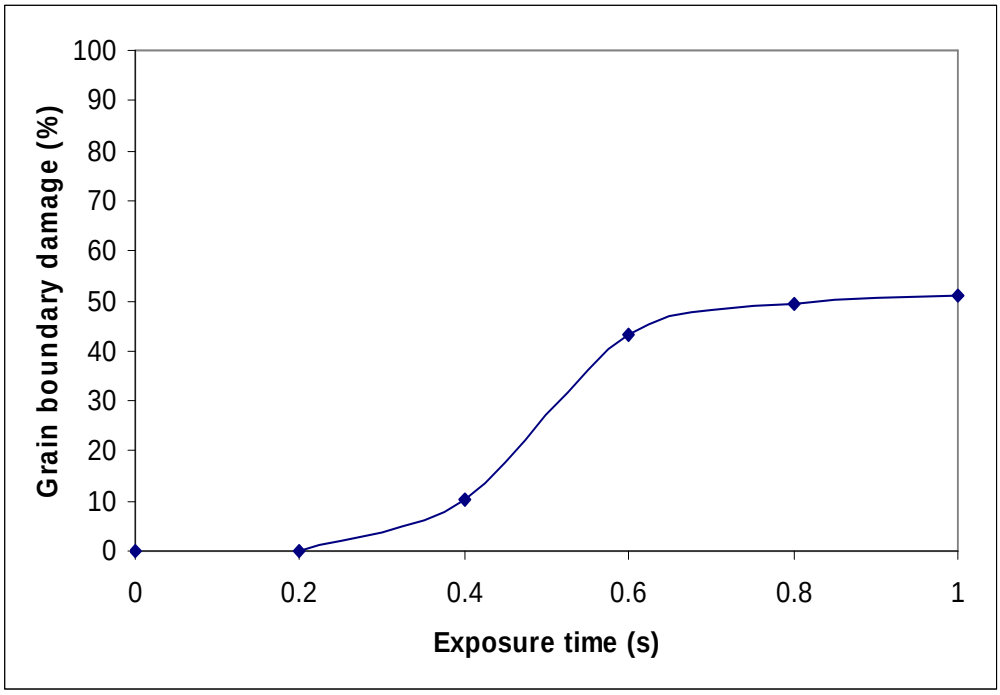

Figure 7.19: Damage around grain boundary regions of fine-grained magnetite-dolomite treated at $P_d = 1 \times 10^9$ W/m^3

As can be seen from Figures 7-18 and 7-19, 84.6% damage was obtained using an energy input of 5×10^8 J/m^3 when the power density was 1×10^{10} W/m^3, whereas only 51% damage was achieved at power density of 1×10^9 W/m^3 even if the energy input is doubled. It is evident that a higher power density is needed for this ore in order to induce a greater damage. The practical implication of this is that ores which appears to be less amenable to microwave in continuous wave equipment (of low power density) could be treated economically using very high power pulsed equipment.

It is well known within the microwave processing field that the most important design parameters for a microwave unit are the required power density and energy input, as these determine the required power and all other design specifications required for an economical analysis. The simulation results obtained from this study in general suggest that it would be necessary to determine these parameters for different ore types and design the required microwave system accordingly in order to maximize the benefit of microwave treatment of ores.

7.1.4 Conclusions

A new method of quantifying damage around the grain boundaries of microwave treated ores has been developed. Using the method, the influence of power density has been elucidated. It has been shown that it is possible to induce considerable grain boundary damage without significantly increasing the absolute temperature of the ore. It has also been shown that it is possible to reduce the required energy input substantially by operating at higher power density. It was shown that the amount of grain boundary damage incurred at a specific power density and energy input is strongly dependent both on the ore mineralogy and its texture. It was also shown that for a given mineralogy and ore texture there is a power density level below which no further increase in grain boundary damage is possible by increasing exposure time.

7.2 Construction of Damage Maps for Different Ores

7.2.1 Introduction

This section details how the method developed in the previous section was used for constructing operating windows for different ores types and textures. It has been previously shown that the most important design parameters for a microwave unit are the required power density and energy inputs. These parameters have not been determined for different ore types and textures either theoretically or experimentally (Bradshaw et al., 2007). The effects of mineralogy and grain-size of the absorbent phase on the economic operating conditions of microwave applicators have not been yet investigated. Thus, the aim of this study was to give guidelines concerning the operating conditions for current and future industrial microwave applicators and to examine how the design parameters are affected by mineralogy and texture of ores. Damage maps which show damage as a function of power density and treatment time were constructed for two different binary ores, each having different textures.

7.2.2 Methodology

The construction of the ore models (galena-calcite and magnetite-dolomite) was again made by randomly disseminating one microwave absorbing mineral in a transparent matrix as detailed in the previous section. Here again, the ores were assigned a composition of 10% of microwave absorbing mineral and 90% transparent matrix by volume. For each binary ore, two different textures were simulated: coarse-grained (grain size = 1 - 2.5 mm)**,** and fine-grained (grain size = 0.125 - 0.25 mm). The ores were then exposed to microwave at different power densities.

For coarse-grained galena-calcite, since damage was observed at lower power density ($\approx 1 \times 10^7$ W/m^3), the power densities used for constructing the damage map were between 1×10^7 W/m^3 and 1×10^{11} W/m^3. For coarse-grained magnetite–dolomite and fine-grained galena-calcite, power densities ranging from 1×10^8 W/m^3 to 1×10^{11}W/m^3 were applied. However, for the fine-grained magnetite-dolomite, significant damage was observed only at high power density ($\approx 1 \times 10^9$ W/m^3). Accordingly, the

power densities used for constructing the damage map were between 1×10^9 W/m^3 and 1×10^{11}W/m^3. Using the method developed in the previous section, damage maps which show contours of the fraction of grain boundary zones damaged as a function of power density and exposure time were constructed for each ore. Data used for constructing the damage maps are presented in Appendix F (F1, F2, F3 and F4). It should be noted that the axes on the damage maps are logarithmic to enable very short treatment times and a wide range of power densities to be plotted.

7.2.3 Results and Discussion

Figure 7-20 shows the damage map for coarse-grained galena-calcite, which is the binary ore most amenable to treatment due to the high thermal expansion coefficient of galena and being coarse-grained. Also shown on the figure is a line of constant energy input (10^8 J/m^{3}abs)[4]. It can be seen that for this ore, grain boundary damage up to 90% can be achieved at lower power density ($\approx 1 \times 10^8$ W/m^3) with energy input less than 10^8 J/m^{3}abs (0.868 kWh/t). It can also be seen that the damage contours are always less steep or at most parallel to the constant energy contour. This indicates that it is cheaper in terms of energy to operate at higher powers and shorter times, provided that one increases the power density and decreases treatment time along a contour at least as steep as the damage contours. The practical implication of this is that pulsed equipment (which is capable of producing high power densities) will be cheaper than continuous wave equipment in terms of energy cost.

At very short treatment times, the damage contours and lines of constant energy input become parallel, indicating that there would be no further energy saving by reducing treatment time and increasing power. The optimal power density and treatment time would be obtained by trading off energy savings against the increased capital cost required to generate the extremely high power densities. Further, one would also have to realise that increased power density requires increased electric field strength which increases the risk of dielectric breakdown.

[4] Energy per volume of the absorbent mineral

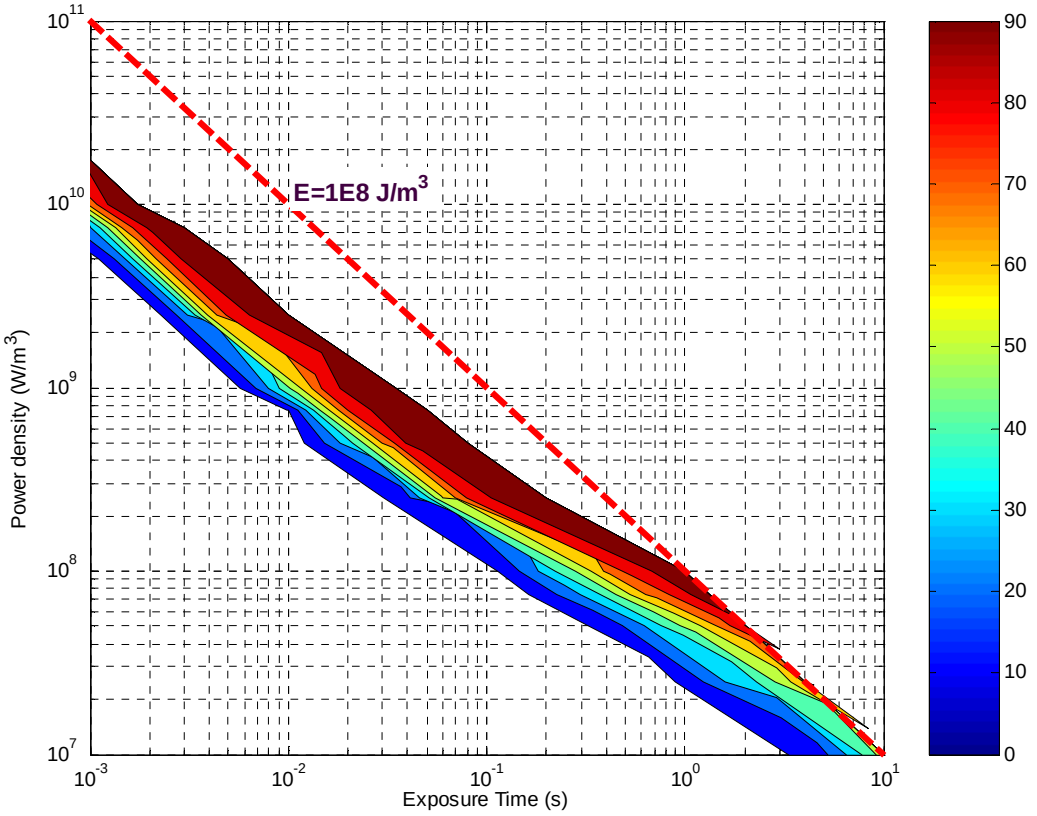

Figure 7.20: Grain boundary damage in coarse-grained galena-calcite

Figure 7-21 shows the damage maps for coarse-grained magnetite-dolomite. It can be seen that the general trends shown by the magnetite-dolomite ore are qualitatively similar to those of the galena-calcite ore; however, the power density required to achieve similar amount of damage is higher for the magnetite dolomite. For example, it required a power density of at least 2×10^9 W/m^3 in order to obtain a 90% damage with energy input of 1×10^8 J/m^{3}abs. Thus, it is evident that for this ore a relatively high power density was required in order to have a significant damage in the ore with lower energy inputs.

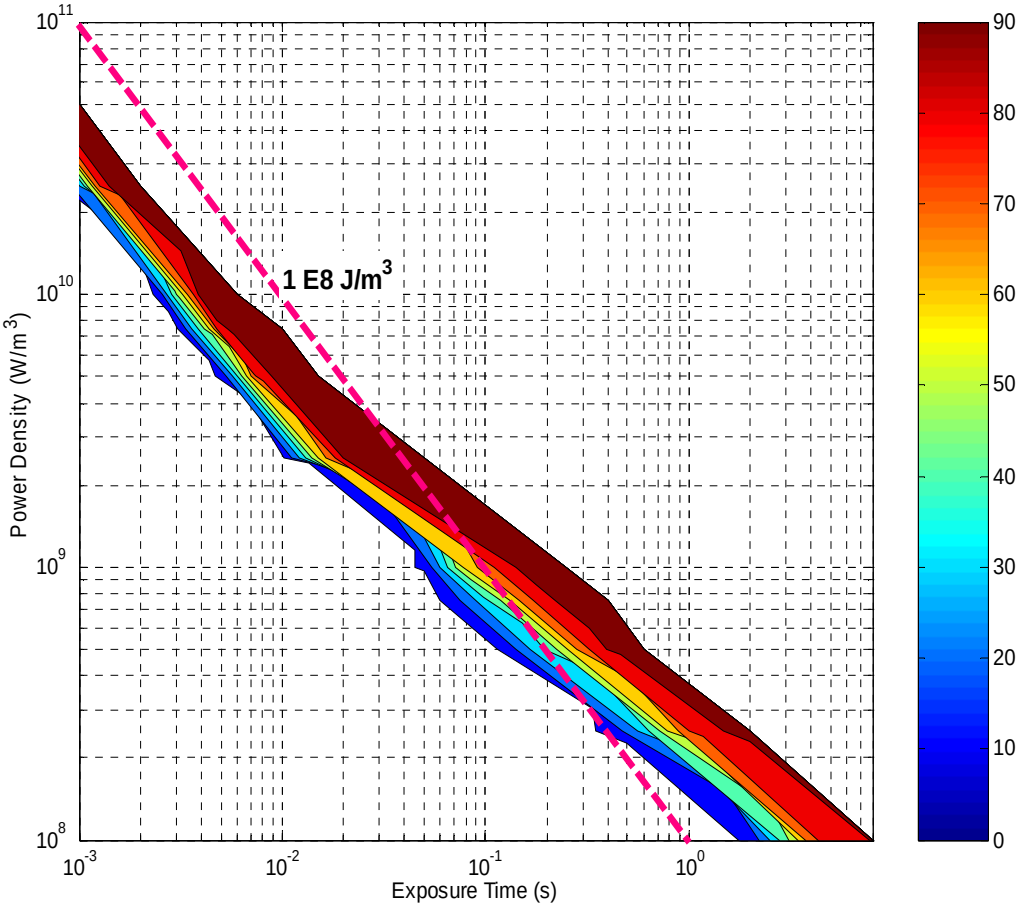

Figure 7.21: Grain boundary damage in coarse-grained magnetite-dolomite

The result of the simulations for fine-grained galena-calcite is shown in Figure 7-22. It can be seen, as expected that the fine-grained ore required significantly higher power density in order to have the same damage as the coarse grained ones. For instance, if 80% or greater grain boundary damage at energy input of 1×10^{8} J/m^{3}abs is desired, a minimum power density of 8×10^{9} W/m^{3} is required, which is high compared with that needed for the coarse-grained one. As can be seen, for this ore, the damage contours and lines of constant energy input are not parallel at any point. Thus, for this ore, increasing the power density up to 1×10^{11} W/m^{3} will decrease the energy input required for incurring the same amount of damage. That means significant energy saving can be achieved by reducing treatment time and increasing power.

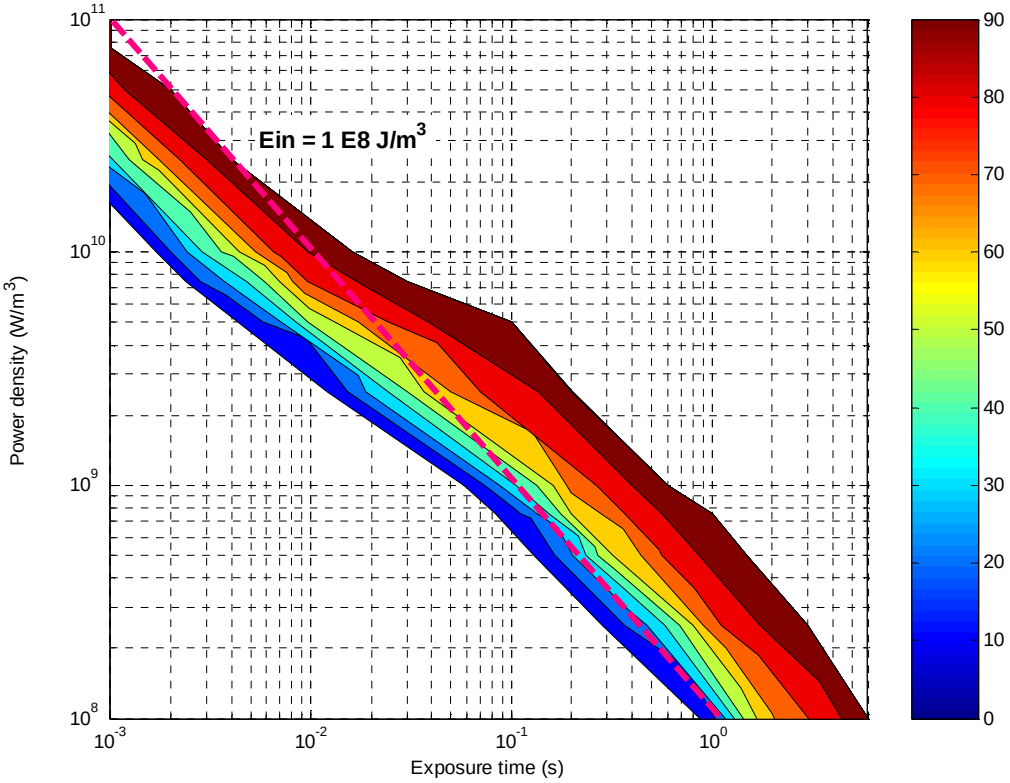

Figure 7.22: Grain boundary damage in fine-grained galena-calcite

Finally, the result of simulation of fine-grained magnetite-dolomite is shown in Figure 7-23. This ore was the least amenable ore for microwave treatment due to the low thermal expansion coefficient of the absorbent phase and also being fine-grained. As can be seen, the maximum damage that can be obtained for this ore using high power density of 1×10^{11} W/m^3 and with energy input of 1×10^8 J/m^{3}abs was about 50%. It is evident that for this ore, in addition to high power density, a relatively high energy input was required in order to achieve the same degree of damage as in the other ores.

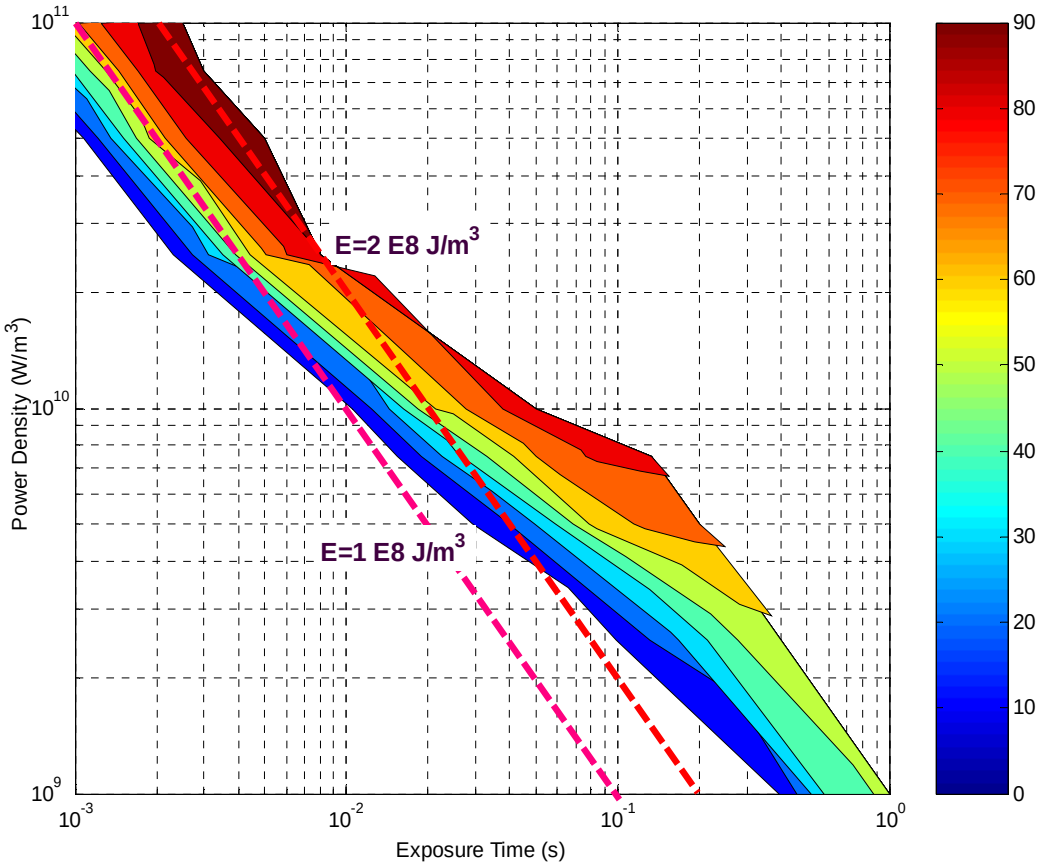

Figure 7.23: Grain boundary damage in fine-grained magnetite-dolomite

As can be seen, a minimum energy input of 2×10^8 J/m^{3}abs was required to obtain damage greater than 80%, provided that the treatment time at this energy input is less than 0.01 s. Thus, it is apparent that economic microwave treatment of such kind of ore needs the use of high power microwave equipment.

7.2.4 Conclusions

Damage maps which show contours of the fraction of grain boundary zones damaged as a function of power density and exposure time were constructed for different binary ores and ore textures. It was shown that both the power density and the energy input required to cause a fixed amount of grain boundary damage strongly depend on the ore mineralogy and its texture. It has been shown that for ores relatively amenable to microwave treatment, it was possible to incur significant amount of grain boundary damage at lower power density. However, a higher power density (for the same energy input) was needed to cause the same amount of grain boundary damage for ores less amenable to microwave treatment. For fine-grained ores less amenable to microwave treatment, both higher power density and higher energy input were required to incur the same amount of grain boundary damage.

The practical implication of this is that continuous wave equipment could be successfully used for ores relatively amenable to microwave treatment. For such ores, there would be no further energy saving by increasing power density, which increases the capital cost to produce the required microwave equipment. However, if the ore is less amenable and fine-grained, then pulsed equipment (which is capable of producing high power densities) is needed for economic microwave treatment.

7.3 Effect of Pulse Repetition Frequency on Grain Boundary Damage

7.3.1 Introduction

Pulse repetition frequency **(**the number of pulses transmitted per second) is an important parameter in pulsed microwave equipment. It fixes the amount of energy available per unit pulse for a given microwave power and exposure time. To date, the effect of pulse repetition frequency (PRF) on the extent of damage in microwave treated ores is not known. Accordingly, different simulations were undertaken to investigate the effect of PRF on microwave treated ores by varying the pulse repetition frequency for a fixed energy input and pulse width. Damage maps which show the amount of damage as a function of pulse repetition frequency and treatment time for the same energy inputs were constructed for two different binary ores.

7.3.2 Methodology

The ores used for the study were coarse-grained galena-calcite and magnetite-dolomite. The construction of the ore models was made by randomly disseminating the absorbent phase in the transparent matrix as discussed in the previous section (refer to Figures 7-1 and 7-3). Here again, the total particle size for each binary ore was fixed as 15 mm $\times$ 15 mm. The ores were also assigned a composition of 10% absorbent phase (galena or magnetite) and 90% transparent matrix (calcite or dolomite) by volume. The grain size of the absorbent grain for both ores was between 1- 2.5 mm.

Six different cases of heating were simulated for each binary ore. The total energy input (after 1 s exposure time) for each heating type was fixed at 5×10^7 J/m^{3}abs (0.434 kWh/t) for galena-calcite and 2×10^8 J/m^{3}abs (1.411 kWh/t) for magnetite-dolomite. These total energy inputs were typical energy inputs required to have a significant damage for the ores considered and were obtained from previous simulation results (refer section 7-2). The first heating case represents heating in continuous wave equipment. Pulsed type microwave heating at five different

operating conditions (Figure 7-24) was simulated by varying the pulse repetition frequency from 5 to 500 Hz for fixed pulse duration (τ) of 1 ms and for a total time of 1 s. Tables 7-1 and 7-2 show the different microwave heating cases investigated for Galena-calcite and Magnetite-dolomite respectively.

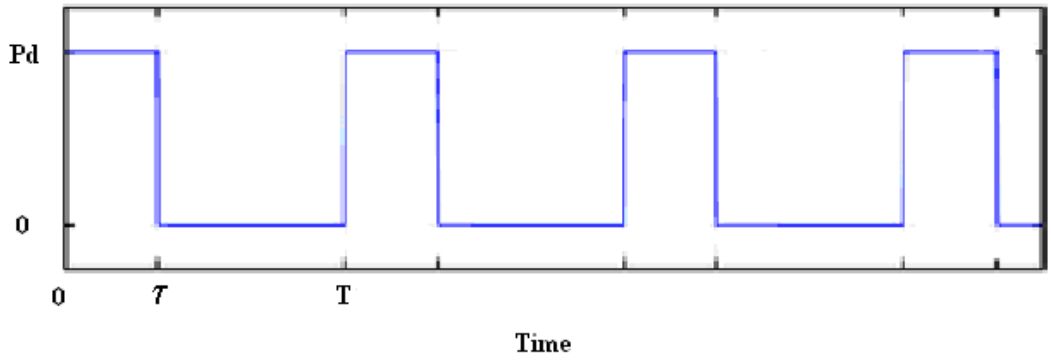

Figure 7.24: Pulsed wave, τ = pulse duration (width), T = Period

Simulations for 10, 50, 100, 500 Hz pulsed wave and for the continuous cases were undertaken at 0.1 s intervals. However, for the 5 Hz pulsed wave case since there is only one pulse in 0.2 s, simulation was carried out at 0.2 s intervals.

Table 7-1: Microwave heating cases used for treating galena-calcite

Power Density (W/m^3abs)	Pulse width (ms)	Pulse repetition frequency (Hz)	Total time (s)	Total energy (J/m^3 abs)	Total energy (kWh/t)
5E7	continuous	-	1	5E7	0.434
1E8	1	500	1	5E7	0.434
5E8	1	100	1	5E7	0.434
1E9	1	50	1	5E7	0.434
5E9	1	10	1	5E7	0.434
1E10	1	5	1	5E7	0.434

Table 7-2: Microwave heating cases used for treating Magnetite-dolomite

Power Density (W/m^3abs)	Pulse width (ms)	Pulse repetition frequency (Hz)	Total time (s)	Total energy (J/m^3 abs)	Total energy (kWh/t)
2E8	continuous	-	1	2E8	1.411
4E8	1	500	1	2E8	1.411
2E9	1	100	1	2E8	1.411
4E9	1	50	1	2E8	1.411
2E10	1	10	1	2E8	1.411
4E10	1	5	1	2E8	1.411

7.3.3 Results and Discussion

The results of simulation of galena-calcite treated at the same energy inputs and with different pulse repetition frequencies are shown in Table 7-3 and Figure 7-25. It can be seen from Figure 7-25 that there was no significant difference in damages between that were obtained for the continuous wave and the higher pulse repetition frequencies (≥ 50 Hz) cases. However, for the lower pulse repetition frequencies cases (PRF = 10 Hz and PRF = 5 Hz), much higher damages were incurred for the same energy inputs. For instance, at 0.2 s, about 11 and 40% grain boundary damage were obtained at PRF = 10 Hz and PRF = 5 Hz, respectively while the damage for the lower pulse repetition frequencies were about 1%.

The mechanical states of galena-calcite treated at the same energy input of 0.434 kWh/t with PRF = 500 Hz and PRF = 5 Hz are also shown in Figures 7-26 and 7-27. The effect of pulse repetition frequencies can be clearly seen from the figures. It is evident that operating at lower pulse repetition frequencies considerably increased the grain boundary damage.

Table 7-3: Grain boundary damage (%) in galena-calcite for different heating cases

PRF (Hz)	0.1 s	0.2 s	0.3 s	0.4 s	0.5 s	0.6 s	0.7 s	0.8 s	0.9 s	1 s
Continuous	0	0.88	3.82	10.62	23.86	35.12	48.45	63.62	71.42	74.52
500	0	0.88	3.82	10.45	23.12	34.31	45.94	61.56	68.63	73.93
100	0	0.88	4.42	11.63	24.74	36.08	46.98	63.47	69.21	74.96
50	0	1.03	5.15	12.96	27.69	38.43	49.33	64.09	70.54	75.85
10	1.03	10.75	23.1	38.59	50.37	63.18	74.81	80.85	83.36	86.45
5	-	39.91	-	75.52	-	87.48	-	93.07	-	98.08

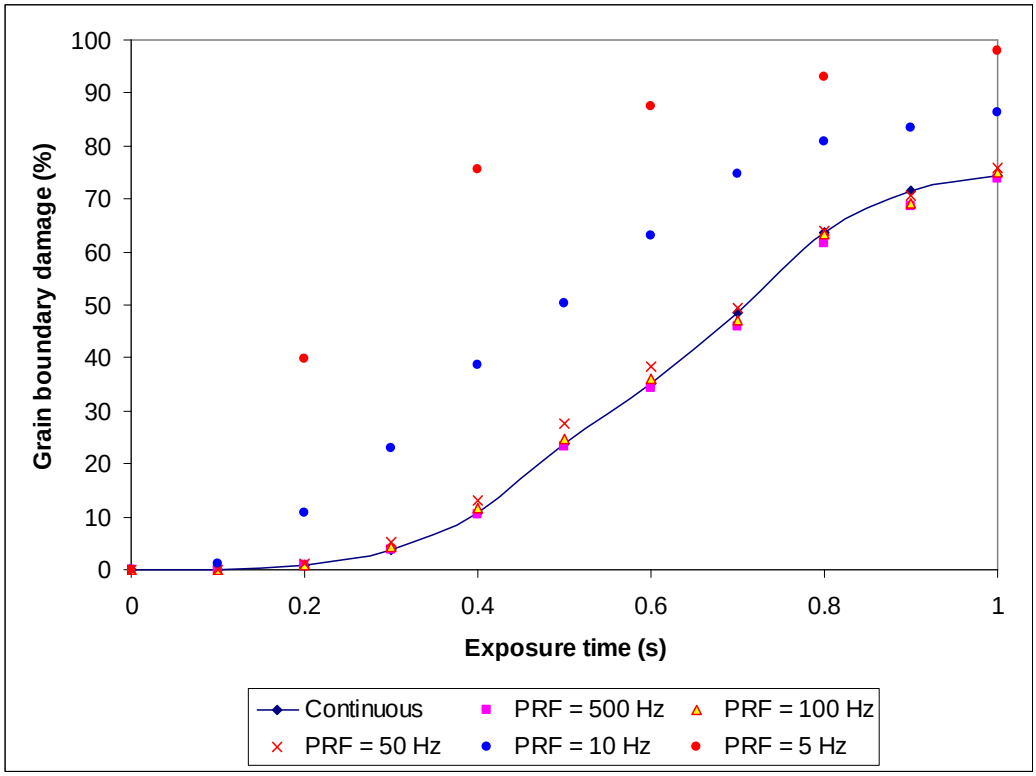

Figure 7.25: Grain boundary damage in galena-calcite for different microwave heating cases

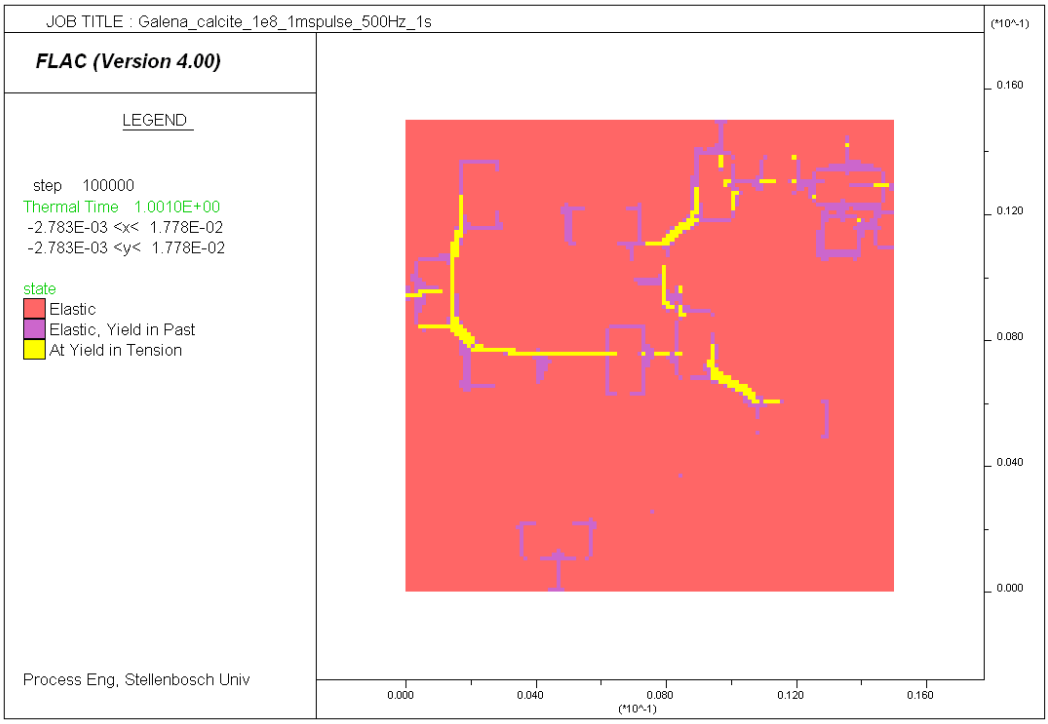

Figure 7.26: Mechanical state of galena-calcite treated at PRF = 500 Hz, pulse width = 1 ms, energy input = 0.434 kWh/t, total time = 1 s

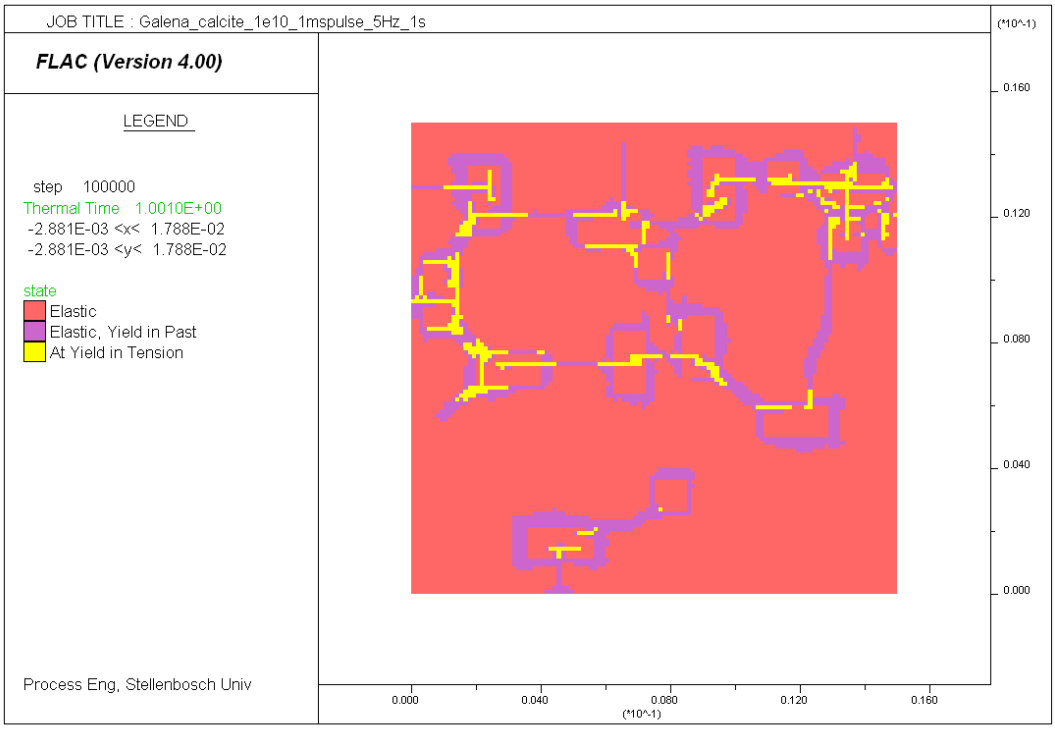

Figure 7.27: Mechanical state of galena-calcite treated at PRF = 5 Hz, pulse width = 1 ms, energy input = 0.434 kWh/t, total time = 1 s

The results of the simulation obtained for magnetite-dolomite are shown in Table 7-4 and Figure 7-28. As can be seen, for this ore also, the damage obtained at higher pulse repetition frequencies were almost similar to that was obtained for the continuous wave case. It can also be seen that at PRF = 10 Hz and PRF = 5 Hz, a much higher grain boundary damage were occurred for the same energy input. It is apparent that even at higher energy input (1.411 kWh/t), the damage obtained for lower PRF cases were much higher. For instance, at PRF = 5 Hz, the damage was 93.3% while only 52.3% damage was achieved at PRF = 500 Hz.

It can be noted that it is always advantageous to deposit as much energy as possible in a short time as possible so that higher temperature gradient is achieved between the microwave absorbent and the transparent phases. However, if the same energy is spread over a longer time, the heat would have time to disperse into the transparent phase and less damage would occur.

Table 7-4: Grain boundary damage (%) in magnetite-dolomite for different heating cases

PRF (Hz)	0.1 s	0.2 s	0.3 s	0.4 s	0.5 s	0.6 s	0.7 s	0.8 s	0.9 s	1 s
Continuous	0	1.93	2.23	7.01	11.01	17.54	23.51	33.93	43.75	51.62
500	0	2.08	2.41	7.14	10.11	16.52	22.77	32.74	44.34	52.53
100	0	2.53	2.54	7.44	10.27	16.96	23.81	34.97	45.83	53.72
50	0	2.67	2.97	8.48	12.08	18.45	25.74	41.07	50.29	57.88
10	1.4	12.22	24.71	33.03	45.53	55.65	64.28	69.34	74.55	77.68
5	-	54.35	-	76.34	-	87.94	-	91.51	-	93.31

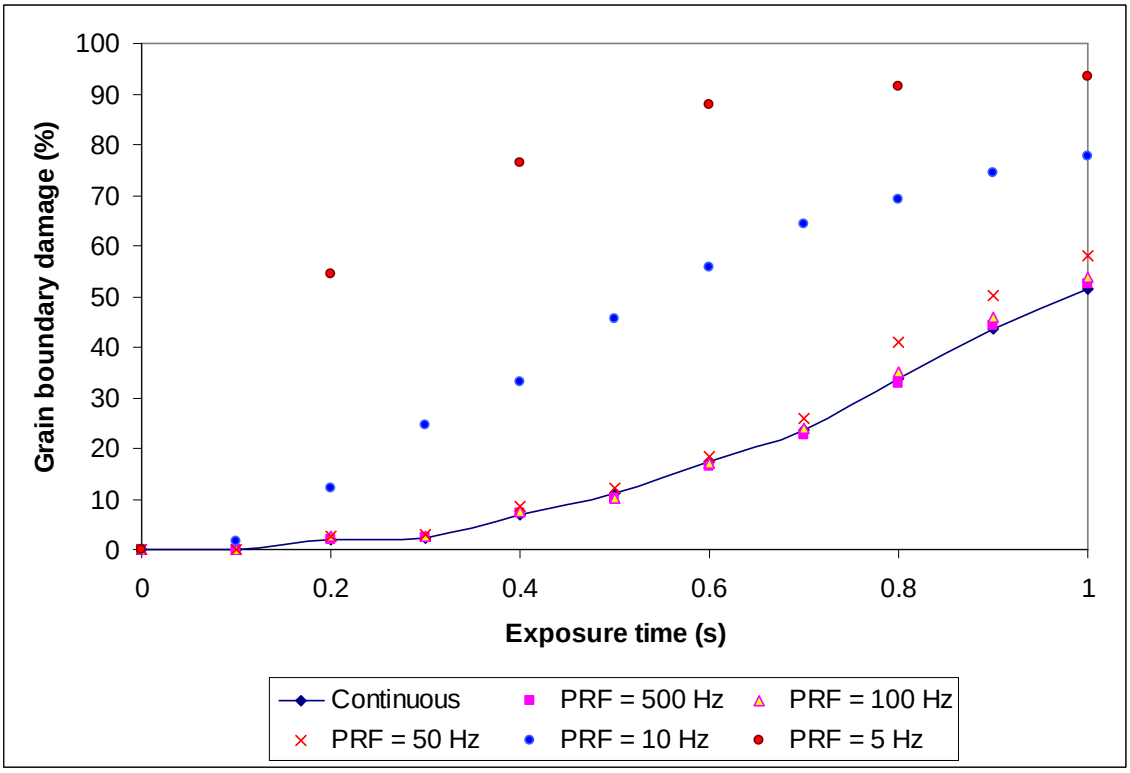

Figure 7.28: Grain boundary damage in Magnetite-dolomite for different microwave heating cases

The practical implication of this is that if pulsed microwave equipment is operated at high pulse repetition frequencies (≥ 50 Hz), it will lose the benefit of the high power available and produce damage in ores similar to what can be achieved in continuous wave equipment. In general, it can be said that for a fixed microwave energy input the best result would be obtained by using the lowest possible pulse repetition frequency and highest peak pulse power.

7.3.4 Conclusions

The effect of pulse repetition frequency on microwave treated ores was examined by varying the pulse repetition frequency for a fixed energy input and pulse width. It was found that high pulse repetition frequencies (≥ 50 Hz) resulted in an amount of grain boundary damage that was indistinguishable from that caused by continuous wave operation for a fixed energy input. This implies that if pulsed microwave equipment is designed to operate at higher pulse repetition frequencies, it will lose the benefit of the high power available and behave like continuous wave equipment. The result also indicated that the most efficient use of microwave energy is in a single pulse of the highest power assuming that there is no limitation on power and that the pulse width is fixed. In general, it was shown that for a fixed microwave energy input the best result would be obtained by using the lowest possible pulse repetition frequency and highest peak pulse power.

Chapter 8

Bonded-particle Modelling of Microwave-induced Damage

8.1 Introduction

In Chapters 6 and 7, it was shown how continuum analysis can be used to understand the patterns of stresses generated inside microwave treated ores. Continuum analysis provides easily and with a relatively less computational time the distribution of stresses inside an ore for a given microwave treatment condition. Hence, it was extensively used to understand the effect of different variables on microwave treatment of ores. However, as has been discussed in Chapter 4, explicit representation of fractures is not possible using continuum methods, as they require continuity of the functions between the neighbouring grid points. In addition, it was not possible to generate irregular shaped absorbent grains, which is expected in natural ores. The discrete element method (DEM) on the other hand utilizes the breakage of individually structural unit or bonds to directly represent damage. It is also possible to create particles of arbitrary shape by attaching two or more particles together. However, the specification of the geometry, properties and solution conditions is not so straightforward as in continuum analysis.

As Jing and Hudson (2002) have reviewed, the choice of continuum or discrete methods depends on many problem-specific factors, and mainly on the problem scale and fracture system geometry. The continuum approach is suitable if only a few fractures are present. The discrete approach is most suitable for modelling moderately fractured rock and fracture process.

There is a considerable variation in existing flaws in natural ores. Examination of polished section using Scan Electro Microscopy (SEM) showed that some ores are virtually free of pores and cracks and some have a very high concentration of flaws (e.g. Tavares and King, 1995).This suggests that both the continuum and discrete approaches can be used for better understanding of the effect of microwave treatment

depending on the nature of the ore (significance of existing cracks) and the kind of investigation.

In this chapter, a discrete element method was utilized to simulate again the thermally induced stresses and examine the micro-crack pattern in microwave treated ores. The intention was to better understand the crack patterns of different ores (of different mineralogy and texture) for different treatment conditions and to consolidate the conclusions drawn from the continuum analysis. Section 8-2 serves as an introduction to specific bonded-particle model code used in this thesis (*PFC^{2D} Version 4.0)*. In section 8-3, the methodology used for modelling the macroscopic properties of the model materials is detailed. Section 8-4 discusses the modelling equations used for coupling thermal and mechanical model and the specification of thermal properties in *PFC*. Sections 8-5 to 8-8 present the different contributions made from this part of the work.

8.2 Bonded Particle Modelling using Particle Flow Code (PFC^{2D})

8.2.1 Introduction

The bonded-particle model software used for the study was the Particle Flow Code (*PFC^{2D} Version 4.0*). *PFC^{2D}* models the movement and interaction of arbitrarily-sized circular particles by the distinct element method (DEM) (refer section 4-8). The particles/balls may represent individual grains in a granular material or they may be bonded together to represent a solid material, in which case, fracturing occurs via progressive bond breakage. The particles are rigid but deform locally at contact points using a soft-contact approach, in which finite normal and shear stiffnesses are taken to represent measurable contact stiffnesses. Any property or parameter, including particle radius, may be changed at any time during a simulation.

However, the specification of the geometry, properties and solution conditions is not so straightforward in *PFC^{2D}* as in continuum methods, exemplified using software programs such as *FLAC*. With a continuum program, a grid is created, initial stresses installed, and boundaries set as fixed or free. In *PFC^{2D}*, a compacted state cannot be pre-specified in general, since there is no unique way to pack a number of particles within a given volume (Itasca, 2008). A process analogous to physical compaction must be followed until the required porosity is obtained. The initial stress state cannot

be specified independently of the initial packing since contact forces arise from the relative positions of particles. Finally, the setting of boundary conditions is more complicated than for a continuum program because the boundary does not consist of planar surfaces.

An additional difficulty arises when it is required to match the behaviour of a simulated solid (comprised of bonded particles) with a real solid tested in the laboratory. This is often a trial-and-error process, as there is no complete theory that can predict macroscopic behaviour from microscopic properties and geometry. However, guidelines are given that should help in the matching process (e.g. Potyondy and Cundall, 2004). It should be realized that such modelling is difficult because it is exercising the limits of current knowledge. However, by performing tests with *PFC*^{2D}, it is possible to gain some fundamental understanding in damage mechanics (Itasca, 2008).

The calculation cycle in *PFC*^{2D} is a timestepping algorithm that consists of the repeated application of a force-displacement law to each contact, the law of motion to each particle and a constant updating of wall positions. At the start of each timestep, the set of contacts is updated from the known particle and wall positions. The force-displacement law is then applied to each contact to update the contact forces based on the relative motion between the two entities at the contact and the contact constitutive model. Next, Newton's second law (force = mass × acceleration) is integrated twice for each particle to provide updated velocities and new positions. Also, the wall positions are updated based on the specified wall velocities.

8.2.2 Contact Models

In *PFC*^{2D}, particles interact with other particles, and with walls, through the forces that develop at their contacts. Every contact involves two entities (ball-ball or ball-wall) and occurs at a single point through which the contact force acts. A contact model describes the physical behaviour occurring at a contact. Although a particle assembly may exhibit complex nonlinear constitutive behaviour, this behaviour is achieved through the use of relatively simple contact models (Itasca, 2008). Each contact model may consist of up to three parts: (1) a contact-stiffness model; (2) a slip

and separation model; and (3) a bonding model. The three elements of a contact model are discussed below.

8.2.2.1 Contact-Stiffness Models

There are two types of stiffness models in *PFC*^{2D} (Figure 8.1): a linear model and a simplified Hertz-Mindlin model. In the linear model, the forces and relative displacements are linearly related by the constant contact stiffnesses. In the simplified Hertz-Mindlin model, the forces and relative displacements are nonlinearly related by the non-constant contact stiffness, which is a function of the geometric and material properties of the two contacting entities as well as the current value of the normal force. The simplified Hertz-Mindlin model is appropriate when modelling assemblies having no bonds, experiencing small-strain conditions and exclusively compressive stresses. It is not suitable for modelling solid rock (Itasca, 2008).

In the linear model, the contact normal and shear stiffnesses (k_n and k_s) relate the contact forces and the relative displacements in the normal and shear directions linearly as:-

$$F_n = k_n U_n \qquad \textbf{8.1}$$

$$\Delta F_s = k_s \Delta U_n \qquad \textbf{8.2}$$

Where F_n and F_s normal and shear force, respectively. U_n and U_s are normal and shear displacement, respectively. The general contact logic is shown in Figure 8.1. In this study, the linear model is utlized.

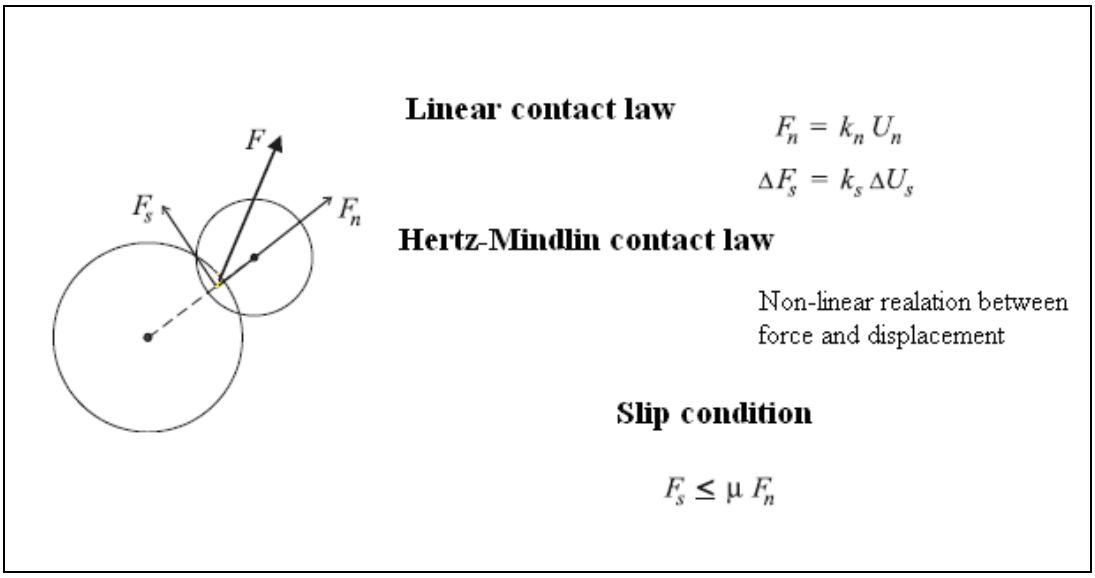

Figure 8.1: *PFC*^{2D} contact logic

8.2.2.2 Slip and Separation Model

This model allows two entities (ball-ball or ball-wall) in contact to slide relative to one another and to separate if they are not bonded and a tensile force develops between them. The slip condition occurs when the shear component of force reaches the maximum allowable shear contact force. This allowable shear contact force is taken to be the minimum friction coefficient of the two contacting entities multiplied by the magnitude of the compressive normal component of force (see Figure 8.1). The slip model continually limits the magnitude of the shear component of force to remain below this maximum allowable value. The slip model also enforces a no-tension criterion by removing the contact force if the entities are not bonded and a finite gap forms between them. A virtual contact may exist between two particles that are separated (Itasca, 2008).

8.2.2.3 Bonding Models

In *PFC*^{2D}, there are two types of bonding models correspond to two physical possibilities: contact bond and parallel bond. The bonding logic is illustrated in Figure 8.2. Contact bonds reproduce the effect of adhesion acting over the vanishingly small area of the contact point, thus the name contact bond. Parallel bonds reproduce the

effect of additional material (e.g., cementation) deposited after the balls are in contact. The effective stiffness of this additional material acts in parallel with the contact point stiffness, thus the name parallel bond.

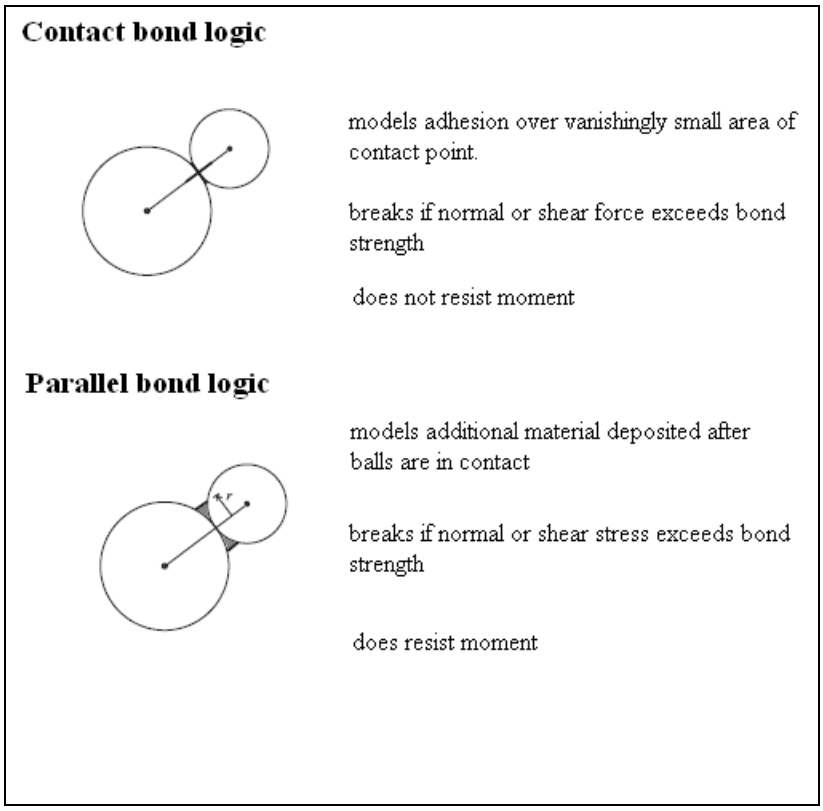

Figure 8.2: *PFC*^{2D} bonding logic

A contact bond provides each contact point with a tensile normal and shear contact-force strength. This allows a tensile force to develop between two particles. If the magnitude of the tensile normal or shear contact force exceeds the respective strength, the bond breaks. Two particles with a contact bond behave as though they are welded together at the contact point; thus, no slip is possible while the bond remains intact. However, a contact bond provides no resistance to rolling. Contact bonds are appropriate when one wishes to provide an absolute fixed limit on the tensile normal and shear contact forces. In the absence of a contact bond, the slip model is active, which provides no tensile normal strength and limits the shear contact force based on the contact friction coefficient and the compressive normal contact force. Contact bonds are often used to create bonded assemblies of particles which will remain

together after the confining walls have been removed. They are not suitable for modelling fracture of solid intact rock.

A parallel bond approximates the physical behaviour of a cement-like substance lying between and joining the two bonded particles. It can be envisioned as a piece of elastic glue that connects the two particles. Parallel bonds are appropriate when one wishes to preclude the possibility of rolling without slip at each contact, and also when one wishes to model the effect of a cementation process occurring after an assembly has already been loaded (Itasca, 2008). Parallel bonds establish an elastic interaction between particles that acts in parallel with the slip or contact-bond constitutive models. They can transmit both force and moment between particles, while contact bonds can only transmit force acting at the contact point. Thus, parallel bonds are appropriate for modelling solid rock.

8.2.3 Choosing Microscopic Properties

While it is relatively easy to assign chosen microscopic properties to a *PFC*^{2D} model, it is often difficult to choose such properties so that they represent a real intact material (with the required macroscopic properties). For codes that model continua (e.g., finite-difference or finite-element programs), the input properties can be derived directly from measurements on laboratory samples. However, *PFC*^{2D} works at a more basic level, as it synthesizes material behaviour from the micro-components that make up the material. If the properties and geometry of these micro-components are known, then they can be used directly as input to *PFC*^{2D}. But if it is desired to simulate a solid, such as rock, the properties of the microscopic constituents are not usually known. In this case, “inverse modelling” should be used i.e., perform a number of tests on samples with assumed properties and compare the results with the desired response of the real intact material. When a match has been found, the corresponding set of properties may be used in the full simulation. This inverse modelling method was also used in this study.

8.3 Mechanical Modelling

8.3.1 Introduction

In a broad sense, one can characterize any model of a synthetic material by the parameters of deformability and strength. In order to ensure that a particular model is reproducing desired physical behaviour, it is necessary to relate each model parameter to a set of relevant material properties. In the case of the *PFC* model, the model parameters cannot, in general, be related directly to a set of relevant material properties because the behaviour of the *PFC* model is also affected by particle size and packing arrangement (Itasca, 2008).

For continuum models, the input properties (such as elastic modulus and strength) can be derived directly from measurements performed on laboratory specimens. For the *PFC* model, which synthesizes macro scale material behaviour from the interactions of micro scale components, the input properties of the components usually are not known. The relation between model parameters and commonly measured material properties is only known a priori for simple packing arrangements.

For the general case of arbitrary packings of arbitrarily sized particles, the relation is found by means of a ***calibration process*** in which a particular instance of a *PFC* model (with a particular packing arrangement and set of model parameters) is used to simulate a set of material tests (e.g., unconfined compression test, Brazilian test, etc.). The *PFC* model parameters are then chosen to reproduce the relevant material properties as measured in such tests.

8.3.2 Calibration Steps Followed

8.3.2.1 Specification of Specimen Geometry

The first step in the calibration process is specification of specimen geometry. This includes total particle size (width and height), ball minimum size (R_{min}) and the radius ratio (R_{max}/R_{min}) of the balls. For the binary ore models examined, the total particle size was fixed as 20 mm × 40 mm. This total particle size was within the range of the particle size that is required in current microwave equipment used for experimentation. The aspect ratio was based on the requirement for a standard biaxial

test. The minimum radius of the balls for all models was fixed at 0.1 mm. Potyondy and Cundall (2004) demonstrated that ball size is an intrinsic part of the material characterization that affects the Brazilian tensile strength thus, it cannot be regarded as a free parameter that only controls model resolution. They also showed that for a given microscopic bond strength, decreasing the ball size (increasing the number of balls) will decrease the tensile strength of the material.

The model materials were produced by using the material-genesis procedure in *PFC*. The material-genesis procedure in *PFC* produces a synthetic material consisting of balls in a material vessel such that it forms an isotropic and well-connected system at a specified confining pressure. The ratio (R_{max}/R_{min}) was set to 1.66 to produce an arbitrary isotropic packing as suggested by Potyondy and Cundall (2004). The radius multiplier ($\overline{\lambda}$), which is used to set the parallel-bond radii was set equal to 1 to produce a material with cement that completely fills the throat between cemented particles. The final bonded particles of the models generated after the material genesis procedure was consisted of 13244 balls. Figure 8-3 shows the specimen filled with balls.

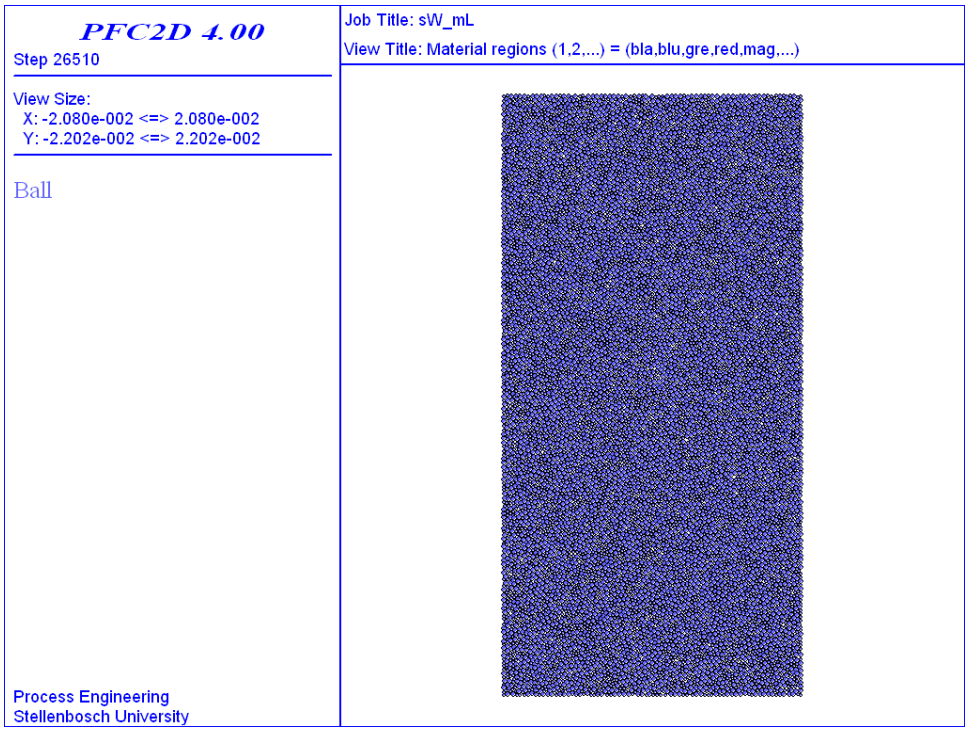

Figure 8.3: Specimen showing balls

8.3.2.2 Specification of Microscopic Properties

After the specimen geometry was constructed, a series of tests was performed in order to determine and match the macroscopic elastic properties of the samples by varying the microscopic properties. The complete set of micro-parameters that characterize a parallel-bonded material is given in Table 8-1.

Table 8-1: Complete set of micro-parameters that characterize a parallel-bonded material

Symbol	Description
ρ_b	Ball density
R_{min}	Minimum radius of the ball
R_{max}/R_{min}	Ratio of maximum radius to minimum radius of the ball
$\overline{\lambda}$	Radius multiplier used to set the parallel-bond radii
E_C	Young's modulus at each particle-particle contact
(k_n/k_s)	Ratio of particle normal to shear stiffness
$\overline{E}_C$	Young's modulus of each parallel bond
$(\overline{k}_n/\overline{k}_s)$	Ratio of parallel-bond normal to shear stiffness
μ	Particle friction coefficient
$\overline{\sigma}_c$ (Mean & std. dev.)	Normal(tensile) strength of the cement
$\overline{\tau}_c$ (Mean & std. dev.)	Shear strength of the cement

The macro mechanical properties of minerals modelled are tabulated in Table 8-2. The elastic properties of the minerals, Young's Modulus (E) and Poisson ratio (v) were calculated from their bulk (K) and shear (G) moduli, which were obtained from Bass (1995) and the tensile strengths of the minerals were typical values quoted for the minerals in (Lama and Vutukuri, 1978).

Table 8-2: Macro mechanical properties of minerals

Mineral	ρ (kg/m^3)	K (GPa)	G (GPa)	E (GPa)	ν	σ_t (MPa)
Calcite	2712	73.3	32.0	83.8	0.31	12
Dolomite	3795	94.5	45.7	118.1	0.29	11.7
Magnetite	5206	161.0	91.4	230.6	0.26	15
Galena	7597	58.6	31.9	81.0	0.27	12

One of the disconcerting issues in using *PFC* to represent a material is that when one wants to match the compressive strength of the model material, the tensile strength that would be obtained is about 0.25 of the uniaxial compressive strength. This is disproportionately high, compared with most rocks where the ratio is typically reported as 0.04 to 0.1 (Cho et al, 2007).

Diederichs (2000) showed that when *PFC* was calibrated to the uniaxial compressive strength, it significantly over-predicted the tensile strength. Potyondy and Cundall (2004) also demonstrated that calibrating *PFC* to the uniaxial strength gave very low triaxial strengths and required a cluster logic to increase the friction angles to more realistic values. Currently, it is not possible to match both tensile strength and compressive strength of a material using the same microscopic properties of spherical/circular particles. Thus, the material strength could be calibrated either with uniaxial compressive strength or the Brazilian tensile strength but not with both.

However, as has been shown previously by many authors and also in Chapter 7 in this study, the main cause of the damage in an ore after microwave treatment is the thermally induced tensile stresses during the expansion of the absorbent phases, exceeding the tensile strength of the ore (Salsman et al., 1996; Whittles et al., 2003; Jones et al., 2005). Thus, it is noticeable that for such model, the tensile strength is more important than the compressive strength of the material. Accordingly, the strengths of the model materials were obtained by comparing the model Brazilian tensile strength with the tensile strength of the materials. However, biaxial tests were also performed to match the elastic properties of the materials.

8.3.2.3 Biaxial Test for Matching Elastic Properties

The bulk properties of any given synthetic material can be determined by performing a series of tests on that particular material. These tests are performed numerically, and are designed to simulate similar tests performed in the laboratory. One such test is the biaxial test. It can be used to estimate the elastic and plastic material responses. The procedures necessary to perform a biaxial test using *PFC*^{2D} are detailed in (Itasca, 2008). In this study, a series of biaxial tests on the model materials (obtained by altering the *PFC*^{2D} micro-properties) were performed.

To reproduce a given modulus, the bond strengths were set to a large value to prevent bond failure and thereby force the material to behave elastically and then a series of biaxial tests were performed to obtain the modulus of the model materials. Then, the microscopic moduli were chosen to match the Young's moduli of the minerals.

PFC simulates a biaxial test by confining a rectangular sample (comprised of a compacted particle assembly) within four walls (Figure 8.4). The top and bottom walls simulate loading platens, and the left and right walls simulate the confinement experienced by the sample sides. The sample was loaded in a strain-controlled fashion by specifying the velocities of the top and bottom walls.

During all stages of the test, the velocities of the left and right walls were controlled automatically by a numerical servomechanism (implemented via a *FISH* function) that maintains a constant confining stress within the sample. The stresses and strains experienced by the sample were determined in a macro-fashion by summing the forces acting upon, and relative distance between, the appropriate walls. Materials responses were computed by tracking the various stress and strain quantities using the *HISTORY* logic.

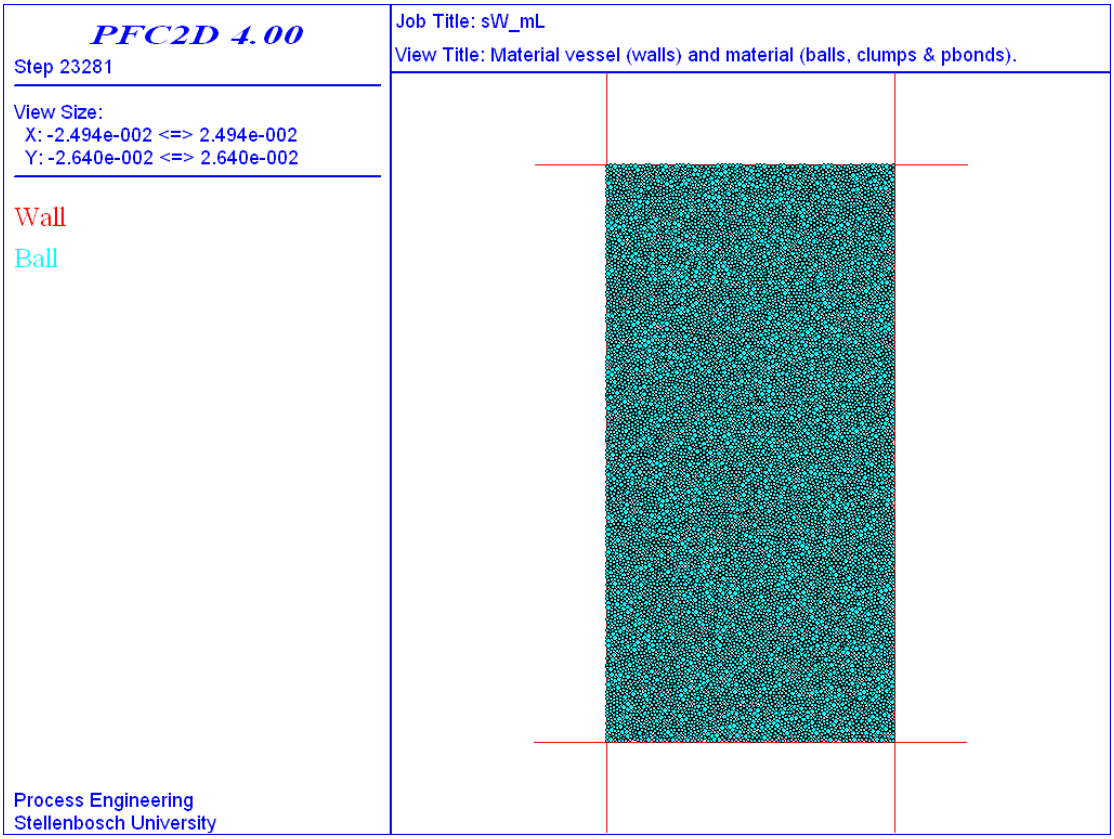

Figure 8.4: Specimen with confining walls prepared for biaxial test

The loading rate should be set sufficiently slow enough to ensure the sample remains in quasi-static equilibrium throughout the test and should be stable so as not to induce any possible strength increase or unexpected material responses within the simulated models (Itasca, 2008). One can ensure that such a response has been obtained by conducting a strain-controlled test at a series of constant platen velocities, and demonstrating that the response is the same for all platen velocities below some critical velocity. After running the test with different loading rates, a value of 0.02 m/s was found to be slow enough for the specimens considered in this study and this was set for testing all the model materials in biaxial test tests at 0.1 MPa confinement.

Figures 8-5 to 8-8 show the final results of simulation of the biaxial tests for different model materials.

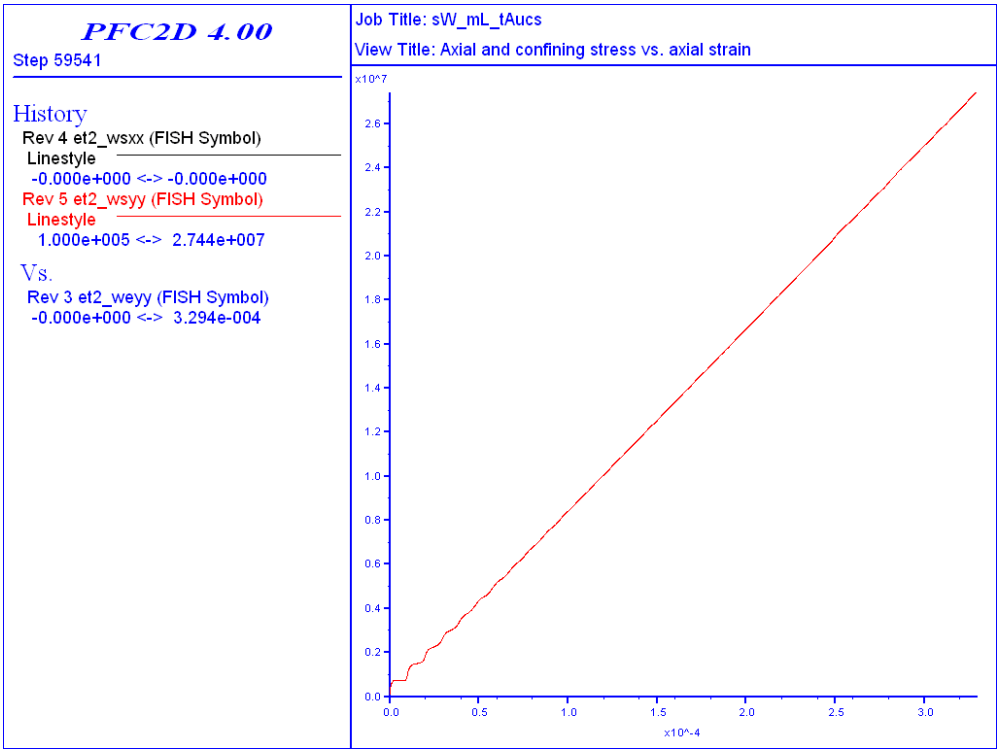

Figure 8.5: Biaxial test final result of calcite (Young's modulus = slope = 83.3 GPa)

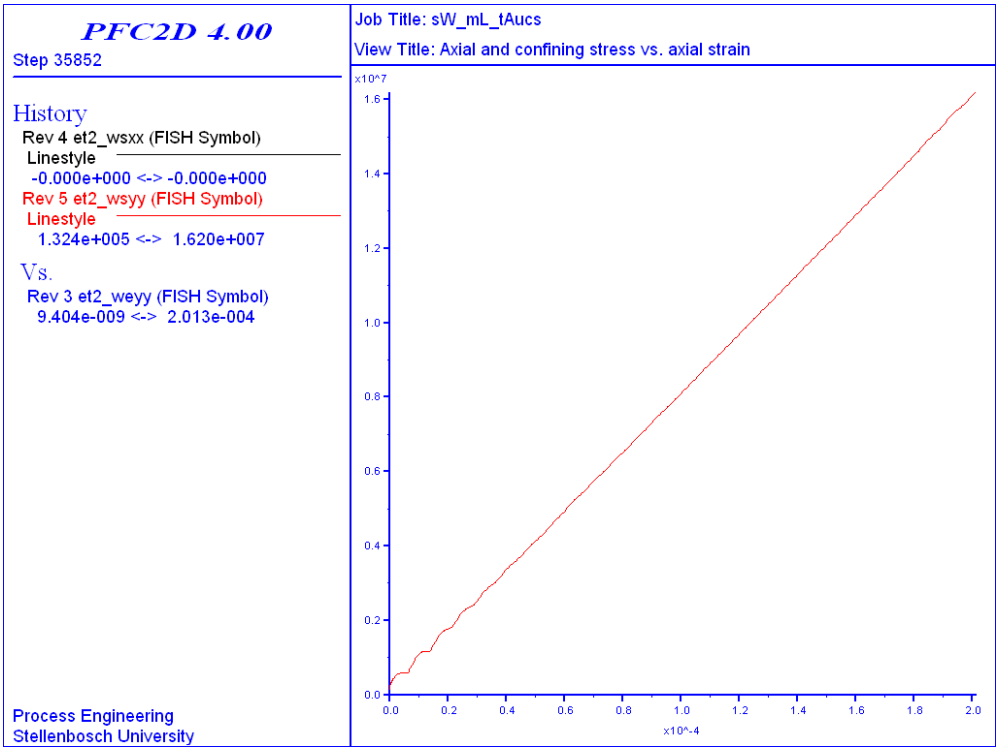

Figure 8.6 : Biaxial test final result of galena (Young's modulus = slope = 80.5 GPa)

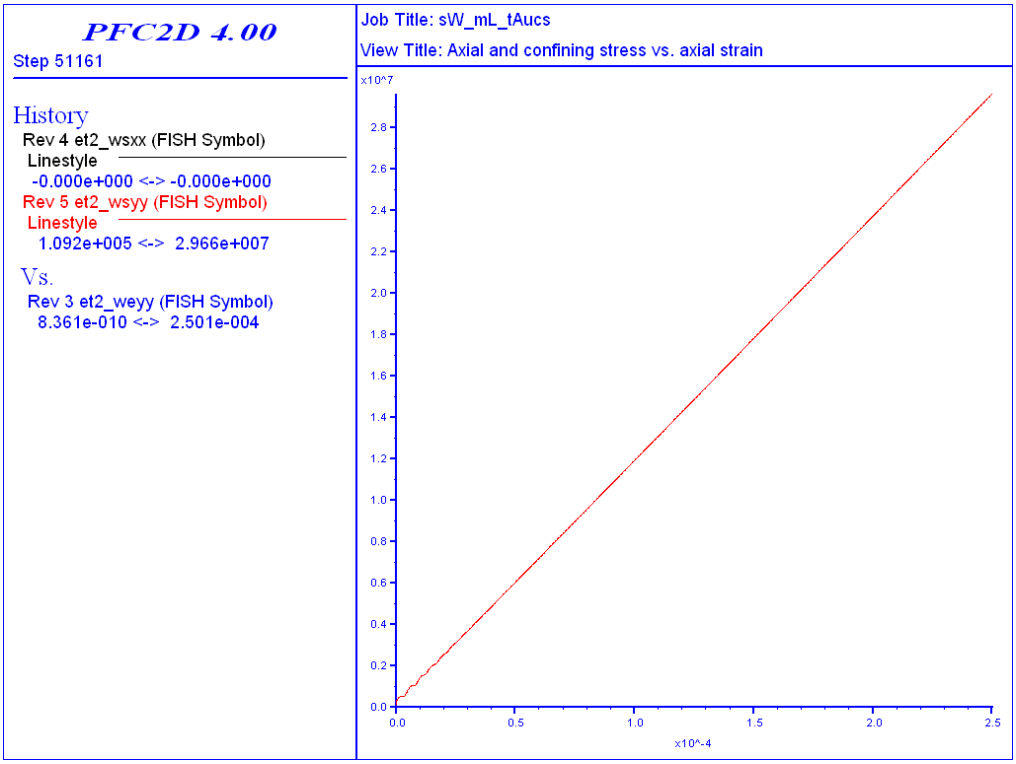

Figure 8.7: Biaxial test final result of dolomite (Young's modulus = slope = 118.5 GPa)

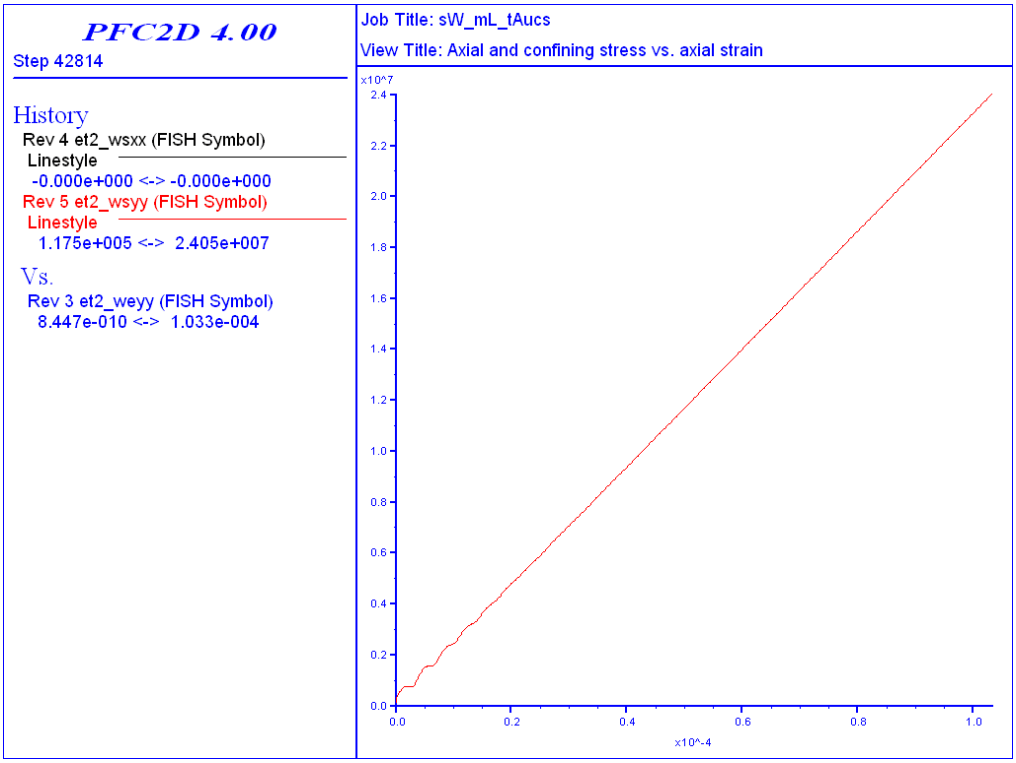

Figure 8.8: Biaxial test final result of magnetite (Young's modulus = slope = 232.8 GPa)

The ratios of normal to shear stiffness are normally chosen to match the material Poisson's ratio. However, as Potyondy and Cundall (2004) mentioned, direct comparison of Poisson's ratio in *PFC*^{2D} with laboratory result is not that meaningful because of the limitation in 2D analysis of *PFC*. The fundamental assumption for particle elements employed in *PFC*^{2D} is that particles are either disks having finite thickness or spheres having single layer toward out of plane direction. The former is similar to the plane strain condition and the latter is similar to the plane stress condition in continuum mechanics.

However, unlike continuum mechanics assumption, there is no out of plane stress in plane strain and no out of plane strain in plane stress in *PFC*^{2D}. Hence, attempts to match volumetric strain or Poisson's ratio in *PFC*^{2D} material to match 3D physical material are not always successful (Potyondy and Cundall, 2004). Hence, no attempt was made for calibrating the ratio with laboratory results and it was fixed to be 2.5 which is typical value used for most common rock (Cho et al., 2007).

Next, the cement shear and tensile strength were set equal to one another so as not to exclude mechanisms that may only be activated by micro shear failure. Potyondy and Cundall (2004) demonstrated that by setting $\bar{\sigma}_c = \bar{\tau}_c$, both tensile and shear micro failures can be allowed to occur.

For all the models a 20% ratio of standard deviation to mean of the cements strength was used, assuming the materials to be brittle. This was deemed to be typical value for a brittle rock (Itasca, 2008). In general, a *PFC* material with a small standard deviation to mean ratio will fail in a brittle fashion (predominantly in tension, whereby bond normal strength is exceeded), while a material with a large ratio will fail in a ductile fashion (predominantly in shear, whereby bond shear strength is exceeded).

Potyondy and Cundall (2004) also demonstrated that the particle-friction coefficient appears to affect only post-peak response, and it is not yet clear to what it should be calibrated. Thus, μ = 0.5 was set for all models as a reasonable non-zero value (Itasca, 2008).

8.3.2.4 Brazilian Test for Matching the Tensile Strengths of the Materials

Finally, a series of Brazilian tests was performed by varying the mean value of the cement strengths to match the tensile strengths of the materials. The tests were made upon specimens created in the polyaxial cell. All walls were frictionless, and the normal stiffnesses of the platen walls and confining walls were set equal to 1 and 0.1, respectively, times the average particle normal stiffness of the material (Itasca, 2008). The polyaxial specimens were seated. Axial and confining stresses were applied by activating the servomechanism for all opposing walls, and cycling (Itasca, 2008). The specimens were trimmed into disk shapes that were in contact with the lateral walls.

Next, the top and bottom walls were moved apart by a distance of 0.05 w, and their velocities were set to zero throughout the remainder of the test. This was done to ensure that only the lateral walls will be in contact with the specimen during the subsequent testing. The specimen was loaded by moving the horizontal platens toward one another at the final velocity, V_p, using the platen-based loading. The average force (F) acting on the lateral walls (obtained by averaging the total force acting on each lateral wall) was monitored, and the maximum value was recorded. During a typical test, this value will increase to some maximum and then decrease as the specimen fails.

The loading rate for Brazilian test should also be set sufficiently slow enough to ensure the sample remains in quasi-static equilibrium throughout the test and should be stable so as not to induce any possible strength increase or unexpected material responses within the simulated models (Potyondy and Cundall, 2004). After running the test with different loading rates, a value of 0.01 m/s was found to be slow enough for the specimens considered and this was set for testing all the model materials in Brazilian test.

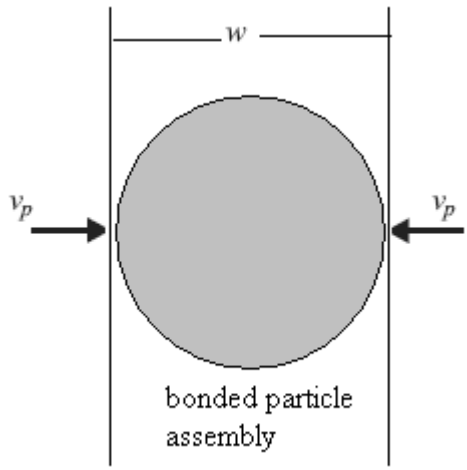

Figure 8.9: Sketch of Brazilian test

After the Brazilian test was completed, The peak force (F_f) acting on the platens was extracted automatically. The Brazilian tensile strength, σ_t, was then computed by using Equation 8.3.

$$\sigma_t = \frac{F_f}{\pi R t} \text{ , } \mathbf{t} = 1.0 \qquad \mathbf{8.3}$$

Where R is the radius of the Brazilian disk.

Figures 8-10 to 8-13 show the final result of the Brazilian tests for different model materials.

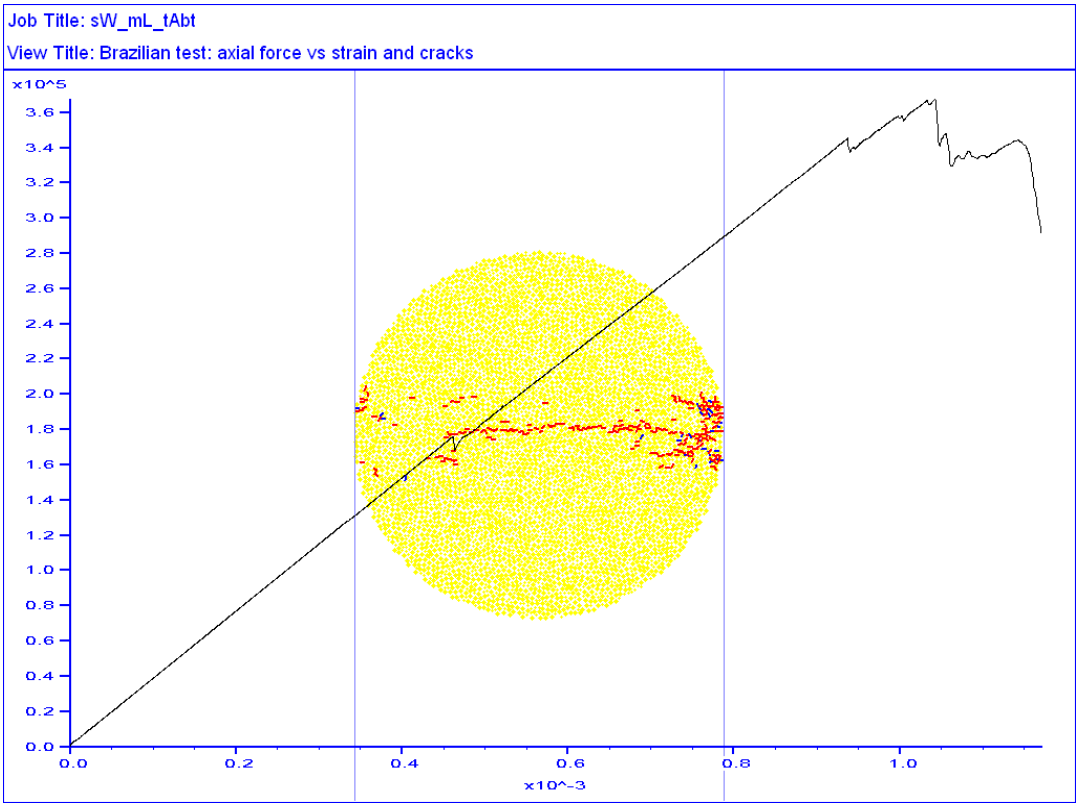

Figure 8.10: Brazilian test final result of calcite, $F_f = 3.77 \times 10^5$ N , $\sigma_t = 12.01$ MPa

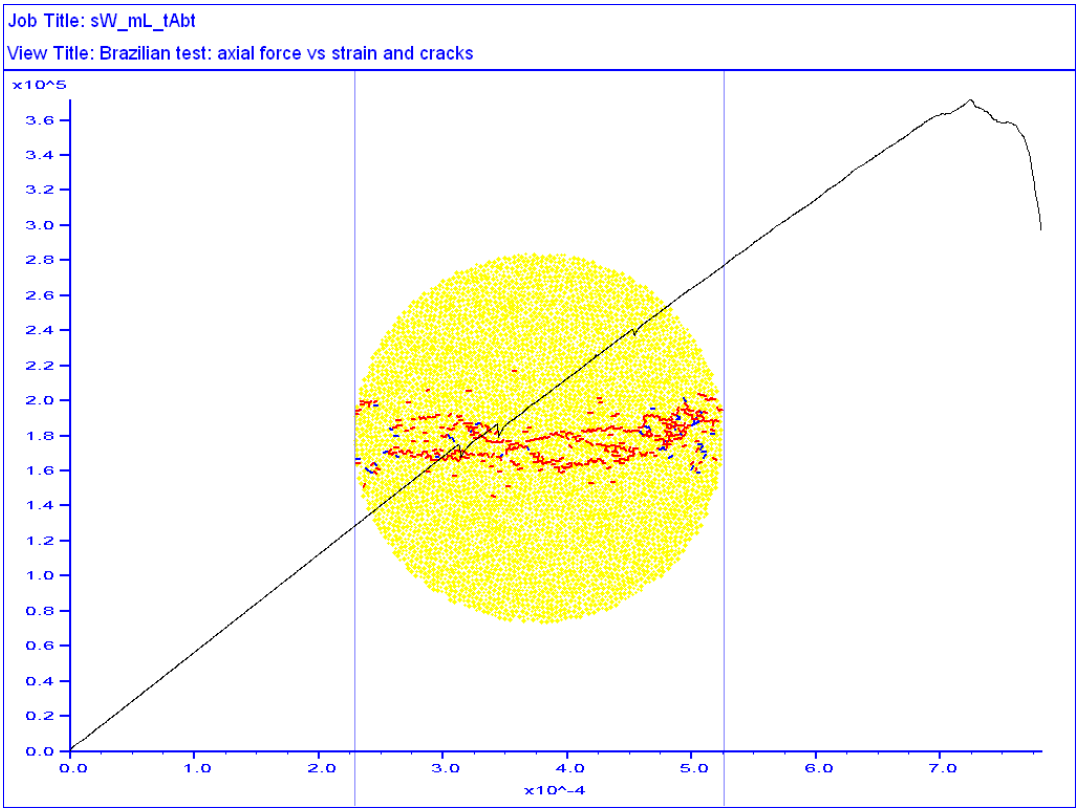

Figure 8.11: Brazilian test final result of dolomite, $F_f = 3.70 \times 10^5$ N , $\sigma_t = 11.78$ MPa

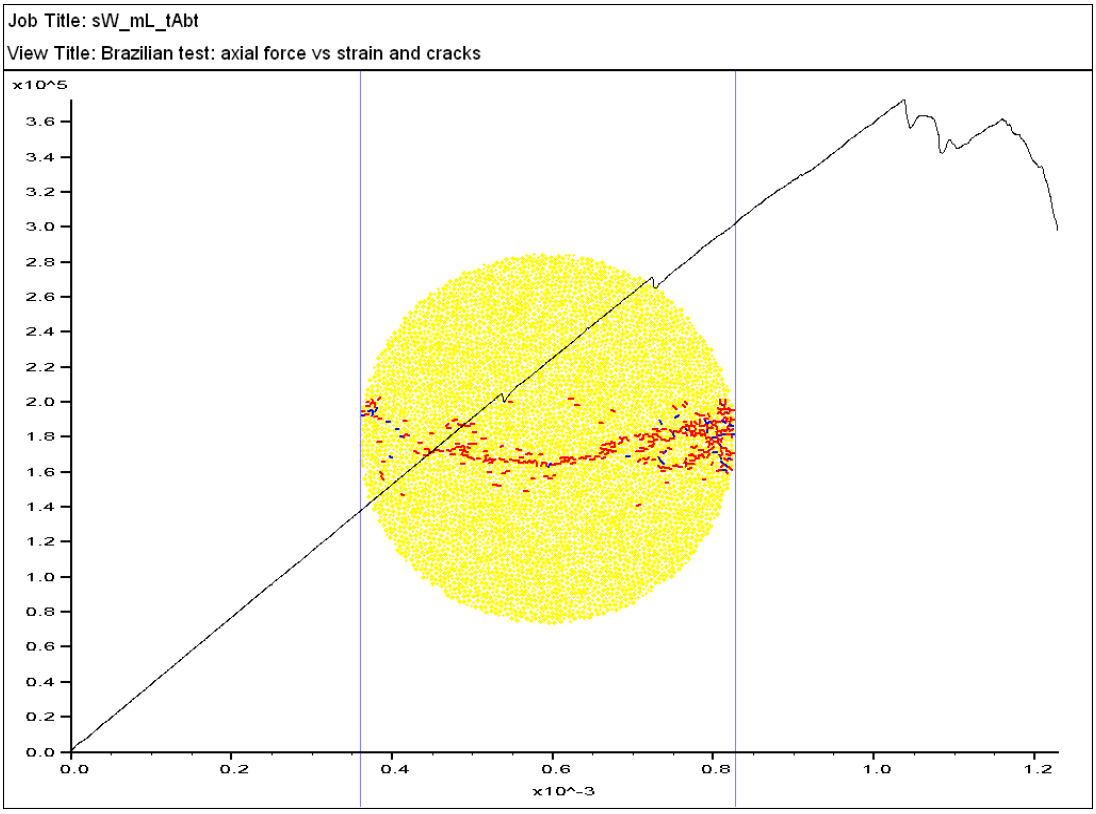

Figure 8.12: Brazilian test final result of galena, $F_f = 3.78 \times 10^5$ N, $\sigma_t = 12.04$ MPa

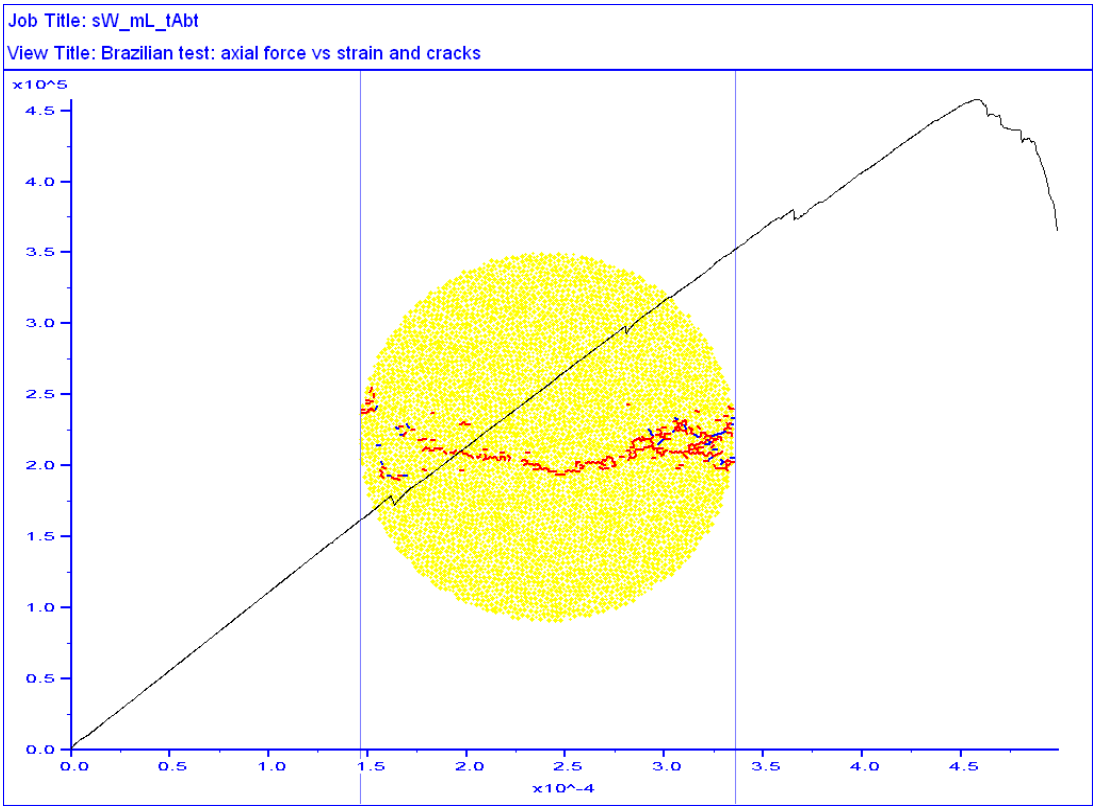

Figure 8.13: Brazilian test final result of magnetite, $F_f = 4.70 \times 10^5$ N, $\sigma_t = 14.98$ MPa

8.3.2.5 Density of Ball

When representing a solid continuum, the density of the ball (ρ_b) should be chosen such that the *PFC*^{2D} material has the same total mass in a fixed volume of material as does the physical material. This condition is satisfied by setting ρ_b as:-

$$\rho_b = \rho / (1-n) \qquad \textbf{8.4}$$

Where ρ is the density of the solid continuum, and n is the average porosity of the *PFC*^{2D} material. For densely packed and bonded *PFC*^{2D} assemblies, the value of n is fixed by the initial microstructure and is approximately 0.16 (Itasca, 2008). Table 8.3 shows the bulk densities and ball densities of the materials modelled.

Table 8-3: Bulk densities and ball densities of minerals

Mineral	Bulk density(ρ) (kg/m^3)	Density of ball (ρ_b)(kg/m^3)
Calcite	2712	3228.6
Galena	7597	9044.0
Dolomite	3795	4517.9
Magnetite	5206	6197.6

Tables 8-4 to 8-7 show the complete model mechanical micro properties used for modelling the materials.

Table 8-4: Model micro properties for calcite

Grains	Cement
ρ_b = 3228.6 kg/m^3	$\bar{\lambda}$ = 1
E_C = 66 GPa	$\bar{E}_C$ = 66 GPa
R_{min}= 0.1 mm	$(\bar{k}_n/\bar{k}_s)$= 2.5
R_{max}/R_{min} = 1.66	$\bar{\sigma}_c = \bar{\tau}_c$ = (mean ± std.dev) = 51 ± 10 MPa
(k_n/k_s)= 2.5	
μ = 0.5	

Table 8-5: Model micro properties for dolomite

Grains	Cement
ρ_b = 4517.9 kg/m^3	$\bar{\lambda}$ = 1
E_C = 95.5 GPa	$\bar{E}_C$ = 95.5 GPa
R_{min}= 0.1 mm	$(\bar{k}_n/\bar{k}_s)$= 2.5
R_{max}/R_{min} = 1.66	$\bar{\sigma}_c$ = $\bar{\tau}_c$ = (mean ± std.dev) = 49 ± 10 MPa
(k_n/k_s)= 2.5	
μ = 0.5	

Table 8-6: Model micro properties for galena

Grains	Cement
ρ_b = 9044 kg/m^3	$\bar{\lambda}$ = 1
E_C = 64.5 GPa	$\bar{E}_C$ = 64.5 GPa
R_{min}= 0.1 mm	$(\bar{k}_n/\bar{k}_s)$= 2.5
R_{max}/R_{min} = 1.66	$\bar{\sigma}_c$ = $\bar{\tau}_c$ = (mean ± std.dev) = 51 ± 10 MPa
(k_n/k_s)= 2.5	
μ = 0.5	

Table 8-7: Model micro properties for magnetite

Grains	Cement
ρ_b = 6197.6 kg/m^3	$\bar{\lambda}$ = 1
E_C = 188 GPa	$\bar{E}_C$ = 188 GPa
R_{min}= 0.1 mm	$(\bar{k}_n/\bar{k}_s)$= 2.5
R_{max}/R_{min} = 1.66	$\bar{\sigma}_c$ = $\bar{\tau}_c$ = (mean ± std.dev) = 56± 11 MPa
(k_n/k_s)= 2.5	
μ = 0.5	

8.4 Thermo-mechanical Coupling

8.4.1 Modelling Equations

PFC supports both thermal-only and coupled thermal-mechanical analysis. Simulation of transient heat conduction and storage in materials consisting of particles, and development of thermally induced displacements and forces are possible.

In *PFC*, the thermal material is represented as a network of heat reservoirs (associated with each particle) and thermal pipes (associated with the contacts). Heat flow occurs via conduction in the active pipes that connect the reservoirs. Each ball represents a heat reservoir. Associated with each reservoir is a temperature, a mass, a volume, the specific heat, and coefficient of linear thermal expansion. The temperature is computed during the thermal simulation, and the mass and volume are determined from the ball density, radius and assumed shape.

A thermal pipe is associated with each contact, but only some of these pipes are active. A pipe is active if the two particles at the contact are overlapping, or if a bond is present. A pipe joins two reservoirs, and heat flow only occurs through pipes. Associated with each pipe is a power, Q, and a thermal resistance, η. Each pipe has a finite length that is equal to the distance between the centroids of the two connected particles (Itasca, 2008).

Thermally induced strains for a temperature change (ΔT) are produced in the model material by modifying the particle radii and the force carried in each parallel bond to account for the thermal expansion of both particles and the bonding material that join them. For a temperature change (ΔT) the change in radius is given by:-

$$\Delta R = \alpha R \Delta T \qquad \textbf{8.5}$$

Where R is the radius of the ball

And the change in the normal component of the bond force (ΔF^n) as:-

$$\Delta F^{n} = \bar{k}_{n} A(\bar{\alpha} L \Delta T) \qquad \textbf{8.6}$$

Where $\bar{k}_{n}$ is the bond normal stiffness, A is the area of the bond cross section and $\bar{\alpha}$ is the expansion coefficient of the bond material (taken equal to the average value of the expansion coefficients of the particles at the two ends of the pipe associated with the bond) and L is the bond length.

8.4.2 Power Density Specification in *PFC*

In *PFC*, like *FLAC*, a heat-generating source can be assigned to each particle in the specified range. However, in *PFC*, the heat generating source is in units of W, as there is no explicit representation of the boundary (unlike in a continuum code, where zone surfaces comprise the boundary). Hence, the power density (W/m^3) should be multiplied by the volume of each ball/particle in order to assign a power source in each ball. Whenever a heat source is applied to a particle, its value replaces the existing source strength. Table 8-8 shows the *FISH* code used for specifying power density in the absorbent mineral.

Table 8-8: Power density specification in *PFC*

```
def  powerdensity
powerdensity=1e11                    ; power density(W/m^3) value
end

thermal set dt_max 1e-6          ; thermal step time

def source       ; specify Heat-generating source (in units of W)
bp=ball_head
loop while bp # null              ; Search all balls
if b_dens(bp)= 9044 then       ;  apply power (W) to the absorbent phase(galena)
power_inwatt=powerdensity*(22/7)*b_rad(bp)*b_rad(bp)*1
b_thpsrc(bp)=power_inwatt
end_if
bp=b_next(bp)
end_loop
end
source            ; execute
```

8.4.3 Specification of Thermal Properties in *PFC*

8.4.3.1 Specific Heat Capacity of Ball

Specific heat capacity of the ball should be set equal to the value for a solid continuum (Itasca, 2008). The specific heat capacity of the balls for each mineral was written as a function of temperature in *PFC*'s *FISH* code. Table 8-9 shows the *FISH* code used for specifying the heat capacity of galena as a function of temperature.

Table 8-9 *FISH* code used for specifying specific heat capacity of galena as a function of temperature in *PFC*

```
if b_dens(bp) = 9044 &
if (b_thtemp(bp) + 273) < 500 then
b_thsheat(bp)=(0.0311*(b_thtemp(bp)+273))+199.68
end_if
end_if

if b_dens(bp) = 9044 &
if (b_thtemp(bp) + 273) >=  500 then
b_thsheat(bp)=(0.03942*(b_thtemp(bp)+273))+195.52
end_if
end_if
```

8.4.3.2 Thermal Resistance per unit Length

In *PFC*, the thermal resistance per unit length (η) should be specified to all pipes. It is also possible to directly specify a mean thermal conductivity of the thermally isotropic material and the software will automatically compute the value of η that, if assigned to all pipes produce the required mean thermal conductivity. For the ore models considered, the mean thermal conductivities were specified. It is not possible to specify thermal conductivity as a function of temperature in *PFC*; hence, constant values were assigned. Table 8-10 shows the *FISH* code for specifying the mean thermal conductivity of calcite in *PFC*.

Table 8-10: *FISH* code used for specifying mean thermal conductivity for calcite

```
CONFIG therm

THERM MAKE conductivity 3.16 measure 2
```

8.4.3.3 Thermal Expansion Coefficient of Ball

The thermal expansion coefficient value of the ball was set to be equal to thermal expansion of the solid material. This appears to be a plane stress condition; however, as has been discussed in section 8-3, there is no out of plane stress in plane strain and no out of plane strain in plane stress in *PFC*^{2D}. Table 8-11 shows the *FISH* code used for specifying thermal expansion coefficient of galena as a function of temperature.

Table 8-11 *FISH* code used for specifying thermal expansion coefficient of galena as a function of temperature in *PFC*

```
if b_dens(bp) = 9044 &
if (b_thtemp(bp) + 273) < 673 then
b_thexp(bp)=((0.0067*(b_thtemp(bp)+273))+58.710)*1e-6
end_if
end_if

if b_dens(bp) = 9044 &
if (b_thtemp(bp) + 273) >= 673 then
b_thexp(bp)=((0.0180*(b_thtemp(bp)+273))+51.091)*1e-6
end_if
end_if
```

The complete simulation codes used for modelling microwave heating and quantifying microwave-induced micro-cracks for each binary ore are presented in Appendices K and N.

8.5 Microwave-induced Micro-cracks in a Simple Ore Model

8.5.1 Introduction

It has been shown previously using the continuum approach that power density has a significant effect on the extent of damage in microwave treated ore. However, this was done by quantifying the stress distribution in the ore samples, as it was not possible to simulate crack propagation using a continuum approach.

The brittle failure of rock is a progressive process. It involves initiation, growth, interaction and coalescence of micro-cracks leading to the formation of macro-fracture. A test was required to quantify thermally induced micro-cracks and examine the crack pattern directly instead of the indirect method used previously. Accordingly, this study details how the distinct element method was used to quantify micro-cracks induced by microwave irradiation. The aim was to better understand the crack formation and propagation in a microwave treated ore; hence, a simple texture model was used for the study. Prior to simulation, it was thought that there would be a marked difference in crack pattern in ore sample treated at different power densities.

8.5.2 Methodology

PFC allows visualization of crack propagation and also quantification of micro-cracks inside the model material. By definition: Micro-crack occurs when the stress in the bond exceeds the assigned normal (tensile) or shear strength. Failure of a bond leads to a force redistribution around the breakage that can lead to further breakage.

Micro-cracks in a PFC^{2D} synthetic specimen may only form between bonded particles. Thus, the number and location of potential micro-cracks are limited by the number and location of the bonds in the initial specimen. The geometry and location of each micro-crack are determined by the sizes and current locations of the two parent particles from which the micro-crack originated.

Each micro-crack is assumed to be a cylinder whose axis lies along the line joining the two parent particles. The geometry and location are fully described by the thickness, radius, and unit-normal and centroid location. The thickness equals the gap between the two parent particles. The unit normal is directed along the line joining the centres of the two parent particles and the centroid lies along the line between the centres of the two parent particles and bisects the gap between the two parent particles.

The ore used for the study was a simple galena-calcite model consisting of a single spherical galena particle (2 mm) placed inside a cylindrical calcite matrix (5 × 10 mm) as shown in Figure 8-14. The ore was treated at power densities of 1×10^9 W/m^3 and 1×10^{11} W/m^3. The crack pattern and the number of micro-fractures for a particular microwave treatment condition were then examined. Micro-cracks that have formed as the result of the parallel-bond normal (tensile) strength having been exceeded were indicated by black colours. Micro-cracks that have formed as the result of the parallel-bond shear strength having been exceeded were indicated by red colours.

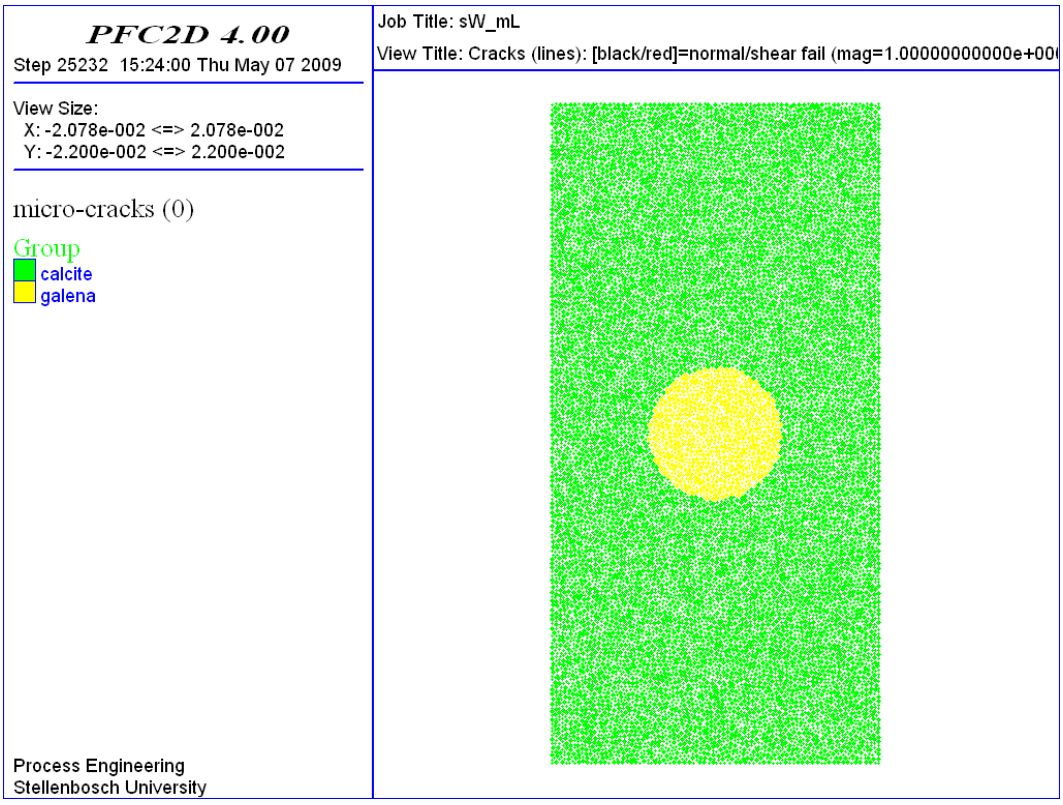

Figure 8.14: Untreated galena-calcite simple model

8.5.3 Results and Discussion

Figures 8-15 shows the crack pattern and the number of micro-fractures that were observed when the ore was treated at power density of 1×10^9 W/m^3. As can be seen, most of the cracks are tensile cracks (black colour) which are radially oriented and originated from the absorbent phase boundary. This is primarily due to the high tensile stresses, which were induced during the thermal expansion of the absorbent phase. Micro-fractures can be seen around the grain-boundary and on the calcite matrix. Few micro- fractures were also occurred inside the absorbent phase. However, most of the damage was outside the microwave absorbent phase (galena). It can be noted that the type of failure around the grain boundary region was predominately a tensile one. This was also seen when the continuum approach was used (refer Chapter 7). More damage was induced both around the grain boundary and on the calcite matrix as the exposure time increased.

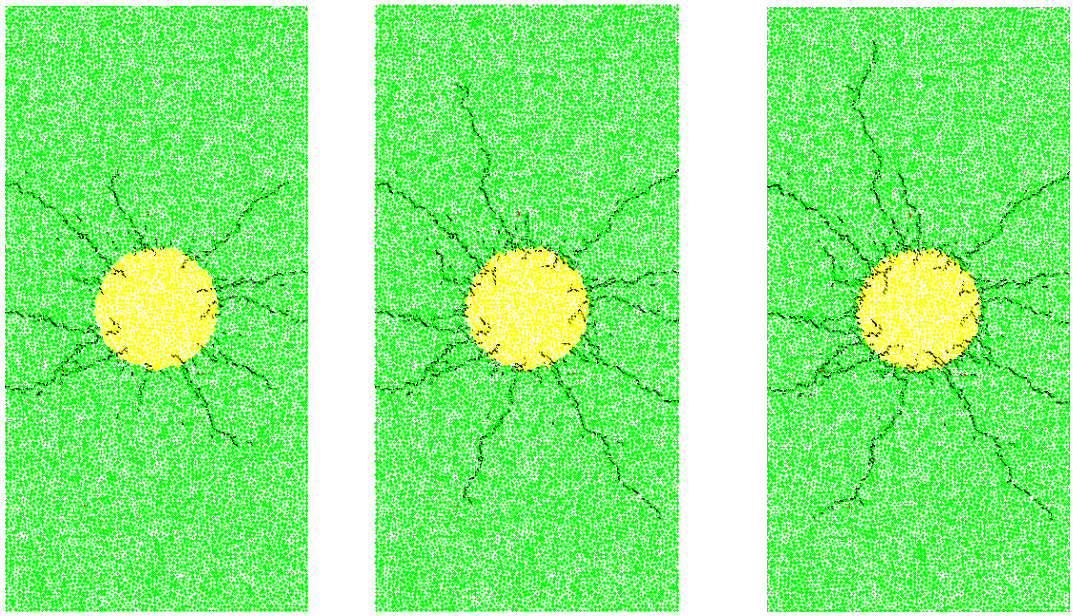

$P_d = 1 \times 10^9$ W/m^3, 0.1 s (Micro-cracks = 545)

$P_d = 1 \times 10^9$ W/m^3, 0.2 s (Micro-cracks = 795)

$P_d = 1 \times 10^9$ W/m^3, 0.3 s (Micro-cracks = 938)

Figure 8.15: Crack pattern in galena-calcite after microwave treatment at $P_d = 1 \times 10^9$ W/m^3

The results of simulation at a higher power density of 1×10^{11} W/m^3 are shown in Figure 8-16. It can be seen, as expected, that more damage was incurred in the ore when the power density increased for the same energy input. This can be noticed by comparing the number of micro–fractures obtained for the same energy input. But more importantly, the fracture patterns obtained at different power densities were also quite unlike. As can be seen from Figure 8-16, fractures were more localized around the grain boundary for the high power density case. There was almost no damage (fracture) in the absorbent phase. It is evident that it is advantageous to deposit much energy in a shorter time so that damage is more localized around the grain boundary. This is also in complete agreement with the result obtained using a continuum approach (refer Chapter 7). It is expected that for such microwave treatment condition there would be a possibility of liberation of the absorbent mineral at original size. The advantage of using high power equipment for microwave treatment of ores can be clearly seen from the figures.

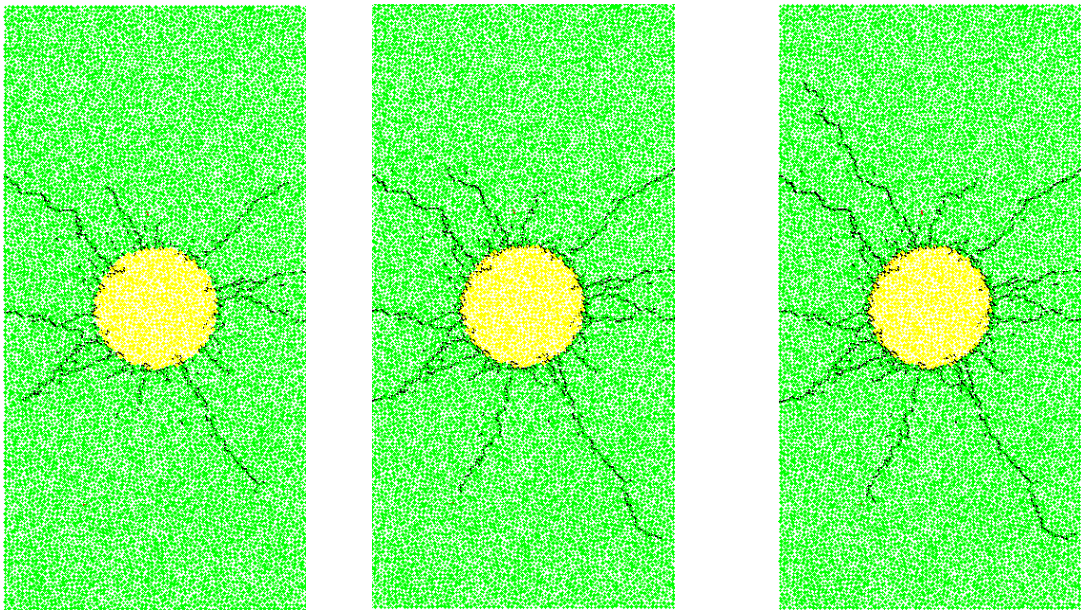

$P_d = 1 \times 10^{11}$ W/m^3, 1ms (Micro-cracks = 623)

$P_d = 1 \times 10^{11}$ W/m^3, 2 ms (Micro-cracks = 864)

$P_d = 1 \times 10^{11}$ W/m^3, 3 ms (Micro-cracks = 964)

Figure 8.16: Crack pattern in galena-calcite after microwave treatment at $P_d = 1 \times 10^{11}$ W/m^3

The pattern of fractures obtained for the high power density case closely matched the Scanning Electron Microscopy (SEM) image shown in Figures 8-17, which was observed experimentally. The ore consists of chalcopyrite in a calcite matrix and it was exposed to microwave irradiation of microwave power 3 MW and pulse duration of 1 μs at a pulse repetition frequency of 50 Hz for a total of 10 s.

Figure 8.17: Chalcopyrite particle in calcite matrix after exposed to pulsed microwave

8.5.4 Conclusions

The effect of microwave treatment of an ore at different power densities on the extent of damage and crack pattern was investigated. It has been shown that it is possible to induce greater number of micro-fractures for the same energy input by operating at higher power density. It was also shown that the micro-cracks for the high power density case were more localised around the grain boundary. It is suggested that this effectively facilitates liberation at original size and it also negates the need for further grinding to separate the heated phase from the transparent matrix.

8.6 Microwave-induced Micro-cracks for Randomly Disseminated Absorbent Phase

8.6.1 Introduction

The previous section showed how the distinct element method can be used to simulate and quantify thermally induced micro-fractures in an ore sample. This section presents the results of simulations of different binary ores having realistic textures exposed to microwave at different treatment conditions. The aim was to investigate in detail the effect of power density, mineralogy and absorbent phase grain size on extent of damage and fracture pattern in microwave treated ores.

8.6.2 Methodology

The model materials were produced by using the material-genesis procedure in *PFC* as discussed in section 8-3. For this case, different irregular shaped absorbent phase (galena/magnetite) grains were randomly disseminated in a transparent matrix (dolomite/calcite). The ores were assigned a composition of 10% of microwave absorbing mineral and 90% transparent matrix by volume. The total particle size was 20×40 mm. For each binary ore, two different textures were simulated: coarse-grained (grain size = 1 - 2.5 mm), and fine-grained (grain size = 0.1 - 0.25 mm). Typical textures are shown in Figure 8-18. Each ore was then exposed to microwave at different power densities ranging from 1×10^8 W/m^3 to 1×10^{11} W/m^3.

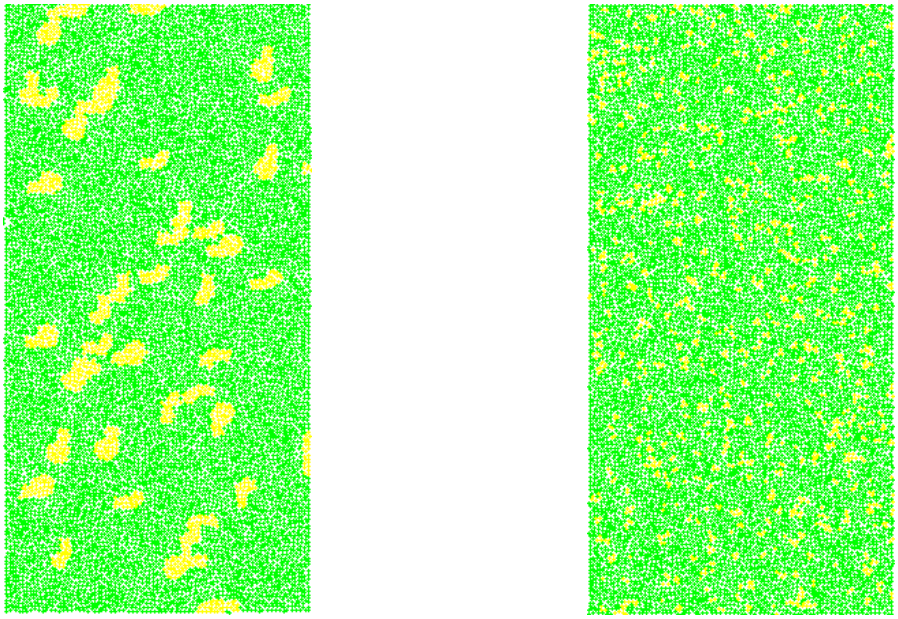

(a) (b)

Figure 8.18: Typical texture showing microwave absorbent phase (yellow) in transparent matrix (green) for a coarse-grained (a) and fine-grained (b) ores

8.6.3 Results and Discussion

Figures 8-19 shows the result of simulation of coarse-grained galena-calcite treated at a lower power density of 1×10^8 W/m^3. As can be seen, few micro-cracks (tensile), which were originated from the absorbent phase (galena) and propagated randomly, were induced even if the exposure time was increased up to 6 s. The driving force for the failure is generally believed to be the strong tensile stresses at the grain boundary of the absorbent phase. Increasing the exposure time increased the number of micro-fractures. However, the crack propagation patterns were similar i.e. they started from the absorbent phase boundary and propagated into the calcite matrix randomly. As can be seen, only few cracks were observed around the grain boundary and most of the cracks were induced in the calcite matrix. Micro-cracks can also be seen inside the absorbent phase (galena).

This type of damage would not have a significant benefit in mineral processing operation, as the damage occurred randomly in the bulk of the sample. In addition, the energy input required to induce significant micro-cracks even in the bulk of the sample was relatively large (> 4 kWh/t). The reason for this was previously explained using continuum approach, it was noted that when the power density was low and the exposure time was long, there would be a significant heat loss by conduction from the absorbent phase to the transparent matrix. This would decrease the temperature gradient between the two phases. Thus, as the exposure time increased, cracks will occur on the bulk of the sample randomly. However, as was discussed in section 8-3, since there is a variation of bond strength inside a *PFC* material (the bond strength was specified with a mean and standard deviation), it was suggested that crack propagation will follow areas at which the bond strength is low. In reality these areas could be natural flaws and pre-existing cracks.

The results of simulation of coarse-grained galena-calcite treated at power density of $P_d = 1 \times 10^9$ W/m^3 are shown in Figure 8-20. As can be seen, for this case, cracks start to occur at short exposure time of 0.05 s. It can also be seen that for the same energy input, more damage (number of micro-cracks) was incurred in the ore when the power density increased. This can be observed by comparing the number of micro–fractures obtained at $P_d = 1 \times 10^8$ W/m^3 for the same energy input. In addition, the fracture pattern observed was also quite different. It can be seen that most of the damage

occurred around the grain boundary of the absorbent phase. However, cracks were also observed inside the absorbent phase especially as the exposure time increased.

Figures 8-21 and 8-22 show the results of simulation of coarse-grained galena-calcite treated at high power density of 1×10^{10} W/m^3 and 1×10^{11} W/m^3, respectively. The effect of power density on microwave treatment of ore can be clearly seen from these figures. From Figure 8-22, it can be seen that damage was more localized around the grain boundary compared to the damage obtained at lower power densities. However, as exposure time increased, few cracks inside the absorbent phase were also observed. It is noticeable that for this case the exposure time should be below 0.03 s in order not to damage the absorbent mineral. In addition, rate of increase in the number of micro-fractures that would be obtained by increasing the exposure time (hence, the energy input) slowed after this time, indicating that the amount of damage tends to an asymptotic value. This situation was previously seen when the continuum approach was used (refer Chapter 7).

It can be seen also from Figure 8-22 ($P_d = 1 \times 10^{11}$ W/m^3) that relatively more damage (number of micro-fractures) was obtained as the power density increased at all energy inputs. However, the crack pattern was very similar to that was seen for the power density of 1×10^{10} W/m^3. As can be seen the majority of the damage was around the grain boundary and there was almost no damage inside the microwave absorbent phase. The practical implication of this is that for such kind of microwave treatment conditions, there would be a possibility of liberation of the absorbent mineral at original size. It is also expected that the energy required for grinding the damaged ore for this case would be significantly reduced.

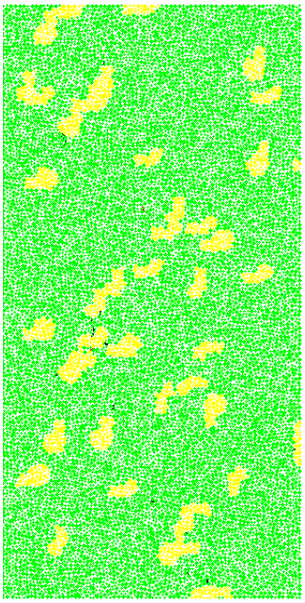

$P_d = 1 \times 10^8$ W/m^3, 1 s
(Micro-cracks = 21)

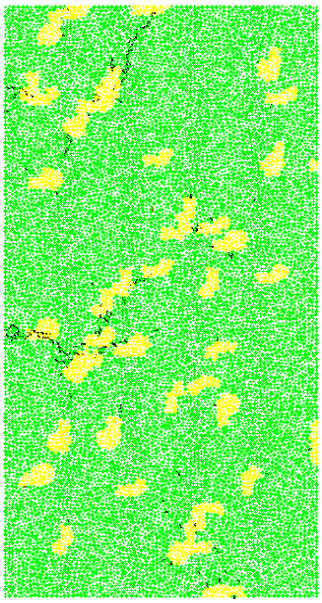

$P_d = 1 \times 10^8$ W/m^3, 2 s
(Micro-cracks = 200)

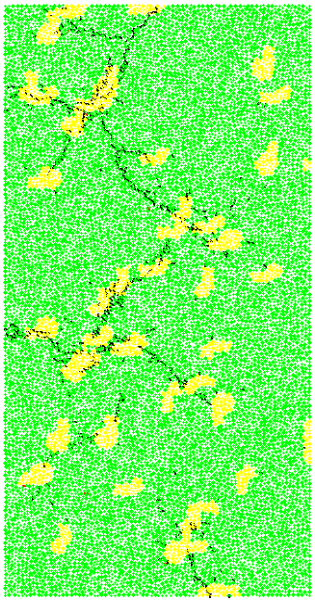

$P_d = 1 \times 10^8$ W/m^3, 3 s
(Micro-cracks = 624)

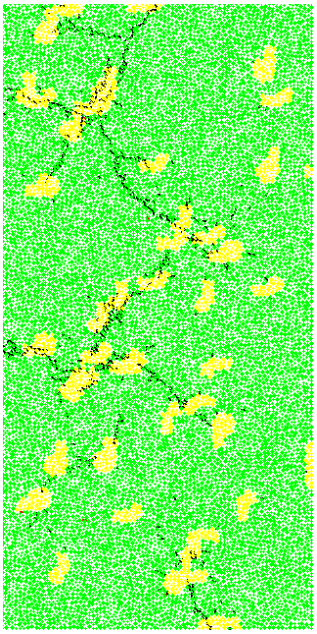

$P_d = 1 \times 10^8$ W/m^3, 4 s
(Micro-cracks = 890)

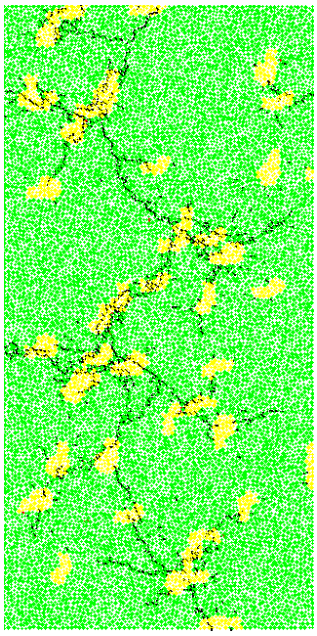

$P_d = 1 \times 10^8$ W/m^3, 5 s
(Micro-cracks = 1200)

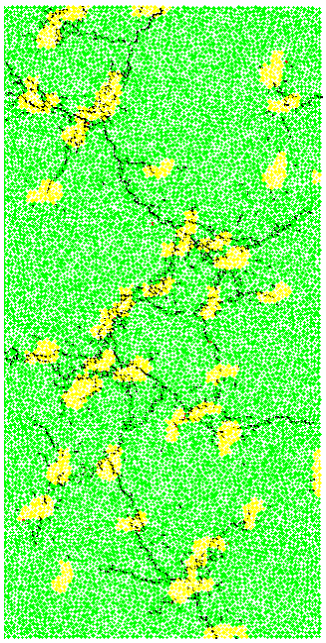

$P_d = 1 \times 10^8$ W/m^3, 6 s
(Micro-cracks = 1411)

Figure 8.19: Micro-cracks in coarse-grained galena-calcite, treated at $P_d = 1 \times 10^8$ W/m

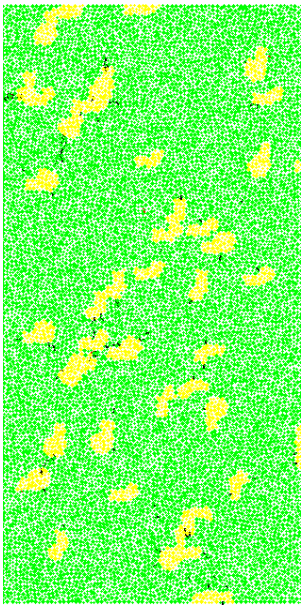

$P_d = 1 \times 10^9$ W/m^3, 0.05 s
(Micro-cracks = 115)

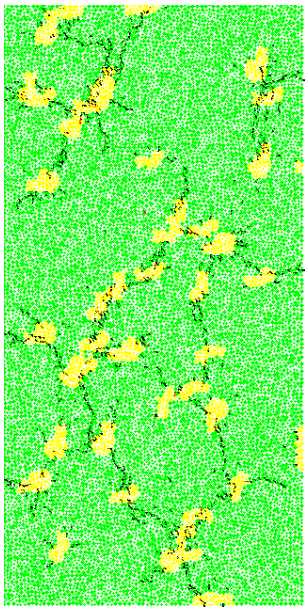

$P_d = 1 \times 10^9$ W/m^3, 0.1 s
(Micro-cracks = 1068)

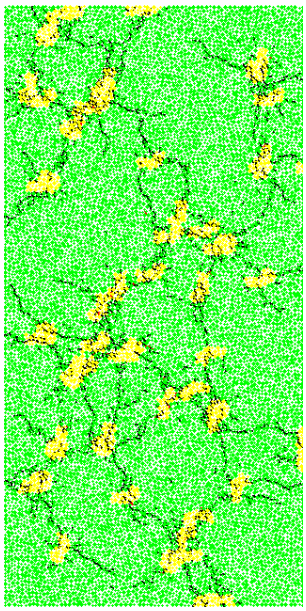

$P_d = 1 \times 10^9$ W/m^3, 0.2 s
(Micro-cracks = 2164)

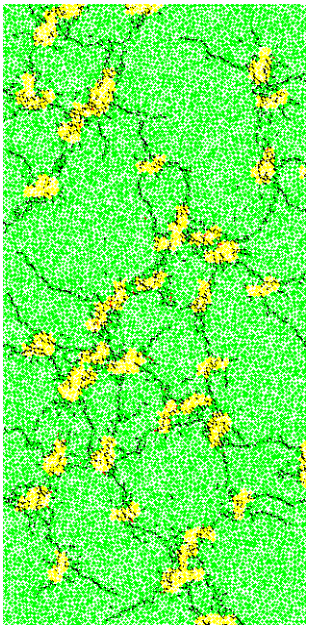

$P_d = 1 \times 10^9$ W/m^3, 0.3 s
(Micro-cracks = 2653)

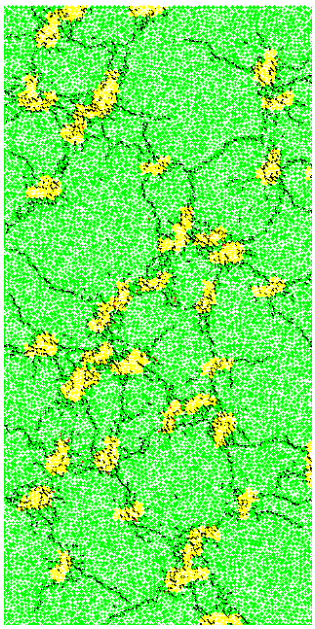

$P_d = 1 \times 10^9$ W/m^3, 0.4 s
(Micro-cracks = 3045)

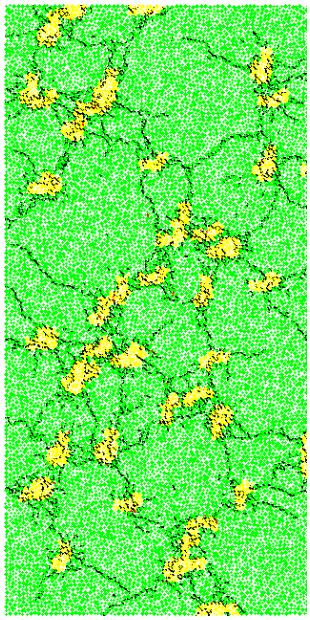

$P_d = 1 \times 10^9$ W/m^3, 0.5 s
(Micro-cracks = 3269)

Figure 8.20: Micro-cracks in coarse-grained galena-calcite, treated at $P_d = 1 \times 10^9$ W/m^3

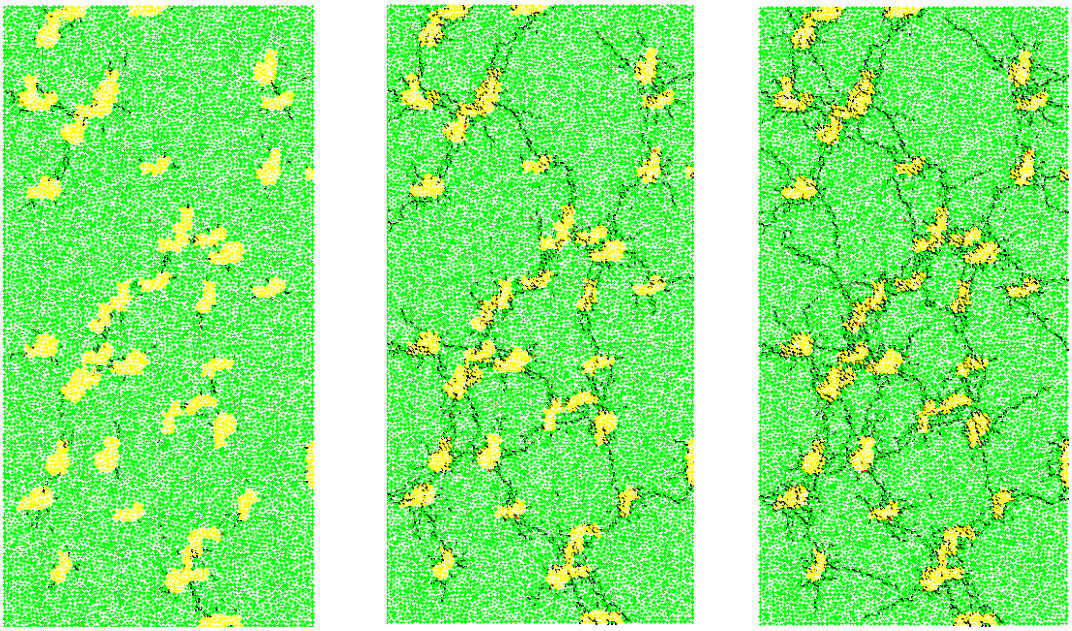

$P_d = 1 \times 10^{10}$ W/m^3, 0.005 s (Micro-cracks = 395)

$P_d = 1 \times 10^{10}$ W/m^3, 0.01s (Micro-cracks = 2037)

$P_d = 1 \times 10^{10}$ W/m^3, 0.02 s (Micro-cracks = 3357)

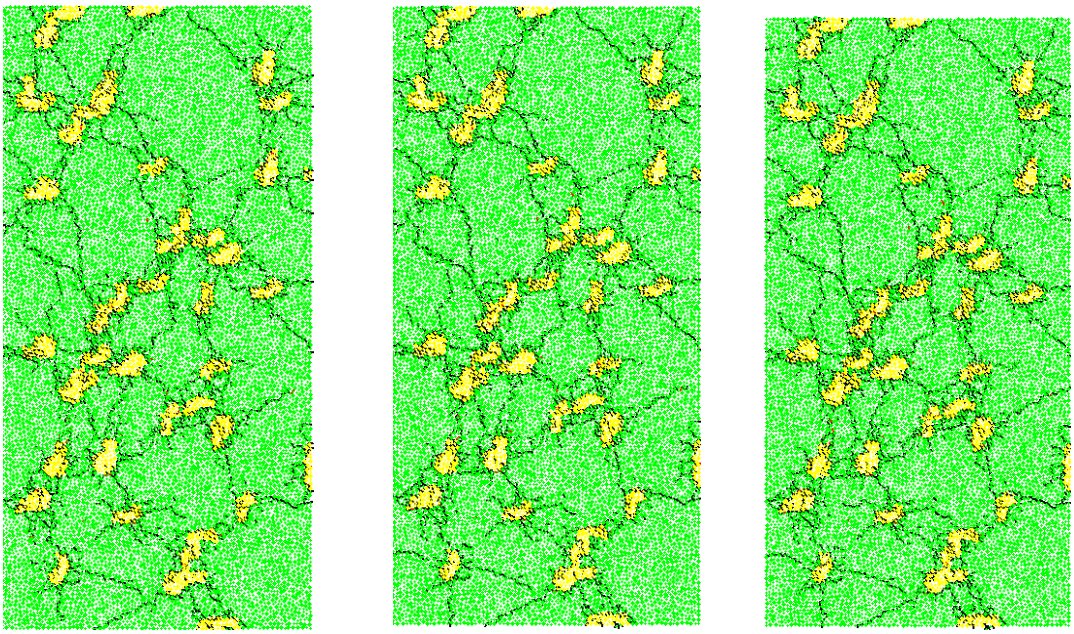

$P_d = 1 \times 10^{10}$ W/m^3, 0.03 s (Micro-cracks = 3707)

$P_d = 1 \times 10^{10}$ W/m^3, 0.04 s (Micro-cracks = 3902)

$P_d = 1 \times 10^{10}$ W/m^3, 0.05 s (Micro-cracks = 4046)

Figure 8.21: Micro-cracks in coarse-grained galena-calcite, treated at $P_d = 1 \times 10^{10}$ W/m^3

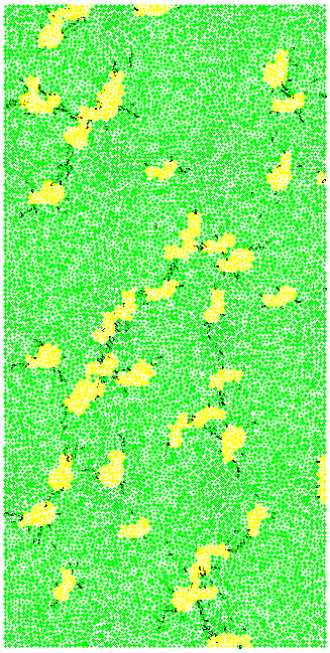

$P_d = 1 \times 10^{11}$ W/m^3, 0.5 ms
(Micro-cracks = 482)

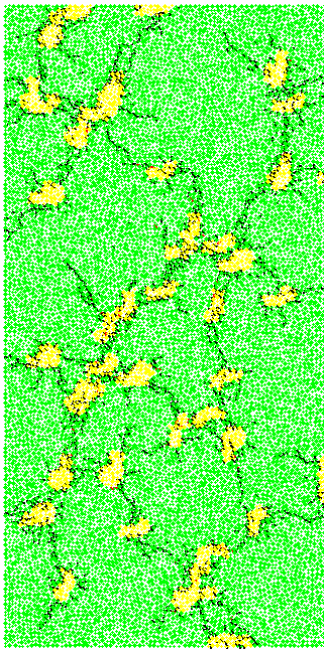

$P_d = 1 \times 10^{11}$ W/m^3, 1 ms
(Micro-cracks = 2271)

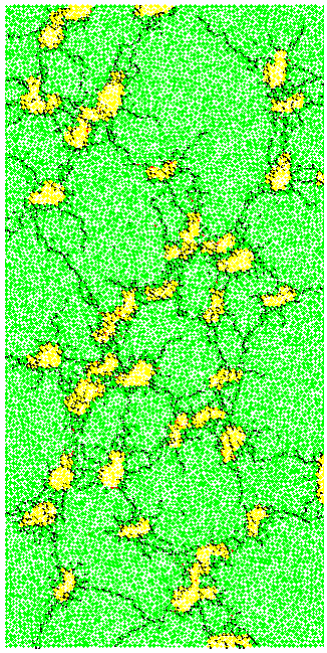

$P_d = 1 \times 10^{11}$ W/m^3, 2 ms
(Micro-cracks = 3600)

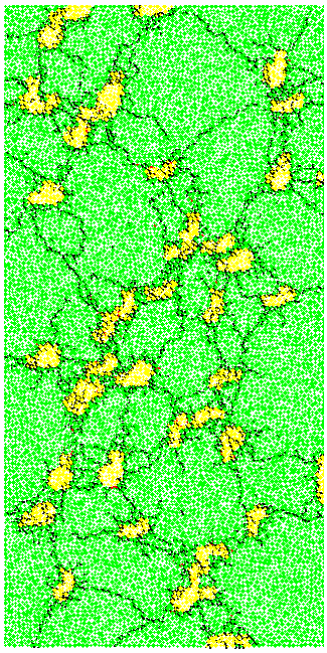

$P_d = 1 \times 10^{11}$ W/m^3, 3 ms
(Micro-cracks = 3900)

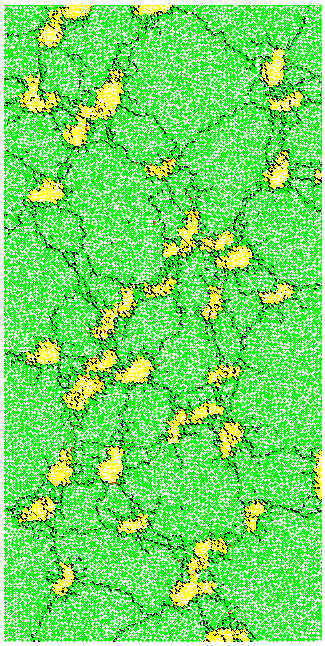

$P_d = 1 \times 10^{11}$ W/m^3, 4 ms
(Micro-cracks = 4041)

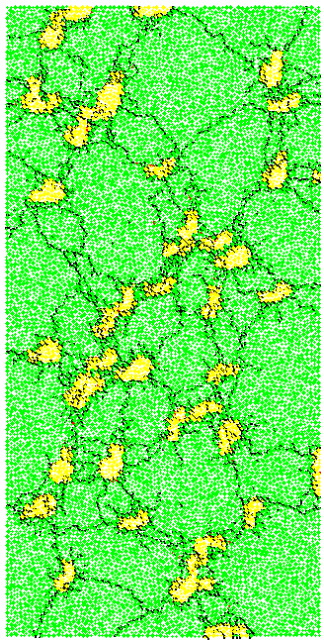

$P_d = 1 \times 10^{11}$ W/m^3, 5 ms
(Micro-cracks = 4089)

Figure 8.22: Micro-cracks in coarse-grained galena-calcite, treated at $P_d = 1 \times 10^{11}$ W/m^3

Figure 8-23 shows the results of simulation of fine-grained galena-calcite treated at power density of 1×10^9 W/m^3. Although simulation was carried out for this ore at power density of 1×10^8 W/m^3, no significant damage was observed in the ore even when the exposure time was increased up to 10 s. It can be seen from Figure 8-24 that relatively few cracks were induced in the ore sample even at a power density of 1×10^9 W/m^3. The effect of absorbent phase grain size can be clearly seen by comparing this figure with Figure 8-20. Although both ores consisted of the same volume of absorbent mineral and treated at the same energy input and power density, the amount of damage incurred in the ore samples were considerably different. It can be seen that the power density and the energy input required for the fine-grained ore was one order of magnitude higher than that required for the coarse-grained ore. As can be seen, the crack pattern for the fine-grained obtained at 1×10^9 W/m^3 was very similar to that was obtained for the coarse-grained ore at 1×10^8 W/m^3 i.e. micro-cracks started from the absorbent phase boundary and propagated to the calcite matrix randomly.

The results of simulation of fine-grained galena-calcite treated at the higher power density of 1×10^{11} W/m^3 are shown in Figure 8-24. It can be clearly seen that a substantial increase in damage was obtained when the power density was increased for the same energy input. The general trend observed for the coarse-grained ore was also repeated for the fine-grained ones i.e. at high power density more micro-fractures for the same energy input was observed and more importantly these micro-fractures mostly occurred around the grain boundary. However, for this ore the effect of power density was considerably higher.

In general, it can be noted that for the same mineralogy and volume of microwave absorbent mineral, the energy input and the power density that were required to induce significant damage in an ore sample (which would reduce the required grinding energy and enhance liberation) depend strongly on the absorbent phase grain size. Higher power density and higher energy input were required for the fine-grained one. This was also in agreement with the results obtained using the continuum approach (refer Chapters 6 and 7).

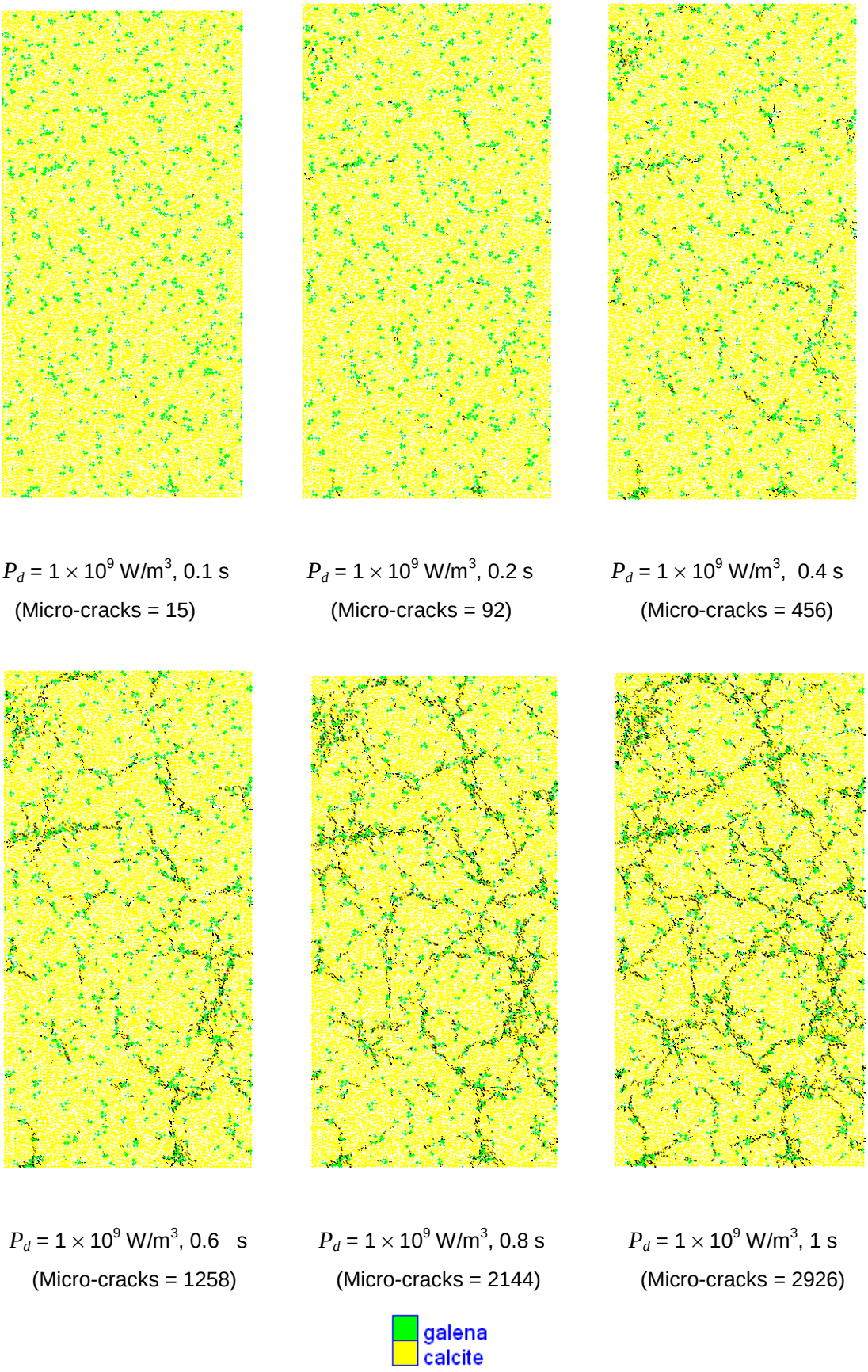

Figure 8.23: Micro-cracks in fine-grained galena-calcite, treated at $P_d = 1 \times 10^9$ W/m^3

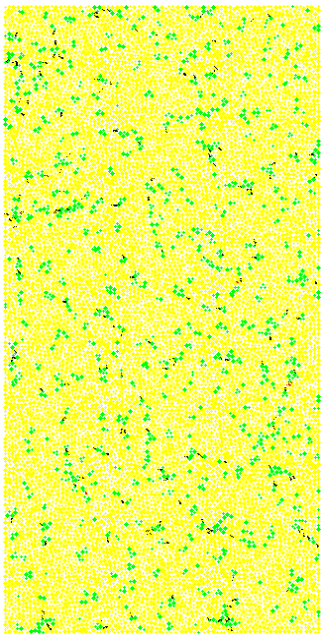

$P_d = 1 \times 10^{11}$ W/m^3, 0.0005 s
(Micro-cracks = 185)

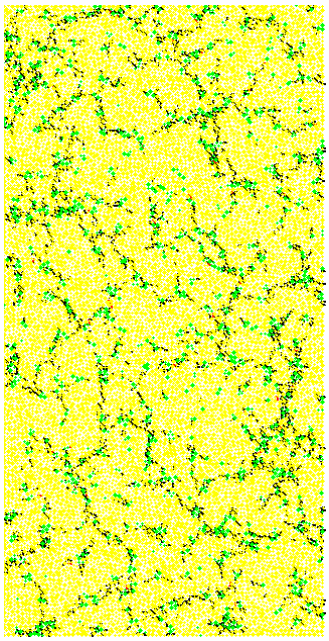

$P_d = 1 \times 10^{11}$ W/m^3, 0.001 s
(Micro-cracks = 2606)

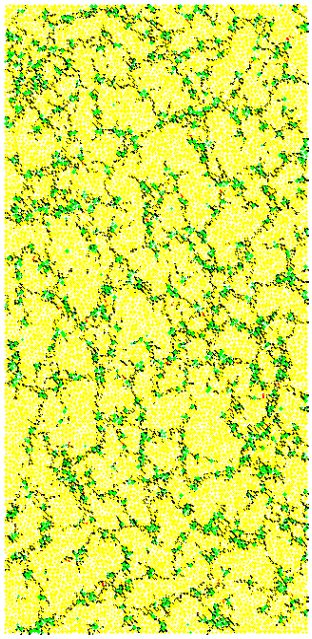

$P_d = 1 \times 10^{11}$ W/m^3, 0.0015 s
(Micro-cracks = 5621)

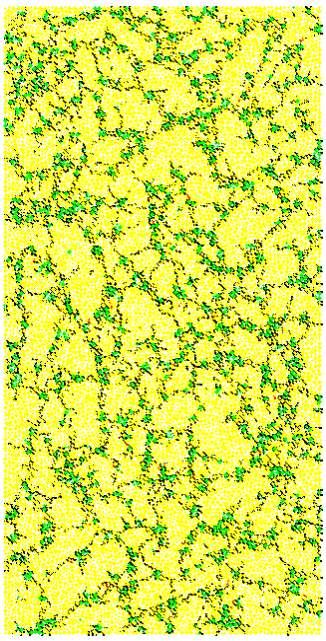

$P_d = 1 \times 10^{11}$ W/m^3, 0.002 s
(Micro-cracks = 7036)

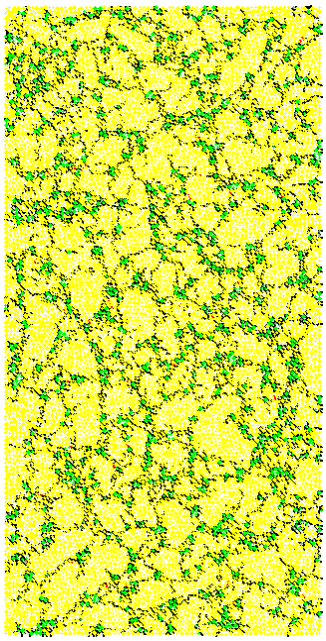

$P_d = 1 \times 10^{11}$ W/m^3, 0.003 s
(Micro-cracks = 8036)

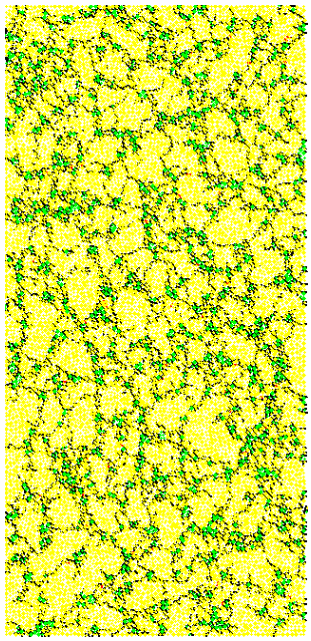

$P_d = 1 \times 10^{11}$ W/m^3, 0.004 s
(Micro-cracks = 8381)

Figure 8.24: Micro-cracks in fine-grained galena-calcite, treated at $P_d = 1 \times 10^{11}$ W/m^3

In Figure 8-25, the result of simulation of coarse-grained magnetite-dolomite treated at a power density of 1×10^9 W/m^3 is shown. It should be noted that the grain-size and the volume of the absorbent phase of this ore were the same as that of the coarse-grained galena-calcite and only the mineralogy was different. Simulation was also carried out for this ore at a power density of 1×10^8 W/m^3; however, no significant damage was observed up to 10 s. It can be seen from Figure 8-25 that significant damage was observed at power density of 1×10^9 W/m^3 after 0.4 s. However, the crack patterns were very different from that obtained for the coarse-grained galena-calcite at the same treatment conditions.

It can be seen that for this ore, at this power density, although the micro-cracks started from the absorbent phase grain boundary, they were not confined to that region; instead they propagated to the transparent matrix randomly. It has been shown previously that this ore is less amenable to microwave treatment due to the constituent minerals' thermo-mechanical properties. The thermal expansion coefficient of magnetite is considerably lower than that of galena. In addition, the thermal expansion coefficient difference between magnetite and dolomite is not as large as that between galena and calcite. Thus, it was suggested that this would considerably affect the cracks pattern. Previous simulation using the continuum approach also demonstrated this situation. It was shown that for a given mineralogy and ore texture there is a power density level below which no further increase in grain boundary damage is possible by increasing exposure time. If a power density lower than this minimum is dissipated, increasing the exposure time can cause damage but the damage would be all over the bulk of the ore sample. Thus, the result obtained here was also in agreement with that result.

The result of simulation of coarse-grained magnetite-dolomite treated at the higher power density of 1×10^{11} W/m^3 is shown in Figure 8-26. As expected, greater damage was induced in the ore for the same energy input and the damage was also more localised around the grain boundary. It can also be seen that for this ore the effect of power density was considerably high particularly on the nature of crack pattern in the ore sample. This also suggests that for a given mineralogy and ore texture, a certain minimum power density should be dissipated to localise damage around the grain boundary.

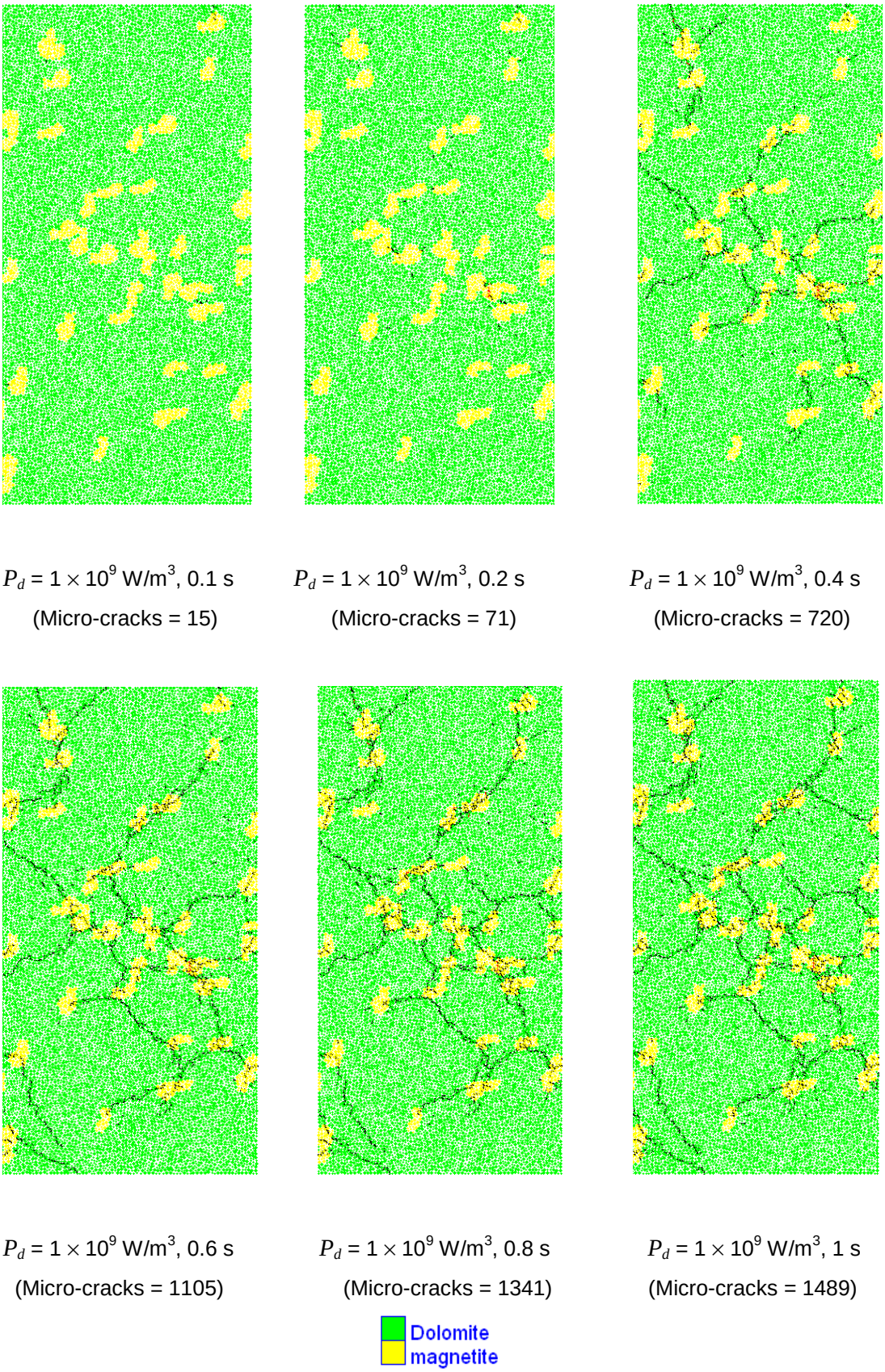

Figure 8.25: Micro-cracks in coarse-grained magnetite-dolomite, treated at $P_d = 1 \times 10^9$ W/m^3

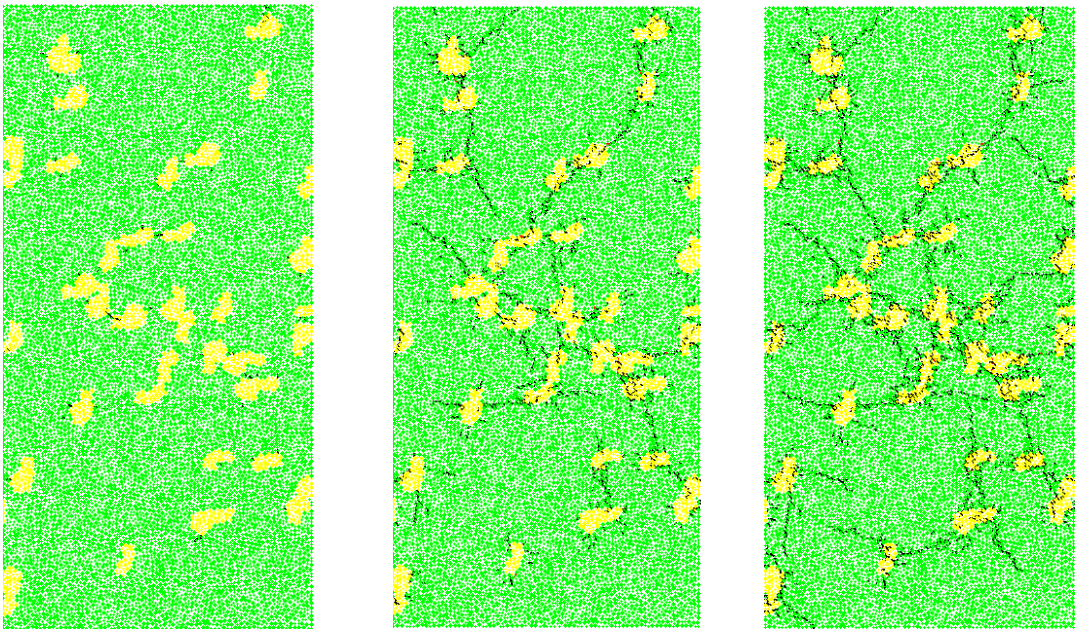

P_d = 1 × 10^{11} W/m^3, 0.001s (Micro-cracks = 64)

P_d = 1 × 10^{11} W/m^3, 0.002 s (Micro-cracks = 1009)

P_d = 1 × 10^{11} W/m^3, 0.003 s (Micro-cracks = 1957)

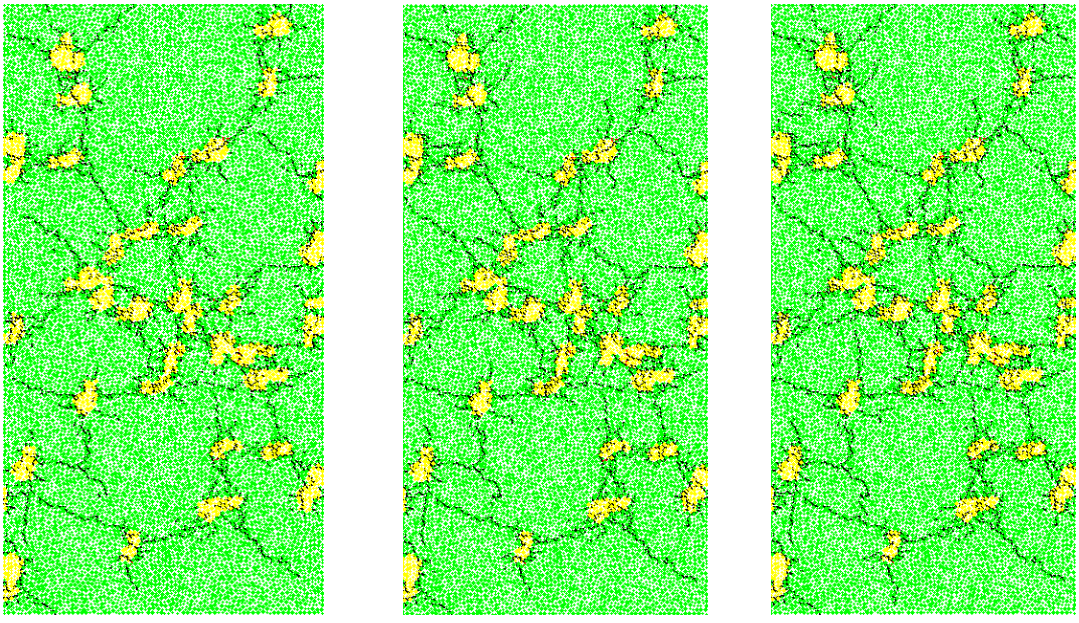

P_d = 1 × 10^{11} W/m^3, 0.004 s (Micro-cracks = 2449)

P_d = 1 × 10^{11} W/m^3, 0.005 s (Micro-cracks = 2837)

P_d = 1 × 10^{11} W/m^3, 0.006 s (Micro-cracks = 3089)

Figure 8.26: Micro-cracks in coarse-grained magnetite-dolomite, treated at P_d = 1 × 10^{11} W/m^3

Figure 8-27 shows the results of simulation of fine-grained magnetite-dolomite treated at a power density of 1×10^9 W/m^3. This ore was the least amenable ore for microwave treatment due to both thermo-mechanical properties of the constituent minerals and its texture. As can be seen, there was almost no damage (no significant micro-fractures) at power density of 1×10^9 W/m^3 even if the exposure time was increased to 1 s. It has been shown previously that for the coarse-grained magnetite-dolomite considerable damage occurred at this power density in 0.4 s. The effect of texture on microwave treatment of an ore can be clearly seen by comparing this figure with Figure 8-26.

It can be said that for this ore, power density of 1×10^9 W/m^3 was not enough to cause significant thermally induced stresses exceeding the bond strength (both in tensile and in shear). As has been discussed earlier, one of the reasons for this is the increase in surface area to volume ratio or heat transfer area as the absorbent grain size decreases, which enhances the conduction heat loss from the absorbent phase to the transparent matrix. However, as was shown previously if the exposure time was increased beyond 1 s at the expense of increased energy input (energy cost), a random micro-fractures throughout the bulk of the sample could still be obtained.

The results of simulation of fine-grained magnetite-dolomite treated at power density of 1×10^{11} W/m^3 is shown in Figure 8-28. Significant micro-cracks started to occur at this power density at exposure time of 0.002 s. The micro-cracks for this ore at higher power density also originated from the absorbent phase grain boundary and there were few micro-cracks inside the absorbent phase. As expected, for the high power density case, considerable micro-fracturing occurred around the grain boundary for the same energy input compared to that were obtained at lower power density. It can be seen that once significant micro-fractures start to occur, force redistribution around the breakage leads to further breakage of bonds and more and more micro-fractures were induced. It can also be seen that for this ore, at this power density, increasing the exposure time beyond 0.006 s didn't have any benefit in terms of liberation. However, this will increase the bulk damage, which reduces the energy required for grinding.

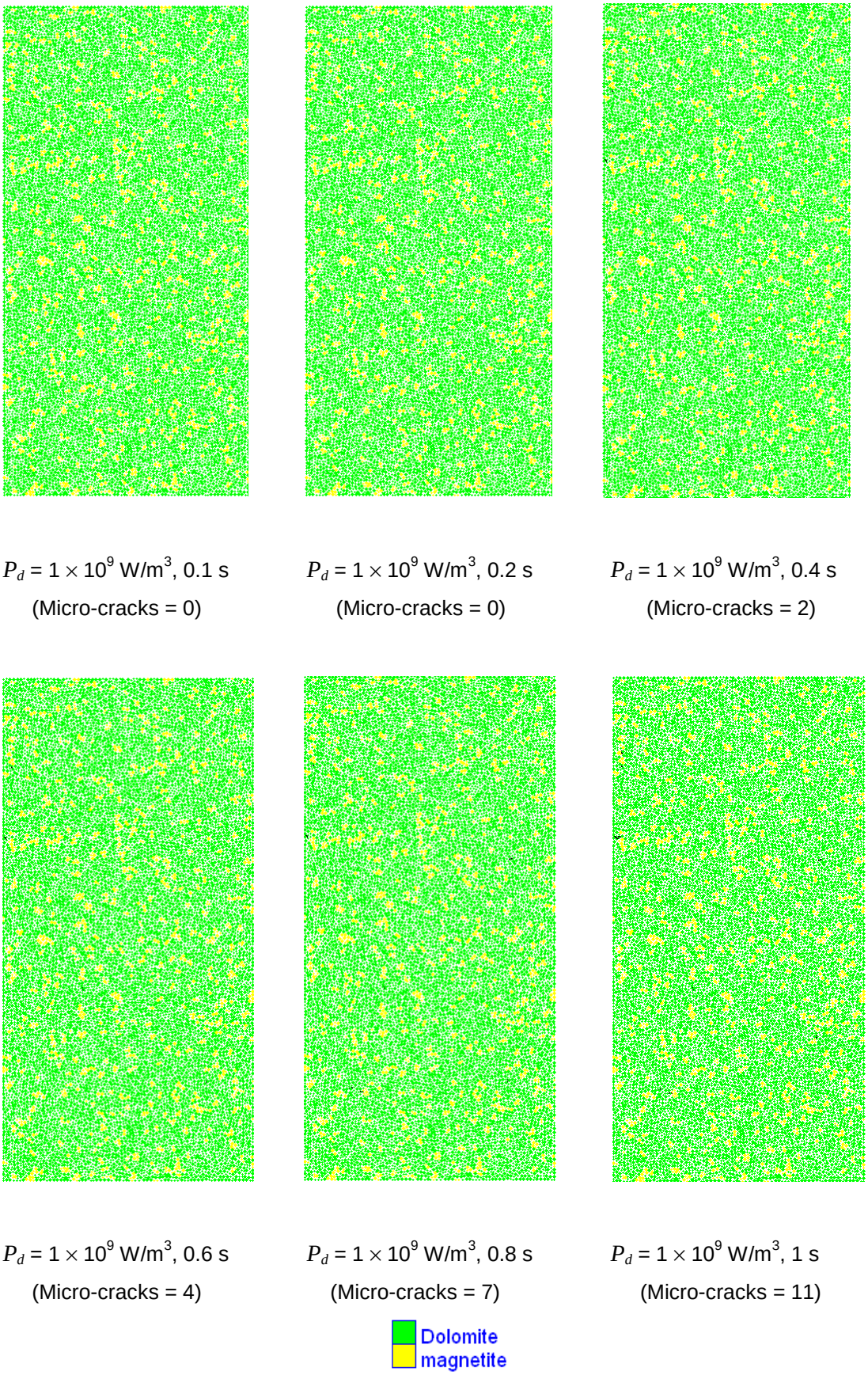

Figure 8.27: Micro-cracks in fine-grained magnetite-dolomite, treated at Pd = 1 × 10^9 W/m^3

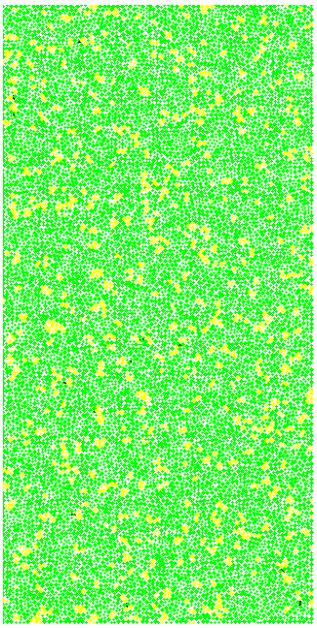

$P_d = 1 \times 10^{11}$ W/m^3, 0.001 s
(Micro-cracks = 12)

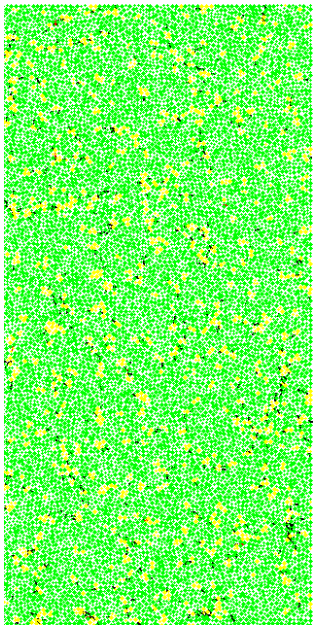

$P_d = 1 \times 10^{11}$ W/m^3, 0.002 s
(Micro-cracks = 482)

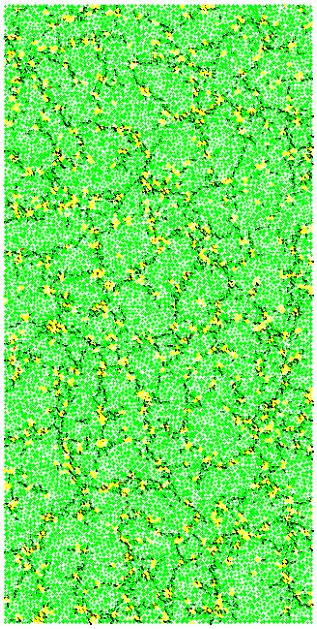

$P_d = 1 \times 10^{11}$ W/m^3, 0.004 s
(Micro-cracks = 3745)

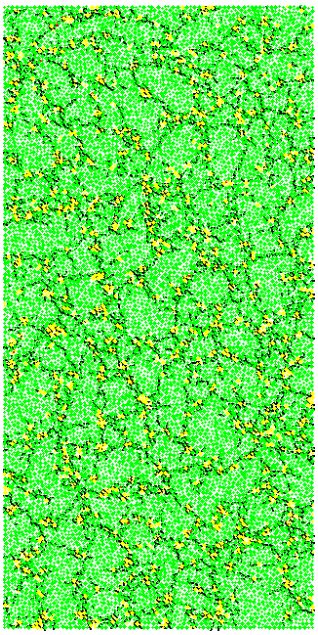

$P_d = 1 \times 10^{11}$ W/m^3, 0.006 s
(Micro-cracks = 5788)

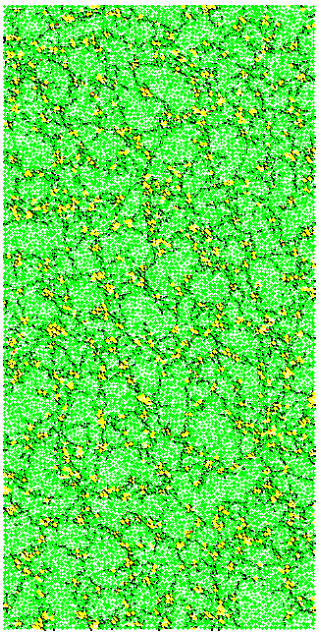

$P_d = 1 \times 10^{11}$ W/m^3, 0.008 s
(Micro-cracks = 6810)

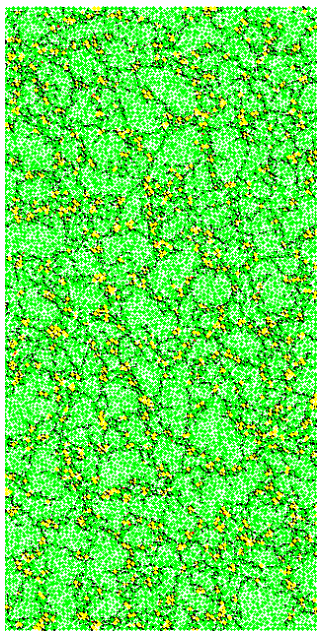

$P_d = 1 \times 10^{11}$ W/m^3, 0.01 s
(Micro-cracks = 7349)

Figure 8.28: Micro-cracks in fine-grained magnetite-dolomite, treated at $P_d = 1 \times 10^{11}$ W/m^3

8.6.4 Conclusions

The effects of power density, mineralogy and absorbent phase grain size on the extent of fracture and type of crack pattern in microwave treated ores were investigated in detail using distinct element method. It has been shown that the amount of micro-cracks and also the cracks pattern in an ore sample after microwave treatment significantly depend on its mineralogy, microwave treatment conditions (power density) and absorbent phase grain size. It has also been shown that a minimum power density is required to localize damage around the grain boundary in an ore sample. This minimum power density was found to strongly depend on the ore mineralogy and its texture. The results obtained were in agreement with those obtained using the continuum approach.

8.7 Construction of Damage Maps for Different Ores in terms of Percentage of Micro-cracks

8.7.1 Introduction

This section details the study carried out for constructing damage maps for different ores in terms of percentage of micro-cracks for various microwave treatment conditions. Damage maps which show percentage of micro-fractures as a function of power density and exposure time for different ores and ore textures were constructed. It should be noted that similar damage maps were constructed using the continuum approach in section 7-2. However, the damage maps in that study were constructed by examining the thermally induced stresses around the grain boundaries and by comparing those stresses with the bulk strength of the material.

As has been discussed in section 8-3, the bond strength of the *PFC* material is significantly higher than its bulk strength. It has been shown that for the binary ore models constructed, the bond strengths were about four times their bulk strengths. Thus, the results from this study should not be compared directly with the results obtained in section 7-2. However, qualitative comparisons can be made.

8.7.2 Methodology

The ore models used for the study were the same as those used in the previous section. In total, four different binary ore models were investigated. These were coarse-grained galena-calcite, fine-grained galena-calcite, coarse-grained magnetite-dolomite and fine-grained magnetite-dolomite. The construction of the damage maps was made as follows. First, each ore was treated at different power densities ranging from 1×10^8 W/m^3 to 1×10^{11} W/m^3. The energy inputs used at each power density were between 1×10^8 J/m^3 and 1×10^9 J/m^3. This means that for example, the exposure times used for the power density of 1×10^9 W/m^3 were between 0.1 s and 1 s. The number of micro-cracks at each treatment condition was then quantified. Typical results are shown in Figures 8-29 to 8-32.

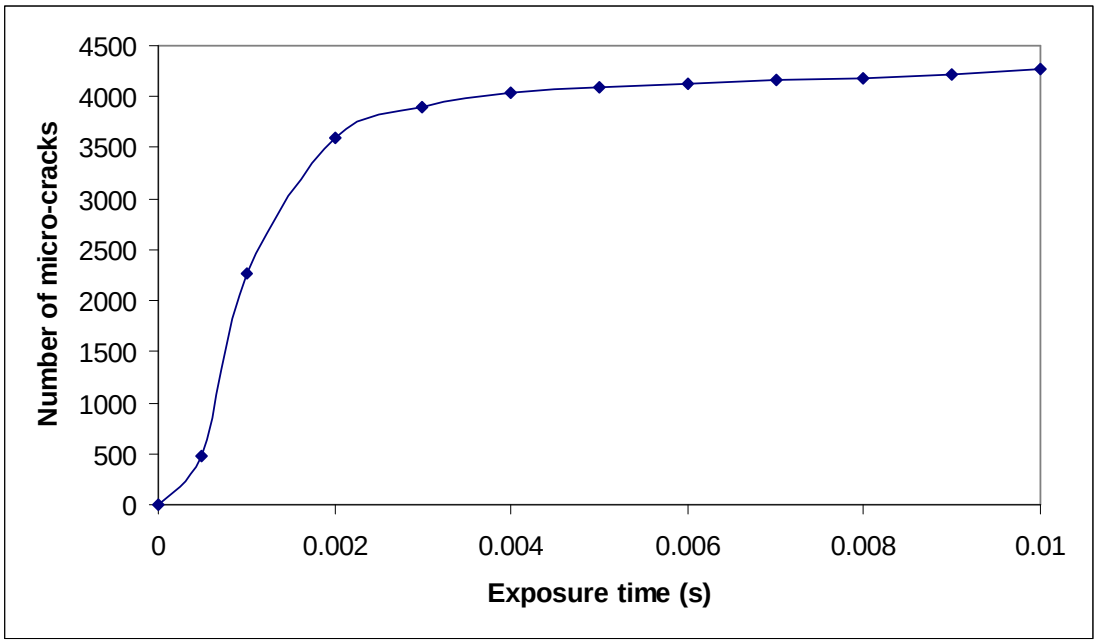

Figure 8.29: Number of micro-cracks as a function of exposure time for coarse-grained galena-calcite treated at $P_d = 1 \times 10^{11}$ W/m^3

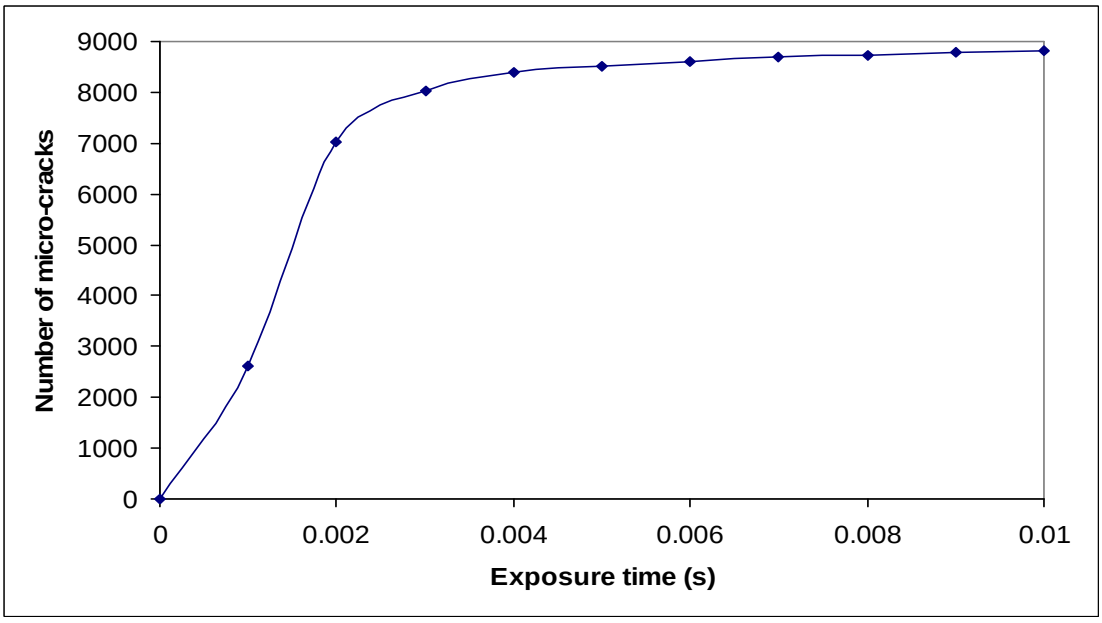

Figure 8.30: Number of micro-cracks as a function of exposure time for fine-grained galena-calcite treated at $P_d = 1 \times 10^{11}$ W/m^3

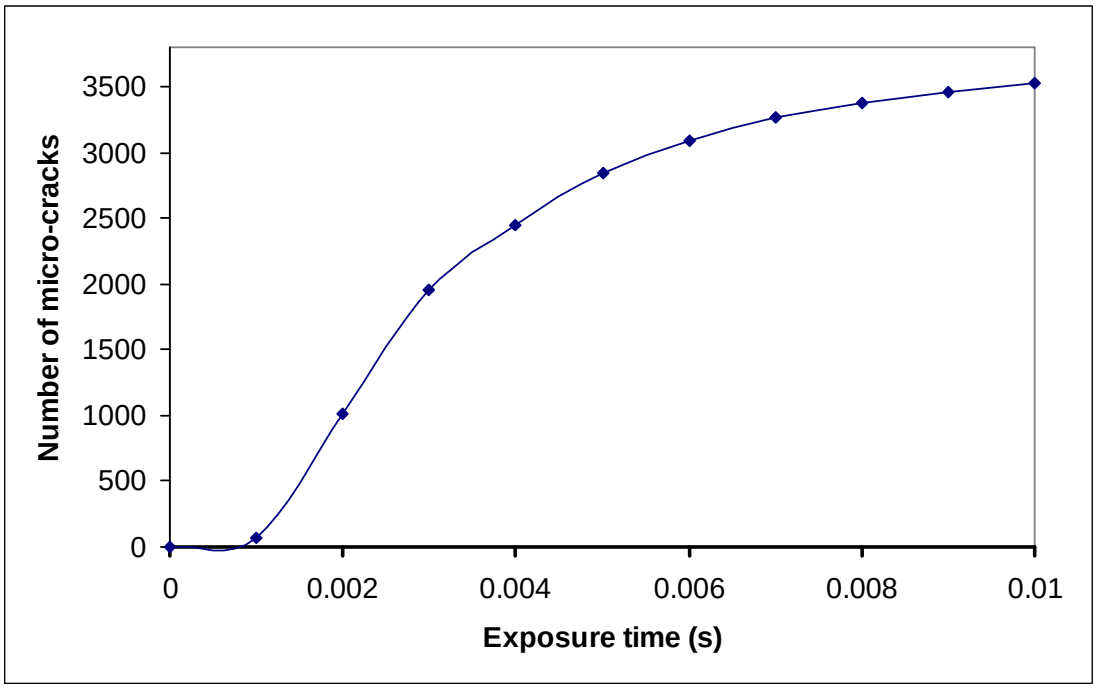

Figure 8.31: Number of micro-cracks as a function of exposure time for coarse-grained magnetite-dolomite treated at $P_d = 1 \times 10^{11}$ W/m^3

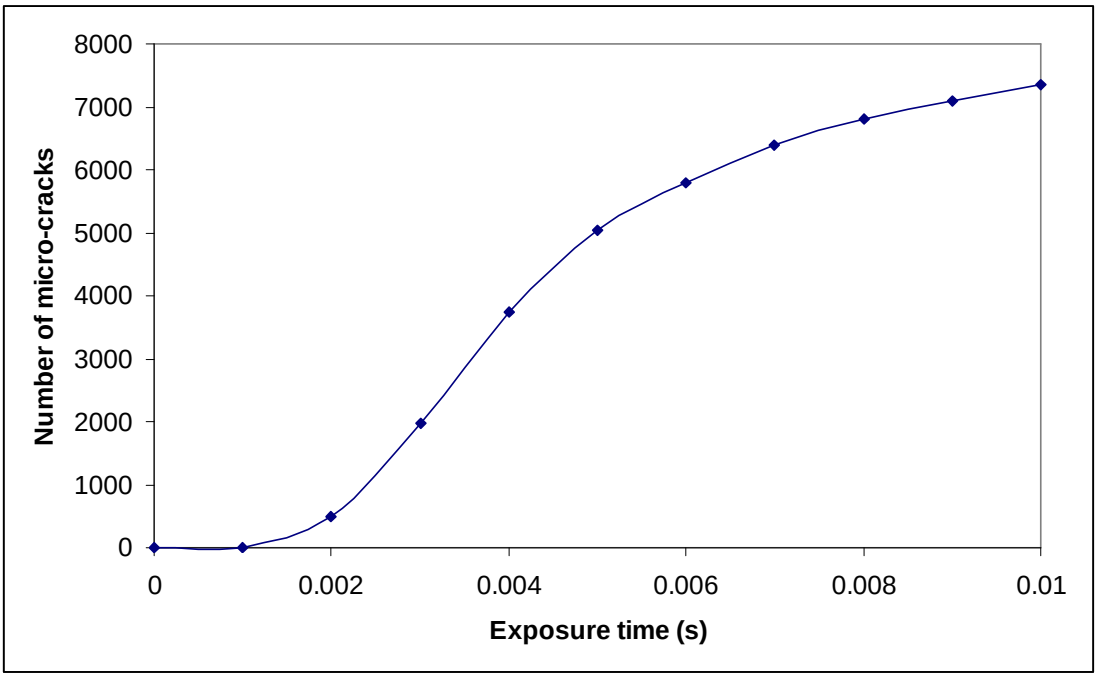

Figure 8.32: Number of micro-cracks as a function of exposure time for fine-grained magnetite-dolomite treated at $P_d = 1 \times 10^{11}$ W/m^3

Next, the maximum number of micro-cracks for a complete failure of the material was determined for each ore by increasing the exposure time as required as possible until it reaches its maximum. This maximum number of micro-cracks was found to strongly depend on mineralogy and ore textures. It is apparent that the maximum number of micro-cracks also depends on the total particle size and number of balls; however, these were the same for all ores. Then, the percentage of micro-cracks was defined as the number of micro-cracks obtained at that treatment condition divided by the maximum number of micro-cracks for a complete failure of the material. For example, from Figures 8-29 and 8-30, it can be seen that the maximum number of micro-cracks for coarse-grained and fine-grained galena-calcite were about 4400 and 8800, respectively. Similarly, the maximum numbers of micro-cracks for coarse-grained and fine-grained magnetite-dolomite were also determined and these were found to be about 3600 for the coarse-grained and 8400 for the fine-grained magnetite-dolomite.

Ultimately, damage map which shows contour of the percentage of micro-cracks as a function of power density and exposure time for each ore was constructed. It should be noted that the axes on the damage maps are logarithmic in order to plot very short treatment times and a wide range of power densities. Data used for constructing the damage maps are presented in Appendix O (O1, O2, O3 and O4).

8.7.3 Results and Discussion

Figure 8-33 shows the damage map for coarse-grained galena-calcite. It can be seen that for this ores, a minimum power density of 5×10^8 W/m^{3}abs was required in order to cause significant micro-fractures at energy input of 10^8 J/m^{3}abs (0.868 kWh/t). It is apparent that increasing the power density for this ore up to $\approx 5 \times 10^9$ W/m^3, increased the amount of micro-fractures obtained at the same energy input. However, it can also be seen that the damage contours were almost parallel to the constant energy contour starting from 5×10^9 W/m^{3}abs. This means that it will be cheaper in terms of energy to operate at higher power density and shorter times up to 5×10^9 W/m^3. Increasing the power density beyond 5×10^9 W/m^{3}abs didn't cause any additional micro-fractures for the same energy input. As has been shown in the previous section, the fracture patterns were also similar at very high power densities. This can be

observed by looking the fracture patterns obtained at 1×10^{10} W/m^3 and 1×10^{11} W/m^3.

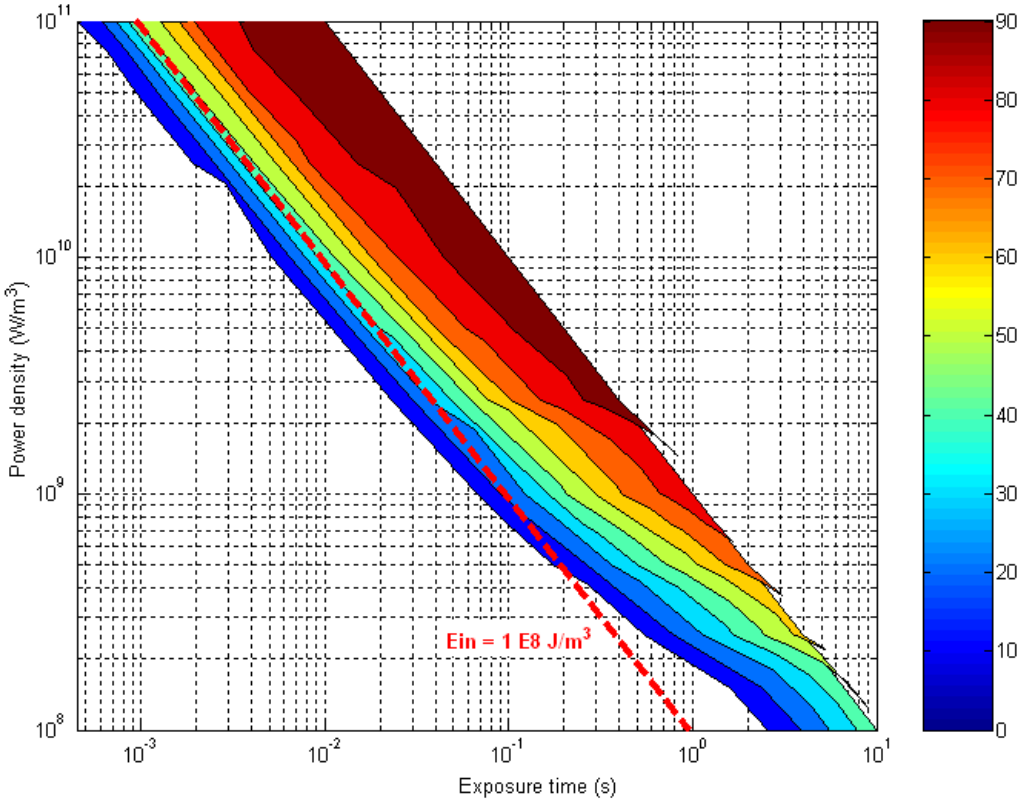

Figure 8.33: Damage map in terms of percentage of micro-cracks for coarse-grained galena-calcite

The result of the simulations for fine-grained galena-calcite is shown in Figure 8-34. It can be seen, as expected, that higher power density was required to induce significant micro-fractures compared to that was needed for the coarse-grained one. In addition, the energy inputs required were also relatively high. As can be seen, for this ore, a minimum power density of 4×10^9 W/m^3 was needed to induce significant micro-cracks at an energy input of 2×10^8 J/m^{3}abs. It can be seen that for this ore significant energy saving can be achieved by reducing treatment time and increasing power. Thus, operating at high power density for this ore has two advantages; first, it will reduce the energy required for causing micro-fractures. Second, as it has been shown in the previous section, operating at high power density will enhance liberation

for this ore, as the micro-fractures will be more localised around the grain boundary. Thus, practically, microwave treatment of such kind of ore should be performed using high power microwave equipment.

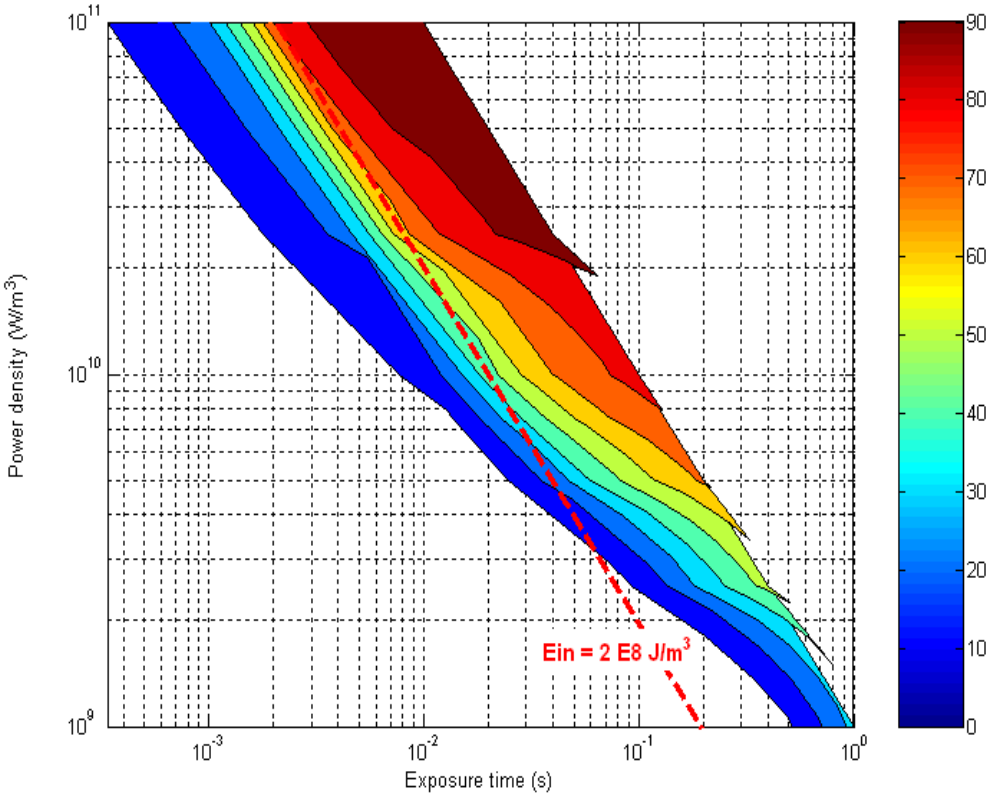

Figure 8.34: Damage map in terms of percentage of micro-cracks for fine-grained galena-calcite

In Figure 8-35, the damage maps obtained for coarse-grained magnetite-dolomite is shown. As can be seen, the energy input and the power density required to cause the same amount of micro-fractures as the coarse-grained galena-calcite were considerably high. The effect of mineralogy can be clearly seen by comparing this figure with Figure 8-33. For example, it required a power density of at least 3×10^9 W/m^3 in order to cause significant micro-fractures at energy input of 2×10^8 J/m^{3}abs. It can also be noted that the general trend shown by coarse-grained magnetite-dolomite ore was qualitatively similar to that was seen for coarse-grained galena

calcite ore i.e. higher micro-fractures were obtained when the power density was increased for the same energy input.

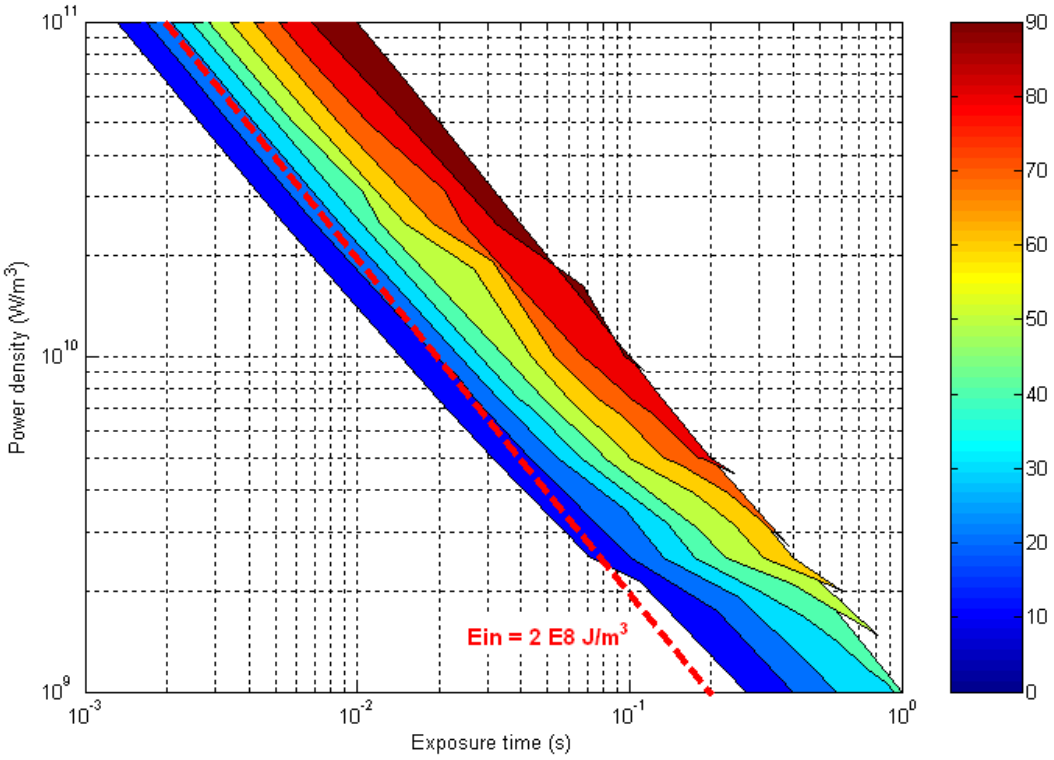

Figure 8.35: Damage map in terms of percentage of micro-cracks for coarse-grained magnetite-dolomite

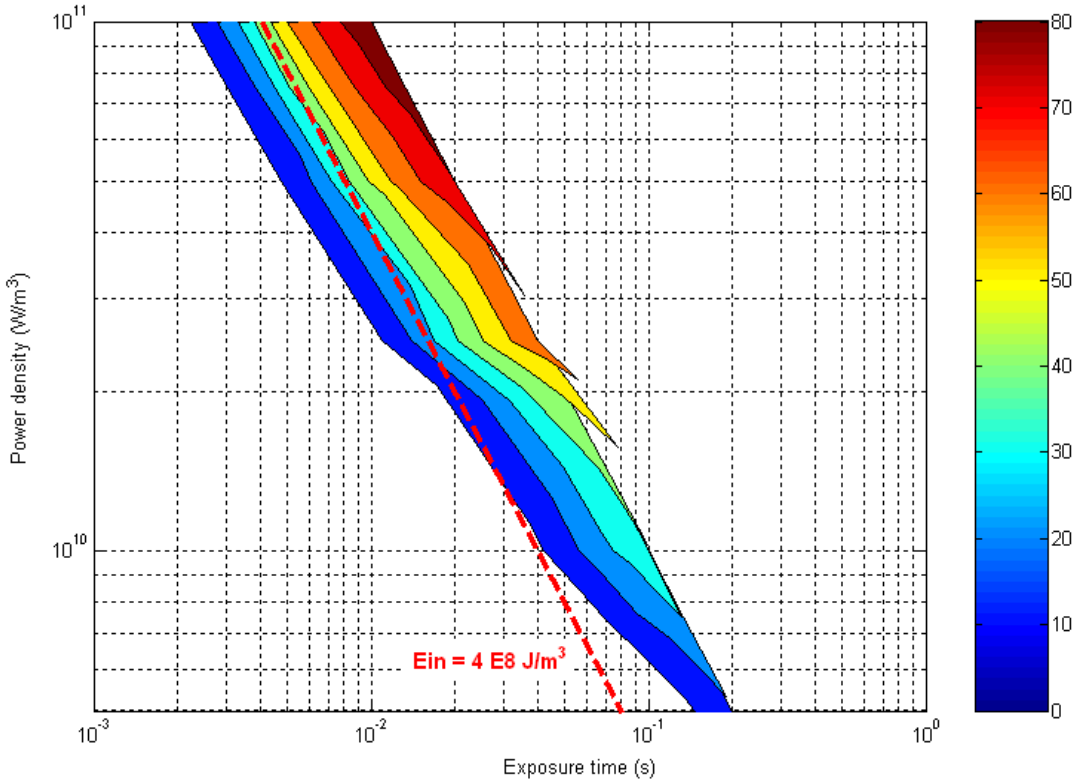

Figure 8.36: Damage map in terms of percentage of micro-cracks for fine-grained magnetite-dolomite

Figure 8-36 shows the damage maps obtained for fine-grained magnetite-dolomite. As can be seen, the energy input and the power density required to cause significant micro-fractures were substantially high. This ore was the least amenable to microwave treatment due to both its mineralogy and texture. A considerably high power density about 2×10^{10} W/m^3 was needed to cause significant micro-fractures at high energy input of 4×10^8 J/m^{3}abs. It is apparent that both high power density and high energy input was required to cause significant micro-fractures in this ore. Again, the effect of texture on microwave treatment of an ore can be clearly seen by comparing this figure with Figure 8-35.

8.7.4 Conclusions

Damage maps which show the percentage of micro-cracks as a function of power density and exposure time for different binary ores and ore textures were constructed. It has been shown that for a given ore mineralogy and texture, there exists a power density beyond which no further increase in micro-fractures would be obtained for the same energy input. In addition, it has been shown that for the same power density and energy input, the fraction of micro-fractures induced by microwave considerably depends on the ore mineralogy and its texture.

The energy input and the power density required for significant micro-fractures in *PFC* materials were relatively higher than those obtained using a continuum approach. However, the damage maps were qualitatively very similar to those obtained using a continuum approach.

8.8 Initial Investigation of the Effect of Microwave Treatment on Liberation of Minerals

8.8.1 Introduction

During crushing in equipment such as jaw crushers and rolls crushers, fracture and hence size reduction is achieved by compression, through forces applied between rigid surfaces. Understanding the breakage pattern of microwave treated ores in a crusher is very useful for selecting the appropriate crusher, which is currently under investigation. The discrete element method has proven to be a good solution for investigating bulk breakage of a particle. In this section, simulation of single particle compression of microwave treated and untreated ore were undertaken to investigate the effect of microwave treatment on liberation of minerals.

8.8.2 Methodology

The ore model used for the study was galena-calcite ore. As a preparation for single particle compression test, the model was trimmed in to a disc shape. It consisted of a single circular 2 mm galena placed inside a 10 mm diameter calcite matrix. The single particle compression test was carried out for three different cases. First, simulation of single particle compression of untreated ore was undertaken. This was done as a reference and to see how the fracture pattern changes as a result of microwave irradiation. Single particle compression of microwave treated ore was investigated for two different treatment conditions: low and high power density cases. The mechanical states of the ore after microwave treatment at different power densities for the same energy input are shown in Figures 8-37 and 8-38.

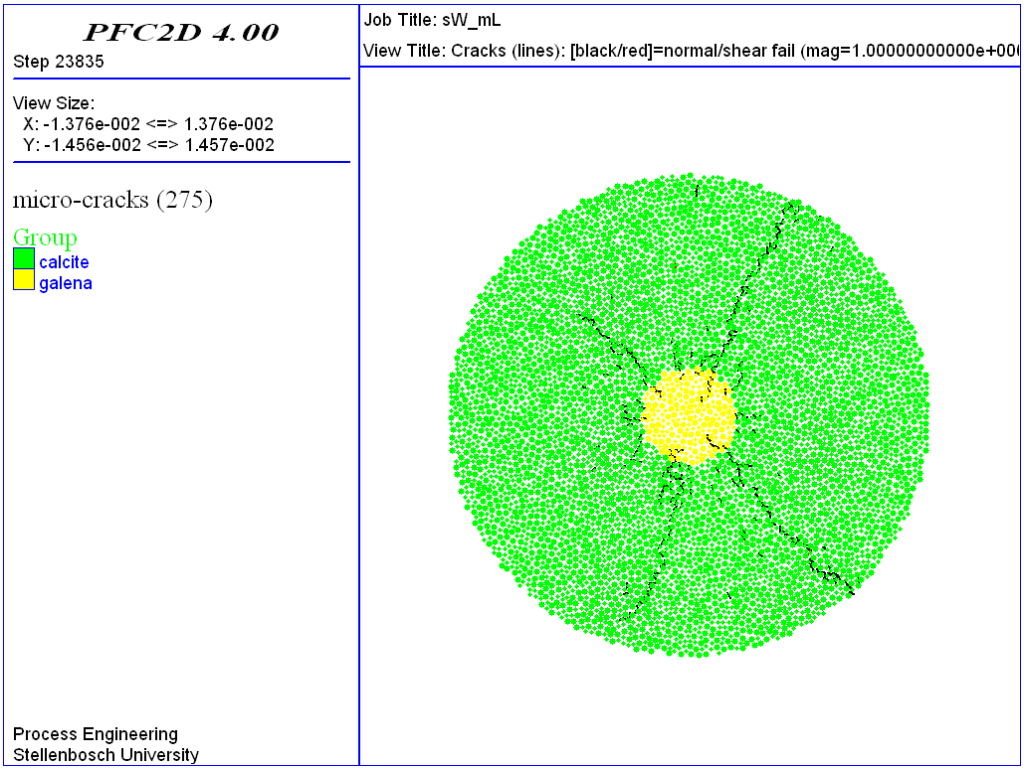

Figure 8.37: Micro-cracks in galena-calcite treated at power density of 1×10^9 W/m^3 for 0.1 s

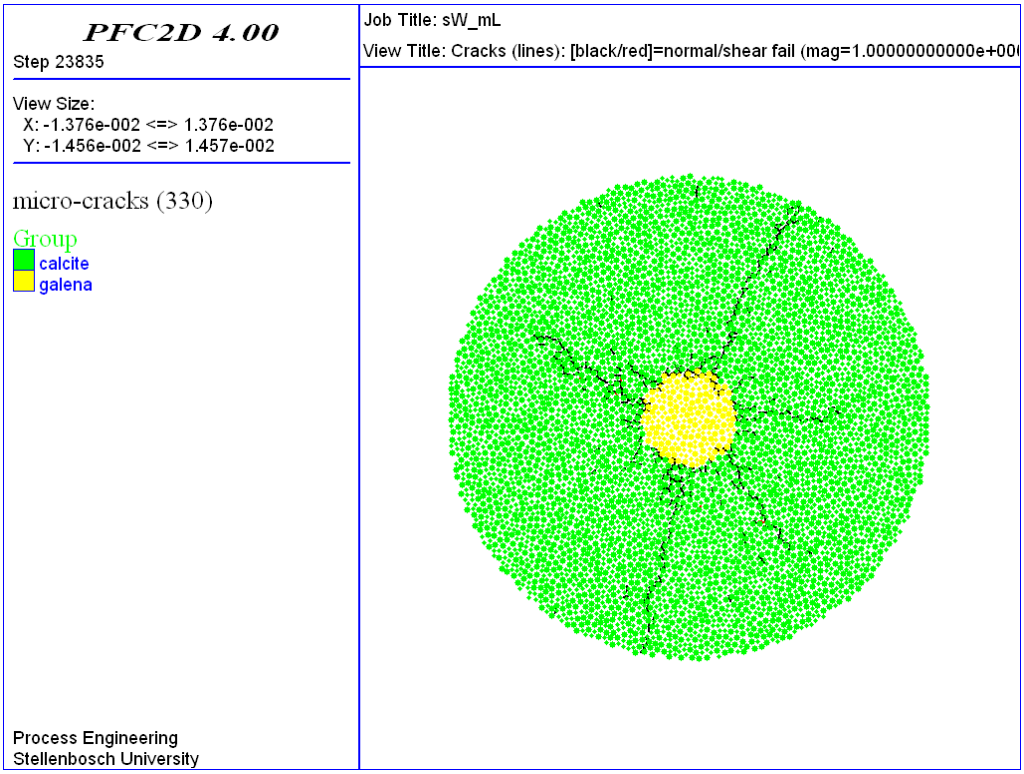

Figure 8.38: Micro-cracks in galena-calcite treated at power density of 1×10^{11} W/m^3 for 1 ms

The crushing process was simulated by placing two parallel walls above and below the samples as shown in Figure 8-39. The strain rate of rock fragmentation in a crusher is in the range of $10^1 – 10^4\ s^{-1}$ (Wang et al., 2009). In this study, a constant vertical velocity of 0.2 m/s was applied at the top and the bottom walls to compress the samples. This corresponds to a strain rate of 40 s^{-1}. The time step for the calculation was about 1×10^{-8}. All simulations were run for the same number of steps; hence, the final gab of the walls for each simulation was fixed. The fracture pattern of microwave treated and untreated ore were then compared.

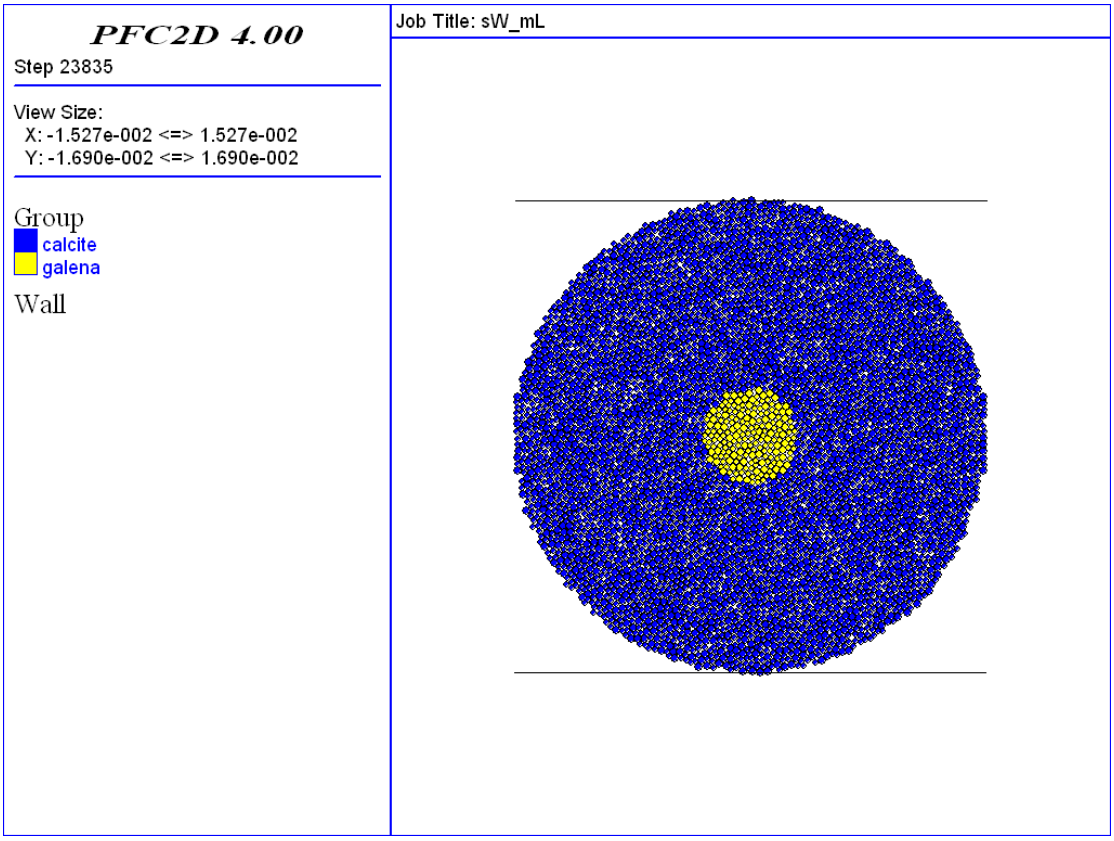

Figure 8.39: Preparation of ore for single particle compression test

8.8.3 Results and Discussion

Figure 8-40 shows the fracture pattern of the untreated ore after single particle compression test. As expected, the fracture was in a splitting mode due to the high tensile stress orthogonal to the direction of loading. Center crack initiation and crack propagation along the loading diameter was occurred. However, more random fractures were also seen after the material split along the loading diameter. This is a typical type of failure for most rocks in compression which is usually occurred in Brazilian test (Rocco et al., 1999; Tang et al., 2001).

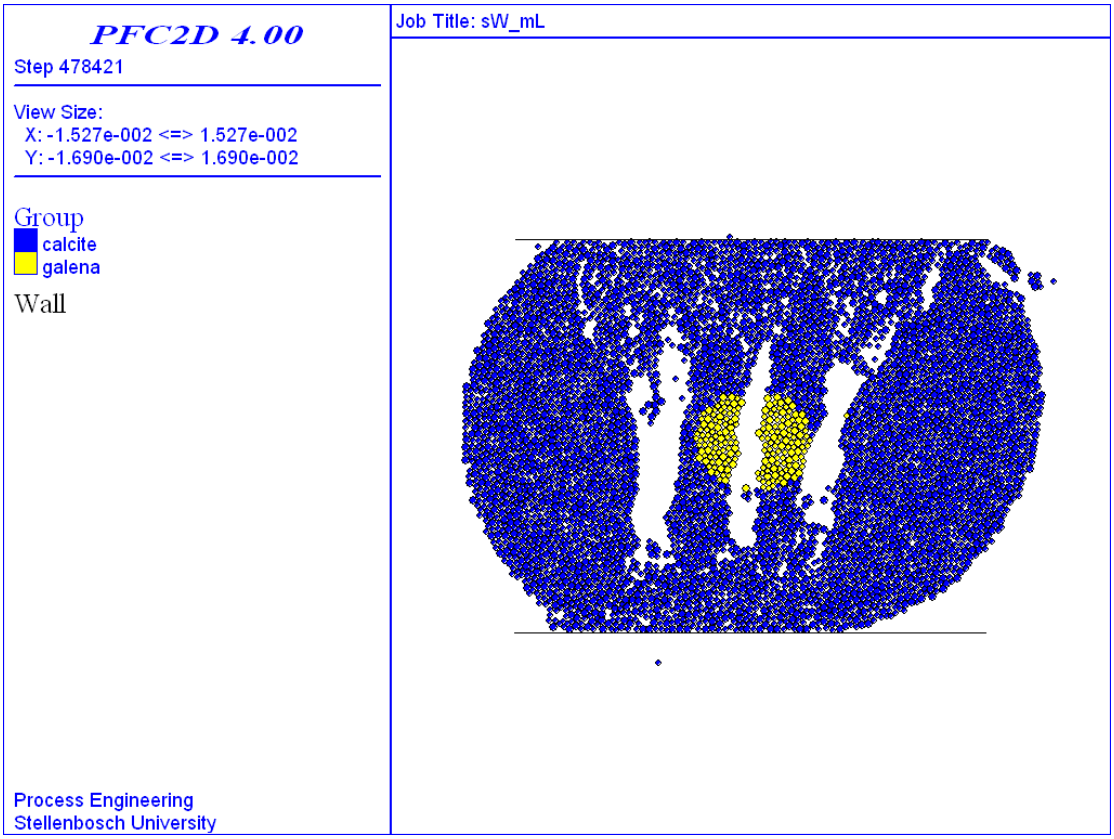

Figure 8.40: Fracture pattern of untreated galena-calcite

The result of simulation of the ore treated at power density of 1×10^9 W/m^3 for 0.1 s is shown in Figure 8-41. As can be seen, the fracture pattern is quite different from that was seen for the untreated ore, as most of the fractures were occurred along the grain boundary. However, it can be seen that the absorbent phase was also fractured.

This might be due to the existence of incipient micro-cracks inside the absorbent phase after microwave treatment (refer Figure 8-37). It should also be noted that the absorbent phase was exactly at the center of the matrix, where high tensile stress orthogonal to the direction of loading occurred, thus, this will also increase the probability of fracture of the absorbent phase.

It is expected that liberation would be enhanced, as most of the absorbent particles detach from the matrix. However, the liberation size (the size at which the absorbent mineral is liberated) would decrease, as transgranular fractures were also created in the absorbent phase.

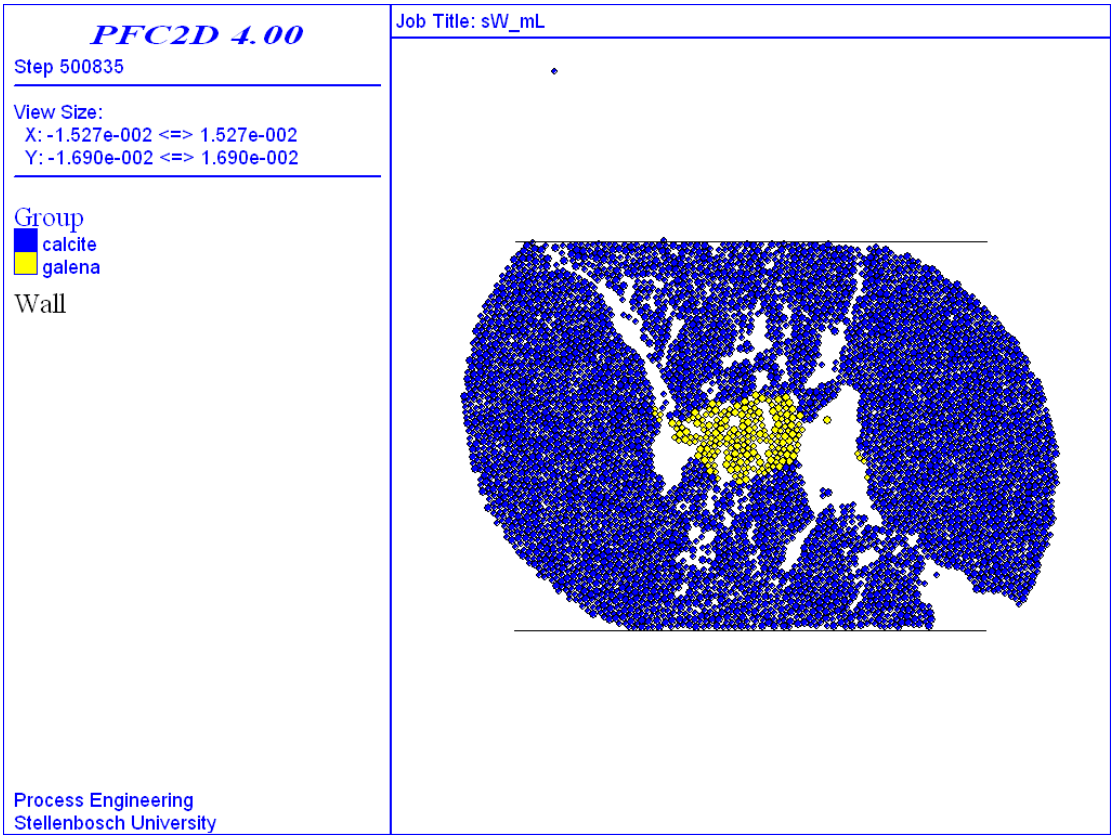

Figure 8.41: Fracture pattern of galena-calcite treated at power density of 1×10^9 W/m^3 for 0.1 s

The result of the simulation obtained for the high power density case, $P_d = 1 \times 10^{11}$ W/m^3, t = 1 ms is shown in Figure 8-42. It can be seen that there was almost no damage in the absorbent phase for this case. The effect of power density on

microwave treatment of ores can be clearly seen from the figure. As can be seen, for the high power density case, the fracture pattern was along the grain boundary and the microwave absorbent mineral was intact. It should also be emphasised that this was achieved using an economically viable specific microwave energy input of 1×10^8 J/m^{3}abs (0.96 kWh/t).

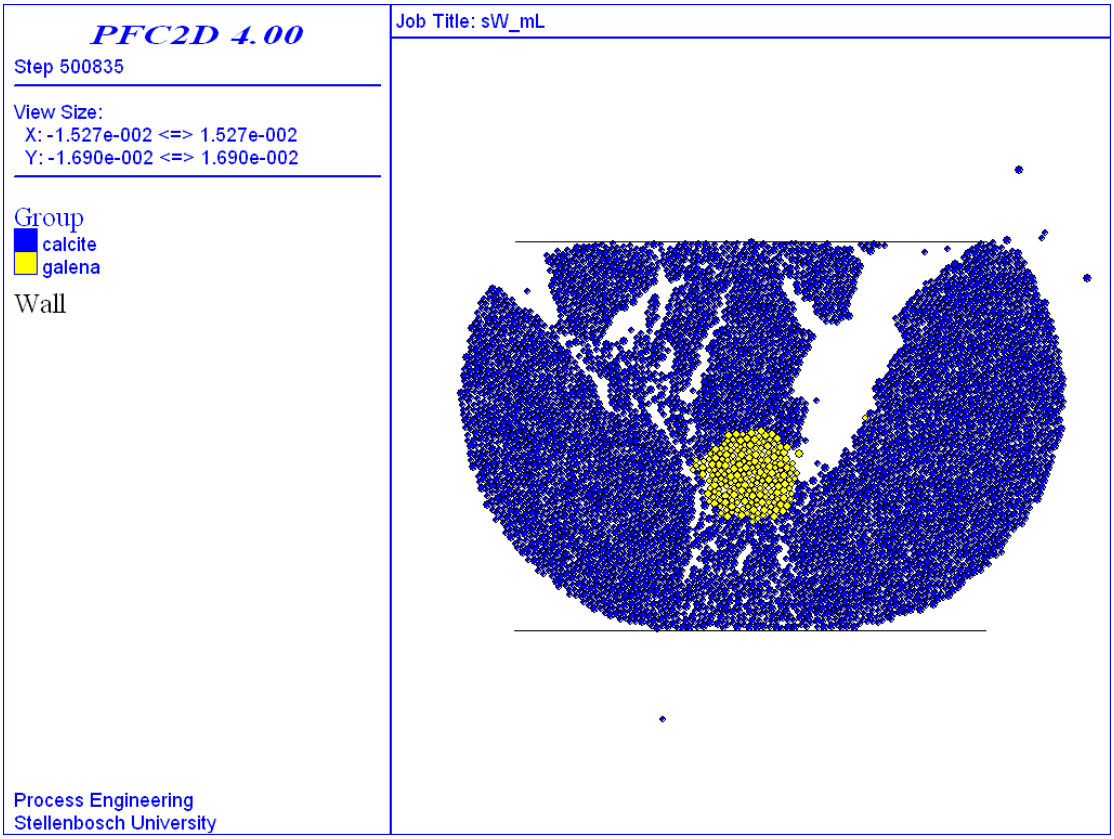

Figure 8.42: Fracture pattern of galena-calcite treated at power density of 1×10^{11} W/m^3 for 1 ms

It should be noted that the breakage behaviour of particles in a crusher is very complex. The breakage behaviour of a single particle without confinement may not sufficiently represent the effect of stressing a large number of particles, which induces more complicated loading conditions for particle surfaces (Liu et al., 2005). However, from the results of this study it is evident that microwave irradiation can indeed change the fracture pattern of an ore considerably. It is suggested that future work be continued for simulating the confined bed comminution of microwave treated ores in order to fully understand the process.

8.8.4 Conclusions

Initial investigation of the effect of microwave treatment on liberation of mineral was carried out by comparing the fracture pattern of untreated and microwave treated ores. It has been shown that microwave irradiation considerably changed the fracture pattern of an ore in a simulated single particle crushing. In the ore exposed to microwave at lower power density, fractures along the grain boundary and also inside the absorbent mineral were observed. The fracture pattern of the ore treated at high power density was along the grain boundary and the absorbent mineral was intact. However, in all cases the fracture patterns were preferentially localized around the grain boundary compared to that of the untreated ore. It is suggested that future simulation work be continued by modelling more realistic ore textures for investigating the fracture pattern of microwave treated ores in a confined bed comminution. And it would also be very useful if simulation models are constructed for quantification of the effect of microwave treatment on liberation of minerals.

Chapter 9

Conclusions and Future Work

9.1 Conclusions

Comminution forms a large proportion of any mineral processing plant's capital and operating costs; 30-50% of the total plant power draw and up to 70% for hard ores is attributable to comminution (Napier-Munn et al, 1996). Thus, there is much to be gained from improving the process. Currently, one area which has shown a significant promise in improving comminution efficiency is microwave treatment of ores. Microwave heating of mineral ores induces fracture around grain boundaries due to the differences in absorption of microwaves and the resulting differential thermal expansion among the various mineral phases in the ore particles. As a consequence, this may reduce the energy required in subsequent grinding and enhance liberation of valuable minerals. The potential benefits of microwave heating also include increased mill capacity, reduced mill wear, and reduction in slimes production.

Application of microwave energy at high power density and with short exposure time has been the focus of recent work. The work by Kingman et al. (2004a, b) has shown for the first time that microwave treatment of ores may be economically viable by using very high power density for short exposure times. However, much work still remains to be done to scale up the process and system designs. Process scaling needs model development and simulation. Numerical simulation is particularly important for understanding the interaction between the microwave and the constituent minerals, as it provides insightful and complete information that can not be measured or difficult

to acquire via experiment. It also offers an alternative tool of various investigations, instead of carrying out expensive, time-consuming or even dangerous experiment in laboratories. Further, it can provide a design target and operating condition for developing microwave applicators for industrial application.

The first part of this study has considered the effects of different variables on microwave treatment of ores. These include the influences of thermo-mechanical properties of minerals, absorbent phase grain size, power density, absorbent phase dissemination and absorbent modal area. The aim of this part of the study was to better understand the influences of these variables on the heating rates and strength reduction of the ores and to identify ores, which are more amenable to microwave treatment.

The effect of thermo-mechanical properties of mineral on strength reduction of microwave treated ores was investigated in detail for the first time. Nine different binary ore models were constructed by randomly disseminating microwave absorbing minerals in transparent matrices. It was shown that the thermo-mechanical properties of both the microwave absorbing and the transparent minerals have a strong influence on strength reduction. It has been shown that in general the thermal properties of the microwave absorbing mineral and the mechanical properties of the transparent matrix have the most significant effect on the strength reduction. Binary ores containing a microwave absorbing mineral that has a high thermal expansion coefficient in a strong transparent matrix achieved higher reductions in strength.

The effect of absorbent phase grain size on bulk strength reduction of microwave treated ores was also examined. It has been shown that the grain size of the microwave absorbent phase considerably affects the extent of damage in microwave

treated ore for the same treatment condition. It was shown that for the same power density, energy input and mineral types, the reductions in strength were much higher in coarse-grained ores.

The influence of power density on unconfined compressive strength reductions of microwave treated ores was also investigated for a narrow range. It was shown that strength reduction of microwave treated ores strongly depends on the applied power density. It was illustrated that by increasing the power density dissipated in the absorbent phase a higher bulk strength reduction of ore could be achieved for the same energy input.

The influence of microwave absorbent phase dissemination on strength reduction of microwave treated ores was also examined. It has been shown that for the same mineralogy and microwave treatment condition, strength reduction of ores significantly depends on the degree of dissemination of the absorbing mineral in the ore. It was shown that ores with poorly disseminated heated phase achieved much higher strength reduction.

The effect of microwave absorbent phase modal area on strength reduction of microwave treated ores was also investigated. The results obtained by fixing the applied power density indicated a higher strength reduction for ores with higher absorbent modal area. The results obtained by fixing the energy input also indicated a relatively higher strength reduction for the ores with high absorbent modal area.

The effect of microwave treatment on the mechanical state of an ore sample was also examined. It was observed that even if a significant tensile damage was occurred in the vicinity of the grain boundary at lower energy input, there was no change in the unconfined compressive strength of the ore. Reduction in unconfined compressive

strength of the ore was observed only at higher energy input where tensile and shear damage occurred throughout the bulk of the sample. It was demonstrated that unconfined compressive strength of an ore is less sensitive to microwave induced micro-fractures and found to be a poor descriptor of liberation behaviour.

A new method of quantifying damage around the grain boundaries of microwave treated ore has been developed. Using the method, the influence of power density, mineralogy and absorbent phase grain size has been elucidated. It has been shown that it is possible to induce considerable grain boundary damage without significantly increasing the temperature of the ore. It has also been shown that it is possible to reduce the required energy input for inducing a given amount of grain boundary damage substantially by operating at higher power density. It was also shown that the amount of grain boundary damage incurred at a specific power density and energy input is dependent both on the ore mineralogy and absorbent phase grain size. It has also been demonstrated that for a given mineralogy and ore texture there is a power density level below which no further increase in grain boundary damage is possible by increasing exposure time.

The developed method was also used to construct damage maps which show contour of the fraction of grain boundary zones damaged as a function of power density and exposure time for different binary ores and ore textures for a range of operating conditions. The intention of this part of the work was to provide design target and operating conditions for current and future industrial microwave applicators. It was shown that both the power density and the energy input required to cause a fixed amount of grain boundary damage strongly depend on the ore mineralogy and its texture. It has been shown that for ore relatively amenable to microwave, it was

possible to incur significant amount of grain boundary damage at lower power density. However, higher power density (for the same energy input) was needed to cause the same amount of grain boundary damage for ore less amenable to microwave. For less amenable fine-grained ore, both higher power density and higher energy input were required to incur the same amount of grain boundary damage.

The energy inputs that were required for significant (> 10 %) grain boundary damage in the ores range from 1×10^7 to 1×10^9 J/m^{3}abs (0.087 - 7.055 kWh/t) depending on the power density applied, the ore mineralogy and its texture. The results also indicated that continuous wave equipment could be successfully used for ores relatively amenable to microwave treatment. For such ores, there would be no further energy saving by increasing power density, which increases the capital cost to produce the required microwave equipment. However, for less amenable fine-grained ores, pulsed equipment (which is capable of producing high power densities) is needed for economic microwave treatment.

The effect of pulse repetition frequency on grain-boundary damage was also examined. It was found that high frequency pulse repetition frequencies (≥ 50 Hz) resulted in an amount of grain boundary damage that was indistinguishable from that caused by continuous wave operation for a fixed energy input. The practical implication of this is that if pulsed microwave equipment is designed to operate at higher frequencies, it will lose the benefit of the high power available and behave like continuous wave equipment. In general, it has been shown that for a fixed microwave energy input the best result would be obtained by using the lowest possible pulse repetition frequency and highest peak pulse power.

A bonded-particle model (BPM) was also used to investigate the effects of power density, mineralogy and absorbent phase grain size on the extent of fracture and type of crack pattern in microwave treated ores. The bonded-particle model utilizes the breakage of individually structural bonds to directly represent damage. It was also possible to create arbitrary shape of absorbent phase grain by attaching particles/balls together. The results from this work showed that the amount of micro-cracks and also the crack patterns in an ore sample after microwave treatment significantly depend on its mineralogy, microwave treatment conditions and absorbent phase grain size. It has also been shown that a minimum power density is required to localize damage around the grain boundary in an ore sample. This minimum power density was found to strongly depend on the ore mineralogy and its texture. This was in complete agreement with the result obtained using a continuum approach.

Damage maps which show the percentage of micro-cracks as a function of power density and exposure time for different binary ores and ore textures were also constructed using bonded-particle model. It was shown that the amount of bond breakage in an ore sample depends strongly on the power density. It has also been shown that for a given ore mineralogy and texture, there exists a power density beyond which no further increase in micro-fractures would be obtained for the same energy input. In addition, it was shown that for the same power density and energy input, the percentage of micro-fractures induced by microwave considerably depends on the ore mineralogy and its texture.

Initial work concerning the effect of microwave treatment of ore on liberation of mineral was also carried out by comparing the fracture pattern of untreated and microwave treated ores in a simulated single particle compression. It has been shown

that microwave irradiation substantially changed the fracture pattern of an ore. The fracture pattern of the ore treated at high power density was along the grain boundary and the absorbent mineral was intact. In the ore treated at lower power density for the same energy input, both intergranular and transgranular fractures were observed. However, in all cases the fracture patterns were preferentially localized around the grain boundary compared to that of the untreated ore.

9.2 Future work

The first part of this thesis has discussed in detail the influences of different variables on microwave treatment of ores. It is recommended that further work be carried out using the result obtained from this part of the study in conjunction with dielectric properties data, in developing a decision tree, which can be used for selecting ores amenable to microwave treatment, and for elucidating the practical success or failure of particular ores to treatment.

Different damage maps which show damage as a function of power density and treatment time were constructed for different ores and ore textures using both continuum analysis and bonded-particle model. These could also be combined with electromagnetic simulation to provide design targets and operating conditions for microwave applicators being developed for industrial application (e.g. Bradshaw et al., 2009). This needs a precise determination of power density inside the absorbent phase. Future advances on measuring dielectric properties of minerals and electromagnetic modeling are required.

This study also showed the effect of microwave treatment of ore on liberation of mineral by using a simple model of crushing. However, more investigation is needed in order to fully understand the breakage behaviour of microwave treated ores. It is

recommended that future simulation work be continued by modelling more realistic ore textures and crushers. Investigations of the influences of crusher type, crushing speed (strain rate), crushing gap, etc on liberation of minerals are decisive, as these have considerable effects on the downstream processing of microwave treated ores and affect directly the optimal plant configuration.

Simulations of fragmentation behaviour, particle size distribution and liberation degree during bed comminution of microwave treated ores are of paramount importance. Further, future simulation work should focus emphatically on quantification of the effects of microwave treatment on liberation of minerals by modelling more realistic ore mineralogy and texture. Once this is achieved, experimental verification of the modelling results should be carried out.

References

Andres, U., Timoshkin, I., Jirestig, J. and Stallknecht, H. (2001) Liberation of valuable inclusions in ores and slags by electrical pulses, *Powder Technology*, 114 , pp. 40–50.

Bass, J.D. (1995) Elasticity of minerals, glasses, and melts. In: T.J. Ahrens, Editor, Handbook of Physical Constants, American Geophysical Union, Washington, DC, pp. 45-63.

Bearman , R.A. (1999) The use of the point load test for the rapid estimation of Mode I fracture toughness, *Int. J. Rock Mech. Min. Sci.*, 36, 2 , pp. 257–263

Bearman, R.A., Brigss, C.A. and Kojovic, T. (1997) The Application of Rock Mechanics parameters to The Prediction of Comminution Behaviour. *Minerals Engineering* ,10, 3, pp. 255–264.

Beer, G. (1983) Finite Element, Boundary Element and Coupled Analysis with Applications in Geomechanics, International Journal for Numerical Methods in Engineering, 19, pp. 567-580.

Beer, G. (1986) Implementation of Combined Boundary Element-Finite Element Analysis with Applications in Geomechanics. Devlopment. In Boundary Element Method. Banarjeeand Watson. London, Elsevier Applied Sciences, 4**,** pp**.** 191-225.

Beer, G. and Meek J. L. (1981) Coupled Finite Element-Boundary Element Analysis of Infinite Domain Problems in Geomechanics. Numerical Methods for Coupled Problems. Bettessand Lewis. Swansea, U.K., Pineridge Press, pp. 605-629.

Birch, F. and Clark, H. (1940) The thermal conductivity of rocks and its dependence upon temperature and composition, *Am. J. Sci.*, 238, pp. 611–635.

Bradshaw, S.M., Beckmann, A. (1998) Microwave processing of chalcopyrite. In: Mineral Processing, 98, Western Cape Branch of SAIMM, Cape Town.

Bradshaw, S., Louw, W., Merwe, C., Reader, H., Kingman, S. Celuch, M., Kijewska, W. (2007) Techno-economic considerations in the commercial microwave processing of mineral ores, J.Microwave Power & Electromagnetic Energy, 40, 4, pp.228-240.

Bradshaw, Steven M., Ali, Abubeker Y., Marchand, R. and Barnard, A. (2009) Performance Quantification of Applicators for Microwave Treatment of Crushed Mineral ore , 12th International Conference on Microwave and High Frequency Heating, Karlsruhe, Germany.

Brady B.G. and Brown, E.T. (1985) Rock Mechanics for Underground Mining, George Allen & Unwin, London.

Brady, B. G. and Wassyng A. (1981) A Coupled Finite Element-Boundary Element Method of Stress Analysis, Int. J. Rock Mech. Min. Sci. Geomech. Abstr., 23, 4, pp.475-485.

Brebbia, C. A. and Georgiou P. (1979) Combination of Boundary and Finite Elements in Elastostatics, Appl. Math. Modelling, 3, pp.212-220.

Broch, E. and Franklin, J.A. (1972) The point load strength test, *Int. J. Rock Mechanics Mining Sci.*, 9, pp. 669–697.

Brown, E. T. and Brady J. (1987) Analytical and Computational Methods in Engineering Rock Mechanics. London ; Boston, Allen & Unwin.

Bykov, Yu.V., Rybakov, K.I. and Semenov, V.E. (2001) Topical review. High-temperature microwave processing of materials. *Journal of Physics. D, Applied Physics* 34, pp. 55–75.

Chan, T. V. C. T. and Reader, H. C. (2000) Understanding Microwave Heating Cavities., Archtech. House, London.

Chen, T.T., Dutrizac, J.E., Haque, K.E., Wyslouzil, W. and Kashyap, S. (1984) The relative transparency of minerals to microwave radiation, *Canadian Metallurgical Quarterly*, 23, 3, pp. 349–351.

Cho , N., Martin, C.D., Sego, .D.C. (2007) A clumped particle model for rock, *Int J Rock Mech Min Sci* , 44, pp. 997–1010.

Chunpeng, L., Yousheng, X., Yixin, H. (1990). Application of microwave radiation to extractive metallurgy,Chin. J. Met. Sci. Technol., 6, 2, pp.121–124.

Clark, D.E., Folz, D.C. and West, J.K. (2000) Processing materials with microwave energy. *Materials Science & Engineering. A*, 287, pp. 153–158.

Clark, S. P. (1966) Handbook of Physical Constants. Geological Society of America, New York, pp. 415-436.

Cumbane, A.J. (2003) Microwave processing of Minerals, PhD thesis, University of Nottingham, Nottingham, UK, pp. 110–115.

Cundall, P. A. (1971). A Computer Model for Simulating Progressive Large Scale Movements in Blocy Rock Systems. Proc. Sympo. Int. Soc. Rock Mech.

Cundall, P. A. and Strack, O. D. L. (1979) A Discrete Numerical Model for Granular Assemblies, Geotechnique, 29, pp. 47-65.

Cundall, P. A. and Strack, O. D. L. (1983) Modelling of Microscopic Mechanisms in Granular Material. In Mechanics of Granular Materials: New Models and Constitutive Relations. J. T. Jenkinsand M. Satake. Amsterdam, Elsevier pp. 137-149.

Desai, C. S. and Christian, J. T. (1977). Numerical Methods in Geomechanics, New York: McGraw-Hill.

Diederichs MS. (2000) Instability of hard rock masses: the role of tensile damage and relaxation, PhD thesis, University of Waterloo, Canada.

Diment, W.H., and Pratt, H.R. (1988) Thermal conductivity of some rock forming minerals: a Tabulation, U.S.G.S. open file report, pp. 88-690.

Edelbro, C. (2003) Rock mass strength—a review. Technical report 2003:16, Luleå University of Technology. ISSN, pp. 1402 - 1536.

Fuerstenau, D.W., Abouzeid, A.-Z.M. (2002) The energy efficiency of ball milling in comminution. International Journal of Mineral Processing, 67, pp. 161–185.

Goodman, R. E. and Shi G. (1985) Block Theory and Its Application to Rock Engineering., Prentice-Hall: Englewood Cliffs, NJ.

Haque, K.E. (1987) Microwave irradiation pre-treatment of refractory gold concentrate. In: Salter, R.S., Wysouzil, D.M. and McDonald, G.W., Editors, 1987. Proc. Int. Symp. on Gold Metallurgy. Winnipeg, Canada, pp. 327–339.

Haque, K.E. (1999) Microwave energy for mineral treatment processes—a brief review. International Journal of Mineral Processing, 57, pp. 1–24.

Harrison, P.C. (1997) A fundamental study of the heating effect of 2.45 MHz microwave radiation of minerals. Thesis, University of Birmingham, Birmingham.

Hoek, E. and Brown, E.T. (1980) Empirical strength criterion for rock masses. *J. Geotech. Engng Div., ASCE* 106(GT9), pp. 1013-1035.

Hoek, E., Carranza-Torres, C., Corkum, B. (2002) Hoek-Brown Failure criterion-2002 edition. In: Proceedings of the North American Rock Mechanics Symposium Toronto, 1, pp. 267-273.

Idehara ,T. , Saito T. , Ogawa, I. , Mitsudo ,S. , Tatematsu , Y. , Sabchevski, S. (2008) The potential of the gyrotrons for development of the sub-terahertz and the terahertz frequency range — A review of novel and prospective applications, Thin Solid Films, 517 , pp. 1503–1506.

Itasca (2000) Fast Lagrangian Analysis of Continua, Version 4.00, Itasca Consulting Group Inc., Minneapolis, MN, USA.

Itasca (2008), PFC2D — Particle Flow code in 2 Dimensions, Version 4.0, Itasca Consulting Group Inc., Minneapolis, MN, USA.

Jaeger, J.C. and Cook, N.G. (1969) Fundamentals of Rock Mechanics. Chapman and Hall, New York.

Jing, L. (1998) “Formulation of Discontinuous Deformation Analysis (DDA) - an Implicit Discrete Element Model for Block Systems.” Eng. Geol. 49: 371-381.

Jing, L. (2003) A Review of Techniques, Advances and Outstanding Issues in Numerical Modelling for Rock Mechanics and Rock Engineering., Int. J. Rock Mech. Min. Sci. 40: 283-353.

Jing, L. and Hudson J. A. (2002) Numerical Methods in Rock Mechanics, Int. J. Rock Mech. Min. Sci. 39: 409-427.

Jones, D.A (2004) Understanding microwave treatment of ores, PhD thesis, University of Nottigham, UK.

Jones, D.A., Kingman, S.W., Whittles, D.N. and Lowndes, I.S. (2005) Understanding microwave assisted breakage, *Min. Eng.* 18, pp. 659-669.

Jones, D.A., Kingman, S.W., Whittles, D.N. and Lowndes, I.S. (2007) The influence of microwave energy delivery method on strength reduction in ore samples, *Chem. Eng. Proc.* 46, pp. 291-299.

Jumikis, A.R. (1979) Rock Mechanics, Trans. Tech. Publications, Clausthal, Germany.

King, R.P. (1990) Calculation of the liberation spectrum in products produced in continuous milling circuits. In: Proceedings 7th European Symposium on Comminution, Ljubljana, vol. 2, pp. 429-444.

Kingman, S.W. (1998) The effect of microwave radiation upon the comminution and beneficiation of minerals. PhD thesis, The University of Birmingham.

Kingman, S.W. and Rowson, N.A.(1997) Application of Microwave Energy to Enhance Performance of Mineral Separation Processes. In: R.A. Williams *et al.*, Editors, *Innovation in Physical Separation Technologies*, Inst Min. Metal.

Kingman, S.W. and Rowson, N.A. (1998) Microwave treatment of minerals—a review. *Minerals Engineering* 11 11, pp. 1081–1087.

Kingman, S.W., Vorster, W. and Rowson, N.A. (2000a) The influence of mineralogy on microwave assisted grinding. *Minerals Engineering* 13 3, pp. 313-327.

Kingman, S.W., Vorster, W. and Rowson, N.A., (2000b). The effect of microwave radiation on the processing of palabora copper ore. *Trans. S. Afr. Inst. Min. Metall.*, pp. 197–204

Kingman, S.W., Jackson, K., Bradshaw, S.M., Rowson, N.A. and Greenwood, R. (2004a) An investigation into the influence of microwave treatment on mineral ore comminution, *Powder Technol.* 146 (3), pp. 176-184.

Kingman, S.W., Jackson, K., Cumbane, A., Bradshaw, S.M., Rowson, N.A. and Greenwood, R. (2004b) Recent developments in microwave-assisted comminution, *Int. J. Min. Proc.* 74 (1–4), pp. 71-83.

Knacke, O., Kubachewski, O., and Hesselmann, K. (1991) Thermochemical Properties of Inorganic Compounds (2nd ed.), Springer-Verlag, Berlin, Germany.

Lama, R. D. and Vutukuri, V. S. (1978) Handbook on Mechanical Properties of Rocks., Trans Tech Publications (Clausthal, Germany) , vol. 2.

Lama, R. D. and Vutukuri, V. S. (1978) Handbook on Mechanical Properties of Rocks., Trans Tech Publications (Clausthal, Germany) , vol. 3.

Liu, H.Y., Kou, S.Q. and Lindqvist , P.-A., (2005) Numerical studies on the inter-particle breakage of a confined particle assembly in rock crushing, *Mech. Mater*. 37, pp. 935–954.

McGill, S.L., Walkiewicz, J.W. and Smyres, G.A. (1988) The effect of power level on the heating rate of selected chemical and minerals. Materials Research Society Symposia Proceedings 124, pp. 247–252.

Malvern, L. E. (1969) "Introduction". In Mechanics of a Continuous Medium, Englewood Cliffs, New Jersey: Prentice Hall.

Marchand, R. (2008) Performance Evaluation of Applicators, unpublished report, Process Engineering Department, Stellenbosch University.

Meredith, R.J. (1998) Engineers' Handbook of Industrial Microwave Heating/Roger Meredith. , Institution of Electrical Engineers, London.

Metaxas, A.C. and Meredith, R.J. (1983) Industrial Microwave Heating. , Peter Peregrinus, London.

Napier-Munn, T.J., Morrell, S., R.D. Morrison and Kojovic, T.(1996) Mineral Comminution Circuits: their Operation and Optimisation. , Julius Kruttschnitt Mineral Research Centre, Brisbane.

Olubambi, P.A., Potgieter, J.H., Hwang, J.Y., Ndlovu, S. (2007) Influence of microwave heating on the processing and dissolution behaviour of low-grade complex sulphide ores, Hydrometallurgy, 89 (1–2), 127–135.

Osepchuck, J. M. (1984) A history of microwave heating applications, *IEEE Transactions on Microwave Theory and Techniques*, MTT , 32, pp. 1200–1224.

Potyondy, D. O. and Cundall, P. A. (2004) A Bonded-Particle Model for Rock, Int. J. Rock Mech. & Min. Sci.,. 41(8), 1329-1364.

Rowson, N.A. and Rice, N.M. (1990) Desulphurisation of coal using low power microwave energy. *Minerals Engineering* 3 3–4, pp. 363–368.

Rowson, N.A. and Rice, N.M. (1990) Magnetic enhancement of pyrite by caustic microwave treatment. *Minerals Engineering* 3 3–4, pp. 355–361.

Sahyoun, C., Rowson, N.A., Kingman, S.W. L. Groves, L. and Bradshaw, S.M. (2005) The influence of microwave pre-treatment on copper flotation, *Trans. S. Afr. Inst. Min. Metall.* **105** (1), pp. 7–13.

Scott, G., 2006. Microwave Pretreatment of a Low Grade Copper Ore to Enhance Milling Performance and Liberation. MSc Thesis, University of Stellenbosch, South Africa.

Scott, G., Bradshaw, S.M and Eksteen, J.J. (2008) The effect of microwave pretreatment on the liberation of a copper carbonatite ore after milling, *Minerals Engineering* 85, 4, pp.121-128

Sass, J.H., Lachenbruch, A.H., Moses, T.H., Jr., and Morgan, P. (1992) Heat flow from a scientific research well at Cajon Pass, California, J.geophys.Res, 97(B4), pp. 5017-5030.

Sheppard, M. S. (1988) Approaches to the Automatic Generation and Control of Finite Element Meshes, Appl. Mech. Rev., 41, pp. 169-185.

Stagg, K. and Zienkiewicz, 0. C. (1968) Rock Mechanics in Engineering Practice, Wiley, New York.

Stein, R. H., Edgar, M. F. , Iskander, D. L., Johnson, S. M., Johnson, C. G., Lob, J. M., Shaw, Sutton, W. H., Tien, P. K. and Munns, T. E. (1994) "Microwave Processing of Materials," Committee on Microwave Processing of Materials, National Materials Advisory Board, Commission on Engineering and Technical Systems, and National Research Council, Microwave Processing of Materials. Washington, DC, National Academy Press.

Tang, C.A., Xu, X.H., Kou, S.Q., Lindqvist, P.-A. and Liu, H.Y. (2001) Numerical investigation of particle breakage as applied to mechanical crushing—Part I: Single-particle breakage, *International Journal of Rock Mechanics and Mining Sciences*, 38, pp. 1147–1162.

Tavares, L.M. and King, R.P. (1995) Application of Thermal Treatment to Improve Comminution, SME Annual Meeting, Denver, Colorado**.**

Tavares, L.M. and King, R.P. (1996) Effect of microwave-induced damage on single-particle comminution of ores, *SME Annual Meeting*, Phoenix, Arizona, pp. 11–14.

Thostenson, E.T. and Chou, T.-W. (1999) Microwave processing: fundamental and applications. Composites. Part A, Applied Science and Manufacturing 30, pp. 1055–1071

Tinga, W.R. (1992) Mixture laws and microwave-material interactions, Dielectric Properties of Heterogeneous Materials 6, p. 40.

Tromans, D. (2008) Mineral comminution: Energy efficiency considerations, Minerals Engineering, 21, pp. 613–620.

Vorster, W., Rowson, N.A. and Kingman, S.W. (2001) The effect of microwave radiation upon the processing of Neves Corvo copper ore, *Int. J. Miner. Process*, 63**,** pp. 29–44

Wang, G., Radziszewski, P. and Ouellet, J. (2008) Particle modeling simulation of thermal effects on ore breakage, Computational Materials Science, 43, 4, pp. 892-901.

Wang, Q.Z., W., Li, W. and Xie, H.P. (2009) Dynamic split tensile test of Flattened Brazilian Disc of rock with SHPB setup, Mechanics of Material, 41, pp. 252-260.

Walkiewicz, J.W., Clark, A.E. and McGill, S.L. (1991) Microwave-assisted grinding. *IEEE Transactions on Industry Applications* 27, p. 239.

Walkiewicz, J.W., Kazonich, G. and McGill, S.L. (1988) Microwave heating characteristics of minerals and compounds. *Minerals and Metallurgical Processing* 39, pp. 39–42.

Walkiewicz, J.W., Lindroth, D.P. and Clark, A.E. (1993) Grindability of taconite rod mill feed enhanced by microwave induced cracking. In: *SME Annual Meeting Reno*, pp. 1–4.

Whiten, W.J. and Narayanan, S.S. (1988) Determination of comminution characteristics from single particle breakage tests and its application to ball mill scale-up, *Transactions of the Institution of Mineral Metallurgy,* 97, pp. C115–C124.

Whittaker, G. (1997) A Basic Introduction to Microwave Chemistry, [Online] Available at http://www.tan-delta.com/basics.html

Whittles, D.N., Kingman, S.W. and Reddish, D.J. (2003) Application of numerical modelling for prediction of the influence of power density on microwave-assisted breakage, *Int. J. Min. Proc.*, 68, pp. 71-91.

Appendices

Appendix A: Published International Conference and Journal Papers

1. **A.Y. Ali** and S.M. Bradshaw (2008), Effect of grain size and thermo-mechanical properties of minerals on strength reduction of binary ores subjected to microwave radiation, *Proceedings of the 1st Southern Hemisphere International Rock Mechanics Symposium*, Perth, Australia, Volume 2, Pages 85–97.

2. **A.Y. Ali** and S.M. Bradshaw (2009), Quantifying Damage around Grain boundaries in Microwave Treated Ores, *Chemical Engineering and Processing: Process Intensification.,* Volume 48, Issues 11-12, Pages 1566-1573.

3. Steven M. Bradshaw, **Abubeker Y. Ali**, Renier Marchand,. Andri Barnard, Performance Quantification of Applicators for Microwave Treatment of Crushed Mineral ore, *12th International Conference on Microwave and High Frequency Heating*, Karlsruhe, Germany, September, (2009).

4. **A.Y. Ali** and S. M. Bradshaw, Bonded-particle Modelling of Microwave-Induced Damage in Ore Samples, *Min. Eng.*, (2010) *(To be submitted for Publication, Manuscript prepared).*

5. S.M. Bradshaw, **A.Y. Ali**, R. Marchand,. A. Barnard, Performance Quantification of Applicators for Microwave Treatment of Crushed Mineral ore, *Journal of Microwave Power and Electromagnetic Energy*, (2009) *(Under review).*

Appendix B: Simulation code used for modelling microwave heating of a binary ore

```
config thermal ; set thermal model
def diam
  diam=10   ; set diameter
end
 def zonemm
 zonemm=0.125 ; set zone size
 end
 def horcoor
 horcoor=diam/zonemm ; set width
 end
 def totalheight
 totalheight=3*horcoor ; total height including the steel platens
 end
 def xplone
 xplone=horcoor+1 ; total number of zones in the X-direction
 end
def heightplone
 heightplone=totalheight+1 ; total number of zones in the Y-direction
 end

 grid horcoor,totalheight          ; specify grid area

 def pbcoor           ; specify coordinate and node of lower platen
 pbcoor=(horcoor*0.5)-1
end
def ptcoor
 ptcoor=totalheight - pbcoor
 end

 def pbplone
 pbplone=pbcoor+1
```

```
    end
    def pbminone
    pbminone=pbcoor-1
    end


    def ptminone          ; specify coordinate and node of upper  platen
    ptminone=ptcoor-1
    end
    def ptplone
    ptplone=ptcoor+1
   end

   def xright          ;specify coordinate and node of upper  platen
    xright=diam*0.001
    end
    def ytop
    ytop=xright*4
    end
    def platbot
    platbot=xright*0.5
    end
    def platop
    platop=ytop-platbot
    end


                              ; generate sample (ore model) area
    gen 0.0,0.0 0.0,platbot xright,platbot xright,0.0 i 1 xplone j 1 pbcoor
    gen 0.0,platbot 0.0,platop xright,platop xright,platbot & i 1 xpone j
pbplone ptcoor
    gen 0.0,platop 0.0,ytop xright,ytop xright,platop & i 1 xplone j
ptplone heightplone
```

```
model ss       ; specify strain softening properties
prop fric 45 tens 12e6 coh 27.9e6  i=1,horcoor j=pbplone,ptminone
prop ttab=1 ctab=2 i=1,horcoor j=pbplone,ptminone
table 1 0,12e6 0.001,0.12e6
table 2 0,27.9e6 0.01,2.79e6

                    ; specify the matrix mechanical properties
group 'User: calcite' region horcoor horcoor
prop den=2712 bulk=7.3299993e10 shear=3.1999998e10 group 'User: calcite'
prop fric 45 tens 12e6 coh 27.9e6 group 'User: calcite'

                  ; specify the percentage of microwave absorber area
def percent
percent=0.125*(horcoor*(totalheight-horcoor))
end
                ; Correction of percentage for multiple zones
def corec1
corec1=0.4*(percent/128)
end
def corec2
corec2=0.2*(percent/64)
end
def corec3
corec3=0.4*(percent/128)
end
```

```
; Randolmly generate absorber grain, count and output the number of absorber zones

def randomMGN1 loop m(1,corec1)
coox=(urand*horcoor)
cooy=(urand*(totalheight-horcoor)) + (horcoor*0.5)
x1=coox+1              ; specify width of the grain(=8 ×zone size)
y1=cooy+15             ; specify height of the grain(=16 ×zone size)
command
model ss      ; mechanical properties of galena
group 'user:galena' i coox X1  j cooy Y1
prop density=7597 bulk=5.86e10 shear=3.19e10 group 'user:galena'
prop fric 45 tens 12e6 coh 27.9e6  group 'user:galena'
end_command
end_loop
end
randomMGN1
def pbcoorplus2
pbcoorplus2=pbcoor+2
end
def ptcoorminus1
ptcoorminus1=ptcoor-1
end
                        ; count the number of absorbent grains
def pyrcon1
loop i (1,horcoor)
loop j (pbcoorplus2,ptcoorminus1)
if model(i,j) # 1 then
if density(i,j)> 4000.0 then
pyrc1 = pyrc1 + 1
end_if
tot1 = tot1 + 1
```

```
end_if
end_loop
end_loop
command
print pyrc1
print tot1
end_command
end

pyrcon1

                                ; Randomly generate another grain size
def randomMGN2
loop m(1,corec2)
coox=(urand*horcoor)
cooy=(urand*(totalheight-horcoor)) + (horcoor*0.5)
x2=coox+7 ; specify width of the grain(=8 ×zone size)
y2=cooy+7 ; specify height of the grain(=8 ×zone size)
command
model ss                    ; mechanical properties of galena
group 'user:galena' i coox X2  j cooy Y2
prop density=7597 bulk=5.86e10 shear=3.19e10 group 'user:galena'
prop fric 45 tens 12e6 coh 27.9e6  group 'user:galena'
end_command
end_loop
end
randomMGN2
def pbcoorplus2
pbcoorplus2=pbcoor+2
end
def ptcoorminus1
ptcoorminus1=ptcoor-1
end
```

```
                    ; count the number of absorbent grain
def pyrcon2
loop i (1,horcoor)
loop j (pbcoorplus2,ptcoorminus1)
if model(i,j) # 1 then
if density(i,j)> 4000.0 then
pyrc2 = pyrc2 + 1
end_if
tot2 = tot2 + 1
end_if
end_loop
end_loop
command
print pyrc2
print tot2
end_command
end
pyrcon2
                    ; Randomly generate another grain size
def randomMGN3
loop m(1,corec3)
coox=(urand*horcoor)
cooy=(urand*(totalheight-horcoor)) + (horcoor*0.5)
x3=coox+15
y3=cooy+7
command
model ss
group 'user:galena' i coox X3  j cooy Y3
prop density=7597 bulk=5.86e10 shear=3.19e10 group 'user:galena'
prop fric 45 tens 12e6 coh 27.9e6  group 'user:galena'
end_command
```

```
end_loop
end
randomMGN3
def pbcoorplus2
pbcoorplus2=pbcoor+2
end
def ptcoorminus1
ptcoorminus1=ptcoor-1
end
                    ; count the number of absorbent grain
def pyrcon3
loop i (1,horcoor)
loop j (pbcoorplus2,ptcoorminus1)
if model(i,j) # 1 then
if density(i,j)> 4000.0 then
pyrc3 = pyrc3 + 1
end_if
tot3 = tot3 + 1
end_if
end_loop
end_loop
command
print pyrc3
print tot3
end_command
end
pyrcon3


        ; apply power density in the absorbent grain
def source
loop i(1,horcoor)
loop j(pbplone,ptminone)
if density(i,j)=7597 then
```

```
    command
    interior source 1e9 i=i j=j
    end_command
    end_if
    end_loop
    end_loop
    end
    source


        ; initialize temperature and specify thermal properties of both the
absorbent and the transparent mineral as a function of temperature


    initial temperature 10 i 1 xplone j pbplone ptminone
    model th_isotropic i 1 xplone j pbplone ptminone
    def trop
    loop i(1,horcoor)
    loop j(pbplone,ptminone)

if density(i,j)<3000 and        ; thermal expansion coefficient of calcite
if (temp(i,j)+273)<673 then
thexp(i,j)=((0.0233*(temp(i,j)+273))+4.398)*1e-6
end_if
end_if
if density(i,j)<3000 and
if (temp(i,j)+273 )>= 673 then
thexp(i,j)=((0.0195*(temp(i,j)+273))+6.975)*1e-6
end_if
end_if

if density(i,j)<3000 and ; thermal conductivity of calcite
if temp(i,j)<500 then
```

```
conductivity(i,j)= ((temp(i,j))*(-0.00261))+3.225
end_if
end_if
if density(i,j)<3000 and
if temp(i,j) >= 500 then
conductivity(i,j)=((temp(i,j))*(-0.00112))+2.48
end_if
end_if

if density(i,j)<3000 and ; specific heat capacity of calcite
if (temp(i,j)+273)<500 then
spec_heat(i,j)=(1.155*(temp(i,j)+273))+473.51
end_if
end_if
if density(i,j)<3000 and
if (temp(i,j)+273) >= 500 then
spec_heat(i,j)=(0.375*(temp(i,j)+273))+863.5
end_if
end_if


    if density(i,j)>4000 and  ; thermal conductivity of galena
    if temp(i,j)<500 then
    conductivity(i,j)= ((temp(i,j))*(-0.00196))+2.83
    end_if
    end_if
    if density(i,j)>4000 and
    if temp(i,j) >= 500 then
    conductivity(i,j)= ((temp(i,j))*(-0.00096))+2.33
    end_if
    end_if

    if density(i,j)>4000 and          ; specific heat capacity of galena
```

```
if (temp(i,j)+273)<500 then
spec_heat(i,j)=(0.0311*(temp(i,j)+273))+199.68
end_if
end_if
if density(i,j)>4000 and
if (temp(i,j)+273) >= 500 then
spec_heat(i,j)=(0.03942*(temp(i,j)+273))+195.52
end_if
end_if

if density(i,j)>4000 and   ; thermal expansion coefficient of galena
if (temp(i,j)+273)<673 then
thexp(i,j)=((0.00667*(temp(i,j)+273))+58.71)*1e-6
end_if
end_if
if density(i,j)>4000 and
if (temp(i,j)+273)>= 673 then
thexp(i,j)=((0.018*(temp(i,j)+273))+51.091)*1e-6
end_if
end_if
end_loop
end_loop
command
step 100                    ; solve for 100 step
end_command
end
set thdt=0.000001          ; set thermal step
trop                       ; execute (100 × 0.000001 s)
```

Appendix C : UCS test simulation code

```
restore galena_calcite_fine_5e8_0.5s.sav  , restore microwave heated ore


                ; specify steel platens properties
mod EL i=1,horcoor j=1,pbminone
prop den=7500 bulk=21e10 shear=8.1e10 i=1,horcoor j=1,pbminone
mod EL i=1,horcoor j=ptplone,totalheight
prop dens=7500 bulk=21e10 shear=8.1e10 i=1,horcoor
j=ptplone,totalheight
            ; specify interface coordinates and stiffness parameters
    INT 1 ASIDE FROM 1,pbcoor TO xplone,pbcoor BSIDE FROM
1,pbplone &
    to xplone,pbplone
    INT 1 KN 2E12 KS 5E12 FRIC 32

    INT 2 ASIDE FROM 1,ptcoor TO xplone,ptcoor BSIDE FROM 1,ptplone
&
    to xplone,ptplone
    INT 2 KN 2E12 KS 5E12 FRIC 32    ; specify stiffness parameters for
interface
    SET thermal=off                  ; set thermal model off
    set st_damp comb         ; set damping conditions
    ini sxx=0 i 1 xplone j 1 totalheight       ; initialize all parameter
    ini sxy=0 i 1 xplone j 1 totalheight
    ini syy=0 i 1 xplone j 1 totalheight
    ini szz=0 i 1 xplone j 1 totalheight
    ini ydis=0 i 1 xplone j 1 totalheight
    ini xdis=0 i 1 xplone j 1 totalheight
    ini xvel=0 i 1 xplone j 1 totalheight
    ini yvel=0 i 1 xplone j 1 totalheight

    apply yvel=-5e-9 j=totalheight       ; apply vertical velocities
    apply yvel=5e-9 j=1
```

```
def load
loop st(1,8000)                    ; set loading simulation
top_stress=0                       ; set initial loading conditions
bot_stress=0
loop ts(1,igp-1)                   ; total stress at each platens
top_stress=top_stress + syy(ts,totalheight);
bot_stress=bot_stress + syy(ts,1);
end_loop
top_stress=top_stress/xplone       ; average stress for top platen
bot_stress=bot_stress/xplone       ; average stress for bottom platen

av_stress=(top_stress + bot_stress)/2 ; define stress parameter (average)
ve= (ydisp(40,1)-ydisp(40,240))/(y(40,240)-y(40,1));define strain
parameter
command
print bot_stress                   ; print bottom stress
print top_stress                   ; print top stress
history av_stress                  ; specify history logged for average stress
history ve                         ; specify history logged for strain
step 5                             ;  logged every 5 steps
end_command
end_loop
end
load ; execute loading function (stress-strain curve can now be obtained by
writing 'His -1 vs 2' in the command window)
```

Appendix D: Simulation code used for specifying absorbent phase with grain-boundary

```
config thermal
def diam
  diam=15       ;specify width
end
 def zonemm
 zonemm=0.125 ; specify zone size
 end
 def horcoor
 horcoor=diam/zonemm ; total zones in the x-direction
 end
 def totalheight
 totalheight=horcoor  ; total zones in the y-direction
 end
 def xplone
 xplone=horcoor+1    ; total nodes in the x-direction
 end
def heightplone
 heightplone=totalheight+1 ; total nodes in the Y-direction
 end
 grid horcoor,totalheight       ; form grid
def xright
 xright=diam*0.001          ; specify X-coordinate
 end
 def ytop
 ytop=1*xright        ; specify Y-coordinate
 end


 gen 0.0,0.0 0.0,ytop xright,ytop xright,0 i 1 xplone j 1 heightplone
```

```
        ; Mechanical properties of calcite
model ss
prop fric 45 tens 12e6 coh 27.9e6  i=1,horcoor j=1,totalheight
prop ttab=1 ctab=2 i=1,horcoor j=1,totalheight
table 1 0,12e6 0.001,0.12e6
table 2 0,27.9e6 0.01,2.79e6
group 'User: calcite' region horcoor horcoor
prop den=2712 bulk=7.3299993e10 shear=3.1999998e10 group 'User:
calcite'
prop fric 45 tens 12e6 coh 27.9e6 group 'User: calcite'



def percent
percent=0.05*(horcoor*totalheight)     ; define absorbent percentage
end
              ; Correction factor for different grain size
def corec1
corec1=0.2*(percent/2)
end
def corec2
corec2=0.6*(percent/4)
end
def corec3
corec3=0.2*(percent/2)
end

        ; Randomly generate absorbent grain with grain boundary
def randomMGN1
loop m(1, corec1)
coox=(urand*horcoor)
cooy=(urand*totalheight)
x1=coox
```

```
y1=cooy+1
xg1=coox-1
xg2=x1+1
yg1=cooy-1
yg2=y1+1



command
model ss
        ; Grain boundary mechanical properties (grain boundary is defined by a single zone next to the absorbent phase)

group 'User: grainboundary' i xg1 coox j yg1 yg2
prop den=2712.1 bulk=7.3299993e10 shear=3.1999998e10 group 'User: grainboundary'
prop fric 45 tens 12e6 coh 27.9e6 group 'User: grainboundary'

group 'User: grainboundary' i coox x1 j yg1 cooy
prop den=2712.1 bulk=7.3299993e10 shear=3.1999998e10 group 'User: grainboundary'
prop fric 45 tens 12e6 coh 27.9e6 group 'User: grainboundary'

group 'User: grainboundary' i  x1 xg2 j yg1 yg2
prop den=2712.1 bulk=7.3299993e10 shear=3.1999998e10 group 'User: grainboundary'
prop fric 45 tens 12e6 coh 27.9e6 group 'User: grainboundary'

group 'User: grainboundary' i coox x1 j y1 yg2
prop den=2712.1 bulk=7.3299993e10 shear=3.1999998e10 group 'User: grainboundary'
prop fric 45 tens 12e6 coh 27.9e6 group 'User: grainboundary'

; Mechanical properties of galena
```

```
group 'user:galena' i coox x1  j cooy y1
prop density=7597 bulk=5.86e10 shear=3.19e10 group 'user:galena'
prop fric 45 tens 12e6 coh 27.9e6  group 'user:galena'

end_command
end_loop
end
randomMGN1
                              ; count the number of absorbent grain zone
def pyrcon1
loop i (1,horcoor)
loop j (1,totalheight)
if model(i,j) # 1 then
if density(i,j)> 4000.0 then
pyrc1 = pyrc1 + 1
end_if
tot1 = tot1 + 1
end_if
end_loop
end_loop
command
print pyrc1
print tot1
end_command
end
pyrcon1
     ; generate another absorbent grain with grain boundary
def randomMGN2
loop m(1,corec2)
coox=(urand*horcoor)
cooy=(urand*totalheight)
x2=coox+1   ; absorbent grain width
```

```
y2=cooy+1; absorbent grain height
                ; Grain boundary coordinates
xg1=coox-1
xg2=x2+1
yg1=cooy-1
yg2=y2+1
command
                ; Grain boundary mechanical properties
model ss
group 'User: grainboundary' i xg1 coox j yg1 yg2
prop den=2712.1 bulk=7.3299993e10 shear=3.1999998e10 group 'User:
grainboundary'
prop fric 45 tens 12e6 coh 27.9e6 group 'User: grainboundary'

group 'User: grainboundary' i coox x2 j yg1 cooy
prop den=2712.1 bulk=7.3299993e10 shear=3.1999998e10 group 'User:
grainboundary'
prop fric 45 tens 12e6 coh 27.9e6 group 'User: grainboundary'

group 'User: grainboundary' i  x2 xg2 j yg1 yg2
prop den=2712.1 bulk=7.3299993e10 shear=3.1999998e10 group 'User:
grainboundary'
prop fric 45 tens 12e6 coh 27.9e6 group 'User: grainboundary'

group 'User: grainboundary' i coox x2 j y2 yg2
prop den=2712.1 bulk=7.3299993e10 shear=3.1999998e10 group 'User:
grainboundary'
prop fric 45 tens 12e6 coh 27.9e6 group 'User: grainboundary'

group 'user:galena' i coox X2  j  cooy  y2
prop density=7597 bulk=5.86e10 shear=3.19e10 group 'user:galena'
prop fric 45 tens 12e6 coh 27.9e6  group 'user:galena'
```

```
end_command
end_loop
end
 randomMGN2
                ; Count the number of absorbent phase zones
def pyrcon2
loop i (1,horcoor)
loop j (1,totalheight)
if model(i,j) # 1 then
if density(i,j)> 4000.0 then
pyrc2 = pyrc2 + 1
end_if
tot2 = tot2 + 1
end_if
end_loop
end_loop
command
print pyrc2
print tot2
end_command
end
pyrcon2
          ; Generate another absorbent (galena) grain size with grain boundary
def randomMGN3
loop m(1,corec3)
coox=(urand*horcoor)
cooy=(urand*totalheight)
x3=coox+1
y3=cooy

xg1=coox-1
xg2=x3+1
yg1=cooy-1
```

```
yg2=y3+1

command
model ss

                ; Grain boundary mechanical properties
group 'User: grainboundary' i xg1 coox j yg1 yg2
prop den=2712.1 bulk=7.3299993e10 shear=3.1999998e10 group 'User:
grainboundary'
prop fric 45 tens 12e6 coh 27.9e6 group 'User: grainboundary'

group 'User: grainboundary' i coox x3 j yg1 cooy
prop den=2712.1 bulk=7.3299993e10 shear=3.1999998e10 group 'User:
grainboundary'
prop fric 45 tens 12e6 coh 27.9e6 group 'User: grainboundary'

group 'User: grainboundary' i  x3 xg2 j yg1 yg2
prop den=2712.1 bulk=7.3299993e10 shear=3.1999998e10 group 'User:
grainboundary'
prop fric 45 tens 12e6 coh 27.9e6 group 'User: grainboundary'

group 'User: grainboundary' i coox x3 j y3 yg2
prop den=2712.1 bulk=7.3299993e10 shear=3.1999998e10 group 'User:
grainboundary'
prop fric 45 tens 12e6 coh 27.9e6 group 'User: grainboundary'



          ; Mechanical properties of galena
group 'user:galena' i coox X3  j cooy Y3
prop density=7597 bulk=5.86e10 shear=3.19e10 group 'user:galena'
prop fric 45 tens 12e6 coh 27.9e6  group 'user:galena'
end_command
end_loop
```

```
end
randomMGN3
        ; Count again the number of absorbent phase zones
def pyrcon3
loop i (1,horcoor)
loop j (1,totalheight)
if model(i,j) # 1 then
if density(i,j)=7597 then
pyrc3 = pyrc3 + 1
end_if
tot3 = tot3 + 1
end_if
end_loop
end_loop
command
print pyrc3
print tot3
end_command
end

pyrcon3
            ; Initialize temperature and specify thermal properties
initial temperature 10 i 1 xplone j=1, heightplone
model th_isotropic i 1 xplone j=1, heightplone
def trop
loop i(1,horcoor)
loop j(1,totalheight)
                    ; specify thermal expansion coefficient of calcite
if density(i,j)<3000 and
if (temp(i,j)+273)<673 then
thexp(i,j)=((0.0233*(temp(i,j)+273))+4.398)*1e-6
end_if
end_if
```

```
if density(i,j)<3000 and
if (temp(i,j)+273)>= 673 then
thexp(i,j)=((0.0195*(temp(i,j)+273))+6.975)*1e-6
end_if
end_if
                ; specify thermal conductivity of calcite
if density(i,j)<3000 and
if temp(i,j)<500 then
conductivity(i,j)= ((temp(i,j))*(-0.00261))+3.225
end_if
end_if
if density(i,j)<3000 and
if temp(i,j)>= 500 then
conductivity(i,j)=((temp(i,j))*(-0.00112))+2.48
end_if
end_if
                ; specify specific heat capacity of calcite
if density(i,j)<3000 and
if (temp(i,j)+273)<500 then
spec_heat(i,j)=(1.155*(temp(i,j)+273))+473.51
end_if
end_if
if density(i,j)<3000 and
if (temp(i,j)+273) >= 500 then
spec_heat(i,j)=(0.375*(temp(i,j)+273))+863.5
end_if
end_if
        ; specify thermal conductivity of galena
if density(i,j)>4000 and
if temp(i,j)<500 then
conductivity(i,j)= ((temp(i,j))*(-0.00196))+2.83
end_if
end_if
```

```
if density(i,j)>4000 and
if temp(i,j)>= 500 then
conductivity(i,j)= ((temp(i,j))*(-0.00096))+2.33
end_if
end_if
                    ; specify specific heat capacity of galena
if density(i,j)>4000 and
if (temp(i,j)+273)<500 then
spec_heat(i,j)=(0.0311*(temp(i,j)+273))+199.68
end_if
end_if
if density(i,j)>4000 and
if (temp(i,j)+273)>= 500 then
spec_heat(i,j)=(0.03942*(temp(i,j)+273))+195.52
end_if
end_if
                    ; specify thermal expansion coefficient of galena
if density(i,j)>4000 and
if (temp(i,j)+273)<673 then
thexp(i,j)=((0.00667*(temp(i,j)+273))+58.71)*1e-6
end_if
end_if
if density(i,j)>4000 and
if (temp(i,j)+273)>= 673 then
thexp(i,j)=((0.018*(temp(i,j)+273))+51.091)*1e-6
end_if
end_if

end_loop
end_loop
command
end_command
end
```

```
set thdt=0.000001       ; set thermal step time
trop                    ; execute

save galena_calcite_model_finetexture_5%.sav       ; save model
```

Appendix E: Simulation code used for quantifying grain boundary damage

```
restore galena_calcite_model_finetexture_5%.sav  ; restore model

set thdt=0.000001        ; set thermal step time

def source1on            ; apply power density in the absorbent phase
loop i(1,horcoor)
loop j(1,totalheight)
if density(i,j)=7597 then
command
interior source 2.5e10 i=i j=j       ; apply power density of 2.5e10
end_command
end_if
end_loop
end_loop
command
step 100                 ; solve for 100 steps
end_command
trop                     ; update thermal properties
end
                          ; call source1on for required number of steps
def treat
loop n(1,10)
source1on
end_loop
end
treat                    ; treat the ore for (10 ×100 × 0.000001 ) s

 def damage2  ;  define damage function
loop i(1,izones) ; search all zones
loop j(1,jzones) ; search all zones
if model(i,j)#1 then
```

```
if cohesion(i,j)< 27.9e6 and
if density(i,j)=2712.1  then ;  if the cohesive strength is less than the orginal
cohesive strength  and if it is a grain boundary zone, count it
cd=cd+1
end_if
end_if
if tension(i,j) < 12e6 and
if density(i,j)=2712.1 THEN  ;  if the tensile strength is less than the orginal
tensile strength  and if it is a grain boundary zone , count it
td1=td1+1
end_if
end_if
if density(i,j)=2712.1 then
totbd=totbd + 1      ;count total grain boundary zones
end_if
tot=tot+1        ;count total number of zones
end_if
end_loop
end_loop
command
print cd        ; display  number of  zones damaged in cohesion
print td1        ; display number of zones damaged in tension
print tot      ; display total zones
print totbd     ; display total grain boundary zones
end_command
cd=0                    ; start from zero for the next simulation
td1=0                    ; start from zero for the next simulation
totbd=0                  ;start from zero for the next simulation
tot=0                    ;start from zero for the next simulation
end
damage2
```

Appendix F: Data used for constructing damage maps in terms of grain boundary damage for different ores

Appendix F1: Galena-Calcite, Coarse-grained

Pd=1 E+07 W/m^3

Time (s)	0	1	2	4	5	8	10
% damaged zones	0.00	0.00	2.84	13.56	18.14	41.48	56.15

Pd=2.5 E+07 W/m^3

Time (s)	0	0.4	0.8	1.6	2	3.2	4
% damaged zones	0.00	2.37	7.57	29.97	35.17	55.84	71.14

Pd=5 E+07 W/m^3

Time (s)	0	0.2	0.4	0.8	1	1.6	2
% damaged zones	0.00	3.47	14.20	42.90	52.37	77.29	88.64

Pd=7.5 E+07 W/m^3

Time (s)	0	0.13	0.27	0.53	0.67	1.07	1.33
% damaged zones	0.00	4.73	26.97	60.09	73.19	90.06	94.95

Pd=1 E+08 W/m^3

Time (s)	0	0.1	0.2	0.4	0.5	0.8	1
% damaged zones	0.00	5.68	35.80	71.77	82.02	95.43	96.85

Pd=2.5 E+08 W/m^3

Time (s)	0.00	0.02	0.04	0.06	0.08	0.12	0.20
% damaged zones	0.00	2.21	17.19	59.62	81.70	95.11	98.42

Pd=5 E+08 W/m^3

Time(s)	0	0.01	0.02	0.03	0.04	0.06	0.08
% damaged zones	0.00	3.15	36.12	71.45	91.96	97.48	98.11

Pd=7.5 E+08 W/m^3

Time (s)	0	0.01	0.015	0.02	0.03	0.04	0.05
% damaged zones	0.00	10.09	55.21	79.97	96.21	98.11	98.58

Pd=1 E+09 W/m^3

Time (s)	0	0.005	0.01	0.015	0.02	0.025	0.035
% damaged zones	0.00	3.15	48.42	82.49	93.69	97.16	98.74

Pd=2.5 E+09 W/m^3

Time (s)	0	0.002	0.003	0.004	0.005	0.008	0.01
% damaged zones	0.00	4.42	26.03	62.78	83.44	98.11	98.74

Pd=5 E+09 W/m^3

Time (s)	0	0.001	0.0015	0.002	0.0025	0.003	0.005
% damaged zones	0.00	4.42	29.18	64.20	82.33	91.80	98.58

Pd=7.5 E+09 W/m^3

Time (s)	0	0.0005	0.001	0.0015	0.002	0.0025	0.003
% damaged zones	0.00	1.74	29.50	74.76	91.64	97.95	98.26

Pd=1 E+10 W/m^3

Time (s)	0	0.0005	0.00075	0.001	0.00125	0.0015	0.00175
% damaged zones	0.00	4.57	36.59	74.29	91.64	97.79	98.74

Pd=2.5 E+10 W/m^3

Time (s)	0	0.0002	0.0003	0.0004	0.0005	0.0006	0.0007
% damaged zones	0.00	4.57	36.44	70.66	87.54	97.00	98.58

Pd=5 E+10 W/m^3

Time (s)	0	0.0001	0.00015	0.0002	0.00025	0.0003	0.00035
% damaged zones	0.00	4.57	40.69	76.18	95.74	98.11	98.90

Pd=7.5 E+10 W/m^3

Time (s)	0	0.00005	0.0001	0.00015	0.0002	0.00025	0.0003
% damaged zones	0.00	1.89	40.54	84.70	97.95	99.05	99.21

Pd=1 E+11 W/m^3

Time (s)	0	0.00005	0.000075	0.0001	0.000125	0.00015	0.0002
% damaged zones	0.00	4.57	40.06	75.71	92.74	97.79	99.05

Appendix F2: Galena-Calcite, Fine-grained

Pd=1 E+08 W/m^3

Time (s)	0	0.75	1	1.5	2	4	6
% damaged zones	0	2.76	17.11	54.67	69.38	89.12	93.32

Pd=2.5 E+08 W/m^3

Time (s)	0	0.2	0.4	1	1.5	2	3
% damaged zones	0.00	0.61	23.63	77.68	87.98	92.18	93.87

Pd=5 E+08 W/m^3

Time(s)	0	0.1	0.3	0.6	0.8	1.2	1.5
% damaged zones	0.00	1.75	58.19	82.83	89.36	93.28	94.00

Pd=7.5 E+08 W/m^3

Time (s)	0	0.075	0.1	0.2	0.4	0.6	1
% damaged zones	0	7.95	14.61	61.15	83.33	91.48	93.85

Pd=1 E+09 W/m^3

Time (s)	0	0.05	0.1	0.2	0.3	0.4	0.6
% damaged zones	0.00	4.71	37.96	73.98	83.51	90.03	93.47

Pd=2.5 E+09 W/m^3

Time (s)	0	0.01	0.02	0.04	0.08	0.16	0.2
% damaged zones	0.00	4.25	33.49	65.27	85.09	92.23	93.06

Pd=5 E+09 W/m^3

Time(s)	0	0.03	0.005	0.01	0.02	0.04	0.1
% damaged zones	0	1.31	14.26	52.45	76.96	91.09	95.07

Pd=7.5 E+09 W/m^3

Time (s)	0	0.002	0.003	0.009	0.012	0.02	0.03
% damaged zones	0	2.69	23.45	78.49	86.01	92.31	94.00

Pd=1 E+10 W/m^3

Time (s)	0	0.0015	0.002	0.003	0.006	0.01	0.016
% damaged zones	0.00	4.34	20.61	43.54	78.60	91.07	94.24

Pd=2.5 E+10 W/m^3

Time (s)	0	0.0005	0.001	0.0015	0.002	0.003	0.004
% damaged zones	0.00	1.01	38.79	63.19	77.25	90.03	94.96

Pd=5 E+10 W/m^3

Time(s)	0	0.0003	0.0004	0.0005	0.0008	0.0012	0.002
% damaged zones	0.00	11.35	29.50	45.38	75.93	90.65	96.08

Pd=7.5 E+10 W/m^3

Time (s)	0	0.0002	0.0003	0.0004	0.0006	0.0008	0.001
% damaged zones	0.00	11.59	37.91	59.18	81.71	91.59	94.55

Pd=1 E+11 W/m^3

Time (s)	0	0.0001	0.0002	0.0003	0.0005	0.0008	0.001
% damaged zones	0.00	0.11	29.74	58.87	85.57	95.68	96.89

Appendix F3: Magnetite-Dolomite, Coarse-grained

Pd=1 E+08 W/m^3

Time (s)	0	1	2	3	4	5	8
% damaged zones	0.00	1.93	12.50	46.58	76.79	87.05	90.18

Pd=2.5 E+08 W/m^3

Time (s)	0	0.4	0.6	0.8	1	1.5	2
% damaged zones	0.00	11.46	35.12	61.61	80.21	90.48	92.71

Pd=5 E+08 W/m^3

Time (s)	0	0.1	0.2	0.3	0.4	0.5	0.6
% damaged zones	0.00	4.76	42.41	76.49	91.07	94.94	95.54

Pd=7.5 E+08 W/m^3

Time (s)	0	0.05	0.1	0.15	0.2	0.3	0.4
% damaged zones	0.00	3.57	37.35	73.21	88.24	96.28	97.47

Pd=1 E+09 W/m^3

Time (s)	0	0.05	0.075	0.1	0.15	0.2	0.25
% damaged zones	0.00	11.16	58.48	77.08	92.26	95.98	97.32

Pd=2.5 E+09 W/m^3

Time (s)	0	0.005	0.01	0.015	0.02	0.03	0.05
% damaged zones	0.00	0.30	7.29	60.71	90.92	95.68	96.43

Pd=5 E+09 W/m^3

Time (s)	0	0.0025	0.005	0.0075	0.01	0.012	0.015
% damaged zones	0.00	0.30	11.46	81.85	96.88	98.51	98.66

Pd=7.5 E+09 W/m^3

Time (s)	0	0.002	0.003	0.004	0.005	0.008	0.01
% damaged zones	0.00	1.04	6.70	44.35	88.69	98.81	99.11

Pd=1 E+10 W/m^3

Time (s)	0	0.002	0.0025	0.003	0.004	0.005	0.006
% damaged zones	0.00	3.27	13.99	50.60	95.24	98.81	99.11

Pd=2.5 E+10 W/m^3

Time (s)	0	0.0005	0.00075	0.001	0.00125	0.0015	0.002
% damaged zones	0.00	0.60	3.13	27.83	77.83	97.62	99.26

Pd=5 E+10 W/m^3

Time (s)	0	0.0003	0.0004	0.0005	0.0006	0.00075	0.001
% damaged zones	0.00	1.49	5.21	28.42	70.98	98.07	99.40

Pd=7.5 E+10 W/m^3

Time (s)	0	0.0002	0.0003	0.00035	0.0004	0.0005	0.0006
% damaged zones	0.00	1.49	11.31	38.69	68.45	97.77	99.40

Pd=1 E+11 W/m^3

Time (s)	0	0.00015	0.0002	0.00025	0.0003	0.00035	0.0004
% damaged zones	0.00	1.49	5.21	24.70	69.20	92.41	98.66

Appendix F4: Magnetite-Dolomite, Fine-grained

Pd=1 E+9 W/m^3

Time (s)	0	0.1	0.2	0.4	0.6	0.8	1
% damaged zones	0.00	0.00	0.09	10.36	43.16	49.18	51.16

Pd=2.5 E+9 W/m^3

Time (s)	0	0.04	0.08	0.16	0.24	0.32	0.4
% damaged zones	0.00	0.00	4.16	28.37	45.52	55.61	57.26

Pd=5 E+9 W/m^3

Time (s)	0	0.02	0.04	0.08	0.12	0.16	0.2
% damaged zones	0.00	1.20	20.22	61.62	71.16	73.56	74.17

Pd=7.5 E+9 W/m^3

Time (s)	0	0.0133	0.027	0.053	0.08	0.107	0.133
% damaged zones	0.00	4.21	42.89	73.76	80.87	82.38	82.85

Pd=1 E+10 W/m^3

Time (s)	0	0.01	0.015	0.02	0.03	0.04	0.05
% damaged zones	0.00	7.02	33.45	57.71	73.97	81.54	84.57

Pd=2.5 E+10 W/m^3

Time (s)	0	0.002	0.003	0.004	0.005	0.006	0.008
% damaged zones	0.00	2.07	27.79	52.40	69.60	79.62	89.84

Pd=5 E+10 W/m^3

Time (s)	0	0.001	0.0015	0.002	0.0025	0.003	0.005
% damaged zones	0.00	4.50	39.80	66.04	78.73	88.06	97.68

Pd=7.5 E+10 W/m^3

Time (s)	0	0.0005	0.00075	0.001	0.0015	0.002	0.003
% damaged zones	0.00	0.25	21.31	41.71	72.36	90.25	97.64

Pd=1 E+11 W/m^3

Time (s)	0	0.0005	0.00075	0.001	0.00125	0.0015	0.0025
% damaged zones	0.00	3.05	49.46	68.49	79.91	87.80	98.48

Appendix G: Simulation code used for quantifying damage for pulsed wave heating of Galena-calcite

```
restore galena_calcite_coarse_model.sav  ; restore model

set thdt=0.000001        ;  set thermal step

def source1on          ; apply power density in galena (when pulse is on)
loop i(1,horcoor)
loop j(1,totalheight)
if density(i,j)=7597 then
command
interior source 2.5e10 i=i j=j
end_command
end_if
end_loop
end_loop
command
step 100             ; apply for 100 steps ( 100 ×0.000001 s)
end_command
trop
end
                     ; remove the heat source (when pulse is off)
def source1off
loop i(1,horcoor)
loop j(1,totalheight)
if density(i,j)=7597 then
command
interior source 0 i=i j=j        , power density is zero when pulse is off
end_command
end_if
end_loop
end_loop
```

```
command
step 4900          ; heat source is zero for 4900 steps (4900 ×0.000001 s)
end_command
trop
end



def treat          ; define pulse heating
loop n(1,2)
source1on          ; pulse on
source1off         ; pulse off
end_loop
end
treat        ; treat for total step of 2 ×5000 = 10000 steps = 0.001 s
             ; quantify grain boundary damage (refer Appendex d)
def damage2
loop i(1,izones)
loop j(1,jzones)
if model(i,j)#1 then
if cohesion(i,j)< 27.9e6 and
if density(i,j)=2712.1  then
cd=cd+1
end_if
end_if
if tension(i,j) < 12e6 and
if density(i,j)=2712.1 THEN
td1=td1+1
end_if
end_if
if density(i,j)=2712.1 then
totbd=totbd + 1
end_if
```

```
tot=tot+1
end_if
end_loop
end_loop
command
print cd
print td1
print tot
print totbd

end_command

cd=0
td1=0

totbd=0
tot=0
end
damage2          ; Execute
```

Appendix H: Simulation code used for quantifying damage for pulsed wave heating of Magnetite-Dolomite

```
restore magnetite_dolomite_model2.sav ; restore magnetite-dolomite model

set thdt=0.000001   ; set thermal step time



def source1on                ;  apply power density in magnetite(when pulse is on)
loop i(1,horcoor)
loop j(1,totalheight)
if density(i,j)=5206 then
command
interior source 4e9 i=i j=j     ;  apply power density of 4e9 W/m^3
end_command
end_if
end_loop
end_loop
command
step 100            ; apply for 100 steps( 100 ×0.000001 s)
end_command
trop
end
                    ; remove the heat source (when the pulse is off)
def source1off
loop i(1,horcoor)
loop j(1,totalheight)
if density(i,j)=5206 then
command
interior source 0 i=i j=j    ,  power density is zero when pulse is off
end_command
end_if
end_loop
```

```
end_loop
command
step 1900       ; heat source is zero for 1900 steps (1900 ×0.000001 s)
end_command
trop
end

def treat              ; define pulsed heating
loop n(1,5)
source1on         ; pulse on
source1off       ; pulse off
end_loop
end
treat                     ; treat for 5 ×(100 + 1900) = 10000 steps = 0.01 s



        ; Quantify grain boundary damage
def damage2
loop i(1,izones)
loop j(1,jzones)

if model(i,j)#1 then

if cohesion(i,j)< 21.7e6  and
if density(i,j)=3795.1 then  ;  if the cohesive strength is less than the orginal
cohesive strength  and if it is a grain boundary zone, count it

cd=cd+1
end_if
end_if

if tension(i,j) < 11.7e6 and
if density(i,j)=3795.1 then
```

```
td1=td1+1            ;  if the tensile strength is less than the orginal tensile strength
and if it is a grain boundary zone, count it



end_if
end_if

if density(i,j)=3795.1 then      ; count all grain boundary zones
totbd=totbd + 1
end_if

tot=tot+1            ; ; count all zones
end_if
end_loop
end_loop

command
print cd    ; display  number of  zones damaged in Cohesion
print td1 ; display  number of  zones damaged in tension
print tot     ; display  total number of  zones
print totbd ; display  total number of grain boundary zones
end_command
cd=0     ; start from zero for the next simulation
td1=0   ; start from zero for the next simulation
totbd=0 ; start from zero for the next simulation
tot=0     ; start from zero for the next simulation
end
damage2    ; Execute
```

Appendix I: Material parameters used for modelling calcite ore in PFC

```
;fname: mL-param.dat
;
; Must provide functions: {mg_set, mp_set}.
;
;.
;
================================================================
================
def mg_set
  mg_Rrat=1.66 ; set ball size ratio
  mg_ts0=-0.1e6 , set target isotropic stress
end
; ----------------------------------
def mp_set
  ba_rho(1) = 3228.6        ; set density of ball
  ba_Ec(1) = 66e9       ; set ball modulus
  ba_fric(1) = 0.50       ; set friction coefficient
  ; -----
  pb_add = 1            ;add parallel bond
  pb_Ec(1) = 66e9        ; set bond modulus
  pb_sn_mean(1) = 51e6 ; set mean normal strength
  pb_sn_sdev(1) = 10e6  ; set normal  strength std.dev
  pb_ss_mean(1) = 51e6 ; set mean shear strength
  pb_ss_sdev(1) = 10e6 ; set shear strength std.dev
end
;
================================================================
================
Return   ; Execute
;EOF: mL-param.dat
```

Appendix J: Simulation code (PFC_FISH) used for randomly disseminating galena in calcite

```
;fname: group1.dat

restore   all_calcite_model.sav ; restore all calcite model

     ; group calcite
group calcite range x=-20e-3,20e-3  y=-40e-3 ,40e-3
prop dens = 3228.6  range group calcite

 ; randomly generate irregular shaped galena grain in the first quarter
def random1
loop n (1,4)              ; number of grains
xx=(urand*12e-3)
yy=(urand*24e-3)
_xx=-1*xx
_yy=-1*yy
k1=xx+0.75e-3        ; specify grain width
k2=yy+1.5e-3         ; specify grain height
command
group galena range x=xx,k1 y=yy,k2
prop dens = 9044  range group galena ; mechanical properties of galena
prop pb_nstrength=51e6  pb_sstrength=51e6 range group galena
prop pb_kn = 3.2e14  pb_ks =1.28e14 range group galena
prop kn = 1.28e11   ks =51.2e9 range group galena
end_command

command
group galena  range circle center=(xx,yy) rad=0.0005 ; specify grain radius

prop dens = 9044  range group galena; mechanical properties of galena
prop pb_nstrength=51e6  pb_sstrength=51e6 range group galena
```

```
prop pb_kn = 3.2e14  pb_ks =1.28e14 range group galena
prop kn = 1.28e11   ks =51.2e9 range group galena
end_command
end_loop
end
random1

; generate another shape in the same quarter (first)
def random12
loop n (1,3) ; number of grains
xx=(urand*12e-3)
yy=(urand*24e-3)
_xx=-1*xx
_yy=-1*yy
k1=xx+0.75e-3 ; specify grain width
k2=yy+1.5e-3; specify grain height

command
group galena range x=xx,k1 y=yy,k2
prop dens = 9044  range group galena ; mechanical properties of galena
prop pb_nstrength=51e6  pb_sstrength=51e6 range group galena
prop pb_kn = 3.2e14  pb_ks =1.28e14 range group galena
prop kn = 1.28e11   ks =51.2e9 range group galena
end_command



command
group galena  range circle center=(xx,yy) rad=0.00075; specify grain radius
prop dens = 9044  range group galena ; mechanical properties of galena
prop pb_nstrength=51e6  pb_sstrength=51e6 range group galena
prop pb_kn = 3.2e14  pb_ks =1.28e14 range group galena
prop kn = 1.28e11   ks =51.2e9 range group galena
end_command
```

```
end_loop
end
random12
    ; generate another shape in the same quarter(first)
def random13
loop n (1,4)  ; number of grains
xx=(urand*12e-3)
yy=(urand*24e-3)
_xx=-1*xx
_yy=-1*yy
k1=xx+1.5e-3  ; specify grain width
k2=yy+0.75e-3 ; ; specify grain height
command
group galena range x=xx,k1 y=yy,k2

prop dens = 9044  range group galena ; mechanical properties of galena
prop pb_nstrength=51e6  pb_sstrength=51e6 range group galena
prop pb_kn = 3.2e14  pb_ks =1.28e14 range group galena
prop kn = 1.28e11   ks =51.2e9 range group galena
end_command

command
group galena  range circle center=(k1,k2) rad=0.0005; specify grain radius
prop dens = 9044  range group galena
prop pb_nstrength=51e6  pb_sstrength=51e6 range group galena
prop pb_kn = 3.2e14  pb_ks =1.28e14 range group galena
prop kn = 1.28e11   ks =51.2e9 range group galena
end_command

end_loop
end
random13
```

```
generate another shape in the same quarter(first)
def random14
loop n (1,4)  ; number of grains
xx=(urand*12e-3)
yy=(urand*24e-3)
_xx=-1*xx
_yy=-1*yy
k1=xx+1.5e-3    ; specify grain width
k2=yy+0.75e-3 ; specify grain height

command
group galena range x=xx,k1 y=yy,k2

prop dens = 9044  range group galena ; mechanical properties of galena
prop pb_nstrength=51e6  pb_sstrength=51e6 range group galena
prop pb_kn = 3.2e14  pb_ks =1.28e14 range group galena
prop kn = 1.28e11   ks =51.2e9 range group galena
end_command

command
group galena  range circle center=(k1,k2) rad=0.00075; specify grain radius
prop dens = 9044  range group galena ; mechanical properties of galena
prop pb_nstrength=51e6  pb_sstrength=51e6 range group galena
prop pb_kn = 3.2e14  pb_ks =1.28e14 range group galena
prop kn = 1.28e11   ks =51.2e9 range group galena
end_command

end_loop
end
random14



; randomly generate irregular shaped galena grain in the second quarter
```

```
def random21
loop n (1,4)    ; number of grains
xx=(urand*12e-3)
yy=(urand*24e-3)
_xx=-1*xx
_yy=-1*yy
k1=_xx+0.75e-3 ; specify grain width
k2=_yy+1.5e-3; specify grain height



command
group galena  range x=_xx,k1 y=_yy,k2
prop dens = 9044  range group galena ; mechanical properties of galena
prop pb_nstrength=51e6  pb_sstrength=51e6 range group galena
prop pb_kn = 3.2e14  pb_ks =1.28e14 range group galena
prop kn = 1.28e11   ks =51.2e9 range group galena
end_command
command
group galena  range circle center=(_xx,_yy) rad=0.0005
prop dens = 9044  range group galena ; mechanical properties of galena
prop pb_nstrength=51e6  pb_sstrength=51e6 range group galena
prop pb_kn = 3.2e14  pb_ks =1.28e14 range group galena
prop kn = 1.28e11   ks =51.2e9 range group galena
end_command
end_loop
end
random21
; generate another shape in the same quarter(second)

def random22
loop n (1,4)
xx=(urand*12e-3)
```

```
yy=(urand*24e-3)
_xx=-1*xx
_yy=-1*yy
k1=_xx+0.75e-3
k2=_yy+1.5e-3



command
group galena  range x=_xx,k1 y=_yy,k2
prop dens = 9044  range group galena; mechanical properties of galena
prop pb_nstrength=51e6  pb_sstrength=51e6 range group galena
prop pb_kn = 3.2e14  pb_ks =1.28e14 range group galena
prop kn = 1.28e11   ks =51.2e9 range group galena
end_command
command
group galena  range circle center=(_xx,_yy) rad=0.00075
prop dens = 9044  range group galena; mechanical properties of galena
prop pb_nstrength=51e6  pb_sstrength=51e6 range group galena
prop pb_kn = 3.2e14  pb_ks =1.28e14 range group galena
prop kn = 1.28e11   ks =51.2e9 range group galena
end_command
end_loop
end
random22
;generate another shape in the same quarter(second)

def random23
loop n (1,3)
xx=(urand*12e-3)
yy=(urand*24e-3)
_xx=-1*xx
_yy=-1*yy
k1=_xx+1.5e-3
```

```
k2=_yy+0.75e-3
command
group galena  range x=_xx,k1 y=_yy,k2
prop dens = 9044  range group galena; mechanical properties of galena
prop pb_nstrength=51e6  pb_sstrength=51e6 range group galena
prop pb_kn = 3.2e14  pb_ks =1.28e14 range group galena
prop kn = 1.28e11   ks =51.2e9 range group galena
end_command
command
group galena  range circle center=(k1,k2) rad=0.0005
prop dens = 9044  range group galena; mechanical properties of galena
prop pb_nstrength=51e6  pb_sstrength=51e6 range group galena
prop pb_kn = 3.2e14  pb_ks =1.28e14 range group galena
prop kn = 1.28e11   ks =51.2e9 range group galena
end_command
end_loop
end
random23
; generate another shape in the same quarter(second)

def random24
loop n (1,3)   ;generate 20 groups
xx=(urand*12e-3)
yy=(urand*24e-3)
_xx=-1*xx
_yy=-1*yy
k1=_xx+1.5e-3
k2=_yy+0.75e-3
command
group galena  range x=_xx,k1 y=_yy,k2
prop dens = 9044  range group galena; mechanical properties of galena
prop pb_nstrength=51e6  pb_sstrength=51e6 range group galena
prop pb_kn = 3.2e14  pb_ks =1.28e14 range group galena
```

```
prop kn = 1.28e11   ks =51.2e9 range group galena
end_command
command
group galena  range circle center=(k1,k2) rad=0.00075
prop dens = 9044  range group galena; mechanical properties of galena
prop pb_nstrength=51e6  pb_sstrength=51e6 range group galena
prop pb_kn = 3.2e14  pb_ks =1.28e14 range group galena
prop kn = 1.28e11   ks =51.2e9 range group galena
end_command
end_loop
end
random24

; randomly generate irregular shaped galena grain in the third quarter

def random31
loop n (1,4)
xx=(urand*12e-3)
yy=(urand*24e-3)
_xx=-1*xx
_yy=-1*yy
k1=_xx+1.5e-3
k2=yy+0.75e-3

command
group galena  range x=_xx,k1 y=yy,k2
prop dens = 9044  range group galena; mechanical properties of galena
prop pb_nstrength=51e6  pb_sstrength=51e6 range group galena
prop pb_kn = 3.2e14  pb_ks =1.28e14 range group galena
prop kn = 1.28e11   ks =51.2e9 range group galena
end_command
command
group galena  range circle center=(k1,k2) rad=0.0005
```

```
prop dens = 9044  range group galena; mechanical properties of galena
prop pb_nstrength=51e6  pb_sstrength=51e6 range group galena
prop pb_kn = 3.2e14  pb_ks =1.28e14 range group galena
prop kn = 1.28e11   ks =51.2e9 range group galena
end_command

end_loop
end
random31
; generate another shape in the same quarter(third)

def random32
loop n (1,4)
xx=(urand*12e-3)
yy=(urand*24e-3)
_xx=-1*xx
_yy=-1*yy
k1=_xx+1.5e-3
k2=yy+0.75e-3

command
group galena  range x=_xx,k1 y=yy,k2
prop dens = 9044  range group galena; mechanical properties of galena
prop pb_nstrength=51e6  pb_sstrength=51e6 range group galena
prop pb_kn = 3.2e14  pb_ks =1.28e14 range group galena
prop kn = 1.28e11   ks =51.2e9 range group galena
end_command
command
group galena  range circle center=(k1,k2) rad=0.00075
prop dens = 9044  range group galena; mechanical properties of galena
prop pb_nstrength=51e6  pb_sstrength=51e6 range group galena
prop pb_kn = 3.2e14  pb_ks =1.28e14 range group galena
prop kn = 1.28e11   ks =51.2e9 range group galena
```

```
end_command

end_loop
end
; generate another shape in the same quarter(third)

random32
def random33
loop n (1,3)
xx=(urand*12e-3)
yy=(urand*24e-3)
_xx=-1*xx
_yy=-1*yy
k1=_xx+0.75e-3
k2=yy+1.5e-3
command
group galena   range x=_xx,k1 y=yy,k2
prop dens = 9044  range group galena; mechanical properties of galena
prop pb_nstrength=51e6  pb_sstrength=51e6 range group galena
prop pb_kn = 3.2e14  pb_ks =1.28e14 range group galena
prop kn = 1.28e11   ks =51.2e9 range group galena
end_command
command
group galena  range circle center=(_xx,yy) rad=0.0005
prop dens = 9044  range group galena; mechanical properties of galena
prop pb_nstrength=51e6  pb_sstrength=51e6 range group galena
prop pb_kn = 3.2e14  pb_ks =1.28e14 range group galena
prop kn = 1.28e11   ks =51.2e9 range group galena
end_command

end_loop
end
random33
```

```
; generate another shape in the same quarter(third)
def random34
loop n (1,3)
xx=(urand*12e-3)
yy=(urand*24e-3)
_xx=-1*xx
_yy=-1*yy
k1=_xx+0.75e-3
k2=yy+1.5e-3
command
group galena   range x=_xx,k1 y=yy,k2
prop dens = 9044  range group galena; mechanical properties of galena
prop pb_nstrength=51e6  pb_sstrength=51e6 range group galena
prop pb_kn = 3.2e14  pb_ks =1.28e14 range group galena
prop kn = 1.28e11   ks =51.2e9 range group galena
end_command
command
group galena  range circle center=(_xx,yy) rad=0.00075
prop dens = 9044  range group galena; mechanical properties of galena
prop pb_nstrength=51e6  pb_sstrength=51e6 range group galena
prop pb_kn = 3.2e14  pb_ks =1.28e14 range group galena
prop kn = 1.28e11   ks =51.2e9 range group galena
end_command

end_loop
end
random34
; randomly generate irregular shaped galena grain in the fourth  quarter

def random41
loop n (1,4)
xx=(urand*12e-3)
yy=(urand*24e-3)
```

```
_xx=-1*xx
_yy=-1*yy
k1=xx+1.5e-3
k2=_yy+0.75e-3

command
group galena range x=xx,k1 y=_yy,k2
prop dens = 9044  range group galena; mechanical properties of galena
prop pb_nstrength=51e6  pb_sstrength=51e6 range group galena
prop pb_kn = 3.2e14  pb_ks =1.28e14 range group galena
prop kn = 1.28e11   ks =51.2e9 range group galena
end_command
command
group galena  range circle center=(xx,_yy) rad=0.0005
prop dens = 9044  range group galena; mechanical properties of galena
prop pb_nstrength=51e6  pb_sstrength=51e6 range group galena
prop pb_kn = 3.2e14  pb_ks =1.28e14 range group galena
prop kn = 1.28e11   ks =51.2e9 range group galena
end_command

end_loop
end
random41
; generate another shape in the same quarter(fourth)

def random42
loop n (1,4)
xx=(urand*12e-3)
yy=(urand*24e-3)
_xx=-1*xx
_yy=-1*yy
k1=xx+2e-3
k2=_yy+0.75e-3
```

```
command
group galena range x=xx,k1 y=_yy,k2
prop dens = 9044  range group galena; mechanical properties of galena
prop pb_nstrength=51e6  pb_sstrength=51e6 range group galena
prop pb_kn = 3.2e14  pb_ks =1.28e14 range group galena
prop kn = 1.28e11   ks =51.2e9 range group galena
end_command
command
group galena  range circle center=(xx,_yy) rad=0.00075
prop dens = 9044  range group galena; mechanical properties of galena
prop pb_nstrength=51e6  pb_sstrength=51e6 range group galena
prop pb_kn = 3.2e14  pb_ks =1.28e14 range group galena
prop kn = 1.28e11   ks =51.2e9 range group galena

end_command

end_loop
end

random42
; generate another shape in the same quarter(fourth)

def random43
loop n (1,3)
xx=(urand*12e-3)
yy=(urand*24e-3)
_xx=-1*xx
_yy=-1*yy
k1=xx+0.75e-3
k2=_yy+1.5e-3
command
group galena range x=xx,k1 y=_yy,k2
prop dens = 9044  range group galena; mechanical properties of galena
```

```
prop pb_nstrength=51e6  pb_sstrength=51e6 range group galena
prop pb_kn = 3.2e14  pb_ks =1.28e14 range group galena
prop kn = 1.28e11   ks =51.2e9 range group galena
end_command
command
group galena  range circle center=(k1,k2) rad=0.00075
prop dens = 9044  range group galena; mechanical properties of galena
prop pb_nstrength=51e6  pb_sstrength=51e6 range group galena
prop pb_kn = 3.2e14  pb_ks =1.28e14 range group galena
prop kn = 1.28e11   ks =51.2e9 range group galena
end_command

end_loop
end
random43

 ; generate another shape in the same quarter(fourth)

def random44
loop n (1,3)
xx=(urand*12e-3)
yy=(urand*24e-3)
_xx=-1*xx
_yy=-1*yy
k1=xx+0.75e-3
k2=_yy+1.5e-3
command
group galena range x=xx,k1 y=_yy,k2
prop dens = 9044  range group galena; mechanical properties of galena
prop pb_nstrength=51e6  pb_sstrength=51e6 range group galena
prop pb_kn = 3.2e14  pb_ks =1.28e14 range group galena
prop kn = 1.28e11   ks =51.2e9 range group galena
end_command
```

```
command
group galena  range circle center=(k1,k2) rad=0.0005
prop dens = 9044  range group galena; mechanical properties of galena
prop pb_nstrength=51e6  pb_sstrength=51e6 range group galena
prop pb_kn = 3.2e14  pb_ks =1.28e14 range group galena
prop kn = 1.28e11   ks =51.2e9 range group galena
end_command

end_loop
end
random44

; show the different mineral phases
plot set title text 'Different mineral phases'
plot creat the_groups3
plot add group BLUE yellow

plot show
print group          ; print the number of balls covered by galena
save galena_calcite_model_ball_new.sav  ; save the model
```

Appendix K: Simulation code (PFC_FISH) used for modelling microwave heating and quantifying microwave-induced micro-cracks in Galena-calcite

```
;fname: heatingmodel_galena-calcite.DAT

; start from new
new
 set safe_conversion on
 SET disk on  ; model unit-thickness cylinders
 SET echo off  ; load support functions
   call %fist%\fist_new.dvr
   call %fist%\2d_3d\md_setup.fis
   call %fist%\2d_3d\md.FIS
   call %fist%\2d\et2.FIS
   call %fist%\2d_3d\flt.FIS
   call %fist%\2d_3d\fishcall.FIS
 SET echo on

restore   galena_calcite_model_ball_new.sav ; restore galena-calcite model
  mv_remove        ; remove walls and allow specimen to relax
  solve ratio=1e-5
  save relaxed2.sav



restore relaxed2.sav     ; restore relaxed model

SET echo off
call crk.FIS      ; call crack FISH function
 SET echo on

crk_init ; Intialize crack
```

```
CONFIG therm
  THERM PROP sheat=817.70 exp=13.1e-6 , specify initial properties
  THERM MAKE conductivity 3.16 measure 2 , specify thermal conductivity
  THERM INIT temp=10.0 , specify initial temperature

def  powerdensity
powerdensity=1e11  ; specify power density
end

thermal set dt_max 1e-6 ; specify thermal step time
thermal set substep  100 ; specify number of mechanical steps per unit thermal
step
; apply power density in galena
def source
bp=ball_head
loop while bp # null
if b_dens(bp)= 9044 then
power_inwatt=powerdensity*(22/7)*b_rad(bp)*b_rad(bp)*1
b_thpsrc(bp)=power_inwatt
end_if
bp=b_next(bp)
end_loop
end
source  ; Execute source(apply power density)
; specify thermal properties
def trop
bp=ball_head
loop while bp # null

; specify specific heat capacity as a function of temperature  for galena
if b_dens(bp) = 9044 &
if (b_thtemp(bp) + 273) < 500 then
b_thsheat(bp)=(0.0311*(b_thtemp(bp)+273))+199.68
```

```
end_if
end_if
if b_dens(bp) = 9044 &
if (b_thtemp(bp) + 273) >=  500 then
b_thsheat(bp)=(0.03942*(b_thtemp(bp)+273))+195.52
end_if
end_if
; specify specific heat capacity of temperature  for calcite
if b_dens(bp) = 3228.6 &
if (b_thtemp(bp) + 273) < 500 then
b_thsheat(bp)=(1.555*(b_thtemp(bp)+273)) + 473.51
end_if
end_if
if b_dens(bp) = 3228.6 &
if (b_thtemp(bp) + 273) >= 550 then
b_thsheat(bp)=(0.375*(b_thtemp(bp)+273))+863.5
end_if
end_if
; specify thermal expansion coefficient as a function of temperature  for galena
if b_dens(bp) = 9044 &
if (b_thtemp(bp) + 273) < 673 then
b_thexp(bp)=((0.00667*(b_thtemp(bp)+273))+58.71)*1e-6
end_if
end_if
if b_dens(bp) = 9044 &
if (b_thtemp(bp) + 273) >= 673 then
b_thexp(bp)=((0.018*(b_thtemp(bp)+273))+51.091)*1e-6
end_if
end_if
; specify thermal expansion coefficient as a function of temperature  for calcite

if b_dens(bp) = 3228.6 &
if (b_thtemp(bp) + 273) < 673 then
```

```
b_thexp(bp)=((0.0233*(b_thtemp(bp)+273))+4.398)*1e-6
end_if
end_if
if b_dens(bp) = 3228.6 &
if (b_thtemp(bp) + 273) >= 673 then
b_thexp(bp)=((0.0195*(b_thtemp(bp)+273))+6.975)*1e-6
end_if
end_if
bp=b_next(bp) ; loop
end_loop
command
step 100   ; treat for 100 steps
end_command
end
      ; call trop for updating thermal properties and treat the material for the
required exposure time
def calltrop
loop n (1,10)
command
trop
end_command
end_loop
end
calltrop      ; Execute
crk_makeview  ; Quantify and plot micro-cracks
plot add group green yellow sort on outline off
plot set background white
plot set foreground blue
plot show              ; Show microwave treated ore
save galena_calcite_coarse_1e11_0.001s.sav ; save microwave treated ore
return
;EOF: heatingmodel.DAT
```

Appendix L: Material parameters used for modelling dolomite ore in PFC

```
;fname: mL-param.dat
; Must provide functions: {mg_set, mp_set}.
;
;;=============================================================
=================
def mg_set
  mg_Rrat=1.66; set ball size ratio
  mg_ts0=-0.1e6, set target isotropic stress
end
; ------------------------------------
def mp_set
  ba_rho(1) = 4517.9 ; set density of ball
  ba_Ec(1) = 95.5e9 ; set ball modulus
  ba_fric(1) = 0.50 ; set friction coefficient
  ; -----
  pb_add = 1 ;add parallel bond
  pb_Ec(1) = 95.5e9 ; set bond modulus
  pb_sn_mean(1) = 49e6; set mean normal strength
  pb_sn_sdev(1) = 10e6; set normal strength std.dev
  pb_ss_mean(1) = 49e6; set mean shear strength
  pb_ss_sdev(1) = 10e6; set shear strength std.dev
end
;
=============================================================
===============
return
;EOF: mL-param.dat
```

Appendix M: Simulation code (PFC_FISH) used for randomly disseminating magnetite in dolomite

```
;fname: group1.dat




restore   all_dolomite_model.sav ; restore all dolomite model
; group dolomite
group Dolomite range x=-20e-3,20e-3  y=-40e-3 ,40e-3
prop dens = 4517.9 range group Dolomite
; randomly generate irregular shaped magnetite grain in the first quarter

def random1
loop n (1,4)       ; number of grains
xx=(urand*12e-3)
yy=(urand*24e-3)
_xx=-1*xx
_yy=-1*yy
k1=xx+0.75e-3; specify grain width
k2=yy+1.5e-3 ; specify grain height
command
group magnetite range x=xx,k1 y=yy,k2
;mechanical properties of magnetite

prop dens = 6197.6   range group magnetite
prop pb_nstrength=56e6  pb_sstrength=56e6 range group magnetite
prop pb_kn = 9.4e14  pb_ks =3.76e14 range group magnetite
prop kn = 3.76e11   ks =1.502e11 range group magnetite
end_command



command
```

```
group magnetite range circle center=(xx,yy) rad=0.0005; specify grain radius
;mechanical properties of magnetite
prop dens = 6197.6   range group magnetite
prop pb_nstrength=56e6  pb_sstrength=56e6 range group magnetite
prop pb_kn = 9.4e14  pb_ks =3.76e14 range group magnetite
prop kn = 3.76e11   ks =1.502e11 range group magnetite
end_command
end_loop
end
random1
; generate another shape in the the same quarter(first)

def random12
loop n (1,3)
xx=(urand*12e-3)
yy=(urand*24e-3)
_xx=-1*xx
_yy=-1*yy
k1=xx+0.75e-3
k2=yy+1.5e-3
command
    ;mechanical properties of magnetite
group magnetite range x=xx,k1 y=yy,k2
prop dens = 6197.6  range group magnetite
prop pb_nstrength=56e6  pb_sstrength=56e6 range group magnetite
prop pb_kn = 9.4e14  pb_ks =3.76e14 range group magnetite
prop kn = 3.76e11   ks =1.502e11 range group magnetite
end_command
command
    ;mechanical properties of magnetite

group magnetite range circle center=(xx,yy) rad=0.00075
```

```
prop dens = 6197.6   range group magnetite
prop pb_nstrength=56e6  pb_sstrength=56e6 range group magnetite
prop pb_kn = 9.4e14  pb_ks =3.76e14 range group magnetite
prop kn = 3.76e11   ks =1.502e11 range group magnetite
end_command
end_loop
end
random12
; generate another shape in the the same quarter(first)

def random13
loop n (1,4)
xx=(urand*12e-3)
yy=(urand*24e-3)
_xx=-1*xx
_yy=-1*yy
k1=xx+1.5e-3
k2=yy+0.75e-3

command
group magnetite range x=xx,k1 y=yy,k2
     ;mechanical properties of magnetite
prop dens = 6197.6   range group magnetite
prop pb_nstrength=56e6  pb_sstrength=56e6 range group magnetite
prop pb_kn = 9.4e14  pb_ks =3.76e14 range group magnetite
prop kn = 3.76e11   ks =1.502e11 range group magnetite
end_command
command
          ;mechanical properties of magnetite

group magnetite range circle center=(k1,k2) rad=0.0005
prop dens = 6197.6  range group magnetite
prop pb_nstrength=56e6  pb_sstrength=56e6 range group magnetite
```

```
prop pb_kn = 9.4e14  pb_ks =3.76e14 range group magnetite
prop kn = 3.76e11   ks =1.502e11 range group magnetite
end_command

end_loop
end
random13
; generate another shape in the the same quarter(first)

def random14
loop n (1,4)
xx=(urand*12e-3)
yy=(urand*24e-3)
_xx=-1*xx
_yy=-1*yy
k1=xx+1.5e-3
k2=yy+0.75e-3

command
group magnetite range x=xx,k1 y=yy,k2
        ;mechanical properties of magnetite
prop dens = 6197.6   range group magnetite
prop pb_nstrength=56e6  pb_sstrength=56e6 range group magnetite
prop pb_kn = 9.4e14  pb_ks =3.76e14 range group magnetite
prop kn = 3.76e11   ks =1.502e11 range group magnetite
end_command
        ;mechanical properties of magnetite
command
group magnetite  range circle center=(k1,k2) rad=0.00075
prop dens = 6197.6   range group magnetite
prop pb_nstrength=56e6  pb_sstrength=56e6 range group magnetite
prop pb_kn = 9.4e14  pb_ks =3.76e14 range group magnetite
prop kn = 3.76e11   ks =1.502e11 range group magnetite
```

```
end_command

end_loop
end
random14



; randomly generate irregular shaped magnetite grain in the second quarter

def random21
loop n (1,4)
xx=(urand*12e-3)
yy=(urand*24e-3)
_xx=-1*xx
_yy=-1*yy
k1=_xx+0.75e-3
k2=_yy+1.5e-3

command
group magnetite range x=_xx,k1 y=_yy,k2
;mechanical properties of magnetite
prop dens = 6197.6   range group magnetite
prop pb_nstrength=56e6  pb_sstrength=56e6 range group magnetite
prop pb_kn = 9.4e14  pb_ks =3.76e14 range group magnetite
prop kn = 3.76e11   ks =1.502e11 range group magnetite
end_command
command
group magnetite  range circle center=(_xx,_yy) rad=0.0005
;mechanical properties of magnetite
prop dens = 6197.6   range group magnetite
prop pb_nstrength=56e6  pb_sstrength=56e6 range group magnetite
prop pb_kn = 9.4e14  pb_ks =3.76e14 range group magnetite
prop kn = 3.76e11   ks =1.502e11 range group magnetite
```

```
end_command
end_loop
end
random21

; generate another shape in the the same quarter(second)

def random22
loop n (1,4)    ;
xx=(urand*12e-3)
yy=(urand*24e-3)
_xx=-1*xx
_yy=-1*yy
k1=_xx+0.75e-3
k2=_yy+1.5e-3



command
group magnetite range x=_xx,k1 y=_yy,k2
;mechanical properties of magnetite
prop dens = 6197.6   range group magnetite
prop pb_nstrength=56e6  pb_sstrength=56e6 range group magnetite
prop pb_kn = 9.4e14  pb_ks =3.76e14 range group magnetite
prop kn = 3.76e11   ks =1.502e11 range group magnetite
end_command
command
group magnetite range circle center=(_xx,_yy) rad=0.00075
;mechanical properties of magnetite
prop dens = 6197.6   range group magnetite
prop pb_nstrength=56e6  pb_sstrength=56e6 range group magnetite
prop pb_kn = 9.4e14  pb_ks =3.76e14 range group magnetite
prop kn = 3.76e11   ks =1.502e11 range group magnetite
end_command
```

```
end_loop
end
random22

; generate another shape in the the same quarter(second)

def random23
loop n (1,3)
xx=(urand*12e-3)
yy=(urand*24e-3)
_xx=-1*xx
_yy=-1*yy
k1=_xx+1.5e-3
k2=_yy+0.75e-3
command
group magnetite  range x=_xx,k1 y=_yy,k2
;mechanical properties of magnetite
prop dens = 6197.6   range group magnetite
prop pb_nstrength=56e6  pb_sstrength=56e6 range group magnetite
prop pb_kn = 9.4e14  pb_ks =3.76e14 range group magnetite
prop kn = 3.76e11   ks =1.502e11 range group magnetite
end_command
command
group magnetite  range circle center=(k1,k2) rad=0.0005
;mechanical properties of magnetite

prop dens = 6197.6   range group magnetite
prop pb_nstrength=56e6  pb_sstrength=56e6 range group magnetite
prop pb_kn = 9.4e14  pb_ks =3.76e14 range group magnetite
prop kn = 3.76e11   ks =1.502e11 range group magnetite
end_command
end_loop
end
```

```
random23
; generate another shape in the the same quarter(second)
def random24
loop n (1,3)
xx=(urand*12e-3)
yy=(urand*24e-3)
_xx=-1*xx
_yy=-1*yy
k1=_xx+1.5e-3
k2=_yy+0.75e-3
command
group magnetite  range x=_xx,k1 y=_yy,k2
;mechanical properties of magnetite
prop dens = 6197.6   range group magnetite
prop pb_nstrength=56e6  pb_sstrength=56e6 range group magnetite
prop pb_kn = 9.4e14  pb_ks =3.76e14 range group magnetite
prop kn = 3.76e11   ks =1.502e11 range group magnetite
end_command
command
group magnetite range circle center=(k1,k2) rad=0.00075
;mechanical properties of magnetite
prop dens = 6197.6   range group magnetite
prop pb_nstrength=56e6  pb_sstrength=56e6 range group magnetite
prop pb_kn = 9.4e14  pb_ks =3.76e14 range group magnetite
prop kn = 3.76e11   ks =1.502e11 range group magnetite
end_command
end_loop
end
random24

; randomly generate irregular shaped magnetite grain in the third  quarter

def random31
```

```
loop n (1,4)
xx=(urand*12e-3)
yy=(urand*24e-3)
_xx=-1*xx
_yy=-1*yy
k1=_xx+1.5e-3
k2=yy+0.75e-3

command
group magnetite range x=_xx,k1 y=yy,k2
;mechanical properties of magnetite
prop dens = 6197.6   range group magnetite
prop pb_nstrength=56e6  pb_sstrength=56e6 range group magnetite
prop pb_kn = 9.4e14  pb_ks =3.76e14 range group magnetite
prop kn = 3.76e11   ks =1.502e11 range group magnetite
end_command
command
group magnetite  range circle center=(k1,k2) rad=0.0005
;mechanical properties of magnetite
prop dens = 6197.6   range group magnetite
prop pb_nstrength=56e6  pb_sstrength=56e6 range group magnetite
prop pb_kn = 9.4e14  pb_ks =3.76e14 range group magnetite
prop kn = 3.76e11   ks =1.502e11 range group magnetite
end_command

end_loop
end
random31



; generate another shape in the the same quarter(third)

def random32
```

```
loop n (1,4)
xx=(urand*12e-3)
yy=(urand*24e-3)
_xx=-1*xx
_yy=-1*yy
k1=_xx+1.5e-3
k2=yy+0.75e-3

command
group magnetite  range x=_xx,k1 y=yy,k2
;mechanical properties of magnetite
prop dens = 6197.6  range group magnetite
prop pb_nstrength=56e6  pb_sstrength=56e6 range group magnetite
prop pb_kn = 9.4e14  pb_ks =3.76e14 range group magnetite
prop kn = 3.76e11   ks =1.502e11 range group magnetite
end_command
command
group magnetite  range circle center=(k1,k2) rad=0.00075
;mechanical properties of magnetite
prop dens = 6197.6  range group magnetite
prop pb_nstrength=56e6  pb_sstrength=56e6 range group magnetite
prop pb_kn = 9.4e14  pb_ks =3.76e14 range group magnetite
prop kn = 3.76e11   ks =1.502e11 range group magnetite
end_command
end_loop
end
random32



; generate another shape in the the same quarter(third)



def random33
```

```
loop n (1,3)
xx=(urand*12e-3)
yy=(urand*24e-3)
_xx=-1*xx
_yy=-1*yy
k1=_xx+0.75e-3
k2=yy+1.5e-3
command
group magnetite   range x=_xx,k1 y=yy,k2
;mechanical properties of magnetite
prop dens = 6197.6  range group magnetite
prop pb_nstrength=56e6  pb_sstrength=56e6 range group magnetite
prop pb_kn = 9.4e14  pb_ks =3.76e14 range group magnetite
prop kn = 3.76e11   ks =1.502e11 range group magnetite
end_command
command
group magnetite  range circle center=(_xx,yy) rad=0.0005
;mechanical properties of magnetite
prop dens = 6197.6  range group magnetite
prop pb_nstrength=56e6  pb_sstrength=56e6 range group magnetite
prop pb_kn = 9.4e14  pb_ks =3.76e14 range group magnetite
prop kn = 3.76e11   ks =1.502e11 range group magnetite
end_command
end_loop
end
random33

; generate another shape in the the same quarter(third)

def random34
loop n (1,3)
xx=(urand*12e-3)
yy=(urand*24e-3)
```

```
_xx=-1*xx
_yy=-1*yy
k1=_xx+0.75e-3
k2=yy+1.5e-3
command
group magnetite  range x=_xx,k1 y=yy,k2
;mechanical properties of magnetite
prop dens = 6197.6   range group magnetite
prop pb_nstrength=56e6  pb_sstrength=56e6 range group magnetite
prop pb_kn = 9.4e14  pb_ks =3.76e14 range group magnetite
prop kn = 3.76e11   ks =1.502e11 range group magnetite
end_command
command
group magnetite range circle center=(_xx,yy) rad=0.00075
;mechanical properties of magnetite
prop dens = 6197.6   range group magnetite
prop pb_nstrength=56e6  pb_sstrength=56e6 range group magnetite
prop pb_kn = 9.4e14  pb_ks =3.76e14 range group magnetite
prop kn = 3.76e11   ks =1.502e11 range group magnetite
end_command

end_loop
end
random34



; randomly generate irregular shaped magnetite grain in the fourth  quarter



def random41
loop n (1,4)
xx=(urand*12e-3)
```

```
yy=(urand*24e-3)
_xx=-1*xx
_yy=-1*yy
k1=xx+1.5e-3
k2=_yy+0.75e-3

command
group magnetite range x=xx,k1 y=_yy,k2
;mechanical properties of magnetite
prop dens = 6197.6   range group magnetite
prop pb_nstrength=56e6  pb_sstrength=56e6 range group magnetite
prop pb_kn = 9.4e14  pb_ks =3.76e14 range group magnetite
prop kn = 3.76e11   ks =1.502e11 range group magnetite
end_command
command
group magnetite  range circle center=(xx,_yy) rad=0.0005
;mechanical properties of magnetite
prop dens = 6197.6   range group magnetite
prop pb_nstrength=56e6  pb_sstrength=56e6 range group magnetite
prop pb_kn = 9.4e14  pb_ks =3.76e14 range group magnetite
prop kn = 3.76e11   ks =1.502e11 range group magnetite
end_command

end_loop
end
random41
; generate another shape in the the same quarter(fourth)



def random42
loop n (1,4)
xx=(urand*12e-3)
yy=(urand*24e-3)
```

```
_xx=-1*xx
_yy=-1*yy
k1=xx+2e-3
k2=_yy+0.75e-3

command
group magnetite range x=xx,k1 y=_yy,k2
;mechanical properties of magnetite
prop dens = 6197.6   range group magnetite
prop pb_nstrength=56e6  pb_sstrength=56e6 range group magnetite
prop pb_kn = 9.4e14  pb_ks =3.76e14 range group magnetite
prop kn = 3.76e11   ks =1.502e11 range group magnetite
end_command
command
group magnetite range circle center=(xx,_yy) rad=0.00075
;mechanical properties of magnetite
prop dens = 6197.6   range group magnetite
prop pb_nstrength=56e6  pb_sstrength=56e6 range group magnetite
prop pb_kn = 9.4e14  pb_ks =3.76e14 range group magnetite
prop kn = 3.76e11   ks =1.502e11 range group magnetite
end_command
end_loop
end
random42

; generate another shape in the the same quarter(fourth)

def random43
loop n (1,3)
xx=(urand*12e-3)
yy=(urand*24e-3)
_xx=-1*xx
_yy=-1*yy
```

```
k1=xx+0.75e-3
k2=_yy+1.5e-3
command
group magnetite range x=xx,k1 y=_yy,k2
;mechanical properties of magnetite
prop dens = 6197.6   range group magnetite
prop pb_nstrength=56e6  pb_sstrength=56e6 range group magnetite
prop pb_kn = 9.4e14  pb_ks =3.76e14 range group magnetite
prop kn = 3.76e11   ks =1.502e11 range group magnetite
end_command
command
group magnetite  range circle center=(k1,k2) rad=0.00075
;mechanical properties of magnetite
prop dens = 6197.6   range group magnetite
prop pb_nstrength=56e6  pb_sstrength=56e6 range group magnetite
prop pb_kn = 9.4e14  pb_ks =3.76e14 range group magnetite
prop kn = 3.76e11   ks =1.502e11 range group magnetite
end_command

end_loop
end
random43
 ; generate another shape in the the same quarter(fourth)

def random44
loop n (1,3)
xx=(urand*12e-3)
yy=(urand*24e-3)
_xx=-1*xx
_yy=-1*yy
k1=xx+0.75e-3
k2=_yy+1.5e-3
command
```

```
group magnetite range x=xx,k1 y=_yy,k2
;mechanical properties of magnetite

prop dens = 6197.6   range group magnetite
prop pb_nstrength=56e6  pb_sstrength=56e6 range group magnetite
prop pb_kn = 9.4e14  pb_ks =3.76e14 range group magnetite
prop kn = 3.76e11   ks =1.502e11 range group magnetite
end_command
command
group magnetite  range circle center=(k1,k2) rad=0.0005
;mechanical properties of magnetite
prop dens = 6197.6  range group magnetite
prop pb_nstrength=56e6  pb_sstrength=56e6 range group magnetite
prop pb_kn = 9.4e14  pb_ks =3.76e14 range group magnetite
prop kn = 3.76e11   ks =1.502e11 range group magnetite
end_command
end_loop
end
random44

plot set title text 'Different mineral phases' ; show different mineral phases
plot creat the_groups3          ; creat groups
plot add group BLUE yellow

plot show
print group ; Print number of balls covered by magnetite
save magnetite_dolomite_model_ball_new.sav ; save treated ore
```

Appendix N: Simulation code (PFC_FISH) used for modelling microwave heating and quantifying microwave-induced micro-cracks in Magnetite-dolomite

```
;fname: heatingmodel_magnetite_dolomite.DAT

; start as a new
New
 set safe_conversion on
 SET disk on  ; model unit-thickness cylinders
 SET echo off  ; load support functions
call %fist%\fist_new.dvr
   call %fist%\2d_3d\md_setup.fis
   call %fist%\2d_3d\md.FIS
   call %fist%\2d\et2.FIS
   call %fist%\2d_3d\flt.FIS
   call %fist%\2d_3d\fishcall.FIS
 SET echo on



restore magnetite_dolomite_model_ball_new.sav  ; restore

  mv_remove         ; remove walls and allow specimen to relax
  solve ratio=1e-5
  save relaxed2.sav

restore relaxed2.sav ; restore relaxed model

SET echo off
call crk.FIS          ; call crack FISH function
 SET echo on
```

```
crk_init          ; initialize cracks




CONFIG therm
  THERM PROP sheat=838.4 exp=18.4   ; set initial properties(not actual)
  THERM MAKE conductivity 4.78 measure 2    ; set thermal conductivity
  THERM INIT temp=10.0        ; set initial temperature

def  powerdensity
powerdensity= 1e10       ; set power density
end

thermal set dt_max 1e-6      ; set thermal step time



      ; specify power density to be applied to magnetite
def source
bp=ball_head
loop while bp # null
if b_dens(bp)= 6197.6 then
power_inwatt=powerdensity*(22/7)*b_rad(bp)*b_rad(bp)*1
b_thpsrc(bp)=power_inwatt
end_if
bp=b_next(bp)
end_loop
end
source        ; execute and apply power density
```

```
  ; specify thermal properties of  minerals as a function of temperature
def trop
bp=ball_head
loop while bp # null

      ; specify specific heat capacity of magnetite
if b_dens(bp) = 6197.6 &
if (b_thtemp(bp) + 273) < 500 then
b_thsheat(bp)=(0.869*(b_thtemp(bp)+273))+395.26
end_if
end_if
if b_dens(bp) = 6197.6 &
if (b_thtemp(bp) + 273) >=  500 then
b_thsheat(bp)=(0.0714*(b_thtemp(bp)+273))+794.12
end_if
end_if
; specify specific heat capacity of dolomite

if b_dens(bp) = 4517.9 &
if (b_thtemp(bp) + 273) < 500 then
b_thsheat(bp)=(0.867*(b_thtemp(bp)+273))+580.58
end_if
end_if
if b_dens(bp) = 4517.9 &
if (b_thtemp(bp) + 273) >= 500 then
b_thsheat(bp)=(0.5*(b_thtemp(bp)+273))+763.63
end_if
end_if
; specify thermal expansion coefficient of magnetite
```

```
if b_dens(bp) = 6197.6 &
if (b_thtemp(bp) + 273)< 673 then
b_thexp(bp)=((0.028*(b_thtemp(bp)+273))+16.056)*1e-6
end_if
end_if
if b_dens(bp) = 6197.6 &
if (b_thtemp(bp) + 273) >= 673 then
b_thexp(bp)=((0.033*(b_thtemp(bp)+273))+12.691)*1e-6
end_if
end_if
; specify thermal expansion coefficient of magnetite

if b_dens(bp) = 4517.9 &
if (b_thtemp(bp) + 273)< 673 then
b_thexp(bp)=((0.0274*(b_thtemp(bp)+273))+8.20)*1e-6
end_if
end_if
if b_dens(bp) = 4517.9 &
if (b_thtemp(bp) + 273) >= 673 then
b_thexp(bp)=((0.0237*(b_thtemp(bp)+273))+10.69)*1e-6
end_if
end_if
bp=b_next(bp)       ; loop next ball
end_loop
command
step 100            ; treat for 100 steps
end_command
end

        ; call trop and treat the material by updating the thermal properties
def calltrop
loop n (1,10)
```

```
command
trop
end_command
end_loop
end

calltrop

crk_makeview     ; quantify and locate micro-cracks



 ; plot the model with micro-cracks
plot add group green yellow sort on outline off
plot set background white
plot set foreground blue
plot show



save magnetite_dolomite_ball_coarse_1e10_0.001s.sav ; save microwave
treated ore



return
;EOF: heatingmodel_magnetite_dolomite.DAT
```

Appendix O: Data used for constructing damage maps in terms of perecentage of micro-cracks for different ores

Appendix O1: Galena-calcite, Coarse-grained

Pd = 1E8 W/m^3

Time(s)	0	0.5	1	2	3	4	5	6	7	8	9	10
Number of Micro-cracks	0	2	21	200	624	890	1200	1411	1611	1772	1911	2090
Micro-cracks (%)	0	0.05	0.48	4.55	14.18	20.23	27.27	32.07	36.61	40.27	43.43	47.50

Pd = 2.5E8 W/m^3

Time(s)	0	0.2	0.4	0.8	1.2	1.6	2	2.4	2.8	3.2	3.6	4
Number of micro-cracks	0	21	169	895	1378	1690	1969	2160	2336	2481	2636	2780
Micro-cracks (%)	0	0.48	3.84	20.34	31.32	38.41	44.75	49.09	53.09	56.39	59.91	63.18

Pd = 5E8 W/m^3

Time(s)	0	0.1	0.2	0.4	0.6	0.8	1	1.2	1.4	1.6	1.8	2
Number of Micro-cracks	0	55	586	1505	2026	2318	2548	2808	3022	3132	3306	3410
Micro-cracks (%)	0.00	1.25	13.32	34.20	46.05	52.68	57.91	63.82	68.68	71.18	75.14	77.50

Pd = 7.5E8 W/m^3

Time(s)	0	0.067	0.133	0.266	0.4	0.53	0.66	0.8	0.93	1.06	1.2	1.33
Number of micro-cracks	0	86	849	1873	2347	2702	2946	3163	3304	3414	3556	3631
Micro-cracks (%)	0.00	1.95	19.30	42.57	53.34	61.41	66.95	71.89	75.09	77.59	80.82	82.52

Pd = 1E9 W/m^3

Time(s)	0	0.05	0.1	0.2	0.3	0.4	0.5	0.6	0.7	0.8	0.9	1
Number of Micro-cracks	0	115	1068	2164	2653	3045	3269	3428	3574	3688	3770	3853
Micro-cracks (%)	0.00	2.61	24.27	49.18	60.30	69.20	74.30	77.91	81.23	83.82	85.68	87.57

Pd = 2.5E9 W/m^3

Time(s)	0.00	0.02	0.04	0.08	0.12	0.16	0.20	0.24	0.28	0.32	0.36	0.40
Number of Micro-cracks	0	242	1504	2746	3315	3606	3811	3928	4014	4099	4145	4210
Micro-cracks (%)	0.00	5.50	34.18	62.41	75.34	81.95	86.61	89.27	91.23	93.16	94.20	95.68

Pd = 5E9 W/m^3

Time(s)	0	0.01	0.02	0.04	0.06	0.08	0.1	0.12	0.14	0.16	0.18	0.2
Number of Micro-cracks	0	329	1809	3079	3578	3806	3948	4049	4129	4195	4232	4285
Micro-cracks (%)	0.00	7.48	41.11	69.98	81.32	86.50	89.73	92.02	93.84	95.34	96.18	97.39

Pd =7.5 E9 W/m^3

Time(s)	0	0.0067	0.013	0.026	0.04	0.053	0.066	0.08	0.093	0.106	0.12	0.133
Number of Micro-cracks	0	376	1942	3236	3661	3870	4001	4121	4210	4269	4320	4381
Micro-cracks (%)	0.0	8.55	44.14	73.55	83.20	87.95	90.93	93.66	95.68	97.02	98.18	99.57

Pd =1 E10 W/m^3

Time(s)	0	0.005	0.01	0.02	0.03	0.04	0.05	0.06	0.07	0.08	0.09	0.1
Number of Micro-cracks	0	395	2037	3357	3707	3902	4046	4129	4192	4275	4324	4365
Micro-cracks (%)	0.0	8.98	46.30	76.30	84.25	88.68	91.95	93.84	95.27	97.16	98.27	99.20

Pd =2.5 E10 W/m^3

Time(ms)	0	2	4	8	12	16	20	24	28	32	36	40
Number of Micro-cracks	0	459	2155	3495	3835	3992	4098	4175	4238	4300	4351	4386
Micro-cracks (%)	0	10.43	48.98	79.43	87.16	90.73	93.14	94.89	96.32	97.73	98.89	99.68

Pd =5 E10 W/m^3

Time(ms)	0	1	2	4	6	8	10	12	14	16	18	20
Number of Micro-cracks	0	464	2195	3592	3897	4045	4122	4190	4234	4295	4345	4383
Micro-cracks (%)	0	10.55	49.89	81.64	88.57	91.93	93.68	95.23	96.23	97.61	98.75	99.61

Pd =7.5E10 W/m^3

Time(ms)	0	0.67	1.33	2.66	4.00	5.32	6.67	8.00	9.32	10.64	12.00	13.33
Number of Micro-cracks	0	469	2243	3635	3944	4065	4140	4199	4233	4289	4341	4379
Micro-cracks (%)	0	10.66	50.98	82.61	89.64	92.39	94.09	95.43	96.20	97.48	98.66	99.52

Pd =1E11 W/m^3

Time(s)	0	0.5	1	2	3	4	5	6	7	8	9	10
Number of Micro-cracks	0	482	2271	3600	3900	4041	4089	4124	4161	4187	4215	4266
Micro-cracks (%)	0	10.95	51.61	81.82	88.64	91.84	92.93	93.73	94.57	95.16	95.80	96.95

Appendix O2: Galena-calcite, Fine-grained

Pd =1E9 W/m^3

Time(s)	0	0.1	0.2	0.3	0.4	0.5	0.6	0.7	0.8	0.9	1
Number of Micro-cracks	0	15	92	239	456	786	1258	1685	2144	2473	2926
Micro-cracks (%)	0.00	0.17	1.05	2.72	5.18	8.93	14.30	19.15	24.36	28.10	33.25

Pd =2.5 E9 W/m^3

Time(s)	0	0.04	0.08	0.12	0.16	0.2	0.24	0.28	0.32	0.36	0.4
Number of Micro-cracks	0	133	626	1433	2212	2930	3381	3767	4158	4451	4710
Micro-cracks (%)	0.00	1.51	7.11	16.28	25.14	33.30	38.42	42.81	47.25	50.58	53.52

Pd =5 E9 W/m^3

Time(s)	0	0.02	0.04	0.06	0.08	0.1	0.12	0.14	0.16	0.18	0.2
Number of Micro-cracks	0	492	2126	3528	4341	4847	5287	5600	5929	6102	6296
Micro-cracks (%)	0.00	5.59	24.16	40.09	49.33	55.08	60.08	63.64	67.38	69.34	71.55

Pd =7.5 E9 W/m^3

Time(s)	0	0.0133	0.0266	0.04	0.0532	0.0665	0.08	0.0931	0.1064	0.12	0.133
Number of Micro-cracks	0	825	3319	4701	5454	6031	6282	6548	6761	6888	6986
Micro-cracks (%)	0.00	9.38	37.72	53.42	61.98	68.53	71.39	74.41	76.83	78.27	79.39

Pd =1 E10 W/m^3

Time(s)	0	0.01	0.02	0.03	0.04	0.05	0.06	0.07	0.08	0.09	0.1
Number of Micro-cracks	0	1141	4060	5498	6178	6546	6801	6974	7143	7284	7347
Micro-cracks (%)	0.00	12.97	46.14	62.48	70.20	74.39	77.28	79.25	81.17	82.77	83.49

Pd =2.5 E10 W/m^3

Time(s)	0	0.004	0.008	0.012	0.016	0.02	0.024	0.028	0.032	0.036	0.04
Number of Micro-cracks	0	1966	5977	7104	7605	7862	8008	8107	8197	8250	8303
Micro-cracks (%)	0.00	22.34	67.92	80.73	86.42	89.34	91.00	92.13	93.15	93.75	94.35

Pd =5 E10 W/m^3

Time(s)	0	0.002	0.004	0.006	0.008	0.01	0.012	0.014	0.016	0.018	0.02
Number of Micro-cracks	0	2351	6687	7670	8090	8319	8431	8560	8625	8700	8712
Micro-cracks (%)	0.00	26.72	75.99	87.16	91.93	94.53	95.81	97.27	98.01	98.86	99.00

Pd =7.5 E10 W/m^3

Time(ms)	0	1.33	2.66	4.00	5.32	6.65	8.0	9.31	10.64	12.00	13.33
Number of Micro-cracks	0	2510	6916	7910	8278	8461	8551	8636	8689	8733	8754
Micro-cracks (%)	0.00	28.52	78.59	89.89	94.07	96.15	97.17	98.14	98.74	99.24	99.48

Pd =1 E11 W/m^3

Time(s)	0	0.001	0.002	0.003	0.004	0.005	0.006	0.007	0.008	0.009	0.01
Number of Micro-cracks	0	2606	7036	8036	8381	8516	8614	8694	8716	8745	8767
Micro-cracks (%)	0.00	29.61	79.95	91.32	95.24	96.77	97.89	98.80	99.05	99.38	99.63

Appendix O3: Magnetite-dolomite, Coarse-grained

Pd =1E9 W/m^3

Time(s)	0.00	0.10	0.20	0.30	0.40	0.50	0.60	0.70	0.80	0.90	1.00
Number of Micro-cracks	0	13	71	483	720	981	1105	1225	1341	1404	1489
Micro-cracks (%)	0.00	0.36	1.97	13.42	20.00	27.25	30.69	34.03	37.25	39.00	41.36

Pd =2.5E9 W/m^3

Time(s)	0.00	0.04	0.08	0.12	0.16	0.20	0.24	0.28	0.32	0.36	0.40
Number of Micro-cracks	0	17	448	962	1308	1694	1854	2014	2197	2356	2474
Micro-cracks (%)	0.00	0.47	12.44	26.72	36.33	47.06	51.50	55.94	61.03	65.44	68.72

Pd =5E9 W/m^3

Time(s)	0.00	0.02	0.04	0.06	0.08	0.10	0.12	0.14	0.16	0.18	0.20
Number of Micro-cracks	0	31	613	1257	1779	2150	2388	2567	2770	2888	2988
Micro-cracks (%)	0.00	0.86	17.03	34.92	49.42	59.72	66.33	71.31	76.94	80.22	83.00

Pd =7.5E9 W/m^3

Time(s)	0.00	0.01	0.03	0.04	0.05	0.07	0.08	0.09	0.11	0.12	0.13
Number of Micro-cracks	0	42	683	1474	1989	2331	2581	2795	2922	3062	3170
Micro-cracks (%)	0.00	1.17	18.97	40.94	55.25	64.75	71.69	77.64	81.17	85.06	88.06

Pd =1E10 W/m^3

Time(s)	0.00	0.01	0.02	0.03	0.04	0.05	0.06	0.07	0.08	0.09	0.10
Number of Micro-cracks	0	44	750	1587	2022	2409	2721	2929	3074	3167	3282
Micro-cracks (%)	0.00	1.22	20.83	44.08	56.17	66.92	75.58	81.36	85.39	87.97	91.17

Pd =2.5 E10 W/m^3

Time(s)	0	0.004	0.008	0.012	0.016	0.02	0.024	0.028	0.032	0.036	0.04
Number of Micro-cracks	0	58	942	1772	2275	2590	2843	3087	3238	3340	3447
Micro-cracks (%)	0.00	1.61	26.17	49.22	63.19	71.94	78.97	85.75	89.94	92.78	95.75

Pd =5 E10 W/m^3

Time(s)	0	0.002	0.004	0.006	0.008	0.01	0.012	0.014	0.016	0.018	0.02
Number of Micro-cracks	0	64	999	1880	2425	2784	2986	3163	3312	3403	3494
Micro-cracks (%)	0.00	1.78	27.75	52.22	67.36	77.33	82.94	87.86	92.00	94.53	97.06

Pd =7.5 E10 W/m^3

Time(ms)	0	1.33	2.66	4.00	5.32	6.65	8.00	9.31	10.64	12.00	13.33
Number of Micro-cracks	0	64	1008	1939	2431	2831	3089	3242	3358	3461	3567
Micro-cracks (%)	0.00	1.78	28.00	53.86	67.53	78.64	85.81	90.06	93.28	96.14	99.08

Pd =1E11 W/m^3

Time(s)	0	0.001	0.002	0.003	0.004	0.005	0.006	0.007	0.008	0.009	0.01
Number of Micro-cracks	0	64	1009	1957	2449	2837	3089	3271	3383	3459	3520
Micro-cracks (%)	0.00	1.78	28.03	54.36	68.03	78.81	85.81	90.86	93.97	96.08	97.78

Appendix O4: Magnetite-dolomite, Fine-grained

Pd =1E9 W/m^3

Time(s)	0	0.1	0.2	0.3	0.4	0.5	0.6	0.7	0.8	0.9	1
Number of Micro-cracks	0	0	0	2	2	3	4	6	7	8	11
Micro-cracks (%)	0.00	0.00	0.00	0.02	0.02	0.04	0.05	0.07	0.08	0.10	0.13

Pd =2.5 E9 W/m^3

Time(s)	0	0.04	0.08	0.12	0.16	0.2	0.24	0.28	0.32	0.36	0.4
Number of Micro-cracks	0	0	2	6	22	39	53	93	136	200	331
Micro-cracks (%)	0.00	0.00	0.02	0.07	0.26	0.46	0.63	1.11	1.62	2.38	3.94

Pd =5 E9 W/m^3

Time(s)	0	0.02	0.04	0.06	0.08	0.1	0.12	0.14	0.16	0.18	0.2
Number of Micro-cracks	0	1	14	55	137	287	487	732	996	1318	1565
Micro-cracks (%)	0.00	0.01	0.17	0.65	1.63	3.42	5.80	8.71	11.86	15.69	18.63

Pd =7.5 E9 W/m^3

Time(s)	0	0.0133	0.0266	0.04	0.0532	0.0665	0.08	0.0931	0.1064	0.12	0.133
Number of Micro-cracks	0	1	32	175	403	757	1234	1656	1948	2288	2507
Micro-cracks (%)	0.00	0.01	0.38	2.08	4.80	9.01	14.69	19.71	23.19	27.24	29.85

Pd =1E10 W/m^3

Time(s)	0	0.01	0.02	0.03	0.04	0.05	0.06	0.07	0.08	0.09	0.1
Number of Micro-cracks	0	1	70	300	719	1331	1902	2393	2670	3048	3317
Micro-cracks (%)	0.00	0.01	0.83	3.57	8.56	15.85	22.64	28.49	31.79	36.29	39.49

Pd =2.5E10 W/m^3

Time(s)	0	0.004	0.008	0.012	0.016	0.02	0.024	0.028	0.032	0.036	0.04
Number of Micro-cracks	0	5	226	1066	2287	3262	4006	4632	5059	5360	5647
Micro-cracks (%)	0.00	0.06	2.69	12.69	27.23	38.83	47.69	55.14	60.23	63.81	67.23

Pd =5E10 W/m^3

Time(s)	0	0.002	0.004	0.006	0.008	0.01	0.012	0.014	0.016	0.018	0.02
Number of Micro-cracks	0	9	375	1627	3134	4327	5097	5674	6064	6389	6713
Micro-cracks (%)	0.00	0.11	4.46	19.37	37.31	51.51	60.68	67.55	72.19	76.06	79.92

Pd =7.5E10 W/m^3

Time(ms)	0	1.33	2.66	4.00	5.32	6.65	8.00	9.31	10.64	12.00	13.3
Number of Micro-cracks	0	10	449	1861	3600	4778	5525	6156	6535	6872	7137
Micro-cracks (%)	0.00	0.12	5.35	22.15	42.86	56.88	65.77	73.29	77.80	81.81	84.96

Pd =1E11 W/m^3

Time(s)	0	0.001	0.002	0.003	0.004	0.005	0.006	0.007	0.008	0.009	0.01
Number of Micro-cracks	0	12	482	1984	3745	5031	5788	6386	6810	7078	7349
Micro-cracks (%)	0.00	0.14	5.74	23.62	44.58	59.89	68.90	76.02	81.07	84.26	87.49

Appendix P: Simulation code (PFC_FISH) used for modelling single particle compression

```
restore galena_calcite_ball_new_oneparticle_1e9_0.1s.sav ; restore
microwave treated ore

SET THERM OFF MECH ON ; set thermal model off and mechanical model on

def make_walls  ; create walls
  command
    wall id=1 kn=5e8 ks=5E8  nodes (5e-3, 5e-3) (-5e-3, 5e-3)
  end_command
  command
    wall id=2 kn=5E8 ks=5E8 nodes (-5e-3,-5e-3) (5e-3,-5e-3)
  end_command
end
make_walls          ; Execute and make walls
def _vfinal
 _vfinal= 0.2 ; velocity of walls
end

def _nsteps
_nsteps= 2000 ; total number of steps
end
def _nchunks
_nchunks= 80    ; number of steps per iteration
End



def accel_platens
  _niter = _nsteps / _nchunks ; iteration to reach the velocity
  loop _chnk (1,_nchunks)
      _vel = _chnk*(_vfinal/_nchunks)
    _mvel = -_vel
```

```
    command
      wall id 2 yvel= _vel          ; specify velocity of the bottom wall
      wall id 1 yvel= _mvel     ; specify velocity of the top wall
      cycle _niter
    end_command
  end_loop
end
accel_platens      , Execute
```